



University of
Nottingham

UK | CHINA | MALAYSIA

Self-Reporting Scaffolds for *In Situ* Monitoring for Regenerative Medicine and Tissue Engineering Applications

Shehnaz Ahmed
University of Nottingham

A thesis submitted for the degree of
Doctor of Philosophy

September 2017

Abstract

This thesis describes the development and utilisation of a self-reporting scaffold to improve current monitoring methods of the cellular microenvironment.

In vitro tissue models hold a lot of promise for regenerative medicine and tissue engineering. However, many models lack the ability to non-invasively monitor *in situ* cellular responses in a physiologically relevant environment. By development of electrospun self-reporting scaffolds and incorporation of flow culture conditions, this limitation can be overcome. Electrospun matrices have been shown to mimic the structural architecture of the native extracellular matrix, whilst flow conditions have been shown to regulate cellular processes, and enhance mass transport and nutrient exchange throughout polymeric scaffolds. Here we show the development of optically transparent self-reporting electrospun scaffolds that incorporate ratiometric pH-sensitive nanosensors and respond to biological and mechanical cues of the native extracellular matrix through exposure to shear stress. Optically transparent self-reporting scaffolds were fabricated by directly electrospinning pH responsive, ratiometric nanosensors within a gelatin biopolymer matrix. The sensors consist of a porous polyacrylamide matrix which encapsulates pH-sensitive fluorophores that exhibit an additive fluorescent response across the full physiological range between pH 3-8, and a pH-insensitive reference fluorophore. The self-reporting scaffold was able to support cell growth whilst being able to simultaneously monitor local pH changes in real time. A Quasi-Vivo[®] bioreactor system was also used to generate a flow of cell culture medium and expose cell-seeded scaffolds to a continual shear stress. This novel diagnostic scaffold and the use of flow conditions can help simulate enhance the understanding of *in vitro* conditions, and generate advanced simulations *in vivo* to facilitate tissue engineering and regenerative medicine applications.

Acknowledgements

I would like to express my sincere gratitude to my supervisors Dr Jonathan Aylott and Prof Amir Ghaemmaghami for believing in me and providing me with this great opportunity to grow not only as a research scientist, but as a person too. Your guidance, immense knowledge, patience, advice and encouragement throughout my PhD project have been invaluable and much appreciated. In addition, I would like to acknowledge my industrial collaborators Kirkstall Ltd for their input and support throughout my project and the BBSRC for my funding.

I would like to thank my Senior Tutor Dr Tracy Bradshaw for her positivity and support during challenging times.

I would like to acknowledge all of the technical staff including the SLIM AMU team, in particular Ian Ward and Dr Chris Gell for their help and guidance in particular with the DMIRE2 microscope, and Denise Mclean for her help with the TEM imaging. Christine Grainger-Boulton for SEM training, Tom Booth and Paul Cooling for their training on various laboratory machines.

I would like give a special mention to thank my wonderful colleagues Dr Veeren Chauhan and Agatha Joseph for their help and technical guidance with my experimental work and for being great friends to me.

I would also like to thank all of my friends in Boots Science Building D38 lab (Abdolelah Jaradat, Mohammed Elsutohy, Yousif Mohamed, Amjad Abouselo, Leigh-Anne Brace), C24 lab (Jacqueline Hikes) and Life Sciences Building B137b lab (Susu Htwe, Dennis Awuah, Arsalan Latif, Amy Donaldson, Sonali Singh, Reem Alzahri), for your advice, stimulating discussions and making the laboratory a great place to work.

In addition I would like to give a special mention to my best friends Miriam Akram (poodle owner) and Raziyah Khalil. You have both been there for me throughout the good times and the bad times. You have supported, motivated and encouraged me to strive towards my goal and I will be forever thankful. The friendships we have are so valuable and precious to me.

Finally, and most importantly I would like to give a special thanks to my beloved family, my mum, dad, brother, nana, nani and Bobby mama and the rest of my family for their continual support throughout my PhD. I owe a lot to my wonderful family who have encouraged and helped me at every stage of my personal and academic life and have longed to see this achievement come true. I am grateful for all of the sacrifices you have made on my behalf and hope I have made you proud. My beautiful, loving mother, I am so thankful you made my life as easy as possible, you have been so supportive with your frequent visits and weekly supplies of home cooked cuisine. My supportive father you have always been there to listen and help me if I ever needed anything. Lastly, but definitely not least, I would like to thank my amazing brother Luqman Ahmed, our strong brother-sister bond means the world to me, you have always been there for me whenever I have needed help with anything and have always looked out for me.

Table of Contents

Abstract	i
Acknowledgements.....	ii
Table of Contents	iv
Table of Figures.....	viii
List of Tables	xix
Abbreviations.....	xx
Chapter 1 Introduction.....	1
1.1. Importance of tissue engineering & regenerative medicine	2
1.1.1. Pharmaceutical industry	2
1.1.2. Tissue replacement	4
1.2. Components required for tissue engineering and regenerative medicine models	5
1.2.1. Cells & Tissues.....	7
1.2.2. Scaffolds.....	12
1.2.3. Bioreactors	31
1.2.4. Monitoring of culture conditions and tissue constructs	48
1.2.5. Monitoring in bioreactors	57
1.3. Thesis Aim.....	61
Chapter 2 Instrumentation, Materials & Methods.....	63
2.2.1. Instrumentation.....	63

2.1.	Materials.....	74
2.1.1.	Electrospinning.....	74
2.1.2.	Polyacrylamide nanosensors.....	75
2.1.3.	Cell culture	76
2.2.	Methods.....	78
2.2.2.	Electrospinning.....	78
2.2.3.	Crosslinking of electrospun gelatin	79
2.2.4.	Preparation of pH sensitive nanosensors.....	80
2.2.5.	Incorporating nanosensors in electrospun scaffolds	87
2.2.6.	Preparation of scaffolds for cell culture	87
2.2.7.	Calibration of electrospun scaffolds containing nanosensors.....	88
2.2.8.	Cell culture techniques	92
2.2.9.	Wound assays.....	96
2.2.10.	Assembly of the Quasi-Vivo [®] flow systems.....	99
2.2.11.	Statistical analysis	101
Chapter 3	Fabrication and characterisation of self-reporting scaffolds	104
3.1.	Polymers for electrospinning.....	104
3.1.1.	Electrospinning gelatin.....	105
3.1.2.	Electrospinning polyethylene terephthalate (PET)	108
3.2.	Electrospun self-reporting scaffolds	109
3.2.1.	Optical nanosensors.....	111
3.2.2.	Polyacrylamide nanosensors.....	112

3.2.3.	Fluorophores	113
3.3.	Results & Discussion	116
3.3.1.	Characterisation of polyacrylamide nanosensors.....	116
3.3.2.	Scaffold Fabrication Optimisation	123
3.4.	Conclusion.....	137
Chapter 4	Evaluation of flow conditions and wound assays	138
4.1.	Introduction.....	138
4.1.1.	2-D wound assays	139
4.1.2.	3-D wound models.....	141
4.2.	Results & Discussion	144
4.2.1.	Calibrating flow rates of the Quasi-Vivo [®] system	144
4.2.2.	Lung fibroblasts exposed to flow conditions using PET scaffold	146
4.2.3.	Mouse fibroblasts cultured on PET exposed to flow conditions.....	149
4.2.4.	Mouse fibroblasts cultured on electrospun gelatin exposed to flow conditions	154
4.2.5.	Wound assays exposed to flow conditions.....	160
4.3.	Conclusions.....	172
Chapter 5	<i>In situ</i> pH measurements using self-reporting scaffolds	173
5.1.	Introduction.....	173
5.1.1.	Importance of extracellular pH.....	173
5.1.2.	Techniques for monitoring extracellular pH.....	174
5.1.3.	pH electrodes	175
5.1.4.	Optical pH sensors	176

5.1.5.	Self-reporting scaffolds	177
5.2.	Results & Discussion	178
5.2.1.	Monitoring pH gradients using self-reporting scaffolds.....	178
5.2.2.	Culturing fibroblasts upon self-reporting scaffolds.....	183
5.2.3.	Effect of fibroblast culture on self-reporting scaffold calibration.....	184
5.2.4.	Capability of self-reporting scaffold to monitor extracellular pH <i>in situ</i> whilst supporting fibroblast growth	185
5.2.5.	Biological application of using self-reporting scaffold to monitor pH changes due to different rates of proliferation	190
5.3.	Conclusion.....	194
Chapter 6	Conclusions & Future Work	196
6.1.	Summary	196
6.2.	Future Work.....	199
Chapter 7	References.....	202

Table of Figures

Figure 1.1 Drug development pipeline adapted from O’Driscoll ⁶	3
Figure 1.2 Image taken from Sbrana & Ahluwalia ¹⁵ , showing the biochemical, physiochemical and mechanostructural cues present in the cellular microenvironment. The cues written in bold are those which can be controlled by using appropriate in vitro design and engineering.	6
Figure 1.3 Histology of loose areolar connective tissue taken from Gallik ²²	10
Figure 1.4 Schematic of the extracellular matrix taken from Papavasiliou ³⁰	12
Figure 1.5 Schematic of solvent casting/particulate leaching process taken from Sampath et al ⁴⁴	18
Figure 1.6 Schematic of melt moulding process adapted from Janik and Marzec ⁵¹ .	19
Figure 1.7 Schematic of freeze drying adapted from Zhu and Chen ⁵⁵	20
Figure 1.8 Schematic of gas foaming taken from Bak et al ⁵⁹	21
Figure 1.9 Schematic of thermal induction phase separation.	22
Figure 1.10 3D printing schematic taken from Anh-Vu et al ⁶⁴	23
Figure 1.11 Representative SEM images of (A) decellularised lung extracellular matrix, (B) electrospun polyethylene terephthalate showing morphological similarities taken from Harrington et al ³³	25
Figure 1.12 Schematic of the electrospinning set up.	25
Figure 1.13 Schematic of spinner-flask bioreactor taken from Maver et al ⁹⁰	32
Figure 1.14 Schematic of rotating wall vessel taken from Maver et al ⁹⁰	33
Figure 1.15 Schematic of displaying configuration of perfusion bioreactor adapted from Wang et al ⁹³	34
Figure 1.16 Photograph of Mcmb taken from Sbrana and Ahluwalia ¹⁵	37

Figure 1.17 Photographs of (A) McmB (B) Quasi-Vivo®500 showing differences in structure.	38
Figure 1.18 Quasi-Vivo®500 system, photograph taken from Kirkstall Ltd ¹⁰⁴	39
Figure 1.19 Quasi-Vivo®600 system, photographs taken from Kirkstall Ltd ¹⁰⁷	40
Figure 1.20 Quasi-Vivo®900 system, photograph taken from Kirkstall Ltd ¹⁰⁹	41
Figure 1.21 Schematic and photograph showing dimensions in millimetres of QV500 compared to QV900.....	42
Figure 1.22 (A) Schematic of Kiyatec 3DKUBE™ (B) Photograph of 3DKUBE™, taken from Kiyatec ¹¹²	43
Figure 1.23 Schematic and photography of microfluidic device taken from Huh ¹¹⁷	45
Figure 1.24 Schematic of optical biosensor taken from Long et al ¹³¹	53
Figure 1.25 Schematic of quantum dot taken from Rusnano ¹⁴⁵	57
Figure 2.1 Olympus light microscope, Lumenara Infinity2-2 CCD Camera.....	63
Figure 2.2 Jablonski energy diagram adapted from Johnson & Davidson ¹⁵⁵	65
Figure 2.3 Photograph of Nikon Eclipse TE300, optiMOS™ sCMOS camera, objective 10X/0.30, working distance 16.0.	66
Figure 2.4 Bio-Rad Zoe™ fluorescent cell imager.....	67
Figure 2.5 Schematic of the fluorescence spectrometry principle.....	68
Figure 2.6 BMG LABTECH FLUOstar Omega fluorescent plate reader.	69
Figure 2.7 Jeol 6060LV variable pressure scanning electron microscope, (B) Leica EM SCD005 sputter coater.	70
Figure 2.8 Schematic of transmission electron microscope, taken from The Chinese University of Hong Kong ¹⁶⁰	71
Figure 2.9 Malvern Zetasizer Nano ZS.	73
Figure 2.10 Semi-micro electrode for pH measurements.	74
Figure 2.11 (A) Schematic of electrospinning apparatus, (B) Photograph of electrospinning set up.	79

Figure 2.12 (A) Electrospun gelatin scaffolds secured in CellCrowns™ (B) CellCrowns™ placed on a plastic mesh, submerged above 1.25% glutaraldehyde vapours in a glass box.	80
Figure 2.13 Deprotonation reaction of phosphate buffer and citric acid buffer ¹⁷¹	84
Figure 2.14 Molecular structure of resazurin molecule found in AlamarBlue® solution reduced to fluorescent resofurin form.....	93
Figure 2.15 Electrospun polyethylene terephthalate scaffold secured by steel ring in a non-tissue culture plate, (A) cells seeded in the centre of the steel ring $3 \times 10^5/500\mu\text{L}$, $500\mu\text{L}$ cell culture medium placed between the outside of the steel ring and the culture plate, (B) Chemical wound assay using a 5mm filter paper disc cut in half, cell culture medium was removed and the filter paper disc was soaked in 0.1mM sodium hydroxide solution and placed onto the centre of the cell-seeded scaffold for 5 seconds.	98
Figure 2.16 Cell seeded electrospun polyethylene terephthalate scaffold exposed to injury by a burn using a needle for 3 seconds.	99
Figure 2.17 Schematic of QV500 bioreactor set up.....	100
Figure 2.18 (A) Polyethylene electrospun scaffold positioning cells near the top of the Quasi-Vivo® 500 bioreactor, (B) Set up of Quasi-Vivo® 500 system with tubing and bioreactors joined together by Luer connectors (C) Quasi-Vivo® 500 system set up in the incubator.	100
Figure 2.19 (A) Quasi-Vivo® 900 system with silicone tubing connected to bioreactors, (B) Quasi-Vivo® 900 system set up in the incubator.....	101
Figure 3.1 Chemical structure of gelatin.....	106
Figure 3.2 Glutaraldehyde bonding the primary amine groups of the gelatin structure to form cross-linked gelatin, image adapted from Yaohui You et al ²⁰⁰	108
Figure 3.3 Compounds involved in the synthesis of polyester ²⁰⁴	108

Figure 3.4 Schematic of polyacrylamide nanosensors adapted by Chauhan et al ¹⁶³	113
Figure 3.5 Chemical structures showing the ionisation of fluorescein ²²⁵	114
Figure 3.6 Chemical structures and pKa values of pH sensitive fluorophores Fluorescein and Oregon Green.....	114
Figure 3.7 (A) Hydrodynamic size distribution of polyacrylamide nanosensors (B) polydispersity index, (n = 9, 3 separate batches).	117
Figure 3.8 (A-B) Representative transmission electron micrographs of polyacrylamide nanosensors n=3 (A) magnification x10,000, (B) magnification x43,000, (C-D) eSEM by Desai ¹⁷² of polyacrylamide nanosensors (C) magnification x200,000, (D) magnification x100,000.....	118
Figure 3.9 Fluorescence spectra obtained using fluorescence spectrophotometer, nanosensors suspended in buffers pH 3.5 – 8.0. (A) Emission curves of pH responsive FAM & OG, (B) Emission curves of pH non-responsive TAMRA, (C) Ratiometric curve achieved by taking ratio of emission from pH responsive channel and pH non responsive channel 520/577 (n = 3 error ± SD).	119
Figure 3.10 Optical characterisation of the pH response of polyacrylamide nanosensors suspended in buffer solutions ranging from pH 3.5 – 8.0. (A) Representative fluorescent images showing a visual change in the green fluorescence intensity of pH sensitive FAM&OG, (B) emission curves of FAM&OG, (C) emission curve of TAMRA, (D) Ratiometric calibration curve for pH. Data shown are representative of n=3 ± SD, scale bar = 250µm.....	122
Figure 3.11 Fibre diameter distribution and representative SEM images of 10% (w/v) electrospun PET scaffolds with and without the incorporation of nanosensors n=3. (A-B) Electrospun PET with nanosensors, (C-D) Electrospun PET without nanosensors. Magnification x500, scale bar 50µm.....	125

Figure 3.12 Optical characterisation of the pH response of electrospun PET scaffold with incorporated polyacrylamide nanosensors suspended in buffer solutions ranging from pH 3.5 – 8.0. (A) Representative fluorescent images showing a visual change in the green fluorescence intensity of pH sensitive FAM&OG, (B) emission curves of FAM&OG, (C) emission curve of TAMRA, (D) Ratiometric calibration curve for pH. Data shown are representative of $n=3 \pm SD$, scale bar = 250 μm127

Figure 3.13 Optical characterisation of the electrospun PET without polyacrylamide nanosensors buffer solutions ranging from pH 3.5 – 8.0. (A) Representative fluorescent images showing a visual change in the green fluorescence intensity of pH sensitive FAM&OG, (B) emission curves of FAM&OG, (C) emission curve of TAMRA, (D) Ratiometric calibration curve for pH. Data shown are representative of $n=3 \pm SD$, scale bar = 250 μm 128

Figure 3.14 Fibre diameter distribution and representative SEM images of 10% (w/v) electrospun gelatin scaffolds with and without the incorporation of nanosensors $n=3$. (A-B) Electrospun gelatin with nanosensors, (C-D) Electrospun gelatin without nanosensors. Magnification x500, scale bar 50 μm130

Figure 3.15 Fibre diameter distribution and representative SEM images of 10% (w/v) electrospun gelatin scaffolds with and without the incorporation of nanosensors $n=3$. (A-B) Uncrosslinked electrospun gelatin with nanosensors, (C-D) Crosslinked gelatin without nanosensors. Magnification x500, scale bar 50 μm132

Figure 3.16 (A-B) Scanning electron micrographs of uncrosslinked vs crosslinked electrospun gelatin scaffolds, at x5000 magnification taken from Sisson et al²⁴⁵, scale bar = 1 μm . (C-D) SEM images of electrospun gelatin scaffolds with polyacrylamide nanosensors acquired at a similar magnification of x3000 for comparison, scale bar = 5 μm132

Figure 3.17 Representative scanning electron micrographs of water droplet placed on centre of electrospun uncrosslinked and crosslinked gelatin scaffold, water

droplet degrades uncrosslinked scaffold, however crosslinked scaffold retains its structural integrity n=3.	133
Figure 3.18 Optical characterisation of the pH response of polyacrylamide nanosensors incorporated in electrospun gelatin suspended in buffer solutions ranging from pH 3.5 – 8.0. (A) Representative fluorescent images showing a visual change in the green fluorescence intensity of pH sensitive FAM&OG, (B) emission curves of FAM&OG, (C) emission curve of TAMRA, (D) Ratiometric calibration curve for pH. Data shown are representative of n=3 ± SD, scale bar = 250µm.....	135
Figure 3.19 Optical characterisation of electrospun gelatin without polyacrylamide nanosensors suspended in buffer solutions ranging from pH 3.5 – 8.0. (A) Representative fluorescent images showing a visual change in the green fluorescence intensity of pH sensitive FAM&OG, (B) emission curves of FAM&OG, (C) emission curve of TAMRA, (D) Ratiometric calibration curve for pH. Data shown are representative of n=3 ± SD, scale bar = 250µm.....	136
Figure 4.1 Schematic of wound healing assays taken from Riahi et al ²⁵² based on (A) scratching, (B) stamping, (C) solid barrier, (D) liquid barrier, (E) droplet chemical assay, (F) microfluidic chemical assay, (G) electrical assay, and (H) laser ablation	140
Figure 4.2 Calibration of Watson-Marlow peristaltic pump at a range of speeds (revolutions per minute). (A) Volume of media expelled after running the single flow Quasi-Vivo® set up (B) curve relating rpm and flow rate µL/min n=3.	145
Figure 4.3 Peristaltic pumps (A) Parker Hannifin (B) Watson-Marlow.	146
Figure 4.4 Representative scanning electron micrographs of MRC5 human lung fibroblasts cultured on PET scaffold exposed to static vs flow conditions ~ 280µL/min, scale bar = 10µm.	148

Figure 4.5 Representative SEM images of MRC5 lung fibroblasts cultured on electrospun PET scaffolds exposed to static vs flow conditions $\sim 145\mu\text{L}/\text{min}$, scale bar = $20\mu\text{m}$	149
Figure 4.6 NIH 3T3 fibroblasts cultured on electrospun PET scaffolds exposed to static vs flow conditions, fluorescent images of cells cultured in static conditions stained with DAPI, AlexaFluor488 phalloidin and Ki67 (B) AlamarBlue [®] proliferation assay shows proliferation is significantly enhanced when exposed to flow conditions $\sim 8\mu\text{L}/\text{min}$, $p \leq 0.05$, $n=3$, scale bar = $30\mu\text{m}$	152
Figure 4.7 Sirius red stain on cell-seeded PET scaffold to show collagen production by NIH 3T3 fibroblasts exposed to static vs flow culture conditions, (B) Standard curve of known Sirius red concentrations vs absorbance (C) Concentration of bound Sirius Red to collagen produced by NIH 3T3 fibroblasts, $n=3$	153
Figure 4.8 CellCrowns [™] in the Quasi-Vivo [®] 900 system, (A) electrospun gelatin scaffold secured by CellCrown [™] , (B) CellCrown [™] ring, (C) CellCrown [™] rings stacked into the QV900 well, (D) electrospun scaffold placed at the bottom of the bioreactor, (E) scaffold placed in the middle of the bioreactor, (F) scaffold placed towards the top of the bioreactor.	155
Figure 4.9 (A) High magnification x500 scanning electron micrographs of NIH 3T3 fibroblasts seeded on electrospun gelatin scaffold, (B) High magnification x3500 images of a fibroblast, (C) AlamarBlue proliferation assay comparing the proliferation of cells exposed differently to flow, $n=3$	157
Figure 4.10 Fluorescently stained 3T3 fibroblasts cultured on gelatin scaffold whilst exposed to static vs flow conditions. Cells were placed at the top of the bioreactor and were exposed directly to the flow of medium at a rate of $8\mu\text{L}/\text{min}$, $n=3$, scale bar = $150\mu\text{m}$	159
Figure 4.11 HUVECs seeded on electrospun gelatin scaffold exposed to a flow rate of $8\mu\text{L}/\text{min}$, scale bar = $100\mu\text{m}$	160

Figure 4.12 Wound closure in a scratch assay performed on confluent NIH 3T3 mouse fibroblasts on a coverslip by scratching with a 200 μ L pipette tip. (A) shows bright field microscopy images of the extent of the closure under static vs flow conditions, (B) quantifies the percentage wound closure calculated using TScratch software, no significant differences were observed, n=3, scale bar = 250 μ m.162

Figure 4.13 Brightfield and fluorescent time-lapse images of scratch assay performed on 3T3-GFP cells on a coverslip at x5 magnification, n=1, scale bar = 250 μ m.163

Figure 4.14 Wound healing scratch assay performed on confluent NIH 3T3 mouse fibroblasts seeded on electrospun polyethylene terephthalate scaffold using a 200 μ L pipette tip. (A) Cells fixed and stained with AlexaFluor488 phalloidin shows extent of wound closure under static vs flow conditions (B) Representative scanning electron microscopy images shows attempted migration of cells into the wound area, n=3.166

Figure 4.15 (A) Fluorescent images of 3T3 fibroblasts stained with Alexa-Fluor488 phalloidin. Chemical wound assay performed on confluent layer of cells seeded on electrospun polyethylene terephthalate scaffold. Wound area is depicted by the black area in the centre of the cell-seeded scaffold, scale bar 1000 μ m, data shown is representative of n=3 experiments, (B) Visual representation of chemical wound assay, 5mm filter paper soaked in 0.1mM sodium hydroxide and placed in centre of cell-seeded scaffold.168

Figure 4.16 (A) Fluorescent images of 3T3 fibroblasts stained with Alexa-Fluor488 phalloidin. Chemical wound assay performed on confluent layer of cells seeded on electrospun polyethylene terephthalate scaffold. Wound area is depicted by the black area in the centre of the cell-seeded scaffold, scale bar = 1000 μ m, data shown is representative of n=3 experiments (B) , (B) Visual representation of chemical wound assay, 5mm filter paper cut in half soaked in 0.1mM sodium hydroxide and

placed in centre of cell-seeded scaffold. Data shown is representative of n=3 experiments.....169

Figure 4.17 Fluorescent images of 3T3 fibroblasts stained with Alexa-Fluor488 phalloidin. Various wound assays performed on confluent layer of cells seeded electrospun polyethylene terephthalate. Wound assays include a burn assay using a needle, and chemical wound assays using different sized filter paper and cotton bud soaked in 0.1mM sodium hydroxide. Wound area is depicted by the black area in the centre of the cell-seeded scaffold, n=3. Schematic shows visual representation of performed wound assay (not to scale).171

Figure 4.18 Cotton bud assay. Fluorescent images of 3T3 fibroblasts stained with Alexa-Fluor488 phalloidin. Cotton bud soaked in 0.1mM sodium hydroxide assay performed on confluent layer of cells seeded electrospun polyethylene terephthalate. Wound area is depicted by the black area in the centre of the cell-seeded scaffold, data shown is representative of n=3 experiments.....172

Figure 5.1 Calibration of polyacrylamide nanosensors in suspension and self-reporting scaffolds respectively submerged in different buffers, (A) pH heat maps produced using MATLAB, (B) Ratiometric calibration curve of nanosensors in suspension, (C) Ratiometric calibration curve of scaffold. Data shown is representative of n=3 experiments.....179

Figure 5.2 Heat maps generated by MATLAB and ImageJ software display pH gradients. (A) A 2.5µL drop of green dye was pipetted into the centre of a self-reporting scaffold to observe the spreading out of the dye and creation of a gradient. (B) Heat map shows the formation of a pH gradient before and after addition of a drop of pH2 hydrochloric acid, (C) Heat maps show the pH gradients in a self reporting scaffold, and suspension of nanosensors post addition of a larger volume (100µL) of HCl at different pH values, in addition to water, data shown is representative of n=3 experiments, scale bar = 250µm.....182

Figure 5.3 (A) Representative scanning electron micrographs of MRC5 human lung fibroblasts cultured on electrospun gelatin scaffolds with and without sensors, (B) AlamarBlue® proliferation assay, data shown is representative of n=3 experiments, n=3, scale bar = 100µm.184

Figure 5.4 Calibration of self-reporting scaffolds by submerging in buffers ranging from pH 3.5 - 8.0, before and after cell seeding, data shown is representative of n=3 experiments.185

Figure 5.5 Data shown representative of n=3 experiments (A) Representative fluorescent images of the cell-seeded self-reporting scaffold, images taken of FAM&OG - scale bar = 250µm, TAMRA – scale bar = 250µm, Hoechst nuclear stain – scale bar = 100µm, representative SEM images show ECM deposition across scaffold by cells – scale bar = 50µm, (B) Individual calibration of self-reporting scaffolds, (C) Values extrapolated from ratiometric curves, and ratiometric intensities from fluorescent images, (D) equation linking fluorescent intensity to pH.....187

Figure 5.6 (A) Graph displaying the extracellular pH measurements of the cell seeded self reporting scaffold vs control self reporting scaffold with media only, (B) Specific values of extracellular pH measurements using the cell seeded scaffold vs scaffold with media only taken at 25°C, C) pH probe values (D) AlamarBlue® proliferation assay**p<0.01,*P<0.05 n=3.189

Figure 5.7 Photographs to display the visual change in pH of the medium surrounding 3T3 fibroblasts seeded on the self-reporting gelatin scaffold.189

Figure 5.8 Treatment of 3T3-GFP NIH fibroblasts with cis-4-methyl sphingosine (n=3) (A) Fluorescent and brightfield images show no comprised morphology or confluency with the treatment (B) AlamarBlue® proliferation assay shows no significant reduction in proliferation after 24 hour treatment with cis-4-methyl sphingosine, scale bar = 250µm.191

Figure 5.9 3T3-GFP fibroblasts cultured on coverslips at different densities incubated with and without 10 μ M cis-4-methylsphingosine, $p < 0.05$, $n=3$, scale bar = 150 μ m.192

Figure 5.10 Data shown are representative of $n=3$ experiments. 3T3-GFP fibroblasts cultured on self-reporting scaffolds incubated with and without 10 μ M cis-4-methylsphingosine (A) Representative scanning electron micrographs of cells on scaffold, (B) AlamarBlue[®] proliferation data.....194

List of Tables

Table 1.1 Generalised components required to make a 3-Dimensional model to mimic in vivo biological systems, adapted from Birnbaum ¹⁶	7
Table 1.2 Different types of connective tissue taken from OpenStax ²⁰	8
Table 1.3 Summary of functions of the ECM in native tissues and of scaffolds in engineered tissues, adapted from Chan & Leong ³⁷	15
Table 1.4 Summary of the effects on fibre morphology due to the changes in electrospinning parameters, information sourced from Pillay and Haider ^{70,71}	27
Table 1.5 Comparison table of different scaffold fabrication method	30
Table 1.6 Features required for an ideal bioreactor system	33
Table 1.7 A variety of perfusion bioreactors available for cell culture applications...	47
Table 1.8 Different types of biosensors, adapted from Shruti et al ¹²⁵	50
Table 1.9 Types of electrochemical transducers for classified type of measurements, with corresponding analytes to be measured, taken from Thévenot et al ¹³⁰	52
Table 2.1 Volumes of sodium phosphate dibasic (0.2M) and citric acid monohydrate (0.1M) to make different pH buffers	85
Table 3.1 Comparison table of fluorescent nanosensors used for pH sensing adapted from Lobnik et al ²³⁶	115

Abbreviations

2D	2-Dimensional
3D	3-Dimensional
°C	Degrees centigrade
%	Percent
λ_{em}	Wavelength emission
λ_{ex}	Wavelength excitation
ALI	Air-liquid interface
APTES	3-aminopropyltriethoxysilane
BBSRC	Biotechnology and biological sciences research council
bFGF	Basic fibroblast growth factor
CO ₂	Carbon dioxide
DCM	Dichloromethane
DMEM	Dulbecco's modified eagle's medium
DNA	Deoxyribonucleic acid
DS-Red	Discosoma red
ECM	Extracellular matrix
EDC's	Endocrine disrupting chemicals
eSEM	Environmental scanning electron microscopy
F-actin	Filamentous actin
FAM	5-(and-6-)-carboxyfluorescein
FAM-SE	5-(and-6-)-carboxyfluorescein, succinimidyl ester
FBS	Foetal bovine serum
FDA	Food and Drug Administration
GFP	Green fluorescent protein

GTA	Glutaraldehyde
HEK293	Human embryonic kidney cells
HCl	Hydrochloric acid
HFIP	Hexafluoroisopropanol
HUVEC	Human Umbilical Vein Endothelial Cell
LED	Light emitting diode
MCmB	Multichamber modular bioreactor
MEM	Minimum essential medium eagle
NaOH	Sodium hydroxide
OG	Oregon green
OG-SE	Oregon green succinimidyl ester
PBS	Phosphate buffer saline
PDMS	Polydimethylsiloxane
PEBBLEs	Probes encapsulated by biologically localised embedding
PEG	Polyethylene glycol
PET	Polyethylene terephthalate
PCL	Polycaprolactone
PGA	Polyglycolic acid
pKa	Dissociation constant
PLA	Poly lactic acid
PLGA	Poly lactic-co-glycolic acid
PMT	Photomultiplier tube
POP's	Persistent organic pollutants
PVC	Polyvinyl chloride
QDots	Quantum dots
QV	Quasi-Vivo [®]

RNA	Ribonucleic acid
S ₀	Ground state
S ₁	First excited singlet state
S ₂	Second excited singlet state
SD	Standard deviation
SEM	Scanning electron microscopy
SEM	Standard error of mean
TAMRA	6-carboxytetramethylrhodamine
TAMRA-SE	6-carboxytetramethylrhodamine,succinimidyl ester
TEM	Transmission electron microscopy
TEOS	Tetramethylorthosilicate
UV	Ultraviolet
v/v	Volume per volume
w/v	Weight per volume

Chapter 1 Introduction

One of the main aims of this thesis was to fabricate and characterise a self-reporting scaffold to help improve current monitoring methods in tissue engineering and regenerative medicine applications. The importance of tissue engineering and the components required for a tissue engineered model will be discussed in this general introduction. Self-reporting scaffolds are composed of a biomaterial matrix with embedded nanosensors which report a specific analyte concentration via a quantifiable fluorescent signal, whilst supporting tissue growth. The use of fluorescence allows measurements to be taken *in situ* over long time frames which removes the need for invasive techniques that can disturb the cellular microenvironment. Alternative methods to monitoring the microenvironment will be discussed in this chapter. To further enhance our developed monitoring technique, polymeric scaffolds were fabricated via an electrospinning process to mimic and recreate the fibrous structural features of the native extracellular matrix which is important for guiding tissue growth; the various methods for scaffold fabrication will be evaluated in this chapter. In addition, bioreactors were used in combination with the scaffolds to enhance diffusion of oxygen and nutrients throughout the constructs as they have been shown to enhance tissue growth. The different types are available bioreactors will be discussed in this chapter.

1.1. Importance of tissue engineering & regenerative medicine

Tissue engineering can be defined as the combination of scaffolds, cells and biologically active molecules to create functional tissues¹. Whereas, regenerative medicine covers a broader field including tissue engineering, but also incorporates research on self-healing, where the body uses its own systems, or sometimes has help from foreign biological material to create cells and rebuild tissues and organs². Tissue engineering is often performed *in vitro*, which can be defined as the biology of a process which takes place in a culture dish or test tube³. One of the end point goals of engineered tissue *in vitro* is to act as a biological substitute to repair, replace or maintain failing organs or tissues^{2,4}. Tissue engineered constructs also allow us to investigate and model specific cellular processes and interactions in disease or clinical conditions to further improve our understanding and subsequently develop counteracting therapeutics.

1.1.1. Pharmaceutical industry

Creating *in vitro* tissue models allows predictions on drug activity, metabolism and toxicity *in vivo* to be made which is important for drug discovery⁵. The pharmaceutical industry in particular is in need of more physiologically relevant and accurate models due to the rising cost-to-delivery ratios and poor predictive value of existing *in vitro* tests⁵. Figure 1.1 shows the key stages involved in the 12-15 year drug development pipeline when developing a therapeutic.

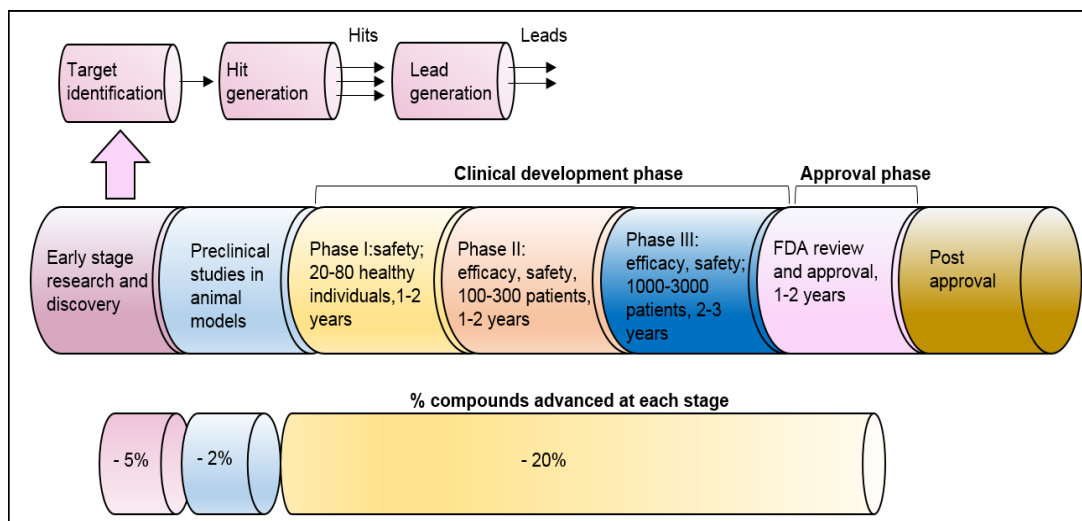


Figure 1.1 Drug development pipeline adapted from O'Driscoll⁶.

The first stages involve early stage research and preclinical studies which involves a variety of high throughput screening of drug candidates to improve the compounds properties⁷. *In vitro* and *ex vivo* assays are then implemented for selectivity and reliability⁷. *In vivo* studies are performed as disease efficacy models, and are used to analyse compound pharmacology and early safety and toxicity⁷. Animals are often used in experimentation because they are systemic, and can provide long term dose-exposure information on the potential harmful effects of a drug metabolised in a human. Most of the failures of the drug occur at the early or preclinical stage, and yet only 20% of compounds that enter human trials are successfully approved, therefore potential 'failures' need to be detected as early in the pipeline as possible to prevent the loss of time and money⁶. Furthermore by creating more advanced *in vitro* models and using *in silico* models as support, we can reduce the need for animal experimentation. UK legislations regulate and restrict the use of animals for scientific research due to ethical and moral reasons by implementation of the Animals (Scientific Procedures) Act 1986⁸. The government also established the National Centre for the Replacement, Refinement and Reduction of Animals in

Research (NC3Rs; London UK) in May 2004 to promote and develop high-quality research that takes the 3Rs into account by limiting and protecting the use of animals in scientific research⁹. Although the overall structure of the immune system in mice and humans is quite similar, significant differences are apparent in immune system development, activation and response to challenge in both the innate and adaptive systems¹⁰. Disadvantages to using animals for experimentation also include the expense, difference in metabolism to humans, licence requirement. Therefore, emphasis should be focused on the research of more complex human conditions than relying on mouse models.

1.1.2. Tissue replacement

Tissue engineering and regenerative medicine can be used in tissue replacement for injured or diseased tissues within patients. A combination of cell types can be seeded onto a scaffold to create a tissue engineered model to mimic interactions in specific complex tissues¹¹. Stem cells can be differentiated into desired tissue lineages, which can allow the production of type-matched tissues for each patient, either through stem cell banking or by the use of therapeutic cloning¹¹. Supplemental skin grafts, small arteries and cartilage have been engineered and implanted into patients but can be very costly¹. More complex organ tissues such as heart, lung and liver tissue have been successfully recreated in the lab lack reproducibility but are not at the stage for implantation¹. One of the reasons for this is because when developing tissue engineered structures for implants, rapid and sufficient vascularisation of the constructs and ample nutrient supply is essential to support graft viability for successful clinical outcomes¹². Therefore recent research has focused on *in vitro* engineering of functional vascular networks which is

expected to lead to more efficient grafting¹². In addition, during implantation of tissue engineered constructs, the injury incurred can trigger an immune response, due to the disruption of host tissue and induction of cell damage. This can then cause the patient to reject the implantation. However, the extent of the inflammatory response is dependent on location, implantation procedure, and biocompatibility of the biomaterial¹³. The natural human host response to the scaffold is an excellent target to modulate and control cell and tissue fate¹³.

1.2. Components required for tissue engineering and regenerative medicine models

When engineering a tissue, recreating and controlling the overall cellular microenvironment is essential as this can strongly influence cell behaviour¹⁴. The cellular microenvironment is made up by factors that directly affect conditions around a cell or a group of cells which have direct or indirect effect on cell behaviour via biophysical, biochemical, or other routes¹⁴. There are two main types of cues within the cellular microenvironment including biochemical and physiochemical¹⁵ as shown in Figure 1.2. Specifically these include: 1) extracellular matrix, 2) homotypic or heterotypic cells surrounding the single cell, 3) cytokines, hormones, and other bioactive agents around the cells due to autocrine, endocrine, and paracrine secretions, 4) nano/microscale topography and physical properties of cells and the ECM, and 5) mechanical forces caused by the movement of the organism or the movement of the physiological fluids such as blood, interstitial¹⁴. Many of these cues (listed in bold of Figure 1.2) can be controlled by careful design and engineering of an *in vitro* model.

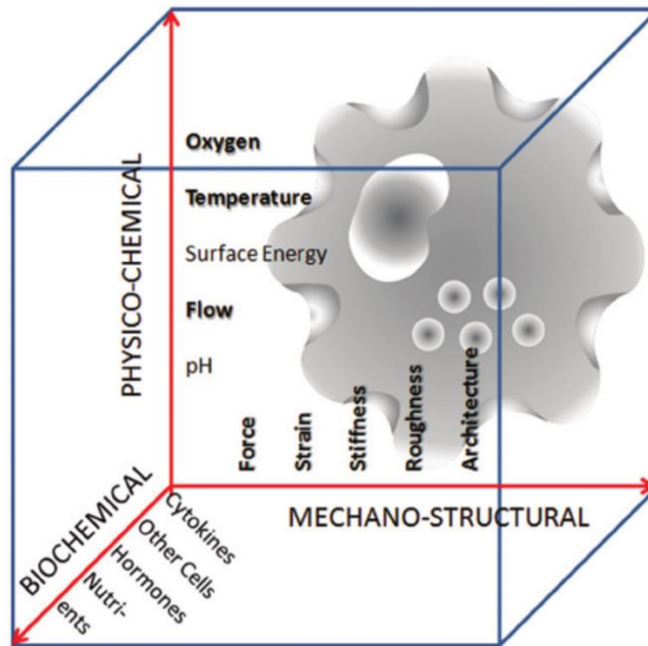


Figure 1.2 Image taken from Sbrana & Ahluwalia¹⁵, showing the biochemical, physiochemical and mechanostructural cues present in the cellular microenvironment. The cues written in bold are those which can be controlled by using appropriate *in vitro* design and engineering.

Tissue constructs are developed in a variety of forms utilising different types of substrates, cell lines and culture conditions to suit a range of specific applications. Birnbaum¹⁶ suggests a variety of components given in Table 1.1 when combined together can create a more biologically relevant 3-Dimensional tissue model compared to conventional 2-Dimensional culture models. However, due to technical challenges and complex interplay between the components it can be difficult to produce a functional model incorporating all of the features.

Component	Details
Scaffold	Purified ECM, synthetic polymers, composites
Cells	Stem/progenitor, differentiated, mixed cell types
Structure	Porosity, topography, stiffness
Spatial/temporal patterning	Cytokines gradients, controlled release
Perfusion	Embedded channels, vascularisation
Bioreactors	Optimised culture conditions, biomechanics
Innervation	Signal propagation, coordinated response
Host response	Generalised inflammation, specific immunity
Functional readout	Real time, label free, non-destructive sensing, imaging
Computational framework	Systems integration, multi-scale modelling, simulation, feedback

Table 1.1 Generalised components required to make a 3-Dimensional model to mimic *in vivo* biological systems, adapted from Birnbaum¹⁶

As listed in Table 1.1, some of the main components required for tissue engineering include cells/tissues, scaffolds, bioreactors and the ability to monitor the cellular microenvironment by providing a functional readout. These will be discussed in more detail below, as they will be the main focus of our proposed tissue model.

1.2.1. Cells & Tissues

Cells are one of the most fundamental requirements when developing an *in vitro* tissue model. They are the basic unit of structure in all living organisms which are responsible for life processes. Within the human body, there are over 200 different types of cells¹⁷. Cells form organised groups known as tissues, which are adapted to carry out specific functions in different regions of the body¹⁸⁻¹⁹. Various cell types can be isolated from specific tissues sourced from organisms such as mice and

humans, and sub-cultured *in vitro* to create models of particular tissues or organs for drug testing or disease modelling applications. The human body is composed of four major types of tissue including epithelial, muscle, nervous and connective¹⁹. Epithelial tissue is made up of tightly packed cells that cover exterior surfaces of the body and lines internal cavities and passageways. Muscle tissue responds to stimulation and contracts to provide movement. Nervous tissue allows the propagation of electrochemical signals in the form of nerve impulses that communicate between different regions of the body. Connective tissues are responsible for binding cells and organs of the body together and functions in the protection, support and integration of all parts of the body²⁰.

1.2.1.1. Connective tissue

Connective tissue will be the focus of this study as it is the most abundant, widely distributed tissue. Connective tissue can be categorised into three main types including connective tissue proper, supportive connective tissue and fluid connective tissue, which contain various sub-groups as given in Table 1.2.

Different types of connective tissue		
Connective tissue proper	Supportive connective tissue	Fluid connective tissue
Loose connective tissue <ul style="list-style-type: none"> • Areolar • Adipose • Reticular 	Cartilage <ul style="list-style-type: none"> • Hyaline • Fibrocartilage • Elastic 	Blood
Dense connective tissue <ul style="list-style-type: none"> • Regular elastic • Irregular elastic 	Bones <ul style="list-style-type: none"> • Compact bone • Cancellous bone 	Lymph

Table 1.2 Different types of connective tissue taken from OpenStax²⁰

Connective tissue usually consists of three main components including fibres, ground substance and cells²¹. Classification of the type of connective tissue involves the identification of the type of cells, fibres and ground substance present. The extracellular fibres can be subdivided into collagen, elastic and reticular fibres which determine the tensile strength and elasticity of a tissue. The ground substance is porous and well-hydrated permitting the rapid diffusion of nutrients, waste metabolites and chemicals between local blood supply and local epithelia. In addition wandering cells such as immune cells which are free to move can rapidly migrate, which is important in immune responses²². Various kinds of cells may reside in the connective tissue according to their location and type of organ or structure, these include; fibroblast, myofibroblast, adipose cells, mast cells, tissue macrophages, white blood cells, osteoblast, chondroblast and blood forming cells²¹.

More specifically, the loose connective tissue is of interest for this study as it is one of the most abundant tissue types. It is found around every blood vessel to keep the vessel in place, and around and between most body organs as support²⁰. Connective tissue tightly binds epithelia to underlying tissue contributing to organ formation, and physically supports blood vessels and nerves that supply the subepithelial area²². Figure 1.3 shows the fibrous structure of the loose areolar connective tissue, which contains collagen and elastic fibres to provide strength and flexibility. The main cell types in the loose connective tissue include fibroblasts and macrophages.

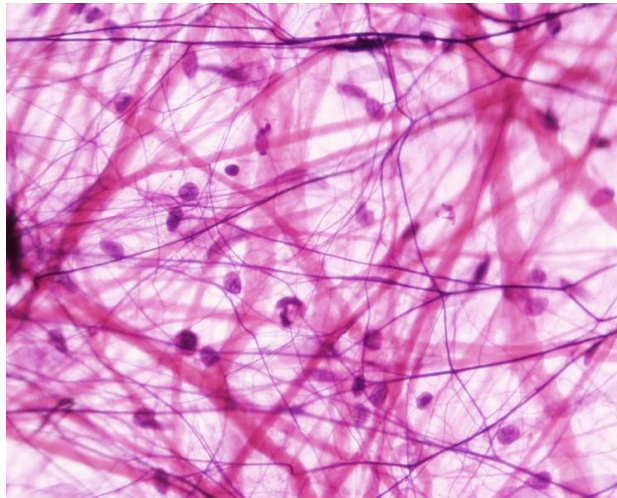


Figure 1.3 Histology of loose areolar connective tissue taken from Gallik²².

1.2.1.2. Fibroblasts

Fibroblasts are spindle shaped cells with a flattened nucleus derived from mesenchymal origin and depending on their location they display multiple morphologies²¹. Fibroblasts are the predominant cell type found in the connective tissue and are involved in various functions including secretion and deposition of the extracellular matrix²³, regulation of epithelial differentiation, regulation of inflammation and involvement in wound healing²⁴. Fibroblasts synthesise many of the fibrillar ECM constituents including type I, type III and type V collagen, and fibronectin. Fibroblasts are also an important source of ECM-degrading proteases such as matrix metalloproteinases (MMPs), which highlights their crucial role in maintaining an ECM homeostasis by regulating ECM turnover²⁴.

Although there are variations in fibroblast subpopulations and subtle differences in fibroblasts isolated from various organs and tissues, these cells exhibit many overriding similarities in appearance and function and are often studied interchangeably from across different tissues and sites of interest²⁵. Fibroblasts can

be easily isolated and grown in culture from many tissues. For example, the spontaneously immortalised 3T3 fibroblast cell line, originally derived from mouse embryo, is widely used in basic cell biology studies²⁵.

1.2.1.3. Extracellular matrix

Within a tissue, a large part of their volume is extracellular space which contains a network of extracellular matrix (ECM) proteins and polysaccharides surrounding the cells²⁶. A schematic showing the main constituents of the ECM are displayed in Figure 1.4. These include collagens, elastin, fibronectin, laminins, glycoproteins, proteoglycans, and glycosaminoglycans which are produced intracellularly by resident cells and secreted by exocytosis²⁷⁻²⁸. This complex network of proteins is important in many processes including cell survival, development, shape, polarity and behaviour²⁶. In addition, most cells need to attach to the extracellular matrix to grow and proliferate, which is referred to as anchorage dependence and is mediated mainly by integrins and the intracellular signals they generate²⁶. Integrins are transmembrane receptors that facilitate interactions between the ECM and the actin cytoskeleton during cell motility and adhesion. Binding specificity is regulated by the extracellular domain of integrins that recognise ligands such as Arg-Glyc-Asp motif (RGD) found on fibronectin²⁹. Electrospun scaffolds have been used in tissue engineering to mimic the structural framework of the extracellular matrix to act as a template for cell growth. Their fibrous porous structure can facilitate cell growth and proliferation, creating more physiologically relevant 3-Dimensional *in vitro* models, compared to conventional 2-D culture in well plates.

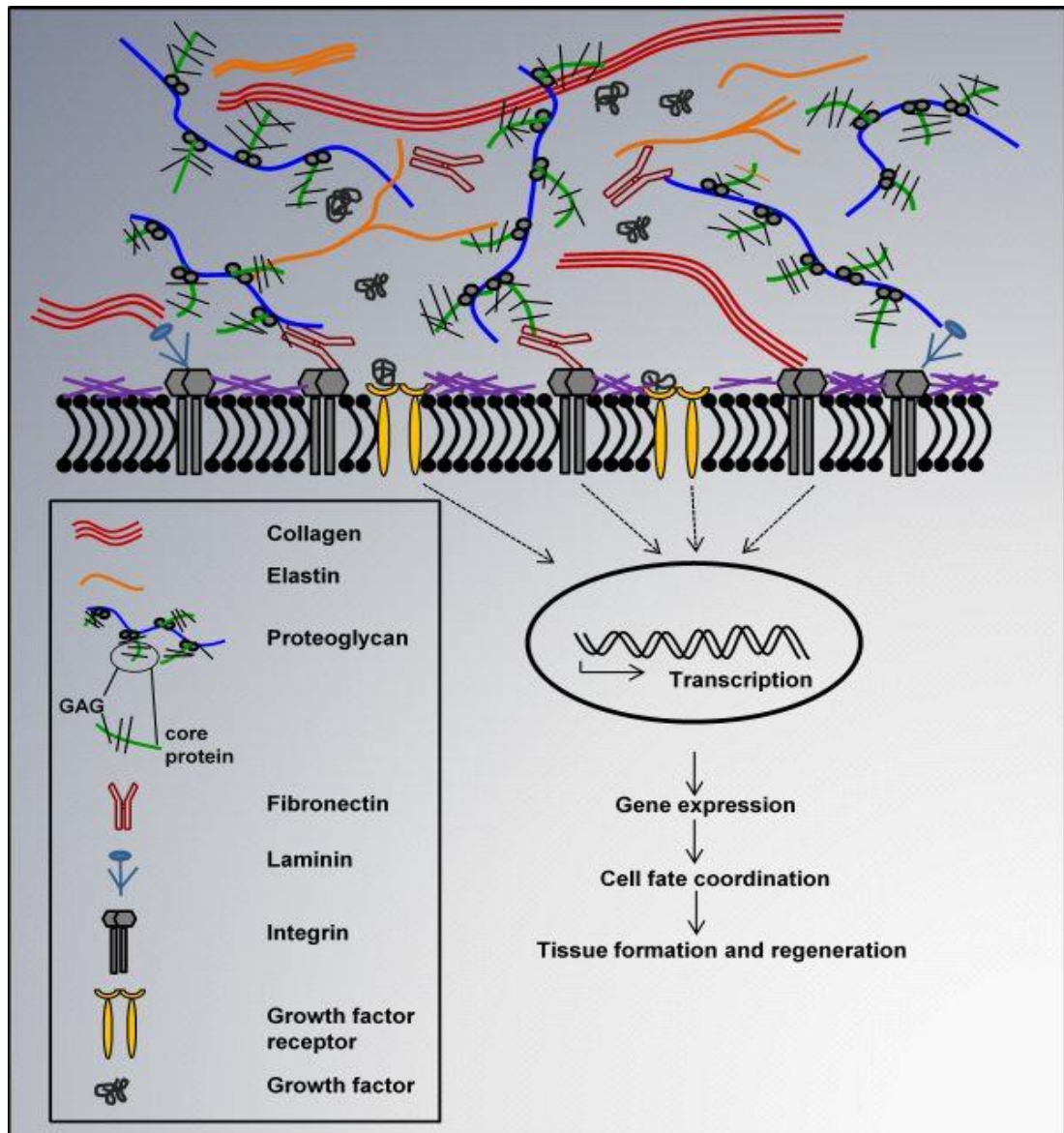


Figure 1.4 Schematic of the extracellular matrix taken from Papavasiliou³⁰.

1.2.2. Scaffolds

Scaffolds are one of the fundamental components of a tissue engineered construct. They can be defined as three-dimensional porous solid biomaterials³¹ where cells can be seeded and the construct will act as template for tissue regeneration to guide the growth of new tissue³². Scaffolds can be fabricated by a variety of methods including electrospinning and 3D printing techniques to create the morphology and

dimensions to mimic the native extracellular matrix³³. They also can be composed of natural or synthetic polymers, or sometimes blends. Natural polymers include purified extracellular matrix proteins which provide biological cues for cell attachment and activity, whilst synthetic polymers give the mechanical support required to maintain the structural framework of the scaffold. When designing the scaffold, parameters such as porosity, topography and stiffness should also be considered as these can affect cell behaviour, such as cellular differentiation³⁴.

Scaffolds not only provide the necessary support for cells to maintain viability, proliferate, and differentiate into specific cells, but they also determine the ultimate shape of the resultant tissue. The attachment, proliferation, and differentiation of cells are strongly affected by the microenvironment associated with a scaffold, including the size, geometry, density of the pores, the windows connecting the pores, and the surface properties³⁵. Scaffolds can act as a template of the extracellular matrix (ECM) to guide cell attachment and tissue formation by providing a platform for structural support³². The complexity of the network of ECM proteins emphasises the importance of preparing a platform that can mimic the structural features of the ECM to facilitate cellular processes including cell adhesion, proliferation and differentiation³⁶. Scaffolds should be porous, to allow efficient nutrient and oxygen diffusion to achieve high cell viability without compromising the mechanical integrity of the scaffold³⁷. If the scaffold is being used for implantation then the scaffold should not induce a severe inflammatory response, as this could reduce healing or cause rejection in the body. Furthermore, scaffolds for implantation should be biodegradable, as the aim is to support the body's own cells to produce their own ECM and replace the implanted tissue engineered construct. Moreover the by-products of this degradation should be non-toxic and exit the body without interfering with other organs³². The chosen scaffold biomaterial should have

biological cues such as cell adhesive ligands to enhance cell attachment or physical cues such as topography to influence cell morphology and alignment³⁷. However, many scaffolds are fabricated from synthetic polymers due to their mechanical strength, so are often coated with natural based polymers/ECM proteins. For example Li et al³⁸ coated electrospun polycaprolactone fibres with gelatin which improved biological activity compared to the uncoated fibres. Gelatin is effective at enhancing cell adhesion because it contains abundant Arg-Gly-Asp (RGD) sequences which are the cell attachment sites recognised by many integrins. The presence of RGD sequences therefore facilitates cell adhesion and spreading³⁹. In addition, Attia et al⁴⁰ coated synthetic polyurethane fibres with a variety of ECM proteins including fibronectin, collagen type I and vitronectin and found that fibronectin demonstrated the greatest cell attachment, and influenced cell spreading and alignment. Fibronectin is a multifunctional glycoprotein present in plasma in a soluble form and in the ECM. It is expressed by many cell types and contributes to cell adhesion, migration, proliferation and tissue development⁴⁰. Some scaffolds can incorporate biomolecules such as growth factors, where the scaffold serves as a delivery vehicle to the cells to accelerate and enhance tissue regeneration³⁷. Growth factors are secreted by cells and act as guidance signals for cell behaviour including cell proliferation, migration, differentiation and tissue regeneration⁴¹. By using an encapsulation technique within scaffold fibres, biomolecules with retained bioactivity can be released in a controlled manner³⁷. However, growth factors often have a short half-life, and being able to deliver the growth factor specifically to the cells can be a drawback during tissue regeneration⁴¹. Some examples of growth factor encapsulation within fibres includes a study by Wang et al⁴². They fabricated electrospun nanofibrous scaffolds and incorporated growth factors including recombinant human vein endothelial growth factor which subsequently enhanced cell viability of human umbilical vein endothelial cells. Zhang et al⁴¹ also prepared

coaxial electrospun fibres with the encapsulation of basic fibroblast growth factor (bFGF) within the core of the fibres. The fibres were able to achieve controlled release of growth factors with different rate and amounts. Table 1.3 describes the functions of the native ECM tissues and the features possessed by scaffolds in order to recreate the biological and biomechanical cues of the ECM.

ECM in native tissues	Scaffolds in engineered tissues
Provides structural support for cells to reside	Porous, interconnected structure to support cell attachment, growth, migration and differentiation.
Contributes to the mechanical properties of the tissues	Provides the shape and mechanical stability to the tissue defect and gives the rigidity and stiffness to the engineered tissues.
Provides bioactive cues for cells to respond to their microenvironment	Can have binding sites such as RGD sequence and surface topography which interacts with cells actively to facilitate activities such as proliferation and differentiation.
Acts as the reservoirs of growth factors and potentiates their actions	Serves as a delivery vehicle and reservoir for applied growth factors.
Provides a flexible physical environment to allow remodelling in response to dynamic tissue processes	Provides a void volume for vascularisation and new tissue formation during remodelling. Porous microstructure allows nutrients and metabolites to diffuse. Degradation mechanisms and rates can be controlled.

Table 1.3 Summary of functions of the ECM in native tissues and of scaffolds in engineered tissues, adapted from Chan & Leong³⁷

1.2.2.1. Scaffold materials (synthetic vs natural polymers)

Scaffold materials can be composed of synthetic or natural polymers which offer different properties such as high porosity, tailored pore sizes, biodegradation, mechanical strength dependent on their composition, structure and arrangement of their constituent macromolecules³¹. They are easy to process and can easily

incorporate bioactive molecules to subsequently mimic the ECM structure. Using synthetic and natural polymers as constructs for tissue engineering has its advantages and disadvantages as reviewed by Bhatia⁴³. However, synthetic polymers are more stable than natural polymers and therefore have a longer shelf life, can be readily sterilised, and are less temperature sensitive than natural polymers. They are also more cost effective than natural polymers, can be produced under controlled conditions, and exhibit predictable and reproducible mechanical and physical properties such as tensile strength, elastic modules and degradation rate. Examples of synthetic polymers used for scaffolds include: poly(vinylchloride), poly(caprolactone), poly(lactic acid), poly(lactic-co-glycolic acid) and poly(ethylene terephthalate). Natural polymers are derived from living sources such as the human body or animals. As natural derivatives, they have bioactive properties which allow them to have better interactions with cells compared to synthetic polymers³¹, in addition to enhanced biocompatibility and less toxicity. Examples of natural polymers used for scaffolds include gelatin, collagen, fibrinogen and elastin.

1.2.2.2. Scaffold fabrication techniques

There are a variety of approaches to fabricate scaffolds for tissue engineering which should consider variables such as biocompatibility, biodegradability, mechanical strength, pore size, scaffold architecture and manufacturing technology³². Each approach has its own advantages and disadvantages in preferred tissue engineering applications, whilst different types of cells prefer different scaffold structures. Various techniques used for scaffold fabrication are described in the following section including solvent-casting and particulate leaching, melt moulding, freeze drying, gas foaming, thermally induced phase separation, hydrogel polymerisation,

3D printing and electrospinning. At the end of this section a summary of the features and drawbacks of the fabrication techniques are given in Table 1.5.

1.2.2.2.1. Solvent casting and particulate-leaching

Solvent casting and particulate-leaching involves a simple and cost effective process of mixing a polymer solution with salt particles of a specific diameter to produce a porous scaffold. The polymer is firstly dissolved in an organic solvent and then poured into a mould containing a porogen such as sodium chloride⁴⁴. The solvent then evaporates leaving behind a polymer matrix with salt particles within. The construct is then immersed in water where the salt particles leach to fabricate a porous structure⁴⁵. An advantage to this technique is that the pore size and overall porosity can be tuned by changing the particle size⁴⁶ which is fairly reproducible. Solvent casted/particulate leached scaffolds can be used for applications such as bone tissue engineering and have been shown to support osteoblastic cell growth and mineral deposition⁴⁷. Constructs have been fabricated from polymers such as FDA approved polycaprolactone which exhibits excellent biocompatibility and mechanical strength⁴⁷. Highly porous scaffolds can be produced which is important for mass transport requirements for cell nutrition, porous channels for cell migration and surface features for cell attachment⁴⁸. However, an increased porosity can compromise the structural stability of the biomaterial, and therefore a balance is needed between the mechanical and mass transport function of the construct to create an optimal scaffold system⁴⁹. A drawback of this method is that new tissue formation is often limited to the surface of the construct with minimum cell growth near the centre of necrotic zones in the centre of the construct⁵⁰. Furthermore solvent residues from the porogen or solvent could be harmful/toxic to cells⁵⁰.

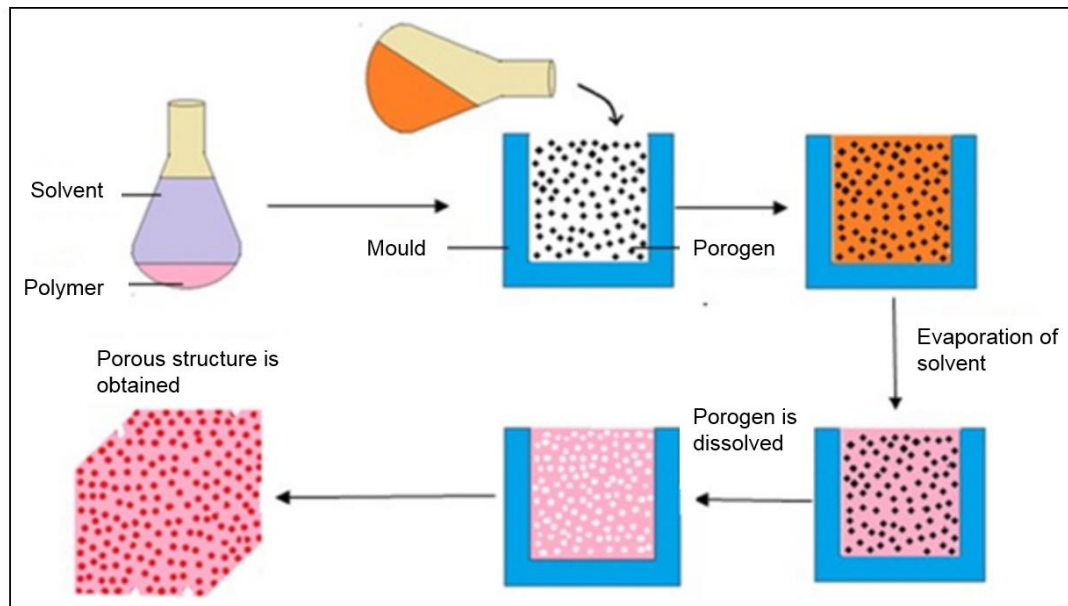


Figure 1.5 Schematic of solvent casting/particulate leaching process taken from Sampath et al⁴⁴.

1.2.2.2. Melt moulding

Melt moulding can be used to create polymeric scaffolds. The process involves filling moulds with a powdered polymer, and porogen compounds above the polymer's glass transition temperature at an elevated pressure⁵¹. These combine together to form a scaffold in the shape of the mould. The scaffold is removed from the mould, and the porogen is leached out by washing with water to yield a porous polymer scaffold⁵². A schematic of the process is shown in Figure 1.6. Heang et al⁵³ fabricated poly(lactic-co-glycolic acid) and poly vinyl alcohol scaffolds blended scaffolds using this technique. The constructs exhibited high porosity and bone formation within the scaffold for bone tissue engineering applications. The advantages of this method is that it is convenient, economical and doesn't require toxic solvents. Furthermore, polymer scaffolds can be rapidly produced of various shapes, sizes and tailored pore size dependent on the porogen used⁵¹. The

limitations of this method involve difficulty in leaching out residual porogens which could affect tissue culture⁵¹. In addition, if incorporating bioactive compounds into the construct, the high temperatures used may destroy the molecules.

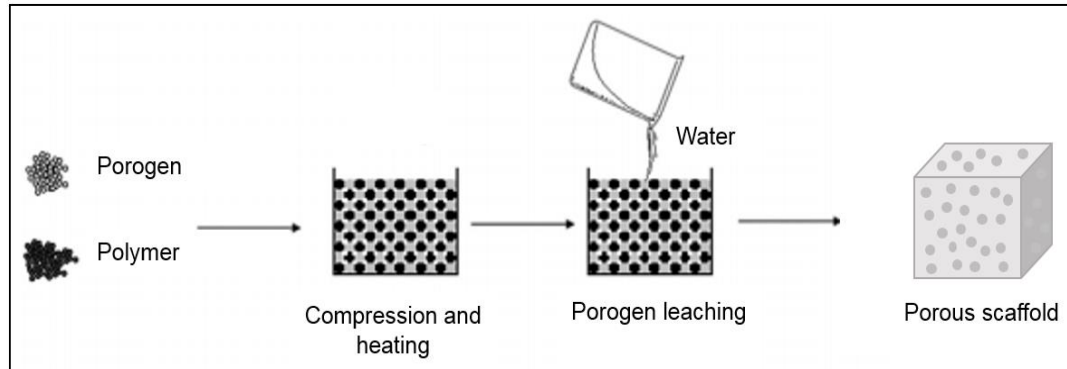


Figure 1.6 Schematic of melt moulding process adapted from Janik and Marzec⁵¹.

1.2.2.2.3. Freeze-drying

Freeze drying is a method used to make porous materials for regenerative medicine applications⁵⁴. The first stage of freeze-drying involves cooling a polymer solution to a frozen state. The solvent then forms ice crystals forcing the polymer molecules to aggregate in between⁵⁵. The solvent is removed by applying pressure and subliming the solvent. This leaves behind a dry polymer scaffold with a highly porous interconnected porous microstructure⁵⁵. The process is shown in the schematic in Figure 1.7. Jin et al⁵⁶ fabricated polycaprolactone/chitosan composite scaffolds via freeze drying for bone regeneration applications. An advantage to the freeze-drying method is that water can be used as the solvent instead of an organic solvent which is more suitable for biomedical applications⁵⁷. A disadvantage to this method is that, although a highly porous construct can be fabricated, it is more difficult to control the pore size.

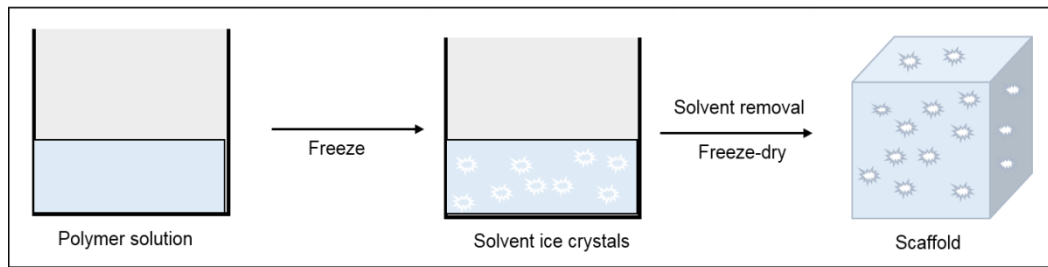


Figure 1.7 Schematic of freeze drying adapted from Zhu and Chen⁵⁵.

1.2.2.2.4. Gas foaming

Gas foaming eliminates the use of harsh chemical solvents by creating highly porous polymer scaffolds by using high pressure carbon dioxide. Solid discs of a polymer such as polyglycolide and poly-L-lactide are first formed by compression moulding at high temperatures⁴⁹. High pressure carbon dioxide (800psi) is then applied to saturate the polymer within an isolated chamber over a certain period of time. Rapid depressurisation causes thermodynamic instability and leads to form nucleated gas cells creating pores inside the polymer matrix⁴⁴. A schematic of the gas foaming chamber is shown in Figure 1.8. Scaffolds sourced from poly(D,L-lactic-co-glycolic acid)/nano-hydroxyapatite (PLGA/HA) have been fabricated by this technique for bone tissue engineering, and have shown to exhibit efficient osteoblast growth and activity for future bone regeneration applications⁵⁸. A disadvantage to this technique is the inability to ensure pore connectivity and control pore sizes by gas forming⁴⁹. In addition high temperatures during disc formation can inhibit the use of bioactive molecules in the scaffolds⁴⁹.

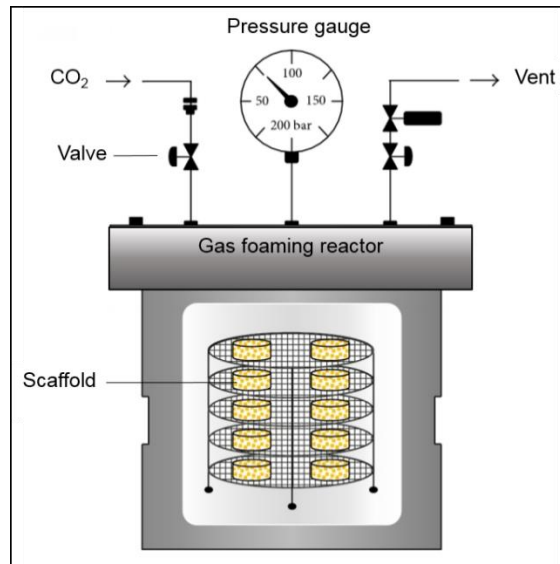


Figure 1.8 Schematic of gas foaming taken from Bak et al⁵⁹.

1.2.2.2.5. Thermally induced phase separation

Phase separation is a thermodynamic process involving the separation of phases due to physical incompatibility to create scaffolds for tissue engineering⁶⁰. The first step in scaffold preparation is to make a uniform and homogeneous polymer solution. The polymer is dissolved in a solvent and becomes thermodynamically unstable by heating the mixture for a certain period of time and temperature, in addition to subsequent cooling. The thermal energy helps induce the phase separation which separates the solution into a polymer rich and polymer lean phase⁶¹. The solvent is then removed by either freeze-drying or freeze-extraction⁶¹. The polymer-rich phase will solidify to form a 3D matrix while the polymer-poor phase will become the void space⁶⁰. The process is demonstrated in a schematic in Figure 1.9. Yen et al⁶² fabricated nanoporous polycaprolactone scaffolds which demonstrated controlled drug release for drug delivery applications. In addition, Conoscenti et al⁶³ fabricated highly porous, well defined pore sized poly(L-lactic acid) scaffolds for bone engineering applications, and demonstrated the scaffolds

were able to support chondrocyte differentiation. An advantage to this technique is that by easily changing parameters such as polymer type, solvent/non-solvent ratio, polymer concentration, heating temperature and time, and cooling rate; porous constructs can be fabricated with specific morphologies for a particular application⁶¹. Thermally induced phase separation is a useful technique for developing scaffolds with well-defined pore shape and pore size and can be combined with other fabrication methods to control the final 3D structure⁶⁰. However, the drawbacks of this technique includes minimal control over fibre orientation and diameter, long fabrication time, and lack of mechanical properties⁶⁰.

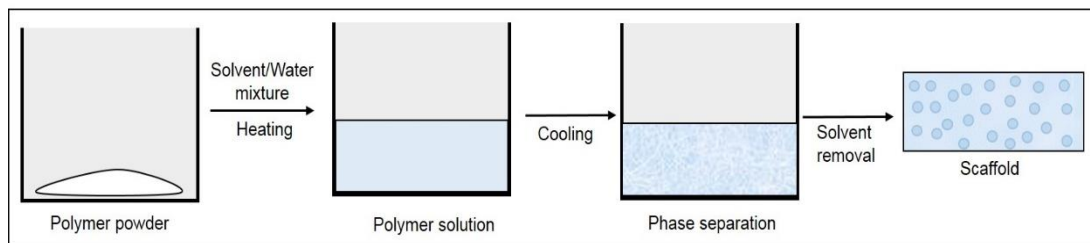


Figure 1.9 Schematic of thermal induction phase separation.

1.2.2.2.6. 3D printing

3D printing uses an inkjet printing liquid binder to make a 3D object from digital model data⁴⁴, as shown in Figure 1.10. The first step of 3D printing involves modelling a virtual model using computer-aided design where the machine uses this as a template to print⁴⁴. A thin layer of powder is deposited onto a powder bed and is spread and levelled onto a building platform using a roller system⁶⁴. The machine reads the design of the digital model data and a printer nozzle selectively lays down liquid binder solution into a powder bed to form a 2D pattern⁴⁴. This process is

repeated layer by layer to produce a 3D model. Once the binder solution and powder are combined the excess unbound powder is removed⁶⁴.

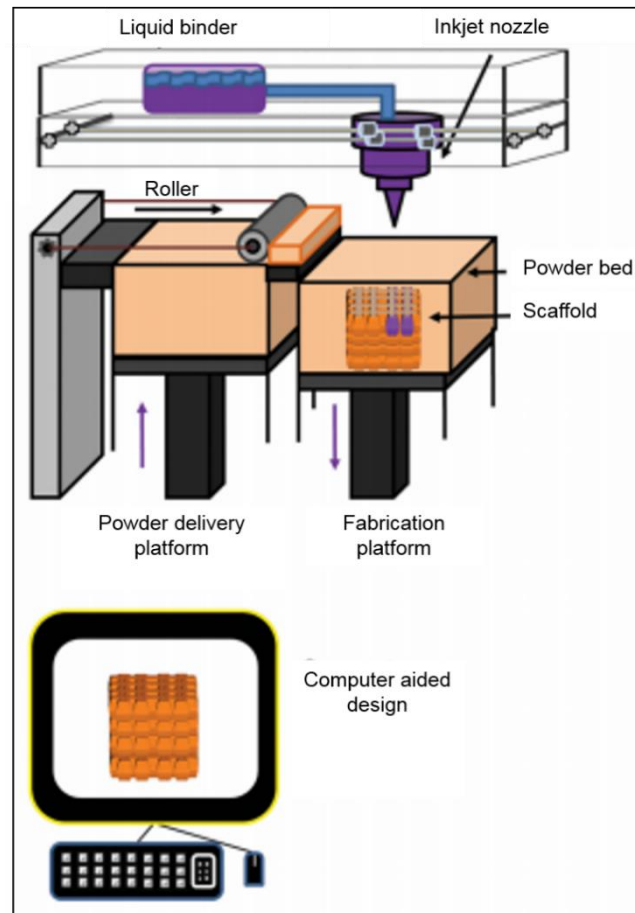


Figure 1.10 3D printing schematic taken from Anh-Vu et al⁶⁴.

Sun et al⁶⁵ fabricated highly porous collagen/silk constructs using 3D printing for applications in bone tissue engineering. They found that bone mesenchymal stem cells were able to maintain their viability, proliferate and deposit ECM proteins efficiently. In addition the 3D printing technology was found to be simple, easy to operate, was fast at printing and can print and assemble bioactive tissue. However, attention needs to be paid when selecting the composition ratio of the material for printing as unsuitable proportions or incompatible materials can result in interference

with the spray nozzle or block the print head resulting in unstable three-dimensional scaffolds and poor performance⁶⁵. The main advantages of 3D printing include the ability to fabricate versatile scaffolds with complex shapes and the ability to imitate the extracellular matrix⁶⁴. However, this can be limited by the use of printable materials that have the stability and desired properties for 3D printing, often alternative material methods processing methods are required to work with materials not easily printed⁶⁶. Furthermore, incorporating bioactive molecules can be a challenge as they may be sensitive to the printing environment⁶⁷; particularly if the printing processes involve a solvent or extreme temperature the proteins folding may be affected, or they can be denatured⁶⁷. Production time for scaffold fabrication can become lengthy as the scaffold design becomes more precise and intricate⁶⁴. Other methods of 3D printing reviewed by Mota et al⁶⁸ include selective laser sintering, stereolithography, fused filament fabrication and solvent casting 3D printing.

1.2.2.2.7. Electrospinning

Electrospinning was the chosen method for the fabrication of the self-reporting scaffolds. This is because one of the greatest advantages of this simple technique compared to the others is the ability to easily control specific parameters to fabricate a scaffold on the nano/micro scale to mimic the fibrous structure of the native extracellular matrix. Figure 1.11 displays the morphological similarities between decellularised lung extracellular matrix and an electrospun polymeric scaffold, taken from Harrington et al³³.

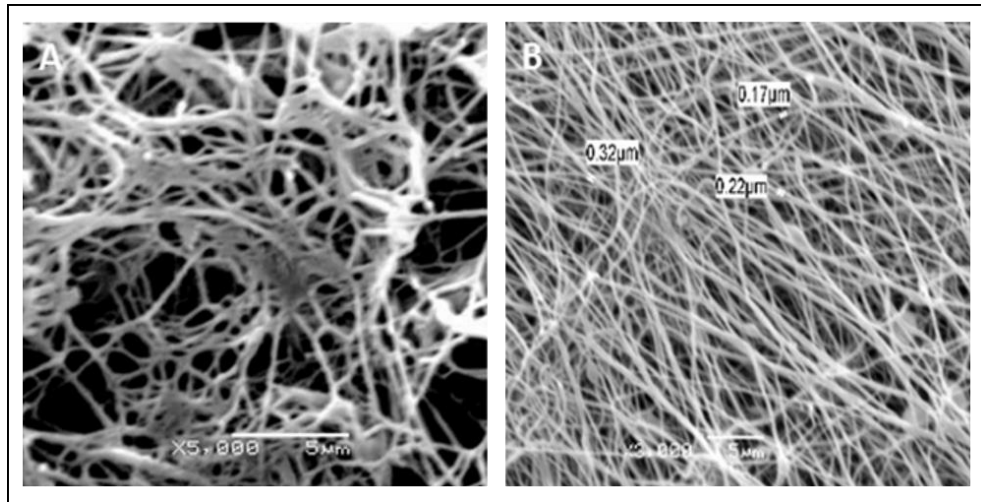


Figure 1.11 Representative SEM images of (A) decellularised lung extracellular matrix, (B) electrospun polyethylene terephthalate showing morphological similarities taken from Harrington et al³³.

Electrospun scaffolds also offer a high surface area, tuneable porosity, flexibility to cater to a different sizes and shapes, and the ability to control the fibre composition to achieve the specific properties or functionality⁶⁹. The basic electrospinning set up consists of a syringe pump, polymer solution, blunt needle, voltage supply and steel collecting plate⁷⁰, as shown in Figure 1.12.

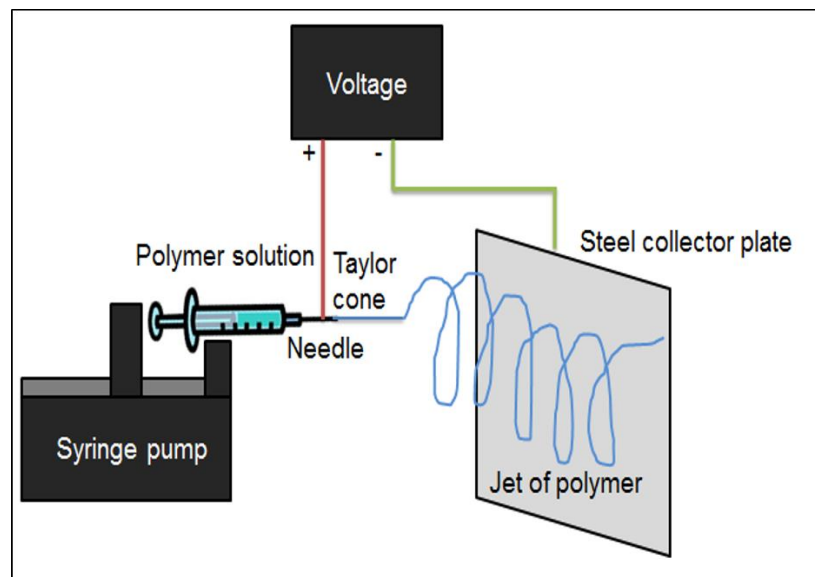


Figure 1.12 Schematic of the electrospinning set up.

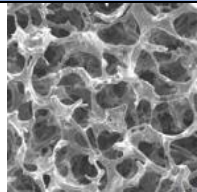
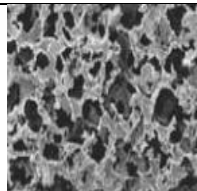
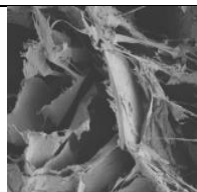
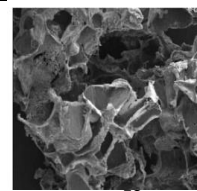
The electrospinning process is usually conducted at room temperature and begins when a high voltage is applied to the polymer solution and the polymer droplet at the needle tip is held by surface tension. At a critical voltage the surface tension of the liquid is overcome causing the droplet to elongate into a Taylor Cone. A continuous fine fibre jet is ejected from the tip of the Taylor Cone and is accelerated towards the oppositely charged grounded collecting plate. As the fibre travels through the air the solvent evaporates and solid polymer fibres are deposited on grounded collector as a scaffold^{70,71}. Although electrospinning appears to be a simple process, a disadvantage to this technique is that a number of parameters can affect the fibre morphology and need to be optimised to produce smooth uniform fibres such as: voltage, flow rate, polymer concentration, solvent, distance from the needle tip to the collecting plate, and temperature. Without the optimal conditions, fibres produced may be too thick or too thin, or can become beaded leading to a non-uniform structure, or may not spin at all. Table 1.4 below summarises the effects of these variables on the electrospinning abilities and resulting fibre morphology and diameters. In addition, electrospinning is discussed in further detail in Chapter 3.1.

Parameter	Effect
Voltage	High voltage supply of the polymer solution causes the droplet to form a Taylor cone and produce fibres at a critical voltage. The critical voltage varies in different polymer solutions. A voltage above or below the critical value causes the formation of beaded fibres or can inhibit polymer jet formation.
Flow rate	A critical flow rate is required to produce smooth fibres. Increasing the flow rate above the critical value can cause beaded fibres, ribbon like defects or unspun droplets due non-evaporation of the solvent, low stretching and incomplete drying of the polymer jet during the flight between the needle tip and collector. Lower flow rates are preferred to maintain a balance between the leaving polymer solution and replacement of the solution with a new one during jet formation.
Polymer concentration	Stretching of the charged jet is affected by changing the concentration of the polymer solution. Low polymer solutions cause entangled polymer chains to break into fragments before reaching the collector causing the formation of beaded fibres. Increasing the concentration leads to an increase in viscosity which increases polymer chain entanglement which overcome the surface tension and form smooth fibres. If the concentration is beyond the critical value, the flow of solution may be hindered causing the solution to dry at the needle tip, resulting in beaded fibres.
Solvent	Solvents should be able to solubilise the polymer. Moderately volatile solvents allow easy evaporation of the solvent from the fibres during the flight between the needle tip and collector. The deposition of solvent containing nanofibers on the collector causes the formation of beaded nanofibers. Highly volatile solvents are avoided because the polymer jet at the needle tip will dry, blocking the jet ejection. Less volatile solvents are avoided as they prevent drying during the fibre jet flight.
Distance	Distance between the needle tip and collector varies with the polymer solution, and can affect deposition time and evaporation rate. A critical distance needs to be maintained as this can affect fibre morphology. A shorter distance has been shown to increase fibre diameter, and a greater distance reduces fibre diameter. However some studies have shown a change in distance showed no effect on fibre morphology.
Temperature	Temperature increases the rate of evaporation of the solvent and decreases the viscosity of the solution which can lead to a decrease in the mean fibre diameter.

Table 1.4 Summary of the effects on fibre morphology due to the changes in electrospinning parameters, information sourced from Pillay and Haider^{70,71}

Electrospinning is a versatile technique and has been used for many tissue engineering applications, including skin tissue using PLGA scaffolds⁷², bone tissue using PCL, PLLA, silk, collagen scaffolds reviewed by Khajavi et al⁷³, corneal tissue using PCL, PLGA, gelatin, silk, collagen reviewed by Kong and Mi⁷⁴ and cardiac tissue using PLGA scaffolds⁷⁵. Other applications of electrospun scaffolds include drug delivery due to the high ratio of surface volume of produced fibres as reviewed by Hu et al⁷⁶. Antibiotics such as tetracycline hydrochloride have been incorporated into nanofibres for wound dressings⁷⁷. In addition Kim et al⁷⁸ fabricated PCL fibres with mussel adhesive protein which were shown to enhance wound healing of rat skin. Electrospun PAA fibres have also been used as a sensing material, with incorporation of pyrene methanol to detect metal ions Fe^{3+} and Hg^{2+} in water.

Overall, the electrospinning technique provides the most favourable features for our tissue engineering platform.

Method	Features	Downfalls	Common applications	Structure
Solvent casting/ particulate leaching	Tuneable pore size	Residual solvents/porogen	Bone and cartilage tissue engineering	 Sin et al ⁷⁹
Melt moulding	No toxic solvents, tuneable pore size	Residual porogen, bioactive molecules may be destroyed by high temperature	Bone tissue engineering	 Oh et al ⁵³
Freeze drying	No need for organic solvent or porogen	Long processing time, difficult to tune pore size	Bone tissue engineering	 Jin et al ⁵⁶
Gas foaming	No need for organic solvent or porogen	Difficult to incorporate bioactive molecules with high temperatures, difficult to control pore size and interconnectivity	Bone tissue engineering	 Kim et al ⁵⁸

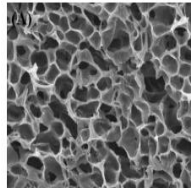
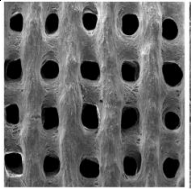
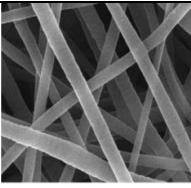
Method	Features	Downfalls	Common applications	Structure
Thermally induced phase separation	Defined pore size and shape	Minimal control over fibre diameter and orientation	Drug delivery and bone tissue engineering	 Yen et al ⁶²
3D printing	Tuneable pore size and morphology, automated, highly flexible	Long production time if detailed construct, specialist equipment	Bone tissue engineering	 Sun et al ⁶⁵
Electrospinning	Tuneable pore size and morphology High surface area Can incorporate bioactive molecules	Conditions must be optimised to avoid beading Often organic solvents are needed	Drug delivery Wound healing Tissue engineering	 Schuere et al ⁸⁰

Table 1.5 Comparison table of different scaffold fabrication method

1.2.3. Bioreactors

Bioreactors complement the use of scaffolds in tissue engineering, and can be described as a device that uses mechanical means to influence biological processes³². Cell-seeded porous scaffolds have been placed in a range of different bioreactors including orbital shakers, spinner flasks , rotating wall vessels and microfluidic devices⁸¹ to aid the production of functional 3D tissues. Firstly, they maintain a desired uniform cell concentration within the scaffold during cell seeding⁸² which facilitates adequate cell-cell interactions⁸³. Secondly, exposure to medium fluid flow can be used to mimic physiologic delivery of oxygen, nutrient supply, chemical signals and continuous waste removal from 3-D tissue engineered constructs which has been shown to provide significantly higher mass transfer rates compared to static cultures⁸⁴. Finally the fluid shear stress caused by mixing or perfusion of culture medium will expose cells to mechanical stimulation⁸⁵ which can mimic stimulants such as interstitial flow which can affect cellular alignment and differentiation⁸⁶. A limitation to the use of bioreactors, is that there is no specific or guidelines available in terms of which flow rate/speed to use or volume of culture medium, as different cells have different cell culture requirements⁸⁷.

1.2.3.1. Spinner flask

The spinner-flask bioreactor was developed to create a convective flow and produce hydrodynamic forces that help mass transport throughout cell seeded scaffolds⁸⁵. Spinner flasks consist of a cylindrical glass container in which growing tissues are suspended and a stirring element such as a magnetic stirrer is placed at the bottom of the tank ensuring the mixing of the culture medium⁸⁸. The scaffolds are in fixed positions, threaded in needles attached to the cap of the container⁸⁵, see Figure 1.13. The mixing mechanism of this bioreactor has been shown to improve cellular

distribution and differentiation in scaffolds⁸⁹. Spinner flasks are commonly used for bone tissue engineering as they can mimic some aspects of the native bone environment⁸⁵. However, spinner flasks are thought to only permit the extracellular matrix production at the scaffolds surface and mixing the media can create turbulent shear at the surfaces which can be unfavourable to cell growth and tissue formation⁸⁵.

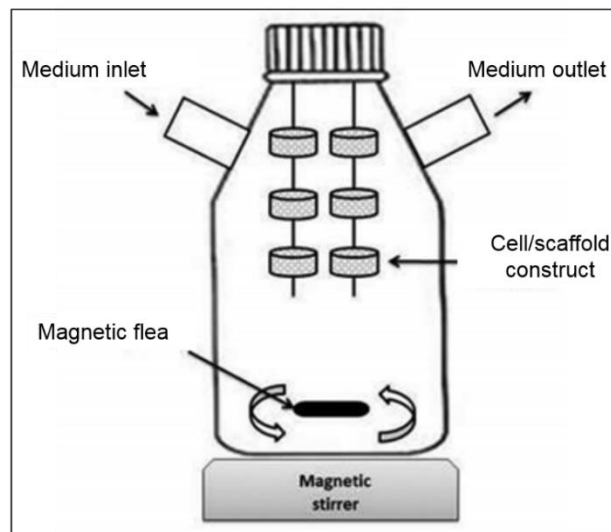


Figure 1.13 Schematic of spinner-flask bioreactor taken from Maver et al⁹⁰.

1.2.3.2. Rotating wall vessel

Rotating wall vessels consist of cylindrical bioreactors which are completely filled with culture medium and rotated along a horizontal axis. The physiological low fluid shear stress environment is usually used for suspension cultures, where the cells can aggregate based on their natural cellular natural cellular affinities, form 3-D structures and acquire properties of highly differentiated cells⁹¹. Studies have performed to investigate the effects on dynamic flow in a 3D environment on bone cell biology and bone formation *in vitro*. Adherent cell lines can be cultured on scaffolds, however these can experience repeated collisions with the bioreactor wall which has been shown to limit achievable cell density⁹².

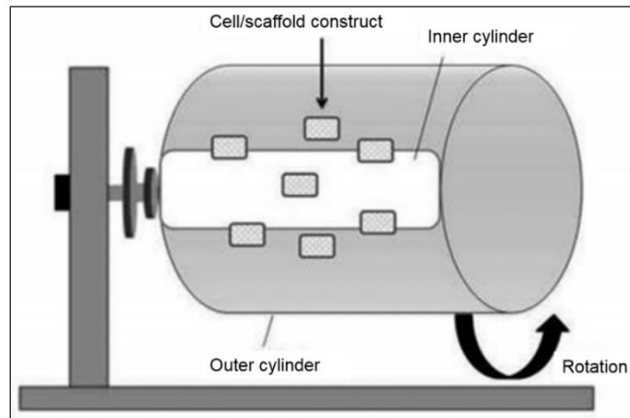


Figure 1.14 Schematic of rotating wall vessel taken from Maver et al⁹⁰.

1.2.3.3. Perfusion bioreactors

Perfusion bioreactors are used to provide a flow of medium through or over a cell population, in order to help push the oxygen and nutrients through the pores of 3D scaffolds⁸². Different types of perfusion bioreactors are available some of which are commercially available whilst others are produced in-house for various types of applications. Table 1.6 provides important features that should be considered when selecting a bioreactor for cell culture.

Features	Description
Leak proof	Reduces risk of contamination, and loss of reagents
Optically transparent	Allows <i>in situ</i> real time monitoring
Easy to assemble	Less training required, rapid experimental set-up
Ability to monitor microenvironment	Provide data on culture conditions such as pH, oxygen, carbon dioxide, metabolites
Allows use of different flow types/rates	Different flow rates/types are required for different cell types/applications
Allows easy insertion and retrieval of scaffolds	Allows 3D cell culture and post analysis.
High throughput	Quicker data acquisition
Flexible configuration	Modular interconnected systems allow co-culture and cell-cell signalling
No air bubble formation	Presence of air bubbles can disrupt the flow rate and disturb cells

Table 1.6 Features required for an ideal bioreactor system

Perfusion bioreactors are very versatile and generally can be set up in different configurations, including a closed set up where the media recirculates to provide media containing naturally produced growth factors, or single pass set up where only fresh media is supplied to the cells avoiding the accumulation of metabolites. Figure 1.15 displays a simple schematic of the configuration of a perfusion bioreactor system. Flow rates should be optimised when setting up perfusion bioreactor systems, as cells can be damaged at high flow rates, or may not have sufficient nutrient and oxygen supply at low flow rates. Different types of flow can be used to deliver shear stress such as unidirectional laminar, pulsatile laminar, turbulent and oscillating flow.

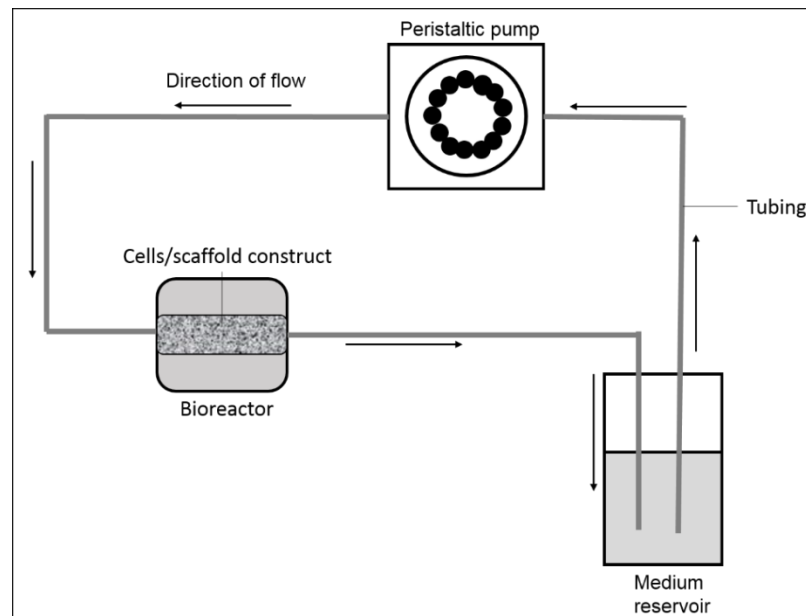


Figure 1.15 Schematic of displaying configuration of perfusion bioreactor adapted from Wang et al⁹³.

1.2.3.3.1. Quasi-Vivo[®]

The Quasi-Vivo[®] (QV) is a perfusion bioreactor system commercially available in different formats and configurations. “Quasi” is derived from the Latin definition of ‘as if, almost’, and “vivo” from the same derivation meaning ‘living thing’, together

the name represents a system that can create conditions that are very similar to physiologically relevant conditions in living organisms. There are a variety of different QV bioreactor systems to suit different tissues and applications including QV500, QV600 and QV900. Some of the advantages of the QV systems is that all of the systems can be set up to either provide a single flow of fresh medium, or recirculating medium which removes the risk of shock or disturbance to the cells during feeding⁹⁴. In addition, recirculating media enables the production of conditioned media containing a cocktail of growth factors and cytokines. All of the chambers can accommodate an adjustable laminar flow rate and chamber pressure to suit the specific requirements of different tissue types⁹⁴. Furthermore, the QV systems can cater to a variety of flow rates whether it's high shear, laminar or a pulsatile flow. In addition, the QV systems all have a flexible modular configuration, the individual bioreactors can be interconnected to allow multiple or the same cells types to be cultured in separate chambers. This can enable cross talk between the tissues which is important when recreating specific organ interactions. Moreover, all of the bioreactors systems have an internal width same as a 24 well plate which enhances transferability from conventional cell culture techniques. The QV900 is also optically transparent which enables non-invasive real time monitoring of cultures.

The early stage prototype of the QV500 was developed by the University of Pisa and was initially referred to as the multicompartmental bioreactor (McmB)⁹⁵, as shown in Figure 1.16. Mathematical modelling was used to optimise the design and flow mechanics within the chamber. During development they found that to prevent bubble entrapment and turbulence in the bioreactor chamber, a slightly larger and sloped lid could help collect any bubbles and convey them to the outlet tube⁹⁵. In addition the difference in diameters of the inlet and outlet tubes, 1mm and 3mm respectively helped to force out bubbles in the chambers⁹⁵. Bubbles can be an

issue by influencing the laminar flow of the medium causing pressure changes that may disrupt cells⁹⁶. Mazzei et al⁹⁵ also investigated the effect of various flow rates on rat hepatocytes was investigated as hepatocytes are the most important cell types in drug metabolism and toxicity studies¹⁵. It was found that between the flow rates of 180 and 500 μ L/min the viability is very close to the control and the viability peaks at 300mL/min, this could be due to the high oxygen concentration as demonstrated by the mathematical computer modelling. A further increase in flow rates above about 500 μ L/min cell viability was compromised despite the increased availability of oxygen, due to the high shear and impact angle of flow on the collagen coating and cells⁹⁵.

The McM^B has been used for several applications which demonstrate the importance of flow. Vinci et al⁹⁷ used the McM^B to recapitulate aspects of glucose and lipid metabolism *in vitro* by culturing hepatocytes, endothelial cells and adipose tissue in a three way culture set up to mimic inter-organ crosstalk. Vinci et al⁹⁸ also used the McM^B for drug testing applications and investigated the effect of flow conditions on detoxification genes in hepatocytes which showed that detoxification genes were downregulated in static conditions compared to flow conditions. In addition, again for drug testing and regenerative medicine applications Vinci et al⁹⁹ cultured hepatocytes on polymeric scaffolds to investigate differences in cell activity between static and flow conditions. The results showed that when exposed to flow conditions there was an increase in cell density and cell metabolic function compared to static conditions. Therefore *in vivo*-like stimulation of cells and tissues by flow encourages them to behave with metabolic competency, resulting in improved function, viability and cell-cell signalling⁹⁴.

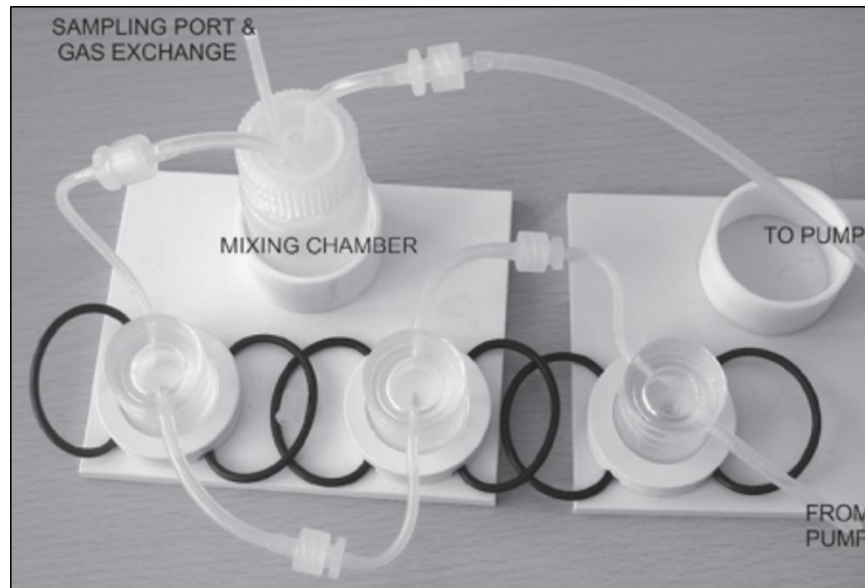


Figure 1.16 Photograph of Mcmb taken from Sbrana and Ahluwalia¹⁵.

The commercialised QV500 bioreactor is very similar to the original McmB prototype with similar dimensions, and are both fabricated from polydimethylsiloxane (PDMS) which has many excellent properties, including inexpensive, good chemical stability, inert, nontoxic, biocompatible, non-flammable, durable, good thermal stability and permeable to nonpolar gases such as oxygen¹⁰⁰. One of the major differences is that the commercialised QV500 bioreactor has a more secure locking mechanism with the three lugs to prevent leakages from medium flow as shown by the difference in structure in Figure 1.17.

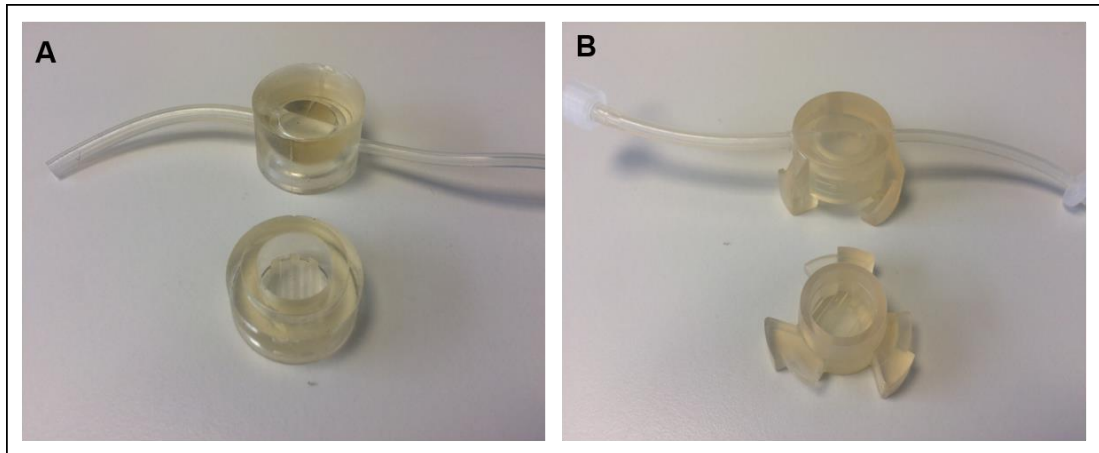


Figure 1.17 Photographs of (A) McM B (B) Quasi-Vivo®500 showing differences in structure.

The chambers hold a volume of around $\sim 1500\mu\text{L}$ and has a distance of at least 1mm between the wall of the tube and the top of the chamber to ensure mechanical stability of the tube/chamber junction⁹⁵. The chamber design permits 2D or 3D culture and allows the easy insertion of scaffolds and coverslips into the base of the chamber. Cell constructs and medium samples can be easily removed and retrieved for staining and biochemical analysis. The QV500 is also autoclavable allowing thorough sterilisation and multiple uses. One of the major drawbacks of the QV500 is its lack of optical transparency, which means that cells cannot be monitored *in situ* whilst exposed to flow conditions. Publications using the commercialised QV500 include applications such as cardiovascular engineering; Pagliari et al¹⁰¹ cultured stem cells on gelatin scaffolds whilst exposed to flow conditions to promote cell colonisation of the inner layers and create a physiological environment. The combination of the scaffold with flow conditions resulted in enhancement of cardiac gene activation compared to static conditions. Rashidi et al¹⁰² cultured hepatocyte like cells in the QV500 to study the effect of fluid shear stress on their performance. Cytochrome P450 drug metabolism and serum protein secretion was investigated and it was found that the fluid stress improve the CYP gene activity and improved hepatocyte phenotype compared to static conditions. Ucciferri et al¹⁰³ et al used the

QV500 system to create a more physiologically relevant *in vitro* model to investigate the toxic effects experienced *in vivo* when of nanoparticles pass through biological barriers and cause cardiovascular damage on the endothelium. Physiological culture conditions were created by using the QV500 flow system, which found that endothelial cells were more susceptible to toxicity caused by silver nanoparticles when exposed to flow conditions compared to static conditions. Therefore the incorporation of flow is important and using static conditions only may not be sufficient enough to define safe exposure limits.



Figure 1.18 Quasi-Vivo@500 system, photograph taken from Kirkstall Ltd¹⁰⁴.

The QV600 is an air liquid interface (ALI) bioreactor shown in Figure 1.19 is useful for recreating barrier models, including skin and respiratory epithelium. The bioreactor can accommodate the incorporation of commercially available Transwell inserts for cell culture at the air liquid interface. By controlling the gaseous phase, toxic components or aerosols can be introduced into the air of the chamber for drug testing applications. Care needs to be taken when optimising the flow rates, as a constant level should be maintained at the air liquid interface. Not only can the bioreactor create an air liquid interface configuration, the bioreactor accommodates the dual flow of media within the bioreactor which is useful for cocultures, as shown

in Figure 1.19B. Very limited published work is available using the QV600, Giusti et al¹⁰⁵ used the QV600 as a model for the intestinal epithelium. The intestinal epithelium is made up of epithelial cells and acts as a barrier against the external environment. It is selectively permeable and permits the absorption of nutrients, electrolytes and water whilst maintaining a defence against toxins. The epithelium maintains its selective barrier function by the formation of complex protein-protein networks such as tight junctions, which mechanically link adjacent cells and seal the intracellular space¹⁰⁶. By incorporating flow conditions into the intestinal epithelium model, it was found that the barrier integrity and tight junction expression increased compared to static conditions.

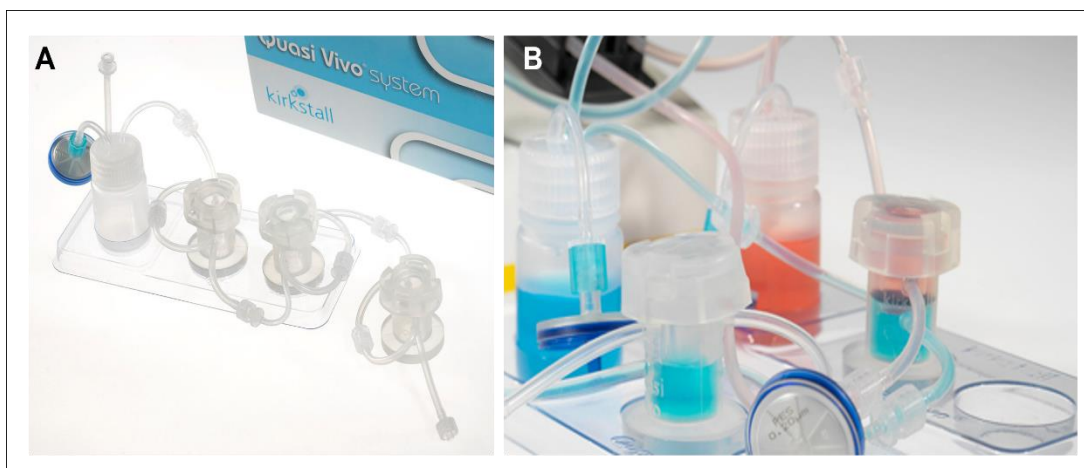


Figure 1.19 Quasi-Vivo@600 system, photographs taken from Kirkstall Ltd¹⁰⁷.

The most recently developed QV900 consists of six optically transparent bioreactors integrated into a tray shown in Figure 1.20. This is to allow higher throughput, easier handling and *in situ* imaging with each chamber. In addition, for applications where non-specific binding of proteins or chemicals is important, the QV900 should be selected as this is manufactured from a different plastic material (acrylic)⁹⁴. The QV900 is not autoclavable and is designed for disposable use, however sterilisation can be performed with ethanol or industrial methylated spirit however, care should be taken as this can cause the bioreactors to become cloudy and mechanically

weak making them susceptible to leakages. Again, like the QV600, limited publications are available using this system. Nithiananthan et al¹⁰⁸ used the QV900 to expose fibroblasts to investigate the effect interstitial fluid flow on fibroblast response. They found that compared to static conditions, some genes were upregulated and markers of differentiation were increased.

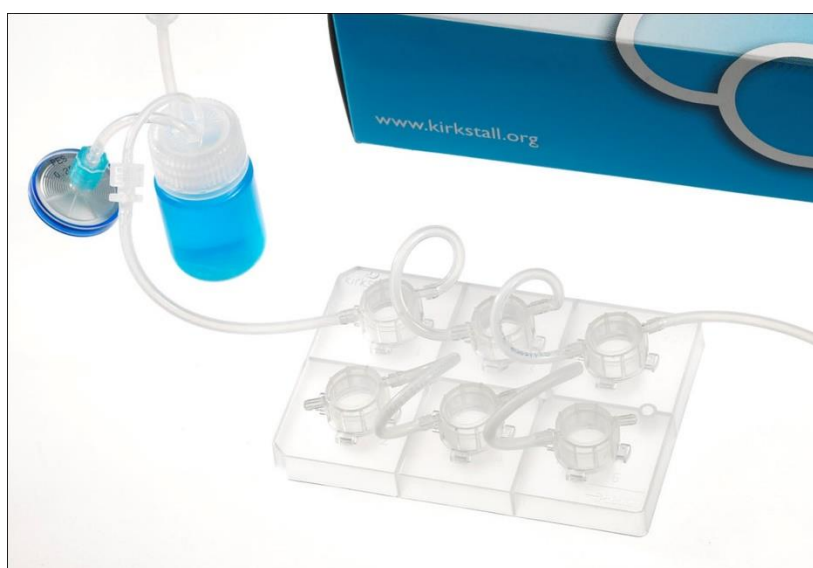


Figure 1.20 Quasi-Vivo@900 system, photograph taken from Kirkstall Ltd¹⁰⁹.

The QV900 chambers also have slightly different dimensions to the QV500 as shown in Figure 1.21. The QV900 is able to hold a larger volume of medium $\sim 3000\mu\text{L}$ compared to the QV500 which can hold approximately half of that volume. In addition, the QV900 is taller, and the inlet and outlet for the tubing both have the same diameter of $3/32''$, whereas the QV500 had a smaller inlet tube of $1/16''$ and a $3/32''$ outlet tube which was shown to alleviate air bubbles⁹⁵. Moreover, the inlet and outlet of the QV900 is positioned much further from the base than the QV500 due to the depth of the chamber, so if cells were placed at the bottom of the QV500 and QV900 chambers they would be exposed to different levels of shear stress. Therefore, if transferring an experiment from the QV500 to the optically transparent

QV900, the flow rates may need to be reoptimised and an insert may need to be utilised to adjust the positioning of the cells within the bioreactor.

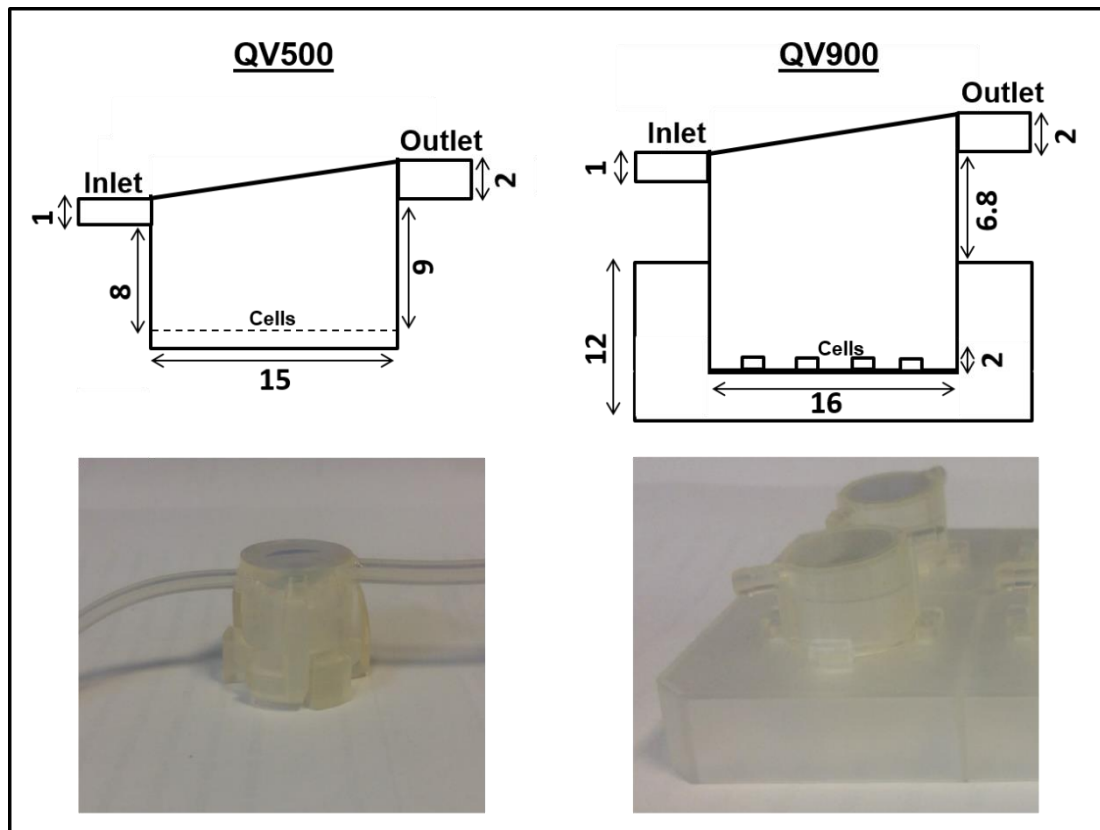


Figure 1.21 Schematic and photograph showing dimensions in millimetres of QV500 compared to QV900.

1.2.3.3.2. KIYATEC 3DKUBE™

A similar perfusion bioreactor to the Quasi-Vivo® is the KIYATEC 3DKUBE™ as shown in Figure 1.22. The 3DKUBE™ is a small, disposable polystyrene bioreactor which can accommodate scaffolds for 3D cell culture. The dimensions of the chamber are 6mm in diameter which is approximately half of the size of the Quasi-Vivo® chamber diameter, and can hold 250µL of cell culture medium. Alternative configurations of the chamber are available for different applications. The bioreactor has an optically transparent window with the identical imaging capability as a 96 well plate to enable *in situ* monitoring. In addition the chambers can connect together to

create multi-chamber experiments for more complex models, and the chamber configuration can be altered for segregated co-culture or cell migration. Various flow rates can also be used. One of the disadvantages to this system is that handling the scaffolds on a smaller scale could be tricky. Ward et al¹¹⁰ have used this feature by combining with two photon imaging to noninvasively monitor tissue engineered human adipose tissue structure and function *in vitro*. The 3D vascularised human adipose tissues were engineered *in vitro* and then exposed to a perfused environment and tracked over time by automated quantification of endogenous markers of metabolism using two-photon excited fluorescence (TPEF). Abbott et al¹¹¹ used the 3DKUBE™ to expose adipose tissue to physiologically relevant flow conditions. 2D and 3D cell culture systems were investigated, with the 3D system more robust, providing the mechanical structure required to contain the large, fragile adipocytes that were lost in 2D perfused culture systems. Perfusion conditions were shown to enhance adipocyte activity.

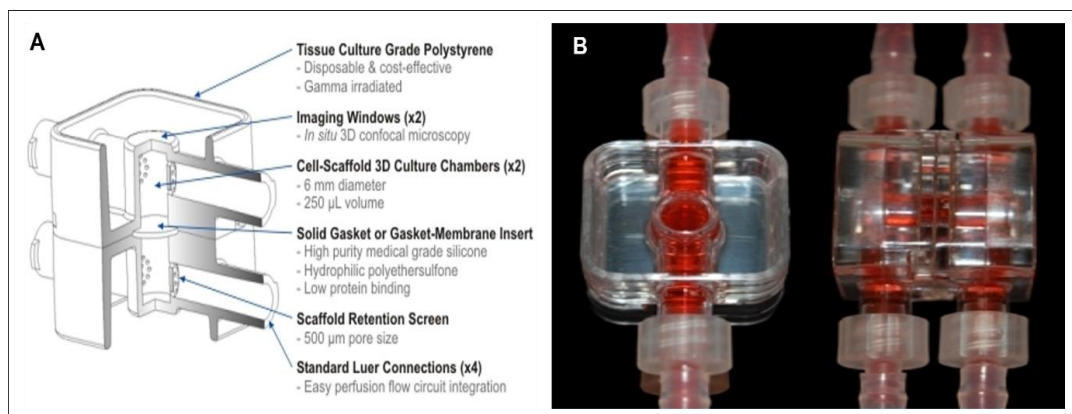


Figure 1.22 (A) Schematic of Kiyatec 3DKUBE™ (B) Photograph of 3DKUBE™, taken from Kiyatec¹¹².

1.2.3.3.3. Microfluidics

Perfusion bioreactors can also come in the form of microfluidic devices in order to miniaturise macroscopic systems for higher throughput of biological experiments. In addition, they enable studies of cell behaviour of organisms with precise and

localised application of experimental conditions which are difficult to achieve using macroscopic tools¹¹³. Microfluidic devices include organ-on-chips where specific cell types are cultured and continuously perfused within micrometer-sized chambers to model physiological functions of a particular tissue or organ¹¹⁴. Devices are often fabricated from PDMS using rapid, simple, and inexpensive techniques such as soft lithography, which involves the replication of a topographically defined structure on a master in a soft elastomer¹¹⁵. Photolithography has also been used to create patterns within microfluidic devices. The principle is based on the exposure of light-sensitive polymers (photoresists) to ultraviolet (UV) light. The pattern transfer can be parallel through a mask that consists of opaque features on a transparent substrate with a focused beam. The exposure causes the photoresist to be chemically modified, so that the exposed areas either become soluble in the subsequent developing step (positive tone photoresist) or becomes insoluble (negative tone resist). The patterned photoresist layer protects the material from the etching, and the unprotected areas are etched¹⁰⁰. The designs of microfluidic devices are very flexible and can therefore cater to a variety applications, however each device is highly specific to single experimental configurations. Due to the very small nature of the platform, only a low number of cells and reagents are required which is more cost efficient. Live cell imaging and real time on chip analysis can be performed with direct coupling to down-stream analysis systems¹¹⁶. Some of the drawbacks of the microfluidic devices include the non-standard culture protocols entail complex operational control and chip design. In addition, the reduction in scaling can provide challenges in adapting biological protocols to fit experiments based in a microsystem, such as the media and cell concentration¹¹³. Small working volumes for seeding and reagents can also be challenging for subsequent analytical chemistry, complex operational control and chip design¹¹⁶. Furthermore, many *in vitro* models now push the use of scaffolds in order to create the native microenvironment, however loading and retrieving scaffolds from the microfluidic

devices can be difficult, and even when inserted the scaffold area would be very small. Dongeun Huh¹¹⁷ describes the fabrication of a PDMS microfluidic device to replicate the microarchitecture and dynamic microenvironment of the alveolar–capillary unit of the living human lung as shown in Figure 1.23.

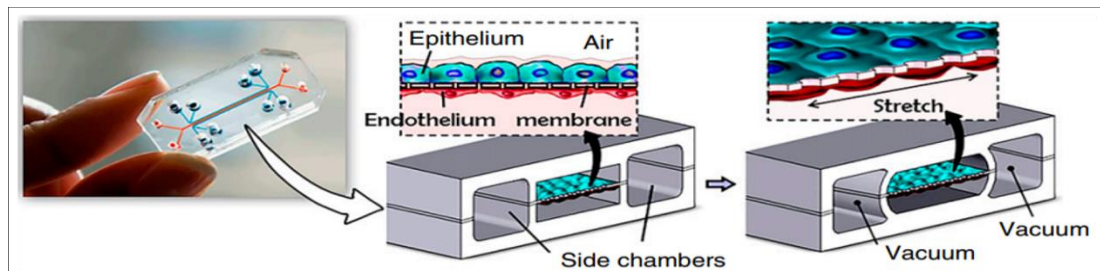
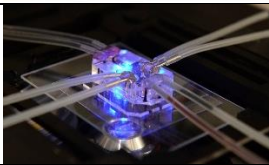


Figure 1.23 Schematic and photography of microfluidic device taken from Huh¹¹⁷.

A variety of commercially available perfusion bioreactors are available for different applications, however all of which come with their advantages and limitations.

Table 1.7 summarises and compares some of the key features found in various commercial perfusion bioreactors.

The Quasi-Vivo[®] systems were used for this study because of their simplicity, ease of use, and variety of published studies showing the enhanced cell activity using these bioreactor. The ability to easily insert /retrieve scaffolds from the bioreactor is essential for our study as the sensing component enabling *in situ* monitoring will be incorporated into the scaffold. Furthermore, the QV has an optically transparent window available, which again is important to enable *in situ* monitoring. Moreover, the bioreactors can be reused and interconnected to allow multiple repeats to be performed simultaneously.

Product	Image	Optically transparent	Scaffold insertion	Auto-clavable	High throughput	Automated measurements	Inter-connected (modular)	Micro-scale
Quasi-Vivo [®] 500			X	X			X	
Quasi-Vivo [®] 600			X	X			X	
Quasi-Vivo [®] 900		X	X				X	
3DKube [™]		X	X				X	
Lung-on-a-chip		X				X		X

Product	Image	Optically transparent	Scaffold insertion	Auto-clavable	High throughput	Automated measurements	Inter-connected (modular)	Micro-scale
Alvetex perfusion plate		X	X				X	
MINUSHEET [®]		X	X	X			X	
3D Biotek bioreactor			X	X				
CellASIC [™] ONIX System		X			X	X		X

Table 1.7 A variety of perfusion bioreactors available for cell culture applications

1.2.4. Monitoring of culture conditions and tissue constructs

Many complex *in vitro* models have been developed for specific tissue engineering and regenerative medicine applications. However, one of the challenges is continuous monitoring of cellular activities within 3D, generally opaque thick structures¹⁴. Many of the developed *in vitro* models are limited by the ability to monitor cell culture conditions in a non-invasive manner. With the lack of ability to monitor the tissue regeneration processes *in situ*, it can limit our understanding of optimal conditions required for growth¹¹⁸. Therefore, novel techniques for monitoring *in vitro* cultures at all stages of tissue growth, repair and regeneration in a more insightful, non-invasive and quantitative manner is imperative¹¹⁹⁻¹²⁰. With non-invasive *in situ* monitoring in real time we can monitor cell growth, cellular differentiation and tissue morphogenesis¹²⁰, and develop more reliable tissue engineered constructs that are more physiologically relevant models for disease and drug testing. Moreover, non-invasive monitoring can provide real time functional read outs, without having to disturb the cellular microenvironment or introduce potential contamination. Currently widely used methods of monitoring tissue engineered constructs include destructive end point determination and biochemical or histological methods to determine cell number, viability and tissue growth throughout the construct¹¹⁹. Therefore simple and readily applicable non-destructive methods of monitoring changes in cell metabolism, viability and tissue deposition particularly within long term cultures would be invaluable and could point out adverse responses during the early stages of culture¹²¹.

1.2.4.1. Biosensors

Biosensors can be used for direct real-time monitoring of processes within engineered tissues¹⁴. Biosensors can be defined as “a self-contained analytical device that combines a biological component with a physicochemical component for the detection of an analyte of biological importance”¹²². By detecting cellular analytes, electrical activity, physical and chemical signals transmitted by cells, biosensors can provide insights into cellular activities and responses in real time¹²³. When designing robust biosensors they should meet several requirements such as being able to detect trace amounts of biomarkers within complex biological environments such as cell culture medium, which usually contains a plethora of nonspecific proteins and interfering compounds¹²⁴. In addition, the robust biosensor systems should be able to have continual monitoring capability every few hours or days for kinetics analysis of biomarkers over extended periods¹²⁴. Biosensors are made up of three main components, 1) a detector to detect the stimulus, 2) a transducer to convert the stimulus to output signal, 3) a signal processing system to process the output and present it in an appropriate form¹²². Hasan et al¹²² reviews the different kind of biosensors and its components. The sensing component or bioreceptor includes enzymes, microbes, cells, nucleic acids, and antibodies. The transducer can be electrochemical, optical, magnetic or thermometric, as listed in Table 1.8. The applications of biosensors include sensing small molecules such as glucose, hydrogen peroxide, adenosines, functional protein molecules, pathogenic microbes.

Type of transducers	Measured property
Electrochemical	Potentiometric, Amperometric, Conductometric, Nanotechnology, Bioelectronics
Protein	Immunosensor
Electrical	Surface conductivity, Electrolyte conductivity
Optical	Fluorescence, Adsorption & Reflection
Mass sensitive	Resonance frequency of piezocrystals
Light	Bioluminescence

Table 1.8 Different types of biosensors, adapted from Shruti et al¹²⁵

1.2.4.1.1. Electrochemical biosensors

Electrochemical sensors operate by reacting with an analyte of interest to produce an electrical signal proportional to the analyte concentration¹²⁶. Different types of electrochemical biosensors measurements include potentiometric, amperometric and conductometric which can detect a variety of analytes as given in Table 1.9. One of the key advantages of electrochemical biosensors is their simplicity. Inexpensive electrodes can be easily integrated with simple electronics to perform rapid measurements in miniaturised easy-to-use portable systems. Miniaturisation is important because biological samples are often available in small amounts, and tissue damage must be minimised in cases of *in vivo* monitoring¹²⁷. Being able to determine the concentration of an analyte within a complex sample at the point-of-care and in near real time with short response times is extremely attractive for medical diagnosis, monitoring of existing conditions and environmental monitoring¹²⁶.

The different types of electrochemical biosensor measurements have been reviewed by Stradiotto et al¹²⁸. The ion selective electrode is an example of an

electrochemical biosensor and consists of an indicator electrode capable of selectively measuring specific ions. They are generally composed of a working electrode (potential is determined by its environment) and a reference electrode (potential fixed by a solution containing ion of interest at a constant activity)¹²⁸. Since the potential of the reference electrode is constant, the value of the potential difference (cell potential) can be related to the concentration of the dissolved ion¹²⁸. The most widely used potentiometric device is the pH electrode due to its simplicity, rapidity, low cost, applicability to a wide concentration range and particularly to its extremely high selectivity for hydrogen ions. Glass electrodes are composed of a thin ion-sensitive glass membrane and can monitor cations including sodium, lithium, ammonium and potassium¹²⁸. Disadvantages to using pH electrodes are that they are bulky and invasive for tissue engineering applications, they require frequent recalibration, the glass tip can be easily damaged should always be kept wet to prevent dehydration of the hydrated glass gel layer on the external surface of the electrode. Amperometric biosensors are one of the most common types of electrochemical sensors and have been widely used in point-of-care testing for applications such as monitoring glucose levels in people with diabetes¹²⁶. Amperometric biosensors function by the production of a current when a potential is applied between two electrodes¹²⁹. Some of the drawbacks of amperometric sensors are electrochemical interferences (detection of non-specific analytes), the lack or low response reproducibility, particularly since sensing biocomponents often have a limited lifetime. In addition, modifying the electrode surface to favour a single electrochemical process can be a difficult task. In addition, in the case of *in vivo* measurements biocompatibility and biofouling can be critical issues¹²⁷. Conductometric sensors rely on changes of electric conductivity of a film or a bulk material, whose conductivity is affected by the analyte present¹²⁸. Thin films are used mostly as gas sensors, due to their conductivity changes following surface chemisorption¹²⁸

Measurement type	Transducer	Transducer analyte
Potentiometric	Ion-selective electrode Glass electrode Gas electrode Metal electrode	K ⁺ , Cl ⁻ , Ca ²⁺ , F ⁻ , H ⁺ , Na ⁺ , CO ₂ , NH ₃ , Redox species
Amperometric	Metal or carbon electrode Chemically modified electrodes	O ₂ , sugars, alcohols, Sugars, alcohols, phenols, oligonucleotides
Conductometric	Interdigitated electrodes Metal electrode	Urea, charged species, oligonucleotides

Table 1.9 Types of electrochemical transducers for classified type of measurements, with corresponding analytes to be measured, taken from Thévenot et al¹³⁰

1.2.4.1.2. Optical biosensors

Optical biosensors are one of the most common type of biosensor used for applications such as environmental monitoring, food safety, drug development, biomedical research, and diagnosis¹³¹. The main goal of optical biosensors is to produce a signal which is proportionate to the concentration of an analyte¹³². Optical biosensors that exploit light absorption, fluorescence, luminescence, refractive index, Raman scattering and reflectance are powerful alternatives to conventional analytical techniques¹³¹. They allow rapid, highly sensitive, highly specific, real-time, cost effective detection of biological and chemical substances without any time-consuming sample concentration or prior sample pretreatment steps^{132,131}. Figure 1.24 shows a schematic of a biosensor which displays the first stage as the target of interest, these are identified by biorecognition molecules, an optical transducer converts the signal into another signal form which can be amplified and analysed. Optical biosensors can be split into two main categories including label-free and label-based¹³². Label-free detection involves the generation of a signal directly by the interaction of the analysed material with the transducer. Whereas label-based involves the use of a label and the optical signal is then generated by a colorimetric, fluorescent or luminescent method. For example glucose can be detected by

enzymatic oxidation using label-assisted sensing. Jankowska et al¹³³ developed a biosensor based system to monitor pH and glucose concentration during wound healing. The hydrogel coating composed of a fluorescent pH indicator dye and a metabolite-sensing enzymatic system, based on glucose oxidase and horseradish peroxidase. Changes in metabolite and enzyme concentration in artificial wound extract were successfully converted into a fluorescent signal. Optical pH sensors are described in section 5.1.4.

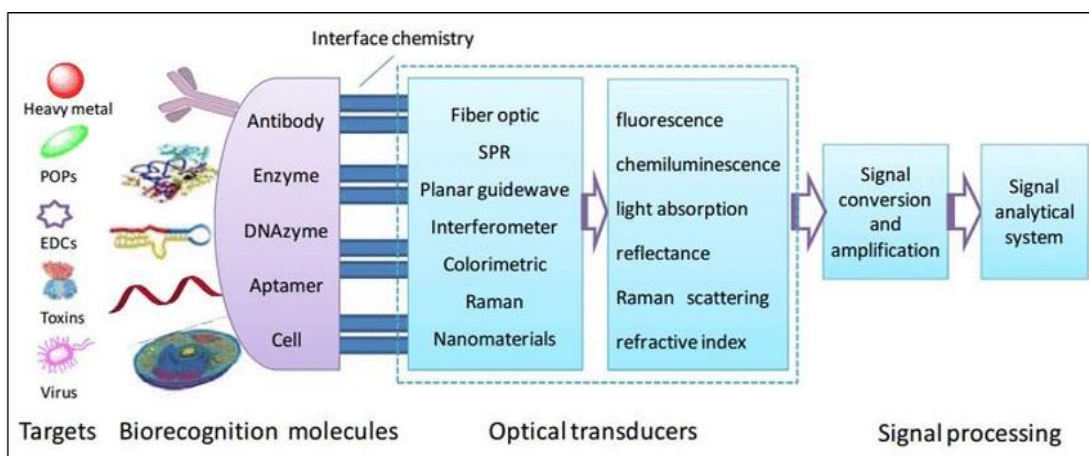


Figure 1.24 Schematic of optical biosensor taken from Long et al¹³¹.

1.2.4.2. Fluorescence probes for monitoring

Fluorescent probes can also be used to monitor the cellular microenvironment. This can be achieved by fluorescently labelling proteins of interest, delivering fluorescent nanoparticles, incorporating fluorescent protein tags and live cell dyes to investigate cellular processes under the microscope¹³⁴.

1.2.4.2.1. Fluorescent proteins

As mentioned, fluorescence monitoring can be performed in tissue engineering and regenerative medicine by fluorescently labelling proteins of interest. Some proteins

or small molecules in cells are naturally fluorescent; which is known as intrinsic fluorescence or autofluorescence and can be used to label live cells for monitoring¹³⁵. The chemically inert, green fluorescent protein (GFP) is an example common naturally occurring fluorescent protein sourced from jelly fish *Aequorea Victoria*¹³⁶. Upon excitation of UV or blue light, the GFP emits a bright green light. By creation of a genetic in-frame fusion of the fluorescent protein to a protein of interest, localisation of that protein to specific tissues, cells or subcellular compartments can be monitored and imaged non-invasively¹³⁵.

Fluorescent proteins can act as reporters by fusing the reporter gene to the promoter or coding sequence of a gene of interest, this will provide information on how much the gene or protein is expressed¹³⁷. Fluorescent proteins have many advantages and disadvantages as reviewed by Noguchi and Golden¹³⁷ and Jensen¹³⁵. (1) They have a very bright fluorescent signal which is useful for visualisation of specific structures within cells¹³⁷. However, on the other hand the brightness emitted can be affected by temperature and can vary depending on the cell type¹³⁵. (2) The fluorescent proteins come in a variety of colours which can be fused to different proteins of interest within the same cell to study the colocalisation and expression of multiple proteins simultaneously¹³⁷. But care should be taken when selecting particular fluorescent proteins for cells, as for example Ds-Red fluorescent protein impairs the viability or growth of hematopoietic stem and progenitor cells¹³⁵. (3) Specific areas in a small area of tissue or cells can be excited by using confocal microscopy, which can also generate 2-D or 3-D images¹³⁷. Disadvantages to using fluorescent proteins are given below. (1) Prolonged exposure to excitation light can generate free radicals (reactive oxygen species) which can damage DNA, RNA and proteins by oxidation, resulting in phototoxicity^{135,137}. (2) Moreover it has also been shown that fluorescent proteins can induce apoptosis in cells, which indicates a possible reason for the difficulty in

establishing stable cell lines expressing the protein¹³⁵. (3) Attaching a fluorescent protein to a protein of interest generally does not affect function, structure, and localization of a protein. However, in some cases, it can impair protein function and expression of this construct can adversely affect cellular function¹³⁵. (4) Prolonged exposure to excitation light causes photobleaching of fluorescent proteins which reduces their ability to fluoresce¹³⁷. (5) Cells contain compounds that exhibit autofluorescence, therefore the signal from the fluorescent proteins needed to be high enough compared to the autofluorescence to rise above the background¹³⁷.

1.2.4.2.2. Fluorescent nanosensors

Probes encapsulated by biologically localised embedding (PEBBLES) are sub-micron sized optical sensors specifically designed for non-invasive analyte monitoring in real time¹³⁸. PEBBLES are generally based on porous matrices composed of crosslinked polyacrylamide which encapsulate a sensing component that is responsive to analytes¹³⁸. such as hydrogen ions¹³⁹, calcium ions¹⁴⁰, magnesium ions¹⁴¹, glucose¹⁴². Buck et al¹³⁸ review the advantages of PEBBLES. Firstly, by encapsulating the sensing component such as a synthetic organic fluorophore, the matrix provides a protective coating which prevents interferences such as non-specific protein binding within a cell and protects the cell from potentially toxic effects of free fluorophores¹³⁸. Ratiometric PEBBLE sensors have been developed which are composed of a fluorescent indicator dye, and a reference dye encapsulated within the matrix. The sensor response is based on the fluorescence emission intensity ratio between the indicator dye and the unresponsive reference dye to the target analyte. By using a ratio a more accurate measurement of the analyte can be achieved¹³⁸. Since the production of PEBBLES, a number of ratiometric fluorescence nanosensors for pH have been reported based on polymeric nanoparticles, silica nanoparticles, quantum dots, cellulose

nanocrystals, latex nanobeads, and zeolite-based nanoparticles¹⁴³. Overall, PEBBLEs are useful for sensing due to their small size, fast response, intense signal, against relatively low background noise, relatively simple instrumental set-up, and ability to monitor non-invasively¹⁴⁴.

1.2.4.2.3. Quantum dots

Quantum dots (Qdots) are semi-conductor nanoparticles of a narrow size between (5-10nm in diameter) and emit light if electricity or light is applied to them¹²². They are very photostable, with a long fluorescence life time and their fluorescence can be controlled by their size, for example larger dots may emit a red fluorescence, whereas smaller dots emit a green fluorescence¹³⁵. Quantum dots generally consist of a three layer-structure, composed of a core, shell and polymer coating¹³⁵, as shown in Figure 1.25. The most common quantum dots have a cadmium chalcogenide core which is usually coated with a zinc sulphide shell to improve photoluminescence. The outer surface of the quantum dot is usually modified so the dots can be directed to a target¹³⁵. The application of quantum dots is similar to the use of organic fluorophores, and can be used for specific labelling of individual cell surface biomolecules¹³⁵. Jensen¹³⁵ reviews the limitations of quantum dots. One of the major limitations is the toxicity of the quantum dots. This is due to the semiconductor material which are usually heavy metals embedded within the core, and the generation of free radicals during excitation. Since they are composed of heavy metals they are potentially toxic during *in vitro* imaging. Another issue is that quantum dots sometimes have specialised coatings which make the overall molecule much larger than small organic dyes. This is more of an issue for cell internalisation and subsequent intracellular tracking. Since the fluorescence intensity of Qdots is highly stable and sensitive, fluorescence transduction based on chemical or physical interaction occurs on the surface either through direct photoluminescent

activation or through quenching. Qdots have been widely investigated for possibilities of sensing pH, ions, organic compounds, and biomolecules (nucleic acids, protein, and enzymes), as well as other molecules of biological interest. While the toxic effects of some Qdots have still remained as a concern, the recent advancements in application of Qdots in tissue engineering to detect the enzyme and biomolecules are significant achievements of biosensing research¹²².

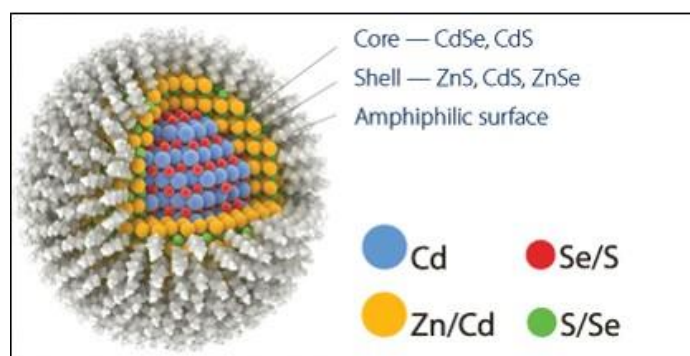


Figure 1.25 Schematic of quantum dot taken from Rusnano¹⁴⁵.

1.2.5. Monitoring in bioreactors

As mentioned, a bioreactor is a vessel that allows biological/chemical reactions or processes to occur, which can be on an industrial scale. Bioreactors have been commonly used for applications such as fermentation for the production of ethanol¹⁴⁶, production of therapeutic proteins¹⁴⁷, viral vaccine production¹⁴⁸. Being able to monitor parameters that affect biotechnological processes is important to ensure productivity and product quality¹⁴⁹. Parameters that should be monitored include temperature, pH, glucose, pO₂, PCO₂, and cell density within the culture medium¹⁴⁹. Bioreactor monitoring techniques can be placed in three main categories, including offline, atline and online¹⁵⁰. Offline measurements include manual or automatic sampling, transferring of a sample to a separate laboratory to

be analysed, which often causes a delay in the analysis¹⁵⁰. Atline monitoring also includes manual or automatic sample, however the collected samples is analysed within close vicinity of the bioreactor. Online monitoring includes *in situ* measurement acquisition, where the sensing device is often incorporated into the bioreactor and the sample is typically not removed¹⁵⁰. The chemical components within bioreactor media are mainly monitored by offline methods that require a biomass separation step, such as high performance liquid chromatography. However these methods can be time consuming and do not enable real time knowledge of the conditions affecting bioprocess performance¹⁵⁰

1.2.5.1. Monitoring in microfluidic devices

Many microfluidic devices used for organ modelling have more recently began incorporating the ability to monitor the cellular environment. Being able to monitor the chemical environment can help improve understanding of cellular responses¹⁵¹.

Oxygen is often a key component that is monitored within microfluidic devices. This is because oxygen imaging is a versatile tool to monitor and control oxygen distribution with spatial resolution enabling more profound understandings of how microfluidic systems work (e.g. fluidic dynamic, concentration profile) differently from bench-scale reactors¹⁵². This is because oxygen is required for aerobic metabolism of carbon compounds and impacts cell viability, in addition oxygen tension can impact cell migration¹⁵¹. Being able to monitor oxygen levels in microfluidic devices is difficult, as conventional methods of oxygen sensing include the use of bulky probes. Compared with electrochemical methods, optical oxygen sensors also do not require a reference electrode and do not consume analytes which is crucial in micro-scale because of the low number of analytes available which can bias an accurate detection. Overall, it appears that optical chemical sensors are the most

commonly used component for integration into microfluidic devices. This is because they are highly sensitive, inexpensive, easy to miniaturise and are allow non-invasive monitoring¹⁵². Some of the demands of optical oxygen sensors include high brightness, capability to be applied as a thin film (below 1 μm thickness), good photostability, compatibility with sample, cheap or established imaging systems, simple and microfluidic production compatible preparation steps, compatibility with the chip materials and low or no toxicity¹⁵².

Examples of oxygen sensors developed include a PDMS microfluidic device fabricated by Acosta et al¹⁵¹ developed a PDMS microfluidic device. This enabled oxygen levels to be successfully monitored non-invasively in the cell microenvironment by using an oxygen sensitive fluorescent dye embedded in the PDMS. Shaegh et al¹⁵³ developed an optical multi-analyte sensing module integrated with a microfluidic bioreactor for *in situ* monitoring of pH and dissolved oxygen in the circulating culture medium. This was used to successfully monitor the oxygen and pH levels of cultured fibroblasts for three days whilst exposed to flow conditions. The real time pH monitoring was detected by the level of light absorption by the phenol red within the cell culture medium, and the oxygen sensing was achieved by measuring the degree of quenching in the luminescent intensity of an oxygen sensitive fluorophore. The advantage of this platform is that it is low cost and user friendly. It is also a miniature and compact detection system which is more desirable over bulky spectrophotometry or microscopy techniques¹⁵³. Being able to monitor the specific pH, it can indicate when circulating medium should be replaced with fresh medium. Whilst being able to monitor oxygen levels in bioreactors is important as changes in oxygen delivery to cells can cause variations in cellular metabolism and physiological pathways.

Shin et al¹²⁴ developed a human liver-on-a-chip microfluidic platform with integrated electrochemical biosensors, for the continual monitoring of the metabolic activity of

the organoids by measuring the levels of secreted biomarkers for up to 7 days which agreed with the data acquired by ELISA. The versatile and robust microfluidic electrochemical biosensor was capable of automated and continual detection of soluble biomarkers, which is useful for long-term monitoring of human organoids during drug toxicity studies or efficacy assessments of *in vitro* platforms. The advantages of this system is the automation of the operation of the electrode, label-free antigen detection process requires minimum medium depletion; regenerative capability of the electrode surface upon saturation with captured antigens; and cost-effectiveness due to the use of the miniaturized electrodes and microfluidic platform, long term continual monitoring of biomarkers.

1.3. Thesis Aim

The experiments in this thesis were completed to address the current lack of platforms/tools for *in situ* monitoring of parameters such as pH within the cellular microenvironment. Being able to accurately quantify local analyte concentrations in real time within the microenvironment can provide insight into disease processes and conditions required for growth.

The aim of **Chapter 3** was to optimise electrospinning of pH responsive self-reporting scaffolds. Firstly the synthesis and characterisation of polyacrylamide nanosensors was demonstrated. PET and gelatin were electrospun respectively with sensor incorporation to mimic the structural features of the native extracellular matrix, the morphology of the constructs was also characterised. The polymers were then evaluated for their suitability as pH responsive self-reporting scaffolds by optical characterisation.

The individual objectives were as follows:

1. Synthesise and characterise size and optical activity of pH responsive polyacrylamide nanosensors.
2. Optimise electrospinning conditions for PET and gelatin with incorporation of sensors and characterise fibre morphology.
3. Optical characterisation of PET and gelatin self-reporting scaffolds for pH responsiveness.

The aim of **Chapter 4** was to optimise the incorporation flow conditions for cell culture in combination with electrospun scaffolds. Bioreactors have been shown to enhance mass transport of nutrients and oxygen throughout the constructs required for cell growth and activity, and help prevent the formation of necrotic regions. PET was initially used for flow optimisation due to its structural integrity and easy

handling. The development of a reproducible wound model was also attempted to observe the effects of flow conditions.

The individual objectives were as follows:

1. Optimise flow conditions of fibroblast culture on PET scaffolds
2. Develop a reproducible wound model for electrospun scaffolds
3. Optimise flow conditions of fibroblast culture on gelatin scaffolds

The aim of **Chapter 5** was to demonstrate the ability of the self-reporting scaffold to accurately monitor local extracellular pH change *in situ* in a non-invasive manner.

The individual objectives were as follows:

1. Demonstrate ability to monitor pH gradients
2. Culture cells upon self-reporting scaffolds
3. Culture cells over time and monitor local extracellular pH *in situ*

The aim of **Chapter 6** was to summarise all research findings and future work.

Chapter 2 Instrumentation, Materials & Methods

2.1. Instrumentation

2.1.1. Brightfield microscopy

For routine cell culture and assays performed on glass coverslips, cells were observed using a light microscope. Bright-field microscopy is a very simple technique and uses light sourced from a halogen bulb, which is aimed through a condenser which focuses and directs light onto the specimen. The sample absorbs the light and is magnified by the objective, and an image is observed via the oculars or camera. Cells can be imaged in real time using brightfield microscopy, but only if the sample is thin and mounted on a transparent substrate.



Figure 2.1 Olympus light microscope, Lumenara Infinity2-2 CCD Camera.

2.1.2. Fluorescence based techniques

2.1.2.1. Fluorescence principle

Fluorescence is a type of luminescence which describes the emission of light from fluorophores in electronically excited states. Fluorophores absorb light at a specific wavelength and then release the emitted light at a longer specific wavelength with lower energy¹⁵⁴. Figure 2.2 displays the processes involved in fluorescence. At the beginning of the process molecules are found in the ground state (S_0), upon exposure to a specific wavelength of light, the molecule absorbs the light resulting in the excitation of electrons to the higher energy singlet states (S_1 or S_2). Energy is released in the form of internal conversion or vibrational relaxation between the S_1 and S_2 states. During the return of the electron to the ground state (S_0), light is emitted in the form of fluorescence at a greater wavelength with lower energy¹⁵⁴. Excited state energy can also be dissipated non-radiatively as heat, and the excited fluorophore can collide with another molecule to transfer energy in a second type of non-radiative process such as quenching. Intersystem crossing may also occur resulting in the emission of a photon through phosphorescence or transition back to the excited singlet state that yields delayed fluorescence¹⁵⁵. The difference in the energy absorbed and the energy emitted is known as the Stokes' shift which is caused by several factors: the rapid decay to the lowest vibrational level of S_1 , further decay of fluorophores to higher vibrational levels of S_0 , solvent effects, excited-state reactions, complex formation, and/or energy transfer¹⁵⁴. Most fluorophores can repeat the excitation and emission cycle hundreds to thousands of times before the highly reactive excited state molecule is photobleached, resulting in the destruction of fluorescence¹⁵⁵.

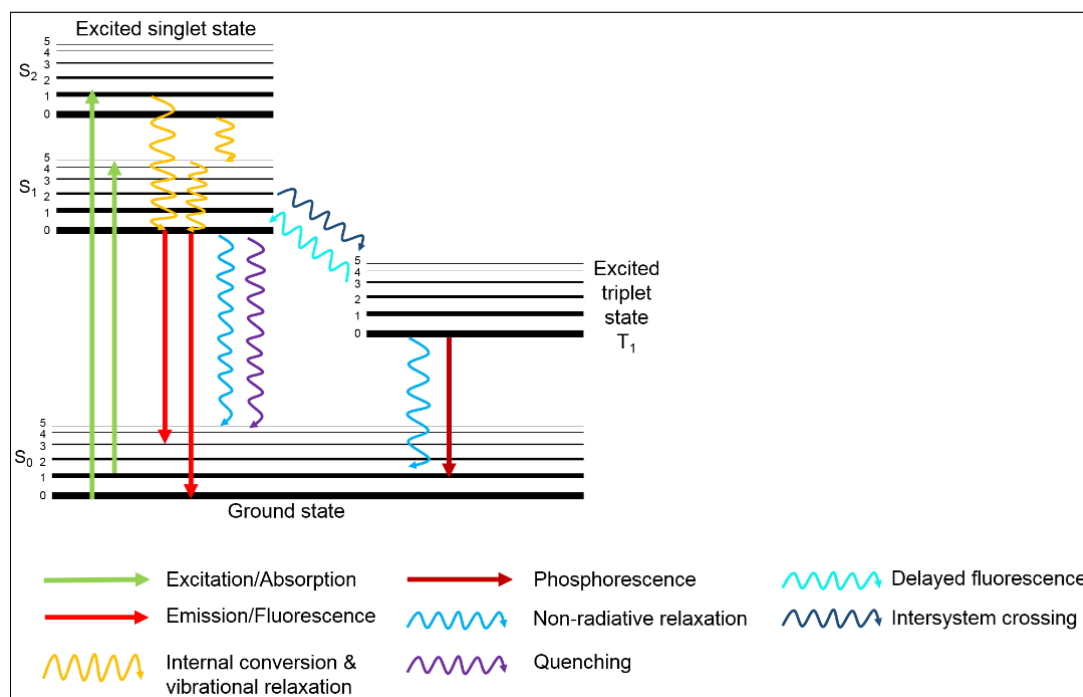


Figure 2.2 Jablonski energy diagram adapted from Johnson & Davidson¹⁵⁵.

2.1.2.2. Fluorescent microscope

Fluorescence microscopy allows direct visualisation of the physiological processes in a living cell or tissue¹⁵⁶. Fluorescence microscopy was used because it is rapid, has a high contrast and is a highly specific imaging technique with the ability to conjugate fluorescent labels to specific dyes or proteins. Greater fluorescent signals/intensities can be correlated to more expression of a dye or protein providing quantitative measurements. The basic principle of fluorescence microscopy involves the illumination of a sample containing fluorophores which are excited by a specific wavelength of light, the fluorophores subsequently emit light in the form of fluorescence which forms an image. The excitation light source containing all of the different wavelengths of light is produced by LED source. The excited light passes through an excitation filter which only allows the specific wavelength of light that is absorbed by the particular fluorophore. The dichroic mirror reflects the specific wavelength of light through the objective lens to the condensers which focus light

onto the sample. The fluorescence produced by the sample, travels back through the objective and is reflected through the dichroic mirror and emission filter, which only allows the specific emission wavelength through produced by the fluorophore. The signal is then sent to the detector and camera to create a fluorescent image.

- For image stitching and fluorescent staining the Leica DMIRE2 time-lapse DiC and fluorescence microscope with a Hamamatsu OrcaER monochrome camera was used. Volocity software was used for stitching.
- For the initial self-reporting scaffold/nanosensor calibration and *in situ* measurements, the Nikon Eclipse TE300 with an optiMOS Q Imaging camera was initially used.
- Due to microscope refurbishment, the scaffold/nanosensor calibration and local pH measurements were transferred to a Nikon Eclipse Ti-U with an optiMOS Q Imaging camera.

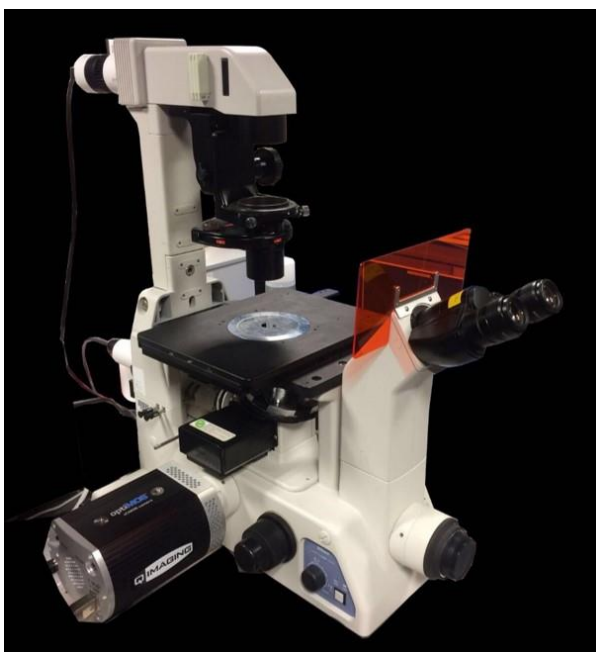


Figure 2.3 Photograph of Nikon Eclipse TE300, optiMOS™ sCMOS camera, objective 10X/0.30, working distance 16.0.

The ZOE™ fluorescent imager was used to for quick viewing of fluorescent cell samples. The sample is excited by a LED light of a specific wavelength. The light is passed through an emission filter and hits a detector. The detector is a complementary metal oxide semiconductor which contains photodiodes and convert the light into an electrical signal.



Figure 2.4 Bio-Rad Zoe™ fluorescent cell imager.

2.1.2.3. Fluorescence spectrometer

An Agilent fluorescence spectrometer was used to measure the fluorescence intensity emitted by the nanosensors whilst suspended in a range of pH buffers between pH 3.5 – 8.0. Fluorescence spectrometry is a rapid, easy and sensitive method to perform analysis of fluorescent compounds. A typical spectrometer contains an excitation source such as a xenon lamp, the sample placed in a cuvette, and a fluorescent detector. During the first step of the process, the excitation light from the lamp passes through a monochromator which passes only a selected wavelength. The sample is excited within the specific wavelength of light, and the emitted light is dispersed by another monochromator. This is detected by a

photomultiplier tube which amplifies the signal and provides a quantitative read out of the emission spectrum.

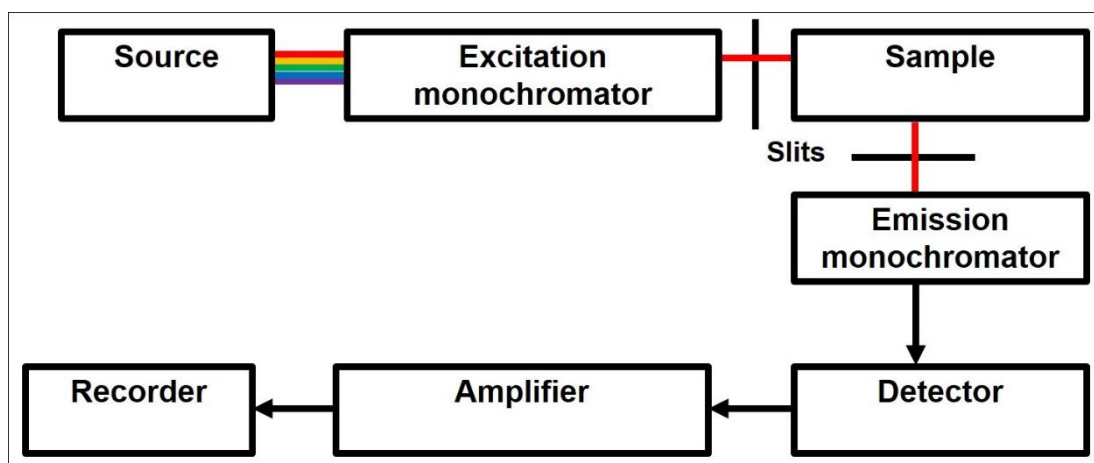


Figure 2.5 Schematic of the fluorescence spectrometry principle.

2.1.2.4. Fluorescent plate reader

A fluorescent plate reader was used to measure the fluorescence intensity from the fluorophore produced by AlamarBlue[®] reduction. Fluorescent plate readers work in a similar way to fluorescence spectrometers. They have a high energy xenon flash lamp which is used as the excitation system and illuminates the sample using a specific wavelength selected by a monochromator. The sample emits light in the form of fluorescence, and a monochromator collects the emitted light and separates it from excitation light. The signal is detected using a low noise photomultiplier tube.



Figure 2.6 BMG LABTECH FLUOstar Omega fluorescent plate reader.

2.1.3. Scanning electron microscopy (SEM)

SEM is useful for characterising the topography and architectural details of different surfaces at a high magnification which are unobservable using a light microscope. This technique was chosen to observe the morphology and structure of electrospun scaffolds and presence of cells.

SEM utilises a high energy electron beam produced by heating a tungsten filament which generates electrons through an electron gun. The electrons are fired through an electromagnetic lens which finely focuses the electron beam onto the sample. A scanning coil then allows the surface of the sample to be scanned by the electrons. The interactions between the electrons and the atoms of the sample produces different types of signals including secondary electrons and back-scattered electrons which provides information on the sample size, texture and composition. Detectors detect signals and are amplified and fed into an observation cathode ray tube to form an image.

2.1.3.1. Gold sputtering

Samples were sputter coated with gold prior to SEM imaging to prevent charging of the samples due to accumulation of static electric fields which can cause errors in observation. Sputter coating also increases the amount of secondary electrons that

can be detected from the surface of the specimen in the, increasing the signal:noise ratio. The sputtering process involves placing a target material (gold) attached to a cathode, and the SEM samples attached to an anode inside a vacuum chamber. A voltage is applied between them, and argon is fed into the chamber and ionised creating a plasma. The ionised argon bombards the target gold and sputters off the gold which deposits onto the samples.

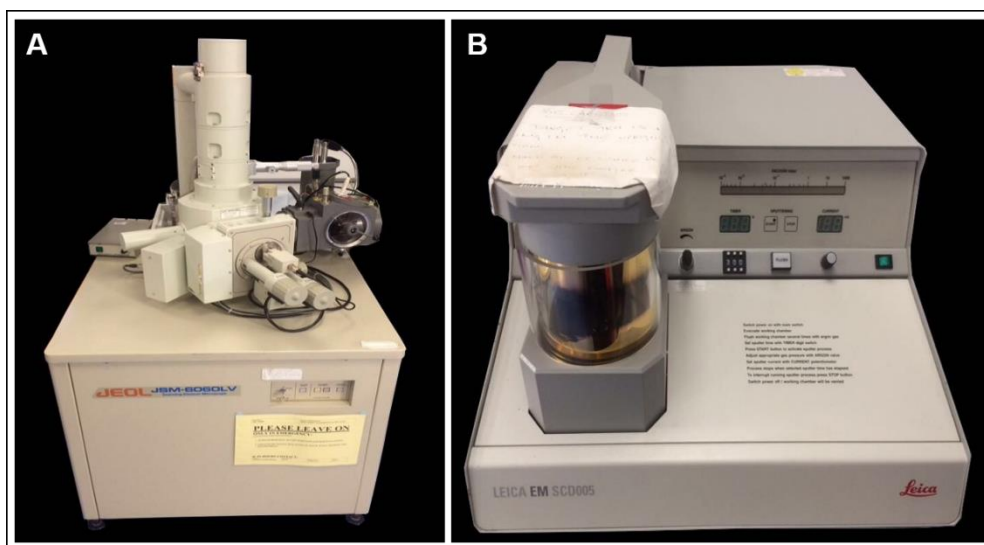


Figure 2.7 Jeol 6060LV variable pressure scanning electron microscope, (B) Leica EM SCD005 sputter coater.

2.1.4. Transmission electron microscopy

One drop of 1mg/mL nanosensor solution was carefully pipetted onto a 3.05mm diameter round hole copper grids and left to air dry. The nanosensor samples were imaged using the FEI Technai 12 Biotwin transmission electron microscope. The principle of transmission electron microscopy can be split into two main parts of illumination and image formation. During illumination a thin beam of electrons are accelerated under vacuum, and then are focused using an electromagnetic condenser lens onto the sample¹⁵⁷. Image formation depends on the density of the sample, some of the electrons are scattered. At the bottom of the microscope, the

unscattered electrons are collected by a detector and provides the contrast in the image of the sample, where the variation in darkness is determined by the variation in density¹⁵⁸. Some of the limitations of TEM is that the equipment is expensive, the procedures can be time consuming and small samples can lead to sample error and misinterpretation. The advantages of using transmission electron microscopy are that it provides high resolution of around 0.2nm¹⁵⁹ and the technique is largely standardised.

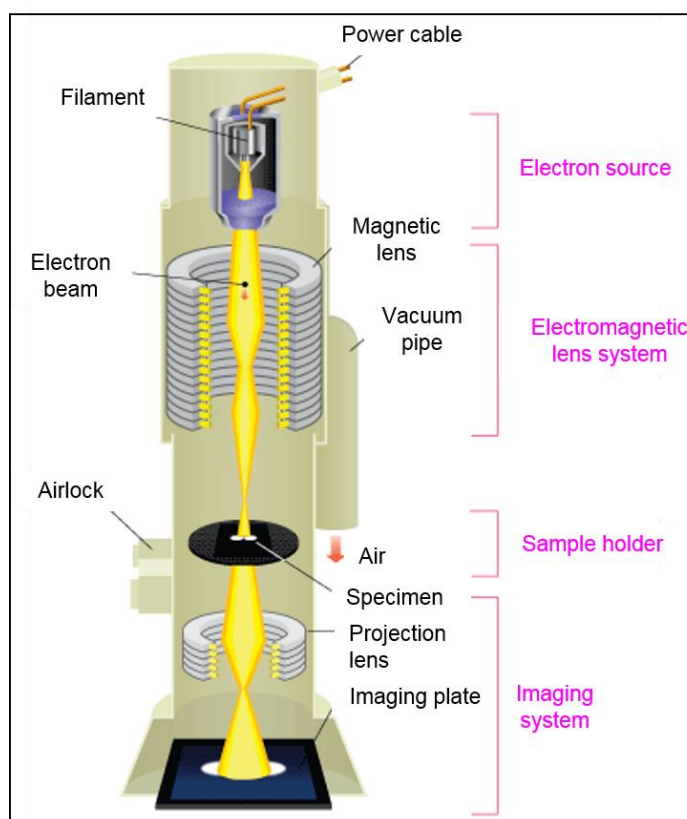


Figure 2.8 Schematic of transmission electron microscope, taken from The Chinese University of Hong Kong¹⁶⁰.

2.1.5. Zetasizer

Dynamic light scattering (DLS) was used to characterise the hydrodynamic size of polyacrylamide nanosensors. This technique measures the speed at which the particles move in suspension due to the interaction with the surrounding solvent

molecules (Brownian motion) by quantifying the scattered light intensities. The Stokes-Einstein equation below relates the random motion measured by dynamic light scattering to particle size where:

- $d(H)$ = hydrodynamic diameter
- k = Boltzmann's constant
- T = thermodynamic temperature
- η = dynamic viscosity

$$d(H) = \frac{kT}{3\pi\eta}$$

The principle of DLS involves initially illuminating the sample contained within a cuvette with a laser. The laser passes through the sample, but some of the light is scattered by the particles which is detected by a detector. Depending on the size and concentration of the sample, an attenuator tailors the amount of light passes through. If too much light is detected, the detector will become saturated so the attenuator reduces the intensity of laser and reduces the intensity of scattering. Samples of small size or low concentration should allow more light through to increase light scattering.



Figure 2.9 Malvern Zetasizer Nano ZS.

2.1.6. pH electrode

The Ross combination pH, semi-microelectrode was connected to a Jenway 3510 pH meter measure the pH of buffers used for nanosensor calibration and extracellular pH measurements (as a comparison to self-reporting scaffold measurements). A temperature probe was also connected.

The principle behind how the pH electrode works, involves the use of a reference electrode which often consists of a silver chloride coated silver wire, and a sensing electrode. The sensing of the pH occurs in the glass membrane in the bulb of the electrode which are submerged in a solution of potassium chloride¹⁶¹. The surface of the glass in contact with the solution in question uptakes water and becomes hydrated, and the hydrated surface is where the ions are exchanged¹⁶¹. The potassium chloride contains hydrogen ions of a known neutral pH; when measuring the pH of an unknown solution, the glass electrode determines the difference in pH between the potassium chloride solution and the unknown solution by measuring the difference in voltages their hydrogen ions produce. The Ag/AgCl electrode is

connected to a pH meter which measures the potential difference and its changes across the glass membrane¹⁶².

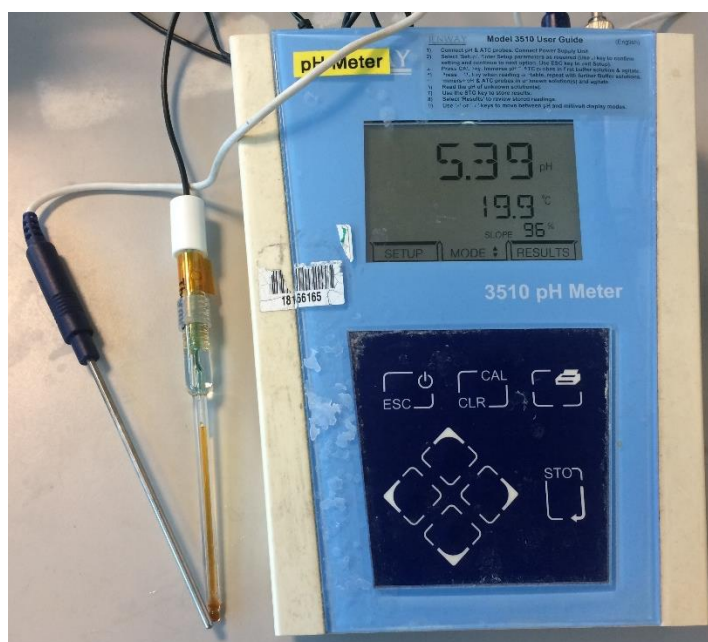


Figure 2.10 Semi-micro electrode for pH measurements.

2.2. Materials

2.2.1. Electrospinning

Electrospinning apparatus: 10mL plastic syringes and 18G blunt needles were purchased from BD Falcon (United Kingdom). Stainless steel collector plate (10 x 15cm), syringe pump (Harvard Apparatus PHD 200), voltage supply box (Genvolt, model 71320), crocodile clips obtained from RS Components (Corby, United Kingdom). Electrospinning safety box was manufactured by University of Nottingham, Chemical Engineering.

Coaxial spinning: Prebuilt coaxial needle (inner needle Gauge 20G, outer needle Gauge 16G), Luer plugs for tubing 1/8" internal diameter, chemical resistant Tygon tubing 1/8" internal diameter.

Polymers: Polyethylene terephthalate (PET) scaffolds: PET and trifluoroacetic acid were purchased from Sigma-Aldrich (Gillingham, United Kingdom). PET was also sourced from Phosphate Saline Buffer bottles purchased from Sigma-Aldrich. Dichloromethane (DCM) was obtained from Fisher Scientific (Loughborough, United Kingdom). Gelatin scaffolds: Gelatin from porcine skin gel strength 300 Type A, 1,1,1,3,3,3-hexafluoro-2-propanol (HFIP), glutaraldehyde (GTA) solution for crosslinking were purchased from Sigma-Aldrich (Gillingham, United Kingdom). Deionised water (18.2M Ω) for GTA dilution was generated by Elga Purelab Ultra. CellCrown™ 24 well inserts to secure the scaffolds were purchased from Sigma-Aldrich (Gillingham, United Kingdom).

2.2.2. Polyacrylamide nanosensors

Nanoparticles: Acrylamide 99% minimum, N,N'-methylenebis (acrylamide) and Brij30® ammonium persulfate (APS), dioctyl sodium sulfosuccinate salt (AOT), and N,N,N',N'-tetramethylethylenediamine (TEMED) were purchased from Sigma-Aldrich (Gillingham, United Kingdom). Hexane HPLC grade and Ethanol analytical grade were obtained from Fisher Scientific (Loughborough, United Kingdom). Argon gas acquired from BOC Gases (Manchester, United Kingdom). Deionised water (18.2M Ω) was generated by Elga Purelab Ultra (ULXXXGEM2). N-(3-aminopropyl) methacrylamide hydrochloride (APMA) was obtained from Polysciences Inc (Warrington, United Kingdom). Sodium borate decahydrate was obtained from Sigma-Aldrich (Gillingham, United Kingdom)¹⁶³

Fluorophores: Fluorophores 5-(and-6)-carboxyfluorescein succinimidyl ester (FAM-SE), Oregon Green[®] 488 carboxylic acid succinimidyl ester (OG-SE), and 5-(and-6)-carboxytetramethylrhodamine succinimidyl ester (TAMRA-SE) were purchased from Invitrogen[™] (Paisley, United Kingdom)¹⁶³.

Buffers: Citric acid monohydrate $\geq 99.0\%$ and sodium phosphate dibasic $\geq 99.0\%$ were purchased from Sigma-Aldrich (Gillingham, United Kingdom). Deionised water (18.2M Ω) was generated by Elga Purelab Ultra (ULXXXGEM2)

2.2.3. Cell culture

Cell lines: MRC5 Human lung fibroblasts (LGC Standard, United Kingdom) \leq passage 30 were purchased from Sigma-Aldrich (Gillingham, United Kingdom). NIH-3T3 Mouse embryonic fibroblasts and 3T3-GFP \leq passage 45 were kindly supplied by Dr. James Dixon (University of Nottingham, School of Pharmacy).

Cell maintenance: Minimum Essential Medium (MEM), Dulbecco's Modified Eagle's Medium (DMEM), foetal bovine serum, 2mM L-glutamine solution, penicillin/streptomycin solution, non-essential amino acid solution, phosphate buffered saline antibiotic/antimycotic solution, trypsin-EDTA x10, trypan blue were purchased from Sigma-Aldrich (Gillingham, United Kingdom).

Staining: Paraformaldehyde was purchased from Electron Microscopy Sciences (Hatfield, United States), Alexa Fluor[®]488 phalloidin was purchased from Cell Signalling Technology, inc. (Denvers, United States). Anti-ki67 rabbit monoclonal primary antibody was purchased from Abcam (Cambridge, United Kingdom), and Alexa Fluor[®]594 goat anti rabbit secondary antibody was purchased from Thermofisher (Loughborough, United Kingdom). 4',6-Diamidine-2'-phenylindole dihydrochloride (DAPI), Direct Red 80, Triton-X, and Goat Serum were purchased

from Sigma-Aldrich (Gillingham, United Kingdom). Hoechst[®] 33342 trihydrochloride, trihydrate 10mg/mL solution in water was purchased from Life technologies[™] (Paisley, United Kingdom).

Wound healing assay: 13mm glass coverslips were purchased from VWR international (Leicestershire, United Kingdom). 1M hydrochloric acid, sodium hydroxide pellets, Whatman[®] qualitative filter paper were purchased from Sigma-Aldrich (Gillingham, United Kingdom). Cosmetic cotton tip buds were purchased from Boots (Nottingham, United Kingdom).

Flow culture systems: Peristaltic pumps were purchased from Parker Hannifin Ltd (Warwick, United Kingdom) and Watson-Marlow (Cornwall, United Kingdom). *Quasi-Vivo*[®] 500 kit: Purchased from Kirkstall Ltd (Rotherham, United Kingdom), consists of QV500 bioreactors, 3/32" silicon tubing, 1/16" silicone tubing, medium reservoir, 13mm glass coverslips, loading tray, 0.20µm filter (Millipore). *Quasi-Vivo*[®] 900 kit: Purchased from Kirkstall Ltd (Rotherham, United Kingdom), consists of QV900 optically transparent bioreactor, 3/32" silicon tubing, medium reservoir, 0.20µm filter (Millipore).

Consumables: T75 flasks (Corning[®]), 24 well non-tissue culture plates (Corning[®]Costar[®]), 12 well non-tissue culture plates (Corning[®]Costar[®]) were all purchased from Sigma-Aldrich, 96 flat well plates were obtained from Appleton Woods (Birmingham, United Kingdom). Sterilin standard 90mm petri dishes were purchased from ThermoFisher (Loughborough, United Kingdom).

2.3. Methods

2.3.1. Electrospinning

Electrospinning was used for the fabrication of electrospun scaffolds. This technique produces fibres in the submicron range by using an electrostatic force to draw threads of the polymer solution. The polymer solution is injected at a constant flow rate through a needle and a high voltage is applied to the liquid droplet at the tip of the needle. The liquid droplet becomes charged and at sufficient voltage the droplet is stretched and forms a Taylor cone. This is elongated to form a jet of charged polymer solution undergoes a whipping process caused by electrostatic repulsion which is attracted to the oppositely charged earthed collector. The solvent evaporates from the polymer solution depositing dry fibres.

Electrospinning setup: Polymers gelatin and PET were dissolved in the chosen solvent(s) respectively at the desired concentration, and allowed to stir on a magnetic stirrer for 24 hours at room temperature. The polymer solution was put into a 10mL syringe with an 18G blunt end needle attached and secured onto a syringe pump to provide a constant flow rate. A high voltage supply was applied to the polymer solution by placing a crocodile clip attached to a voltage supply onto the needle tip. A steel collector plate with a crocodile attached for earthing, was placed opposite the needle tip at a specific distance as shown in Figure 2.11.

- **Polyethylene terephthalate (PET):** PET was dissolved in 1:1 ratio of trifluoroacetic acid (TFA) and dichloromethane (DCM) to create a 10% (w/v) solution. The electrospinning apparatus was set up at room temperature using a flow rate of 0.5mL/hr on the syringe pump, a voltage of 15kV was supplied and along with a distance of 15cm from the needle

tip to the steel collector plate. The scaffolds were left in a fumehood for 24 hours to allow residual solvent TFA and DCM to evaporate.

- **Gelatin:** Gelatin from porcine skin Type A was dissolved in 1, 1, 1, 3, 3, 3-hexafluoro-2-propanol (HFIP) on a magnetic stirrer for 24 hours to make a solution of 80mg/mL. The electrospinning apparatus was set up at room temperature using a flow rate of 0.8mL/hr on the syringe pump, a voltage of 15kV was supplied along with a distance of 15cm from the needle tip and steel collector plate. The scaffolds were air dried in a fumehood for 24 hours to allow residual solvents HFIP to evaporate.

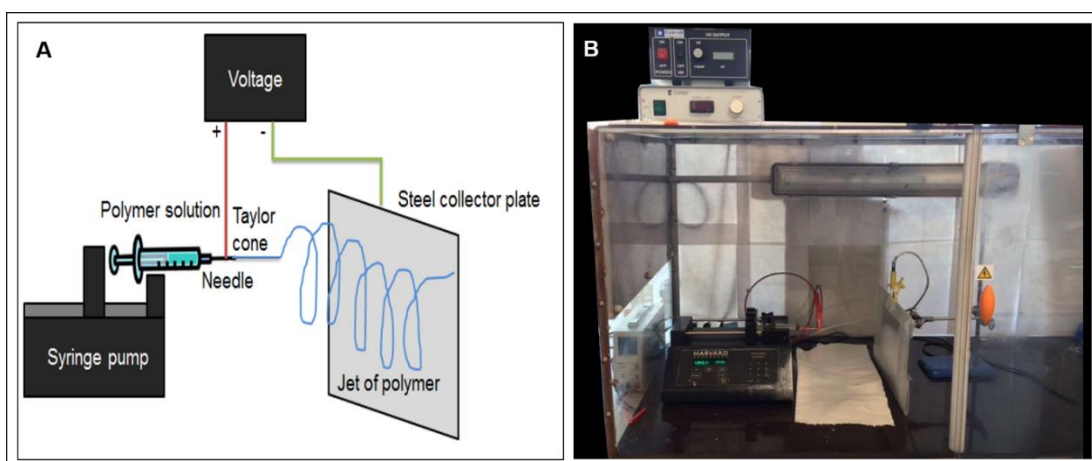


Figure 2.11 (A) Schematic of electrospinning apparatus, (B) Photograph of electrospinning set up.

2.3.2. Crosslinking of electrospun gelatin

The electrospun gelatin scaffolds were cut into 1.5cm x 1.5cm and secured by CellCrowns™. This held the scaffolds in place to prevent them from falling apart. CellCrowns™ are a plastic insert made up of two components, a cylindrical ring and an 'O' ring. The scaffold is placed over the cylindrical ring and the 'O' ring is placed on top with the scaffold draping over the sides, to tightly secure the scaffold see Figure 2.12A. They were then placed onto a plastic mesh in a sealed glass

container and suspended 2.5cm above glutaraldehyde solution (25mL, 1.25% (v/v) in deionised water) for 24 hours at room temperature to allow the vapours to crosslink gelatin, see Figure 2.12B.

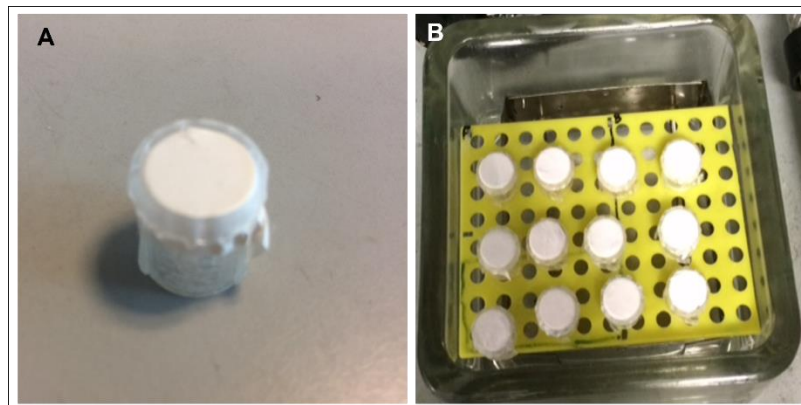


Figure 2.12 (A) Electrospun gelatin scaffolds secured in CellCrowns™ (B) CellCrowns™ placed on a plastic mesh, submerged above 1.25% glutaraldehyde vapours in a glass box.

2.3.3. Preparation of pH sensitive nanosensors

Nanosensors were synthesised as outlined by Chauhan et al¹⁶³.

Conjugation of fluorophores: N-(3-aminopropyl) methacrylamide (APMA) (5mg, 0.028mM) was dissolved in sodium borate solution (2.5mL, 50mM, pH 9.5). Fluorophores 5(6)-FAM-SE (1mg, 0.002mM), OG-SE (1mg, 0.02mM) and TAMRA-SE (1mg, 0.002mM) were added to separate light resistant vials of APMA stock solution. The vials were stirred for 24 hours to allow the fluorophores to conjugate to the APMA via a nucleophilic addition reaction.

Synthesis of nanosensors: All deoxygenation steps were conducted using argon. Initially, 42 mL of hexane (oil phase) was deoxygenated for 30 minutes, followed by surfactants Brij 30 (3.080 g, 8.508 mmol), dioctyl sodium sulfosuccinate salt (1.590 g, 3.577 mmol) which were then combined and stirred under argon for a further 15

minutes, the flask was then sealed under an inert argon atmosphere using a balloon.

Acrylamide (0.540g, 7.579 mmol), and N,N'-methylenebis(acrylamide) (0.160 g, 1.307mmol) were dissolved in 2mL of deionised water using sonication. Fluorophores conjugated to APMA were added to the acrylamide solution (FAM-APMA (15 μ L, 5 mg/mL), OG-APMA (15 μ L, 5 mg/mL), TAMRA-APMA (60 μ L, 5 mg/mL). This monomer solution was then added to the stirring hexane surfactant solution and allowed to deoxygenate for a further 10 min. Polymerisation initiators ammonium persulfate (30 μ L, 10% w/v) and N,N,N',N'-tetramethylethylenediamine (15 μ L, 0.1 mmol) were added to the stirring solution to initiate polymerisation. The mixture was left to stir for 2 hours under argon in a light protected flask. Hexane was removed via rotary evaporation.

Nanoparticles were precipitated and washed with ethanol (30 mL) using centrifugation (7 times, 6000 rpm, 10 min), with a Hermle centrifuge (Z300). After the final wash, the pellet was resuspended in 10mL of ethanol and rotary evaporated in a water bath at 40°C until dry. Nanoparticles were stored in a light protected glass vial at 4°C.

2.3.3.1. Size determination of nanosensors

Dynamic light scattering was performed using a Malvern Zetasizer Nano ZS to characterise the hydrodynamic size of the polyacrylamide nanosensors. The system is equipped with a 5mW He-Ne laser source (633nm) and operating an angle of 173°. Polyacrylamide nanoparticles were suspended in deionised water at 1mg/mL. Measurements were made at 25°C using a disposable Sarstedt® cuvette. The mean hydrodynamic diameter of the samples was calculated from the intensity of the scattered light using the Malvern Zetasizer software.

2.3.3.2. Assessing pH responsiveness of nanosensors

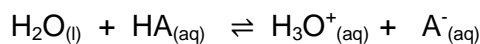
2.3.3.2.1. Buffer solutions

A buffer solution is an aqueous solution able to resist changes in pH change upon the addition of a limited amount of acid or base¹⁶⁴. The change is resisted by the addition or removal of hydrogen ions (protons) or hydroxide ions known as ionisation. A buffer system is usually composed of a weak acid or base and its conjugate salt, these components are always in equilibrium, and act in such a way that the addition of an acid or base results in the formation of a salt causing only a small change in pH¹⁶⁴.

The relative capacity of an acid to donate a proton to a common base such as water under identical conditions is quantified as the acidity constant K_a ¹⁶⁵. Each buffer has a specific pH range at which it works best, above or below this range means that the buffer loses its capability to resist pH change.

The magnitude of the equilibrium constant for an ionisation reaction can be used to determine the relative strengths of acids and bases¹⁶⁶. The equilibrium constant gives the ratio of concentrations of products over reactants for the ionisation reaction that is at equilibrium¹⁶⁷.

The general equation for the ionisation of a weak acid in water below is based on the Brønsted–Lowry theory. The fundamental concept of the theory is that when an acid and a base react with each other, the acid is a proton donor and dissociates to forms its conjugate base, and the base is a proton acceptor and forms its conjugate acid by exchange of a proton¹⁶⁸.



H_2O = water (base)

HA = weak acid

H_3O^+ = hydronium, a cation which forms in the presence of hydrogen ions
(conjugate acid)

A^- = conjugate base

This equation can be rewritten to provide the acid dissociation constant which refers to the acid ionisation constant K_a . The numerical value of K_a is used to predict the extent of acid dissociation and strength of acid in solution. A large K_a value means a stronger acid and higher acid dissociation, whereas a small K_a value means a weaker acid and less acid dissociation¹⁶⁹. Strong acids completely ionise and easily lose a proton when dissolved in water, whereas weak acids do not ionise completely, forming an equilibrium between the non-ionised and ionised forms of the acid. Two key factors which contribute to the ease of deprotonation are the polarity of the H-A bond and the size of atom A, which determines the strength of the H-A bond. Acid strengths also depend on the stability of the conjugate base.

$$K_a = \frac{[\text{H}_3\text{O}^+][\text{A}^-]}{[\text{HA}]}$$

Based on this expression for K_a , we can derive the Henderson-Hasselbalch equation by rearranging and taking the negative log of the acid dissociation constant as shown below¹⁷⁰. By taking the negative log of the acid dissociation constant, it gives the pKa which can be used to describe acid dissociation. The lower pKa the more easily it gives up a proton and the stronger the acid. The Henderson-Hasselbalch equation is used to mathematically describe the properties of buffers. It shows that the pH of a buffer is determined by the pKa of the weak acid used in

these different pH buffers, different fluorescent intensities from the nanosensors are emitted.

pH	Volume	
	Sodium phosphate dibasic (0.2M)	Citric acid monohydrate (0.1M)
3.5	6.04	13.96
4.0	7.72	12.28
4.5	9.00	11.00
5.0	10.28	9.72
5.5	11.36	8.64
6.0	12.84	7.16
6.5	14.20	5.80
7.0	17.44	2.56
7.5	17.98	2.02
8.0	19.53	0.47

Table 2.1 Volumes of sodium phosphate dibasic (0.2M) and citric acid monohydrate (0.1M) to make different pH buffers

2.3.3.2.2. Fluorescence spectrophotometry

Polyacrylamide nanosensors were suspended in deionised water, followed by suspension in a range of individual buffers between pH 3.5 – 8.0 to make a final concentration of 1mg/mL. The suspension was placed in a disposable cuvette and placed in the fluorescence spectrophotometer. The nanosensors were excited at a wavelength of 488nm using a green filter, along with an excitation slit of 2.5 and an emission slit of 5.0. Nanosensors were also excited at a wavelength of 540nm using a red filter, along with an excitation slit of 2.5 and an emission slit of 5.0.

2.3.3.2.3. Fluorescence microscopy and image analysis

Polyacrylamide nanosensors were suspended in deionised water, followed by suspension in a range of individual buffers between pH 3.5 – 8.0 to make a final concentration of 1mg/mL. The individual suspensions were placed in a 24 well plate and imaged using a fluorescent microscope.

Image acquisition settings from the microscope including exposure and gain were set on the sample with the brightest fluorescent intensity, the settings were kept constant throughout all image acquisition. The pH responsive fluorophores 5(6)-FAM and OG were excited using the green channel (excitation wavelength 488nm), and the reference fluorophore TAMRA was excited using the red channel (excitation wavelength 551nm). LED intensity for the green channel was 90% and red channel was 75%, with exposures of 150m/s and 100m/s respectively. Fluorescent images were taken at x10 magnification, and the fluorescent intensity was quantified using Image J. The green and red fluorescent intensities corresponding to each pH buffer value were plotted to provide an emission curve. A ratiometric curve was produced by taking a ratio of the emission from the pH responsive channel and the reference channel (520nm/577nm).

Automated image analysis: MATLAB and Fiji Image J was used for automated image analysis. The script was developed and programmed by Gianni Orsi from the University of Pisa, and the algorithm used is described by Chauhan et al¹⁶³. The process involved firstly calibration of the nanosensors, by suspending in buffer solutions ranging from pH 3.5 – 8.0. The microscope acquired images with a canvas size of 1024 x 1024 in a TIFF file format. All images were taken with using the green channel excitation wavelength with exposure of 400m/s, LED 75%, the red channel excitation wavelength with exposure 150m/s, LED 100%. Automated imaging of the calibration images was performed using an algorithm implemented with MATLAB®.

Initially, random saturated and blank pixels were removed from the FAM and OG (green) and TAMRA (red) channels images with a median filter (2.0 pixels). Background corrected images were generated through subtraction of green and red fluorescent intensities of suspensions containing nanoparticles by solutions without nanoparticles. Ratiometric calibration images were created by taking a pixel wise ratio of the background corrected green and red fluorescent channels. An additional median filter (2.0 pixels) was applied to remove any further saturated/unsaturated pixels. A ratiometric image was generated by taking a pixel-wise ratio of green and red fluorescent channels to produce a grey scale image which was transformed into a false colour pH heat map using FIJI Open source software.

2.3.4. Incorporating nanosensors in electrospun scaffolds

The electrospinning method described in section 2.3.1 was performed with the adjustment of adding polyacrylamide nanoparticles to the polymer solution (10mg/mL), this was then stirred for an additional 24 hours on the magnetic stirrer at room temperature.

2.3.5. Preparation of scaffolds for cell culture

Polyethylene terephthalate (PET): Scaffolds were cut into circles of 2cm in diameter using a scalpel (Swann-Morton) and secured by autoclaved steel rings. To sterilise the scaffolds, they were placed under ultraviolet (UV) light at 254nm for 15 minutes on each side. The PET was transferred to a 12 well non-tissue culture plate (Corning®) and submerged in 70% ethanol for 15 minutes. This was then removed and further sterilised in antibiotic/antimycotic solution overnight (37°C, 5% CO₂).

Following sterilisation, the scaffolds were placed in the relevant cell culture media at 37°C for 24 hours to precondition the scaffold.

Gelatin: Crosslinked scaffold were submerged in 70% ethanol for 30 minutes, this was then removed and the scaffolds were further sterilised in antibiotic/antimycotic solution overnight (37°C, 5% CO₂). Following sterilisation, the scaffolds were placed in the relevant cell culture media at 37°C for 24 hours to precondition the scaffold.

2.3.6. Calibration of electrospun scaffolds containing nanosensors

2.3.6.1. Fluorescence microscopy

Buffers ranging from pH 3.5 – 8.0 were prepared as described in 2.3.3.2.1. Crosslinked gelatin scaffold and PET were submerged in individual buffers ranging from pH 3.5 – 8.0. Fluorescent images at x10 magnification were acquired from 3 different areas of each scaffold, using the reporter green channel (excitation 488/emission 520), and the reference red channel (excitation 551/emission 571). The same exposure and LED settings were used from the nanosensor suspension calibration. The fluorescent intensity of the images were quantified using Image J software. To obtain ratiometric measurements, the emission intensities of the green channel were divided by the constant red channel ($\lambda_{em} 520nm/\lambda_{577nm}$), the values obtained were plotted against the corresponding pH to produce a sigmoidal calibration curve. The settings on each microscope, including the magnification, exposure and LED intensity were kept consistent throughout all of the calibration experiments. Automated image analysis was also performed as described in section 2.3.3.2.3, but the initial stage involved putting the self-reporting scaffolds in a range of buffers instead of the nanosensors.

2.3.6.2. Measuring local pH changes using the electrospun gelatin scaffold containing nanosensors

Cell seeding: NIH-3T3 mouse fibroblasts were seeded onto the sterilised electrospun gelatin scaffolds containing nanosensors at density of $3 \times 10^5/50\mu\text{L}$. The CellCrowns™ (see Figure 2.12) were placed in a 12 well non tissue culture and incubated at 37°C in 5% CO₂ for 2 hours to allow the cell attach. Cells were preincubated with Hoechst stain for 20 minutes at 37°C, 5% CO₂ prior to seeding to track the cells, unbound dye was then removed by centrifugation at 350g for 5 minutes. Following cell attachment, cells were suspended in 2.5mL phenol free, HEPES free, DMEM media and incubated over different time points: 7 days, 4 days and 1 day.

Imaging: Fluorescent images at x10 magnification were acquired at the different time points (7 day, 4 day, 1 day) of the cell-seeded scaffold in 5 different areas per sample, using the reporter green channel (excitation 488/emission 520), and the reference red channel (excitation 551/emission 571) The settings on the microscope were kept consistent throughout all of the experiments and calibration.

Using the ZOE Bio-RAD fluorescent imager, the nuclei of the cells stained with Hoechst were monitored to confirm their presence.

Automated image analysis: The automated image analysis process was performed as described in 2.3.3.2.3. However, with the modification of the background images that were acquired included scaffolds containing nanoparticles and scaffolds without nanoparticles.

Calibration: Cell seeded scaffolds were washed with filter sterilised deionised water and fixed with 4% paraformaldehyde (PFA) (diluted with deionised water) for 20

minutes at room temperature. Scaffolds were then washed again with deionised water to remove residual PFA. Scaffolds were then calibrated as described in 2.3.6.1.

pH measurements: To obtain *in situ* pH measurements using the scaffold, the equation of the ratiometric sigmoidal calibration curves were fitted with the following equation:

- R_i = Indicator to reference ratio (ratiometric intensity)
- R_{min} = Minimum detectable nanosensors response (lower asymptote)
- R_{max} = Maximum detectable nanosensors response (upper asymptote)
- pK_a = pH value where fluorophore shows half the maximum fluorescent response
- $Hillslope$ = Slope of the curve

$$R_i = R_{min} + \frac{R_{max} - R_{min}}{1 + 10^{(pKa - pH \cdot hillslope)}}$$

The equation can be rearranged to provide the pH values:

$$pH = \frac{-\log_{10} \left(\frac{R_{max} - R_{min}}{R_i - R_{min}} - 1 \right)}{hillslope} + pK_a$$

The equation is a common fitting equation used for calibration of various sensors¹⁷². This was established in early work by WolfBeis¹⁷³ on ionophore based electrochemical sensors. Other studies measured intensity ratios have been modelled using a linear equation, particularly if only a few points have been taken to

generate the calibration¹⁷². Therefore this can be a source of error often not considered in measurements.

2.3.6.3. Characterisation of electrospun scaffolds by scanning electrospun microscopy (SEM)

Fibre morphology: Fibre diameter of electrospun PET and gelatin scaffolds were examined by scanning electron microscopy (SEM; JOEL SM 1100, UK). Small sections of the samples (1cm x 1cm) were cut and placed onto 12mm carbon coated aluminium stubs (Agar Scientific, United Kingdom). The samples were sputter coated with gold (300 seconds, Blazers SCD 030 Blazers Union Ltd, Liechtenstein) under an argon atmosphere (BOC, U.K.) prior to analysis. Samples were imaged using SEM analysis (JEOL JMS-6060 LV microscope, JEOL Ltd., U.K.) operating at an accelerating voltage of 10 kV and working distance of 9 – 30cm. SEM images were analysed using Image J to determine fibre diameter of the electrospun scaffolds.

Cells seeded scaffold: Cell seeded scaffolds were dehydrated prior to SEM imaging to reduce distortion caused by evaporation of water molecules within the sample. The samples were washed with phosphate buffered saline (PBS) and fixed with 4% paraformaldehyde (PFA) for 20 minutes at room temperature, residual PFA was removed by washing with PBS. Cell samples were dehydrated by submerging in ascending concentrations of ethanol 10%, 30%, 60% 80%, 100%, and then placed on the carbon coated aluminium stub. Samples were then imaged using the SEM.

2.3.7. Cell culture techniques

2.3.7.1. Routine cell culture

All cells were routinely cultured in tissue culture treated plastic T75 flasks in a humidified incubator at 37°C, 5% CO₂. Cell media was changed every 2 – 3 days and cells were passaged when they reached approximately 80% confluence.

MRC5 (Human lung fibroblasts) cell line: Cultured in Minimum Essential Medium (MEM) supplemented with 10% (v/v) foetal bovine serum, 1% L-glutamine solution (2mM) and 1% penicillin/streptomycin solution, 1% non-essential amino acid solution all purchased from Sigma-Aldrich (Gillingham, United Kingdom).

NIH-3T3 (Mouse embryonic fibroblasts): Cultured in Dulbecco's Modified Eagle's Medium (DMEM) supplemented with 10% (v/v) foetal bovine serum, 1% L-glutamine solution (2mM) and 1% penicillin/streptomycin solution were all purchased from Sigma-Aldrich (Gillingham, United Kingdom).

2.3.7.2. AlamarBlue[®] assay

To measure cellular proliferation, a non-toxic AlamarBlue[®] assay was performed. AlamarBlue[®] contains non-fluorescent, cell permeable molecule resazurin which is converted to the fluorescent molecule resorufin. As the resazurin enters the cell, it is reduced to resofurin by mitochondrial enzymes which provides a red fluorescence which can be quantified to measure viability.

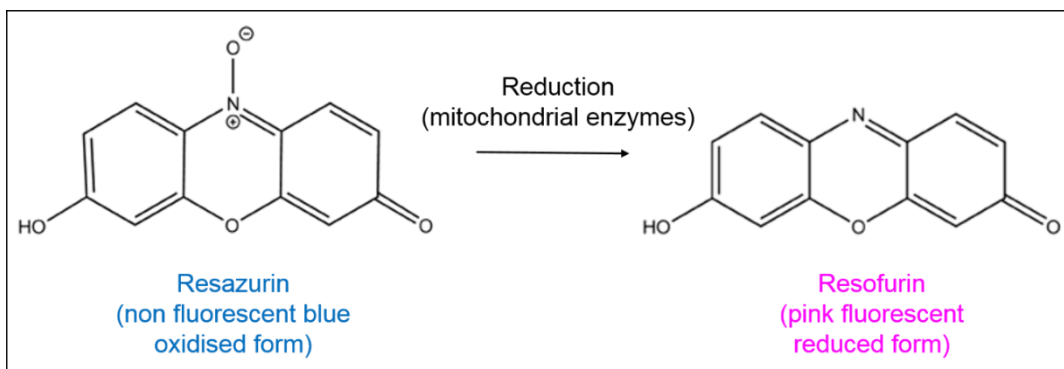


Figure 2.14 Molecular structure of resazurin molecule found in AlamarBlue[®] solution reduced to fluorescent resofurin form.

To perform the assay cell seeded scaffolds and blank control scaffolds were supplemented with fresh cell culture medium and 10% (v/v) AlamarBlue[®] at 37°C, 5% CO₂ for 2.5 hours. As a positive control, 100% reduced form of AlamarBlue[®] was produced by autoclaving a blank control at 121°C for 15 minutes supplemented with 10% (v/v) AlamarBlue[®]. 100µL of the media was transferred to a black 96 well plate in triplicate and the fluorescence was measured using FLUOstar OPTIMA plate reader at excitation 544nm, emission at 590nm. The percentage reduction of AlamarBlue[®] for each experiment was calculated using the formula:

- S^x = AlamarBlue[®] fluorescence signal of the sample
- $S^{100\% \text{ reduced}}$ = signal of the 100% reduced form of AlamarBlue[®]
- S^{control} = signal from blank control

$$\text{Percentage reduction of AlamarBlue} = \frac{(S^x - S^{\text{Control}})}{(S^{100\% \text{ reduced}} - S^{\text{Control}})}$$

2.3.7.3. Sirius red collagen stain

Sirius red stain was performed to assess collagen production by cells. Sirius Red binds specifically to $[\text{Gly-x-y}]_n$ helical structure on fibrillar collagen (type I-V).

Fixed cell-seeded PET scaffold secured in a steel ring were washed with PBS. 0.1% Sirius red solution diluted in PBS was applied and left to agitate on a platform rocker at 35rpm for 24 hours. The excess unbound Sirius red was washed off with PBS and samples were air dried for 30 minutes and photographic images were acquired for qualitative analysis. For quantitative analysis, a standard curve of different known concentrations of Sirius Red were produced. A solution of 0.2M NaOH and methanol (1:1) was used to detach the bound Sirius red from the cellular samples on a platform rocker at 35rpm for 24 hours. The absorbance of the eluate was read at 520nm using the FLUOstar plate reader in a 96 well tissue culture plate.

2.3.7.4. Fluorescent staining

2.3.7.4.1. F-actin cytoskeleton and nuclear stain

To view the cells on the scaffold and their morphology, an F-actin cytoskeleton and nuclear stain was performed on fixed cells. Alexa Fluor488[®] phalloidin is a high-affinity F-actin probe conjugated to a bright, photostable, green-fluorescent dye. DAPI binds upon adenine-thymine regions of DNA within the nucleus and emits a strong blue fluorescence.

Cells were firstly washed with phosphate buffered saline (PBS) three times. For the staining protocol, in between each step, cells were washed with PBS three times. The first step involved submerging cells in 0.15% Triton™ X-100 for 20 minutes at room temperature to permeabilise the cell membranes to allow entry of the dyes. After this, 5% goat serum was added and incubated for 30 minutes at room

temperature to block any non-specific protein binding sites. The next step involved adding Alexa-Fluor488 phalloidin (1:20) for 20 minutes at room temperature, and then DAPI (1:20000) for 5 minutes at room temperature. The samples was mounted onto a 76 x 26 mm glass slide (Thermo Scientific, United Kingdom). A drop of FluorSave™ anti fade (Calbiochem, United Kingdom) and Fluoromount™ mounting media (Sigma-Aldrich, United Kingdom) was placed on top of the sample. Sample preparation was finished by covering the sample with a 25 x 50mm glass coverslip (Menzel-Gläser, Germany).

2.3.7.4.2. F-actin cytoskeleton, nuclear, proliferation marker staining

As a marker of proliferation, a Ki-67 stain was performed. The Ki-67 antigen can be detected in the nucleus during interphase. The stained was performed together with the F-actin and nuclear stain.

Cells were firstly washed with phosphate buffered saline (PBS) three times. For the staining protocol, in between each step, cells were washed with PBS three times. Cells were firstly submerged in 0.15% triton for 20 minutes and then goat serum was added and left for 30 minutes at room temperature. Alexa Fluor-488 phalloidin (1:100) and Ki67 primary antibody (1:100) was applied and incubated at 4°C overnight. Secondary antibody Alexa Fluor-594 was added and incubated at room temperature for 1 hour. Finally 1:20000 DAPI (4',6-Diamidino-2-Phenylindole) nuclear stain for 5 minutes to stain the nucleus. After the final washes with PBS, the sample was mounted onto a 76 x 26 mm glass slide (Thermo Scientific, United Kingdom). A drop of FluorSave™ anti fade (Calbiochem, United Kingdom) and Fluoromount™ mounting media (Sigma-Aldrich, United Kingdom) was placed on top

of the sample. Sample preparation was finished by covering the sample with a 25 x 50mm glass coverslip (Menzel-Gläser, Germany).

2.3.8. Wound assays

2.3.8.1. Scratch assay on coverslips

13mm glass coverslips were pretreated with filtered 1M hydrochloric acid (HCl) and incubated for 24 hours at 37°C, 5% CO₂. The HCl was washed off 3 times using the relevant cell culture medium, and again incubated for 24 hours at 37°C, 5% CO₂. NIH-3T3 fibroblasts were seeded at a density of $6 \times 10^4/500\mu\text{L}$ onto coverslips in a 24 well non tissue culture plate, and incubated for 48 hours at 37°C, 5% CO₂ to form a confluent monolayer. To perform the scratch assay, a linear wound was inflicted across the monolayer on the coverslip using a sterile 200 μL pipette tip. Any cell debris was removed by gently washing the coverslips with cell culture medium. The wound areas were imaged using brightfield microscopy, and wound area was calculated as a percentage using T Scratch software. A scratch assay was also performed using 3T3-GFP fibroblasts, and the wound closure was monitored using time-lapse microscopy.

2.3.8.2. Scratch assay on electrospun scaffolds

NIH-3T3 fibroblasts were seeded at a density of $3 \times 10^5/500\mu\text{L}$ on the preconditioned electrospun PET scaffolds within the centre of the steel ring. 500 μL of media was also placed on the outside of the steel ring. Cells were incubated at 37°C, 5% CO₂ and cultured to confluence over 3 days. To create the wound, the medium was firstly removed. To perform the scratch assay, a linear wound was

inflicted across the cell-seeded PET scaffold using a sterile 200 μ L pipette tip. Any cell debris was removed by gently washing the scaffolds with cell culture medium. Cells were cultured for several days, and fixed at different time points using 4% paraformaldehyde for 20 minutes at room temperature. Cells were stained with Alexa-Fluor 488 phalloidin to observe the wounded cell area. The wound area was imaged using an inverted fluorescent DMIRE2 microscope at x2.5 magnification and stitched together using Volocity software.

2.3.8.3. Chemical wound assay on electrospun scaffolds

NIH-3T3 fibroblasts were seeded at a density of $3 \times 10^5/500\mu\text{L}$ on the preconditioned electrospun PET scaffold within the centre of the steel ring. 500 μ L of media was also placed on the outside of the steel ring. Cells were incubated at 37°C, 5% CO₂ and cultured to confluence over 3 days. To create the wound, the medium was firstly removed. Filter paper or a cotton bud sterilised with 70% ethanol and air dried, was dipped into a solution of 0.1mM sodium hydroxide. Using tweezers this was carefully placed directly onto the centre of the cell-seeded scaffold for 5 seconds to injure the cells. The wound was then washed with media to remove any cell debris and replaced with fresh medium. Cells were cultured for several days, and fixed at different time points using 4% paraformaldehyde for 20 minutes at room temperature. Cells were stained with Alexa-Fluor 488 phalloidin to observe the wounded cell area. The wound area was imaged using an inverted fluorescent DMIRE2 microscope at x2.5 magnification and stitched together using Volocity software.

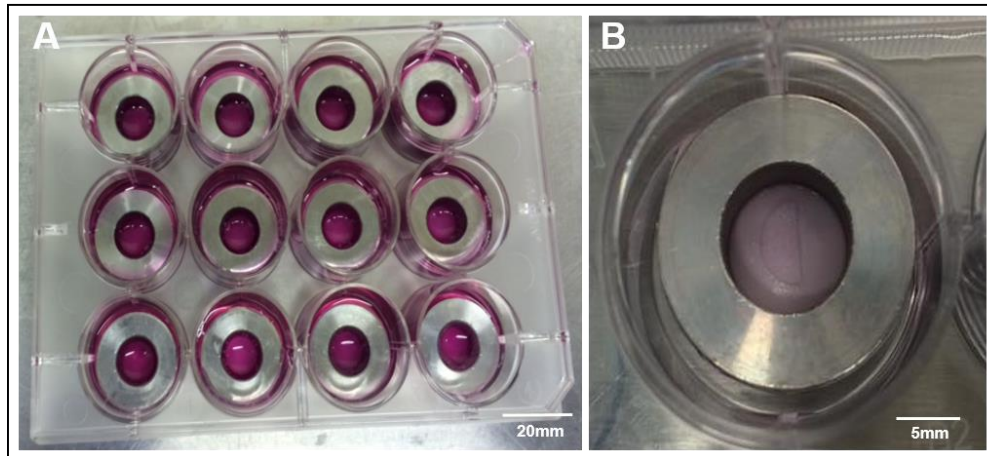


Figure 2.15 Electropun polyethylene terephthalate scaffold secured by steel ring in a non-tissue culture plate, (A) cells seeded in the centre of the steel ring $3 \times 10^5/500\mu\text{L}$, $500\mu\text{L}$ cell culture medium placed between the outside of the steel ring and the culture plate, (B) Chemical wound assay using a 5mm filter paper disc cut in half, cell culture medium was removed and the filter paper disc was soaked in 0.1mM sodium hydroxide solution and placed onto the centre of the cell-seeded scaffold for 5 seconds.

2.3.8.4. Burn assay on electrospun scaffolds

NIH-3T3 fibroblasts were seeded at a density of $3 \times 10^5/500\mu\text{L}$ on the preconditioned electrospun PET scaffold within the centre of the steel ring. $500\mu\text{L}$ of media was also placed on the outside of the steel ring. Cells were incubated at 37°C , 5% CO_2 and cultured to confluence over 3 days. To perform the burn assay, the scaffold was removed from the steel ring and placed flat onto a petri dish. Using tweezers, a needle was heated for 3 seconds and placed directly onto the centre of the cell seeded scaffold for 1 second. The scaffold was then rinsed with cell culture medium once to remove any cell debris, and secured with a steel ring and placed back into a non-tissue culture plate with cell culture medium for culture over several days to monitor wound recovery. Cells were fixed at different time points using 4% paraformaldehyde for 20 minutes at room temperature and stained with Alexa-Fluor 488 phalloidin to observe the wounded cell area. Cells were imaged using an inverted fluorescent DMIRE2 microscope at x2.5 magnification and stitched together using Volocity software.

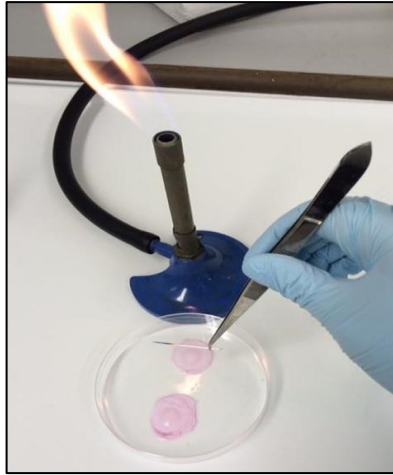


Figure 2.16 Cell seeded electrospun polyethylene terephthalate scaffold exposed to injury by a burn using a needle for 3 seconds.

2.3.9. Assembly of the Quasi-Vivo[®] flow systems

Quasi-Vivo[®]500: Silicone tubing and bioreactors were connected together using Luer lock connectors. The bioreactor system was attached to a peristaltic pump via silicone tubing in a closed set up. A small Bijou was pierced using sterile scissors to allow tubing through for the media supply and air filter. A volume of 7mL of media was placed in the Bijou along with 1mL of media in the bioreactor. A schematic of the setup is shown in Figure 2.17. The flow rates were calibrated manually by measuring the volume expelled each minute. For static control conditions, scaffolds were placed in a petri dish in the same volume of media as flow conditions (8mL).

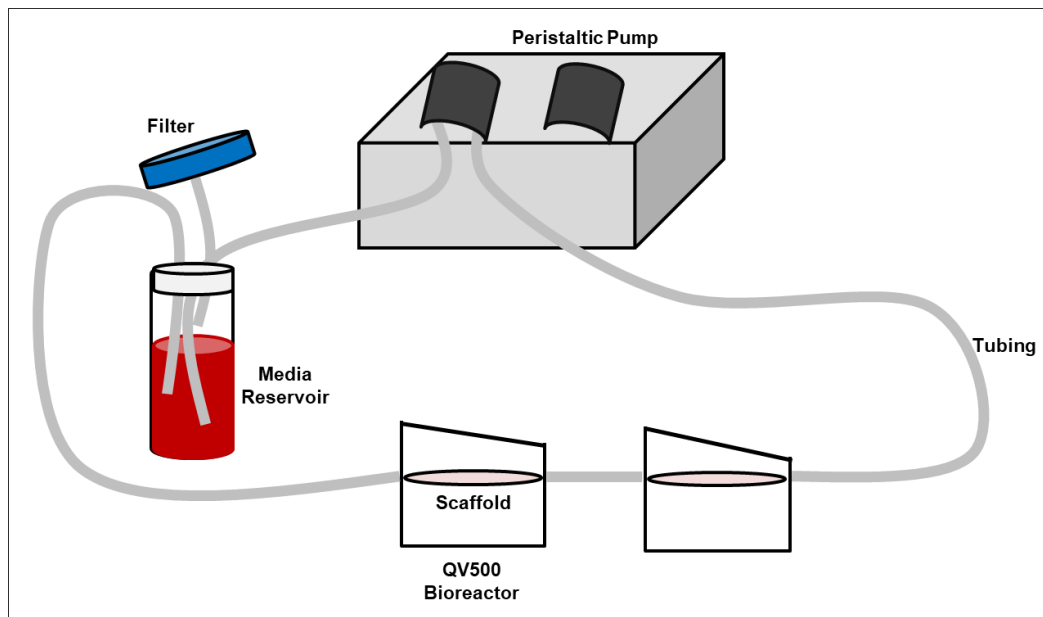


Figure 2.17 Schematic of QV500 bioreactor set up

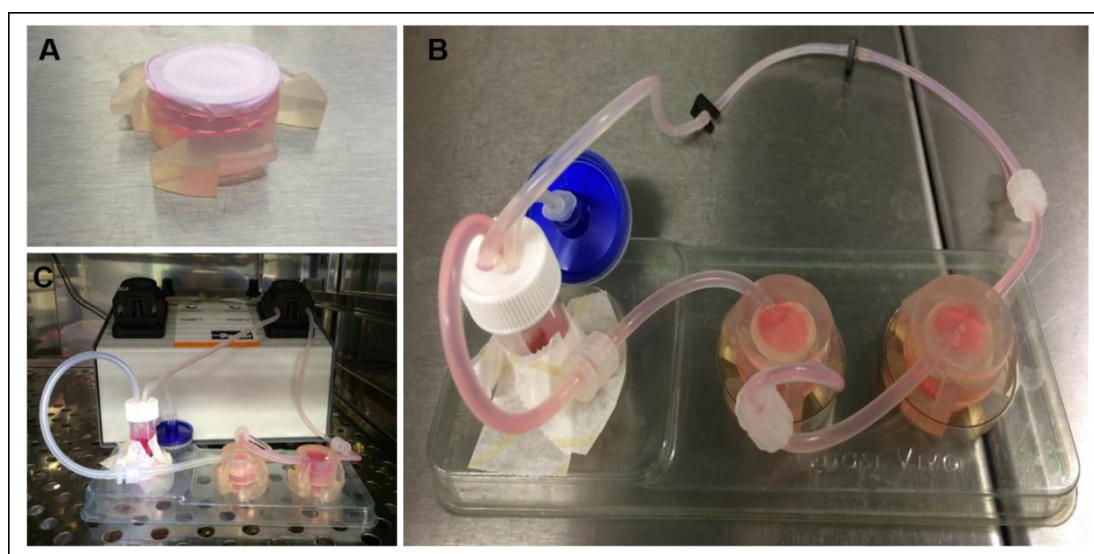


Figure 2.18 (A) Polyethylene electrospun scaffold positioning cells near the top of the Quasi-Vivo[®] 500 bioreactor, (B) Set up of Quasi-Vivo[®] 500 system with tubing and bioreactors joined together by Luer connectors (C) Quasi-Vivo[®] 500 system set up in the incubator.

Quasi-Vivo[®]900: Silicone tubing connects bioreactors in a closed set up attached to a peristaltic pump. A universal tube was pierced using sterile scissors to allow tubing through for the media supply and air filter. A volume of 20mL was placed in the universal tube to ensure a sufficient amount of media was available to recirculate in

the system. For static conditions, a cell crown was placed in a petri dish in the same volume of media as the flow conditions (20mL).

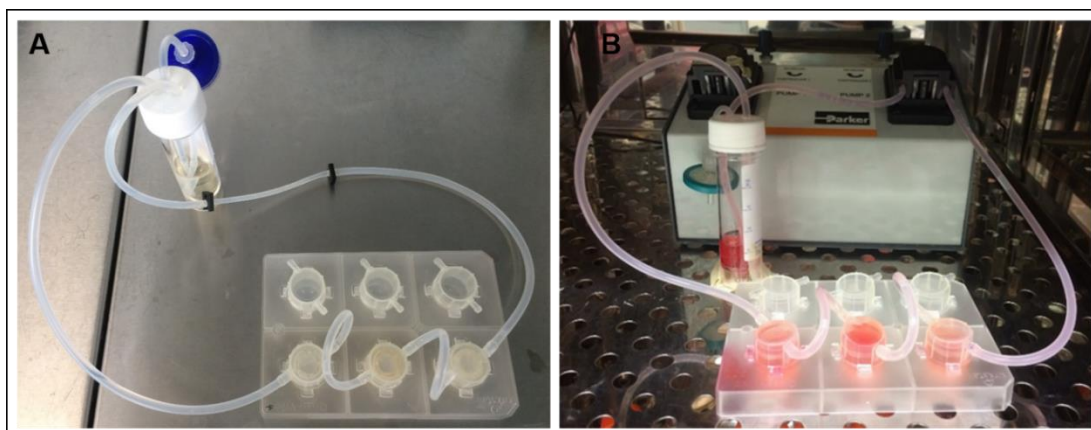


Figure 2.19 (A) Quasi-Vivo[®] 900 system with silicone tubing connected to bioreactors, (B) Quasi-Vivo[®] 900 system set up in the incubator.

2.3.9.1. Calibration of peristaltic pumps

To calibrate the flow rates delivered by the pump, the Quasi-Vivo[®] systems were set up in a single pass manner from one universal tube containing media to an empty universal tube. A specific flow rate was selected, and the system was run for 10 minutes, the amount of media expelled was measured using a pipette. The flow rate $\mu\text{L}/\text{min}$ was calculated using the below equation.

$$\text{Flow rate } (\mu\text{L}/\text{min}) = \frac{\text{Volume of media } (\mu\text{L})}{10 \text{ minutes}}$$

2.3.10. Statistical analysis

2.3.10.1. Standard error

Quantitative data was expressed with the mean \pm standard deviation, or the mean \pm standard error of the mean.

2.3.10.2. Standard deviation

Standard deviation (SD) quantifies the spread of values of a data set from the mean. A low SD means the data values are close to the mean, whereas high SD means the values are spread out over a wide range. GraphPad Prism was used to automatically calculate the standard deviation of the sample size by using the formula below.

n = number of values in data set

x = each value in data set

\bar{x} = sample mean

s = standard deviation

$$s = \sqrt{\frac{\sum(x - \bar{x})^2}{n - 1}}$$

2.3.10.3. Standard error of the mean

The standard error of the mean is the standard deviation of the sampling distribution of the sample mean. A larger sample means the standard error of the mean will be smaller, as the value of the mean will be known with precision even if the data is scattered. GraphPad Prism was used to automatically calculate the standard error of the mean of the sample size by using the formula below.

s = standard deviation

n = number of values in data set

$$s_{\bar{x}} = \frac{s}{\sqrt{n}}$$

2.3.10.4. Student T Test

The Student's t-test compares the mean and standard deviation of two independent data sets to determine whether a significant difference is present between them. The Student's t-test was performed using GraphPrism software. When compared, if the p value was ≤ 0.05 , the data sets were significantly different. A "significant difference" means that the results observed are most likely not due to chance or sampling error. The formula used to perform the Student's t-test is given below:

x_1 = mean of sample one

x_2 = mean of sample two

s_1 = standard deviation of sample one

s_2 = standard deviation of sample two

n_1 = sample size of sample one

n_2 = sample size of sample two

$$t = \frac{(x_1 - x_2)}{\sqrt{\frac{(s_1)^2}{n_1} + \frac{(s_2)^2}{n_2}}}$$

Chapter 3 Fabrication and characterisation of self-reporting scaffolds

Self-reporting scaffolds are constructs with the ability to support tissue culture and the added feature of being able to report and quantify an analyte of interest. Our developed construct consists of an electrospun matrix with the incorporation of ratiometric pH responsive nanosensors which are able to report analyte concentration within the scaffold environment. The biocompatible self-reporting scaffolds have been developed to address the current lack of tools for *in situ* and real time monitoring in tissue engineering applications. An advantage of this novel construct, is that it enables long term cultures to be monitored without disruption, and helps improve our understanding of the cellular microenvironment by being able to monitor throughout all stages of tissue production. In addition the use of an electrospun matrix allows the fibrous network of the native ECM to be mimicked, which can support cell growth and offer morphologic cues that result in enhanced cell response.

The work in this chapter evaluates the use of electrospun polyethylene terephthalate (PET) and gelatin scaffolds as potential polymers for the incorporation and responsiveness of polyacrylamide nanosensors.

3.1. Polymers for electrospinning

As mentioned, electrospinning is an advantageous technique for fabrication of matrices which resemble the structure of the native extracellular matrix. A wide

variety of natural or synthetic polymers can be spun into fibrous mats for tissue engineering and regenerative medicine applications¹⁷⁴. A lot of studies tend to focus on the fabrication of synthetic scaffolds such as PLA¹⁷⁵, PGA¹⁷⁶, PLGA¹⁷⁷, PCL¹⁷⁸ and PET¹⁷⁹, due to their mechanical stability which is useful for biomedical applications. In addition synthetic polymers are also easier to electrospin than natural polymers because of their well-defined molecular structure and well controlled molecular weight¹⁸⁰. Although synthetic polymers are often thought to lack biocompatibility, their chemical, physical and surface properties can be modified to enable good adhesion and proliferation¹⁸¹. Natural polymers possess the biocompatibility properties without the need for modification, natural polymers electrospun include: cellulose¹⁸², chitosan¹⁸³, silk fibroin¹⁸⁴, gelatin¹⁸⁵ and collagen¹⁸⁶. Furthermore natural polymers are environmentally friendly, nontoxic and biodegradable, however they are often limited by their poor mechanical and thermal properties¹⁸⁷.

3.1.1. Electrospinning gelatin

In comparison with synthetic scaffolds, natural biopolymers generally have better biocompatibility and hence are more suitable for tissue engineering and regenerative medicine applications¹⁸⁸. Gelatin is advantageous because it is biocompatible, biodegradable, non-immunogenic and non-antigenic¹⁸⁹. In addition, gelatin is a denatured product derived from the most abundant ECM protein collagen, and therefore displays similar biological properties but is much more cost effective¹⁸⁸. Natural biopolymer gelatin consists of mainly amino acids glycine, proline and 4-hydroxyproline which bond together forming a polymer chain¹⁹⁰ shown in Figure 3.1. There are two types of gelatin, dependent on the pre-treatment methods, type A gelatin is acid-treated which uses pig skin whereas type B is alkali

treated which converts asparagine and glutamine residues to their respective acids and makes use of cattle hides and bones¹⁹¹. Another important feature of gelatin is its transparency, optical transparency is important for tissue engineering applications for monitoring cells via microscopy. Gelatin has been used in a variety of tissue engineering applications. Lee et al¹⁹² electrospun gelatin and immobilised growth factors onto the surface of the fibres which showed increased proliferation and adhesion. This shows that the platform is a promising delivery vehicle for growth factors for successful tissue repair applications. In addition Wang et al¹⁹³ used electrospun gelatin as a drug delivery platform whereby they loaded heparin into the scaffolds for potential use in vascular tissue engineering. It was found that the HUVECs could grow and proliferate and grow better on the drug loaded scaffold compared to the one without which shows the high porosity of the fibres. Yao et al¹⁹⁴ also used gelatin nanofibres to deliver herbal medicine *Centella asiatica* (*C.asiastica*) extract for wound healing application, which showed enhanced fibroblast proliferation and collagen synthesis which may be a promising treatment for skin wounds.

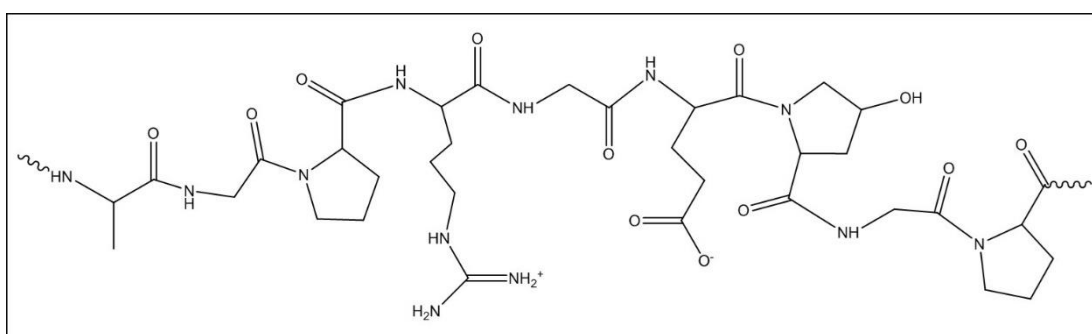


Figure 3.1 Chemical structure of gelatin.

Another advantage of gelatin is that it can be electrospun with water, however the electrospinning process is tricky as the aqueous gelatin solution turns into gel in the syringe needle at room temperature. In addition, water has a slow evaporation rate compromising the transformation of the polymer solution into dry nanofiber during

the travel between the needle and collecting plate¹⁹⁵. Therefore electrospinning of gelatin requires the use of fast evaporating solvents such as trifluoroethanol and hexafluoro isopropanol, which have been found to be good solvents for polypeptides¹⁹⁵. Although electrospun gelatin has great biocompatibility properties, the compromise includes the weak mechanical properties, fast degradation and total dissolution of the construct¹⁹⁶. Therefore further treatment such as crosslinking should be performed to improve these drawbacks¹⁹⁶. A variety of methods have been developed to improve the water-resistant ability and thermomechanical properties of the scaffolds¹⁸⁵. Examples include electrospinning gelatin with synthetic polymer blends such as gelatin combined with polycaprolactone used for wound healing¹⁹⁷, coaxial electrospinning of core shell fibres with polycaprolactone as the fibrous core for mechanical strength, and the gelatin as the surrounding biocompatible shell for future biomedical applications¹⁹⁸ and the addition of compounds to the gelatin fibres such as aluminium potassium sulfate¹⁹⁹. Chemical crosslinking has also been performed by using reagents such as glutaraldehyde²⁰⁰, diisocyanates²⁰¹, genipin²⁰², and carbodiimides²⁰³. Natural cross-linking agent genipin has been used to crosslink gelatin, due to its non-toxic nature, however studies have shown its inability to maintain the fibre morphology of the electrospun scaffolds upon water contact. Glutaraldehyde one of the most commonly used crosslinking agents due to its simplicity, low cost, and high effectiveness to stabilise gelatin-based materials and has successfully been applied to electrospun gelatin fibers²⁰². The mechanism behind glutaraldehyde crosslinking functions by linking the primary amine groups of the gelatin structure with the aldehyde group of glutaraldehyde to form a Schiff base²⁰⁰, Figure 3.2 shows the chemical structures of the gelatin and glutaraldehyde reacting together to form the crosslinked gelatin.

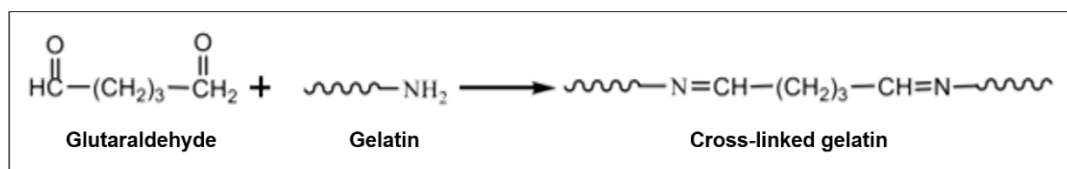


Figure 3.2 Glutaraldehyde bonding the primary amine groups of the gelatin structure to form cross-linked gelatin, image adapted from Yaohui You et al²⁰⁰.

3.1.2. Electrospinning polyethylene terephthalate (PET)

PET is a linear, aromatic, synthetic polymer consisting of polymerised units of the ethylene terephthalate monomer. Polyester monomers are synthesised from the reaction between terephthalic acid and ethylene glycol with addition of a catalyst shown in Figure 3.3. For polymerisation to occur, the conditions required include a high temperature of around 500°C and a catalyst²⁰⁴. The benzene rings in the molecular chain provides the structure with high mechanical strength and high melting points²⁰⁴.

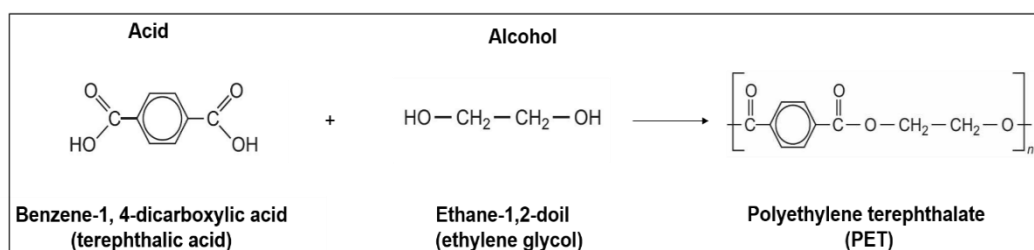


Figure 3.3 Compounds involved in the synthesis of polyester²⁰⁴.

PET is advantageous due to its cost efficiency, biocompatibility, mechanical strength and FDA approval²⁰⁵, making it suitable for a wide range of applications. Common uses include clothing, food packing, bottles, and biomedical applications. Medical applications include vascular grafts, surgical meshes, ligament and tendon repair,

due to its biostability²⁰⁶. Although PET is a synthetic polymer and thought to lack biocompatibility, PET has been electrospun to form fibrous mats which have successfully supported tissue engineering and regenerative medicine applications, including engineering blood vessels²⁰⁷, human upper airway³³, and human airway smooth muscle²⁰⁸. To enhance the biocompatibility of PET, surface modification has been performed. For example, in a study by Zuwei²⁰⁷ gelatin was chemically grafted onto the surface of the PET to improve cell spreading, proliferation and preservation of cell phenotype. In addition Lei et al²⁰⁹ immobilised peptides onto the surface of PET nanofibres to promote endothelial cell attachment. However, other studies have shown no significant differences in cell adhesion, proliferation and phenotype by coating PET fibres with a variety of ECM proteins²¹⁰, which indicates electrospun PET provides a suitable matrix for cell adhesion. A limitation to using synthetic PET for electrospinning, is that PET is insoluble in a large range of solvents. PET is only highly soluble in strong organic acid trifluoroacetic acid, and partially soluble in solvents such as dichloromethane, formic acid and tetrahydrofuran²¹¹. This can become a potential issue for long term cultures if residual solvent has not been completely removed.

3.2. Electrospun self-reporting scaffolds

Self-reporting scaffolds are constructs with the ability to report on the concentration of an analyte of interest. Several studies have been conducted whereby the ability to sense different physical and chemical stimuli has been incorporated into electrospun scaffolds for different applications, also referred to as 'smart scaffolds' reviewed by Weng and Xie²¹². Some of the stimuli monitored using electrospun scaffolds include temperature²¹³, magnetic-fields²¹⁴, metal ions²¹⁵, humidity²¹⁶, and pH²¹⁷.

The advantage of fabricating self-reporting scaffolds for tissue engineering applications is the ability to create highly porous, fibrous structures which can mimic the native extracellular matrix architecture, subsequently recreating a physiologically relevant microenvironment whilst simultaneously acquiring information on different stimuli. In addition, the acquisition of data can be performed *in situ*, removing the need for invasive monitoring methods using probes, or end point determination. In a study by Wenjun Di et al²¹⁸, a pH sensing system was developed by incorporating a free fluorophore directly into an electrospun based system. The fibres were fabricated containing a pH-sensitive fluorophore, ion additive, a plasticiser and a polymer for mechanical stability. Polycaprolactone (PCL) and poly (lactic-co-glycolic acid) (PLGA) were tested for their analytical response, with PCL-based nanofibers exhibiting an *in situ* pH change within a more desired working range. The pH sensitive fluorophore chosen was a chromoionophore II with a pka of 9.16 determined from previous studies, displaying pH changes centred within 7.8 and 9.6 for PCL and PLGA respectively which is above the physiological extracellular pH of 7.4. Ratiometric measurements were also taken using this system, using octadecyl rhodamine B chloride as a reference dye to correct for any unequal sensor loading, leakage, scaffold thickness or photobleaching. Although the addition of the plasticiser was shown not to compromise the morphology or viability of the HEK293 cell line, long term cultures and primary cells could be affected. H. Harrington *et al*¹¹⁸ reported the fabrication of an electrospun poly(lactic-co-glycolic) scaffold with the incorporation of silica pH responsive fluorescent nanosensors for monitoring extracellular pH *in situ*. The sensors consisted of a pH sensitive dye 5-(6)-carboxyfluorescein and pH insensitive reference dye 6-TAMRA encapsulated by a sol-gel matrix to protect the dyes from any interference or potential to cause toxicity. Only one pH-sensitive fluorophore was incorporated permitting pH sensing in the narrow range of 5.0 – 7.5. In addition, it is known that synthetic scaffolds such as PLGA lack native biological cues and binding sites that natural polymers possess to

promote cell adhesion and activity. Cells were only cultured for 3 days to assess cell viability, however increasing the duration of the experiment may have caused degradation of the PLGA scaffold via hydrolysis due to its weak mechanical properties. Further acidification may also be introduced to the extracellular microenvironment due to the production of degradation by-products lactic acid and glycolic acid²¹⁹. The focus of this study was to incorporate pH fluorescent nanosensors which are responsive across the full physiological range between pH 3.5 – 7.5 into a biocompatible scaffold.

3.2.1. Optical nanosensors

As mentioned, nanosensors can be incorporated into electrospun scaffolds for sensing. Optical pH sensors are based on reversible changes in the indicator's structures induced by pH and translated into changes in spectroscopic phenomena such as fluorescence²²⁰. Nanosensors are spherical particles usually ~30-500nm in diameter comprised of a porous matrix encapsulating a sensing component such as pH responsive fluorophores and are often used for intracellular pH measurements²²¹. Ratiometric fluorescent nanosensors have successfully been developed by Clark et al²²² for intracellular pH measurements. The probes consisted of a pH sensitive fluorophore (fluorescein) and a reference fluorophore (sulforhodamine) surrounded by a polyacrylamide matrix which could successfully quantify pH with a correlating fluorescence. The limitation of these sensors is that the pH sensitive fluorophore does not cover the full physiological range between pH 3.5 – 7.5. The advantage of being able to take ratiometric measurements using pH sensitive fluorophores and pH insensitive fluorophore means that any fluctuations in temperature, light source intensity or heterogeneous dye concentrations can be removed¹¹⁸. A variety of ratiometric fluorescent nanosensors have been given in Table 3.1. It is clear to see that most nanosensors only consist of one fluorescent

dye and a reference dye and are mainly used for intracellular pH monitoring due to their small size.

3.2.2. Polyacrylamide nanosensors

Chauhan et al¹⁶³ developed spherical, ratiometric pH sensors that were able to reliably measure pH within the full physiological range of pH 3.5 - 7.5. The nanosensors consist of a polyacrylamide matrix which is synthesised via an inverse nanoemulsion polymerisation reaction performed by using water and an oil phase and crosslinking of acrylamide monomers by N,N methylene bisacrylamide catalysed by TEMED and ammonium persulfate to create the polyacrylamide matrix. The matrix encapsulates two pH sensitive fluorophores and a pH insensitive reference fluorophore, which are conjugated to the N-(3-aminopropyl) methacrylamide matrix as shown in Figure 3.4. This prevents possible leaching of the dyes and avoids any potential cytotoxicity. In addition, uneven leaching rates of the fluorophores can cause differences in fluorophore concentration which could in turn provide an unreliable ratiometric measurement of the pH. The encapsulation of the matrix also prevents any non-specific binding of fluorophores to cellular components²²³. The polyacrylamide matrix is also biocompatible which is non-toxic to cells, and is highly porous allowing the diffusion of analytes in and out of the sensor for rapid interaction and response from the pH-sensitive fluorophores. Another advantage to the use of sensors is that a variety of analytes can be monitored as the sensors are not restricted to using a single fluorophore and can utilise cooperative interactions between ionophores, enzymes, reporter dyes etc. The pH sensitive fluorophores include Oregon Green and carboxyfluorescein which are responsive within the range of pH 3.5 – 6.0 and pH 5.0 – 7.5 respectively to cover the full physiological range. In addition, both their excitation and emission

wavelengths overlap at 488nm and 520nm respectively. To obtain the ratiometric measurements, TAMRA was chosen as the reference fluorophore because it does not respond to changes in pH and the emission spectra does not overlap the emission spectra of the indicator fluorophores. A disadvantage to fluorescent ratiometric probes is that they can suffer from photobleaching and small spectroscopic change upon pH change²²⁴.

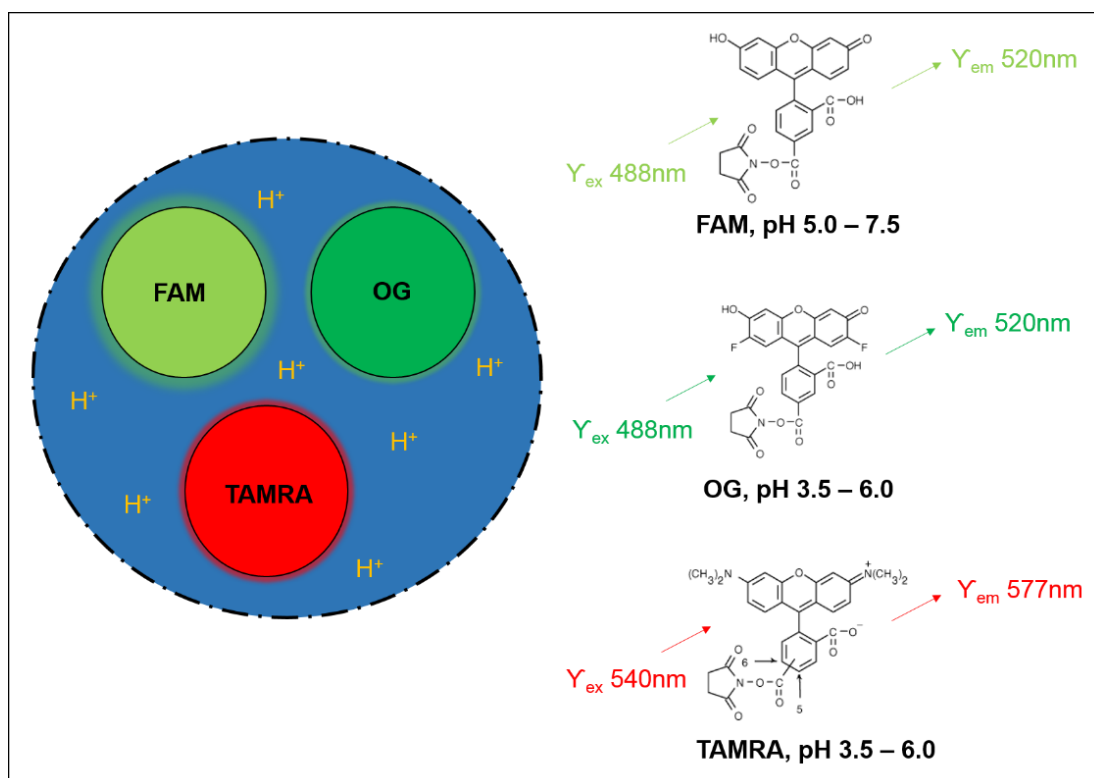


Figure 3.4 Schematic of polyacrylamide nanosensors adapted by Chauhan et al¹⁶³.

3.2.3. Fluorophores

Fluorophores are often used as optical sensors due to their high sensitivity, however finding fluorophores with good properties including excellent photostability, large Stokes shifts, and high quantum yield can be a challenge²²⁰.

Fluorescein is a fluorophore commonly used to measure biological pH, and exhibits pH dependent ionic equilibria within the range of pH 5.0 – 9.0. Above pH 9.0, the

phenol and carboxylic acid functional groups of the molecule are almost completely ionised. When fluorescein is exposed to more acidic solutions, the phenol group of the fluorescein dianion becomes protonated ($pK_a \sim 6.4$), then the carboxylic acid group ($pK_a < 5.0$) to produce the neutral species of fluorescein. Further acidification generates a fluorescein cation ($pK_a \sim 2.1$)²²⁵. Only the monoanion and dianion of fluorescein forms are fluorescent. Figure 3.5 shows the chemical structures of ionisation of fluorescein.

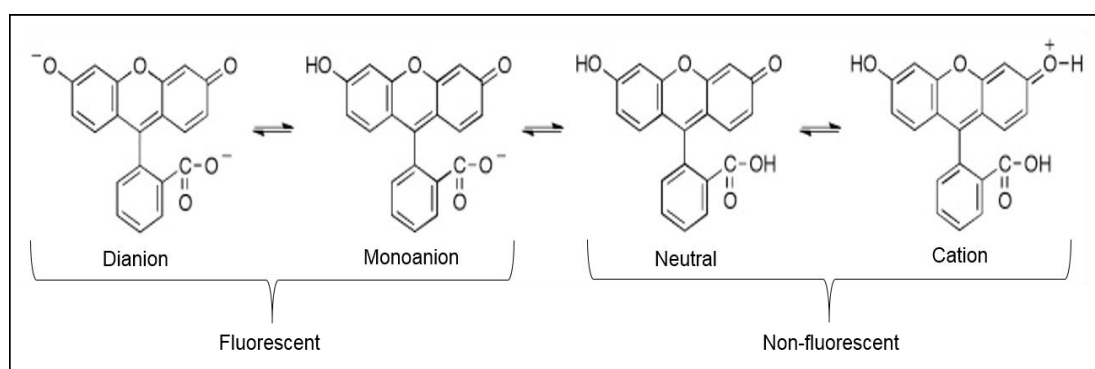


Figure 3.5 Chemical structures showing the ionisation of fluorescein²²⁵.

Oregon Green is a more acidic derivative of fluorescein, whereby the fluorine atoms on the xanthene backbone reduce the pK_a of this dye to 4.8, improving the fluorescence at low pH²²⁶.

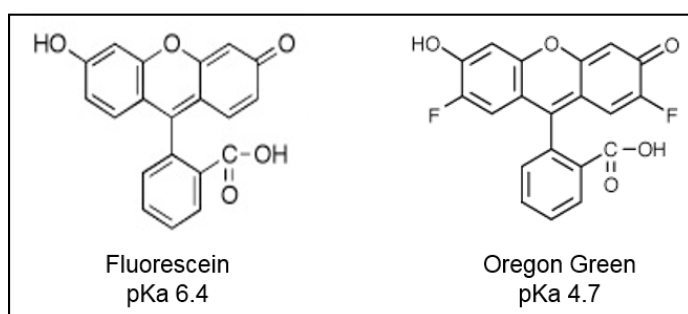


Figure 3.6 Chemical structures and pK_a values of pH sensitive fluorophores Fluorescein and Oregon Green.

Material	Indicator	Ratiometric	Dynamic range	Size	Application	Reference
Polyacrylamide	5-(and-6)-carboxyfluorescein Oregon Green	Yes	3.5 – 7.5	~40nm	Measurement of pharyngeal and intestinal pH in <i>C. elegans</i> .	Chauhan et al ¹⁶³
Sol-gel	5-(and-6)-carboxyfluorescein	Yes	5.0 – 7.5	300-400nm	Tissue engineering	Harrington et al ¹¹⁸
Polyacrylamide	Fluorescein Oregon green	Yes	3.1 – 7.0	~60nm	Intracellular pH/lysosome	Søndergaard et al ²²⁷
Polysaccharide/ Dextran	Fluorescein isothiocyanate	Yes	Not given	500nm	Extracellular/Intracellular measurements	Hornig et al ²²⁸
Silica	Fluorescein isothiocyanate	Yes	5.0 – 7.1	~70nm	Intracellular pH	Korzeniowska et al ²²⁹
Polystyrene	Fluorescein isothiocyanate	Yes	4.0 – 8.0	~20nm	Monitoring cellular environment	Allard and Larpent ²³⁰
Polyacrylamide	M1, N-fluoresceinylacrylamide)	Yes	5.8 - 7.2	50nm	Monitor metabolic processes of cells	Sun et al ²³¹
Silica	Fluorescein	Yes	5.0 – 8.5	50-70nm	Intracellular pH sensing	Burns et al ²³²
Silica	Fluorescein	Yes	4.0 - 8.0	30nm	Bioanalysis	Gao et al ²³³
Polystyrene	Oregon Green	Yes	4.5 – 7.0	Submicrometer	Drug effect on pH of lysosome/Intracellular	Ji et al ²³⁴
Polyacrylamide	N-allyl-4-(N-methylpiperaziny)-1,8-naphthalimide	Yes	5.0 – 8.2	28nm	Intracellular pH sensing	Schulz et al ²³⁵

Table 3.1 Comparison table of fluorescent nanosensors used for pH sensing adapted from Lobnik et al²³⁶

3.3. Results & Discussion

As discussed, electrospinning is an excellent, simple and cost effective method for fabricating platforms for tissue engineering. Electrospinning generates highly porous, fibrous constructs with a high surface area to closely resemble the structure of the native extracellular matrix. Therefore electrospun matrices were chosen for the incorporation of pH responsive polyacrylamide nanosensors. Polyacrylamide nanosensors reported by Chauhan et al¹⁶³ were selected to report pH and for incorporation into the scaffolds. This was due to their biocompatible nano-structure with encapsulated covalently linked fluorophores to prevent possible leaching, along with the ability to accurately measure pH within the full physiological range of pH 3.5 - 7.5.

3.3.1. Characterisation of polyacrylamide nanosensors

3.3.1.1. Size distribution of nanosensors

Dynamic light scattering (DLS) was performed to provide the hydrodynamic diameter of the polyacrylamide nanosensors. The DLS technique is based on the assumption that the nanoparticles are a spherical shape. The average hydrodynamic size was $39.9\text{nm} \pm 1.3\text{nm}$ (average \pm SD) with a polydispersity index of 0.104 ± 0.08 (average \pm SD) displayed in Figure 3.7 which correlates to the same average diameter of the nanoparticles reported by Chauhan et al¹⁶³ of $\sim 40\text{nm}$. The small standard deviation indicates the reproducibility of the production of nanosensors of the same size. In addition, the polydispersity index shows the sensors are monodisperse with a narrow size distribution. Polydispersity index measures the heterogeneity of the size, shape and mass of particles in a mixture. If

values are < 0.05 , the mixture is highly monodisperse, whereas values >0.7 indicate the sample has a very broad size distribution²³⁷. The low standard deviation and polydispersity index demonstrates the reliability and reproducibility of the inverse nanoemulsion polymerisation technique for production of polyacrylamide nanosensors.

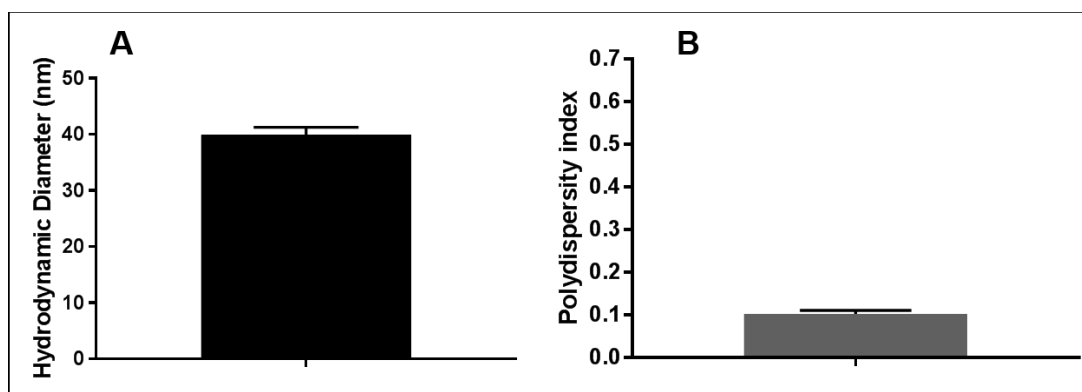


Figure 3.7 (A) Hydrodynamic size distribution of polyacrylamide nanosensors (B) polydispersity index, ($n = 9$, 3 separate batches).

Another technique used to characterise the size and shape of the nanosensors was transmission electron microscopy due to its high spatial resolution of 0.2nm ¹⁵⁹. The diameter of the nanosensors were measured using Image J and had a diameter of $69.4\text{nm} \pm 12.3\text{nm}$ (average \pm SD). The average size of the nanosensors were larger with a bigger SD when characterised by TEM compared to DLS. This could be due to inaccuracies caused by the extensive aggregation of the nanoparticles during TEM sample preparation shown in Figure 3.8(A-B), as DLS did not display data indicating aggregation. Particles were dried before TEM which could have resulted in clustering, making it difficult to measure individual nanoparticle sizes. In addition, the polyacrylamide forms a hydrogel water-like matrix which can cause difficulties in distinguishing the contrast during TEM imaging. Although the TEM images are not defined enough for accurate sizing, they provide an idea of the spherical morphology of the particles with an estimation of size. Desai¹⁷² also found the size

characterisation of polyacrylamide nanoparticles by DLS was $48.5 \pm 4.9\text{nm}$, and $\sim 50\text{nm}$ by environmental scanning electron microscopy which correlates well with our data. Environmental scanning electron microscopy also resulted in aggregation of nanoparticles shown in Figure 3.8 (C-D).

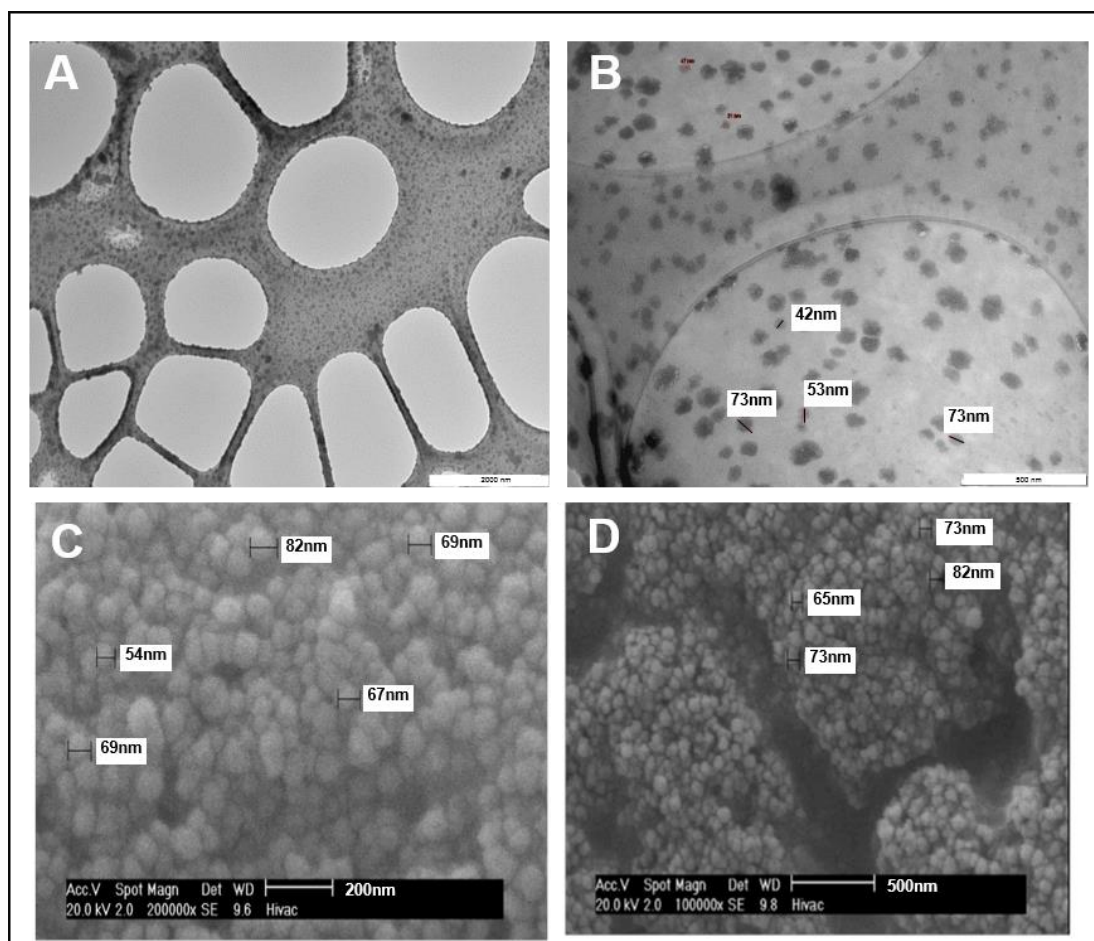


Figure 3.8 (A-B) Representative transmission electron micrographs of polyacrylamide nanosensors $n=3$ (A) magnification $\times 10,000$, (B) magnification $\times 43,000$, (C-D) eSEM by Desai¹⁷² of polyacrylamide nanosensors (C) magnification $\times 200,000$, (D) magnification $\times 100,000$.

3.3.1.2. Optical characterisation of nanosensors

To confirm the pH responsiveness of the polyacrylamide nanosensors containing covalently linked fluorophores, nanosensors were suspended in deionised water and placed in a range of buffers respectively ranging from pH 3.5 – 8.0. Using a fluorescence spectrophotometer, the pH-sensitive fluorophores (FAM & OG) were

excited within the green wavelength (488nm) resulting in an overlapping emission peak at ~520nm and a change in fluorescence intensity with the corresponding buffer (Figure 3.9A). An expected increase in the fluorescence intensity was observed as the pH of the buffers increased. The pH-insensitive fluorophore (TAMRA) was excited in the red wavelength at (540nm), and exhibited an emission peak at ~577nm, but no distinct change fluorescence intensity with the change in buffer as expected (Figure 3.9B). A ratiometric pH calibration curve was generated by taking a ratio of the emission fluorescence intensities of the pH sensitive and pH insensitive channels (520nm/577nm). This data correlates with the fluorescent responses achieved by Chauhan et al¹⁶³ using the fluorescence spectrophotometer.

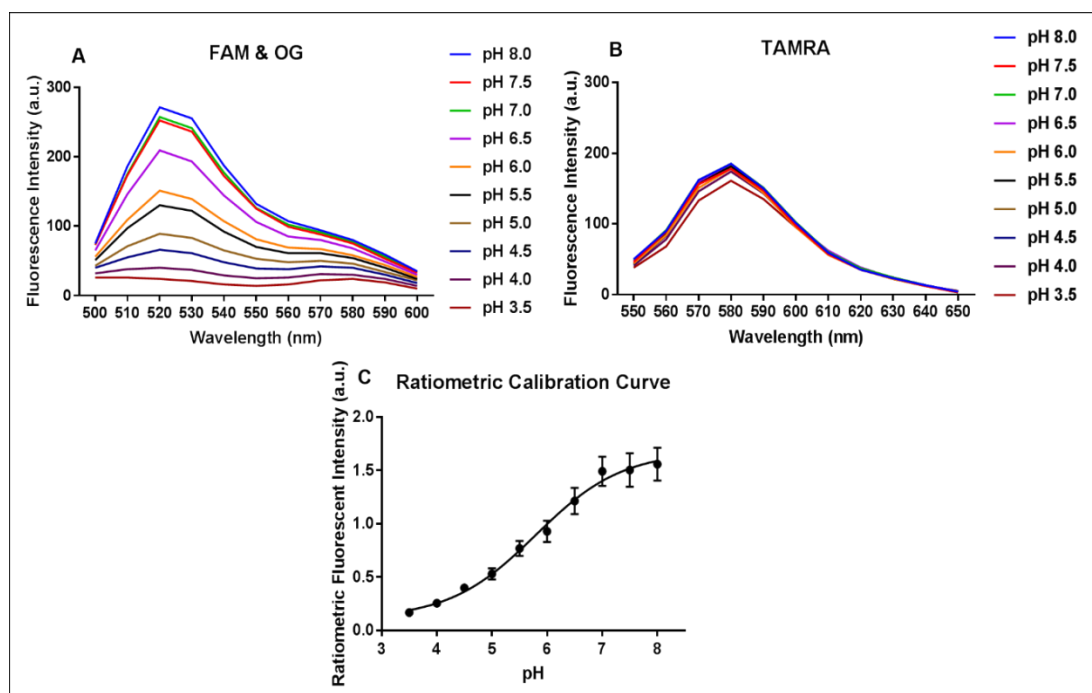


Figure 3.9 Fluorescence spectra obtained using fluorescence spectrophotometer, nanosensors suspended in buffers pH 3.5 – 8.0. (A) Emission curves of pH responsive FAM & OG, (B) Emission curves of pH non-responsive TAMRA, (C) Ratiometric curve achieved by taking ratio of emission from pH responsive channel and pH non responsive channel 520/577 ($n = 3$ error \pm SD).

After confirming the response of the nanosensors using the previously reported method using the fluorescence spectrophotometer by Chauhan et al¹⁶³, a fluorescent microscope was used to monitor the response of the sensors. Being

able to use a fluorescent microscope allows the ability to monitor different regions of a sample to provide the local pH, instead of a general intensity for the whole area of the sample. Nanosensors were suspended in buffers ranging from pH 3.5 – 8.0 in a 24 well plate and imaged in several different areas using a fluorescent microscope. Fluorescent images were acquired in the green and red excitation channels as shown in Figure 3.10A. The fluorescent intensities for the emission of FAM & OG were plotted in Figure 3.10B which shows an increase in fluorescence intensity as the pH rises (hydrogen ion concentration decreases), similarly observed in Figure 3.9A. The reason for this observation is because FAM is sensitive between the ranges of pH 5.0 – pH 7.5, as the pH becomes more alkali the fluorophore is deprotonated causing the fluorescence to increase with the rise in negative charge. At low pH the monoanion form is protonated reducing the fluorescence intensity until neutral non-fluorescent species is produced at pH 5.0. Oregon Green displays a similar shift as a fluorescein derivative, but the fluorophore has a lower sensitivity within the range of 3.5 – 6.0 due to the addition of the halogen electron withdrawing groups to the xanthene backbone. The fluorescent intensities for the emission of TAMRA were plotted in Figure 3.10C which shows a constant fluorescent intensity with minimal change as the buffer is varied from pH 3.0 – 8.0 as observed in Figure 3.9B. This makes TAMRA a useful reference fluorophore, also because its excitation and emission spectra are significantly different to the spectra of both the pH sensitive fluorophores. The ratiometric curve in Figure 3.10D displays a sigmoidal curve in consensus with Figure 3.9. By synthesising these nanosensors with covalently linked fluorophores, errors caused by fluorophore leaching can be prevented²³⁶. If a fluorophore did leach, we cannot be sure if we are taking measurements for the nanosensors or free fluorophore¹⁶³. Furthermore, covalently linked dyes have been found to have a lower or equivalent photobleaching rate compared to corresponding free dyes²³¹. In addition, nanosensors with covalently linked fluorophores have been found to be brighter compared to sensors composed

of encapsulated fluorophores¹⁶³. Brighter sensors mean a lower fluorescent excitation energy can be used which reduces the risk of photobleaching, in addition a reduced exposure time during fluorescence microscopy allowing faster imaging also lower concentrations are required¹⁶³.

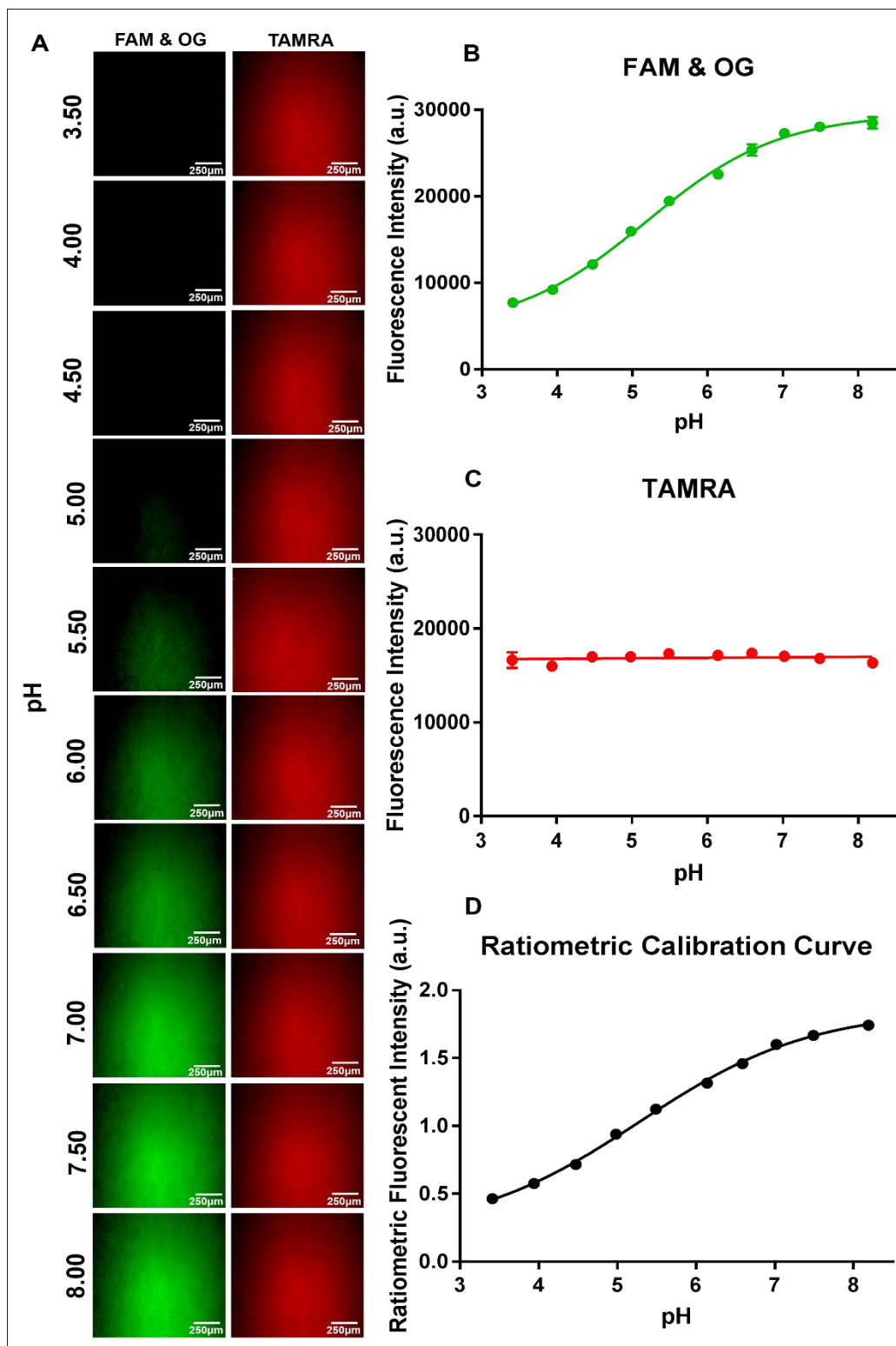


Figure 3.10 Optical characterisation of the pH response of polyacrylamide nanosensors suspended in buffer solutions ranging from pH 3.5 – 8.0. (A) Representative fluorescent images showing a visual change in the green fluorescence intensity of pH sensitive FAM&OG, (B) emission curves of FAM&OG, (C) emission curve of TAMRA, (D) Ratiometric calibration curve for pH. Data shown are representative of $n=3 \pm SD$, scale bar = 250 μ m.

3.3.2. Scaffold Fabrication Optimisation

3.3.2.1. Fabrication of electrospun PET sensor scaffold

To fabricate the 10% (w/v) PET nanosensor scaffold the electrospinning protocol by Harrington et al³³ described in section 2.3.1, was adapted but with the addition of the polyacrylamide nanosensors to the polymer solution prior to electrospinning. A slightly higher voltage of 15kV was used instead of 14kV as this was found to help prevent dripping of the polymer solution and increase the electrospinning stability. Characterisation of the scaffolds involved observing fibre morphology with scanning electron microscopy, measuring the fibre diameter using ImageJ software, and using fluorescence microscopy to determine pH responsiveness of the construct.

3.3.2.1.1. Morphology and fibre diameter characterisation of electrospun PET sensor scaffold

Scanning electron micrographs of PET/nanosensor scaffold shown in Figure 3.11 displays fibre development however bead formation is present with the addition of nanoparticles which could indicate instability of the electrospinning jet. As a control, fibres were electrospun without nanosensors which displayed smooth uniform fibres without any beading. This observation was not expected as Harrington et al¹¹⁸ incorporated silica sol-gel nanosensors into electrospun PLGA and found that fibre morphology was not compromised. However, what they did find was that the nanosensors were clustered on the surface of the fibres but we did not observe this on the scanning electron micrographs of the fibres indicating the sensors should be encapsulated within the fibres. A possible explanation for the beaded fibres

reported by Kalia²³⁸, was that there may be aggregation of the nanoparticles during the electrospinning process causing formation of bead defects along the fibre axis.

The histogram in Figure 3.11 displays the distribution of the fibre diameter. The range of measurements for the PET/nanosensors scaffold was between 72.9 – 254.7nm whereas the PET only, was between 150.0 – 733nm. The range of values for the PET/nanosensors was much smaller compared to the PET only. In addition, the average fibre diameter \pm standard error of the mean was reduced from 340.1 ± 4.7 nm to 161.3 ± 1.1 nm by approximately half with the incorporation of the sensors. A T-test was performed using Graph Prism which showed a significant difference between fibre diameters with the addition of sensors with $p < 0.0001$. The reduction in fibre diameter may be due to a change in viscosity of the polymer solution due to the addition of the nanosensors. Andersson et al²³⁹ found with the increased addition of supermagnetic iron oxide particles to electrospun polymethyl-methacrylate and polyethylene oxide, the fibre diameter decreased due to the increase in zero-shear viscosity of the polymer solution and rapid evaporation of the solvent preventing fusion of the fibres. The average fibre diameter of the electrospun 10% PET fabricated by Harrington et al³³ was reported to be 240nm similar to the 340nm we obtained. Htwe et al²⁴⁰ also used the same protocol as Harrington et al³³ to spin PET to create fibres with an average fibre diameter of 257 ± 16.28 nm. The difference in fibre diameter may be due the day-to-day temperature fluctuation at which electrospinning was performed at, higher temperatures can reduce the fibre diameter by increasing the rate of evaporation of the solvent and decrease the viscosity of the solution⁷⁰. In addition, a slightly higher voltage of 15kV was used instead of the reported 14kV as the higher voltage helped to reduce slight dripping of the polymer solution, stabilising the electrospinning process.

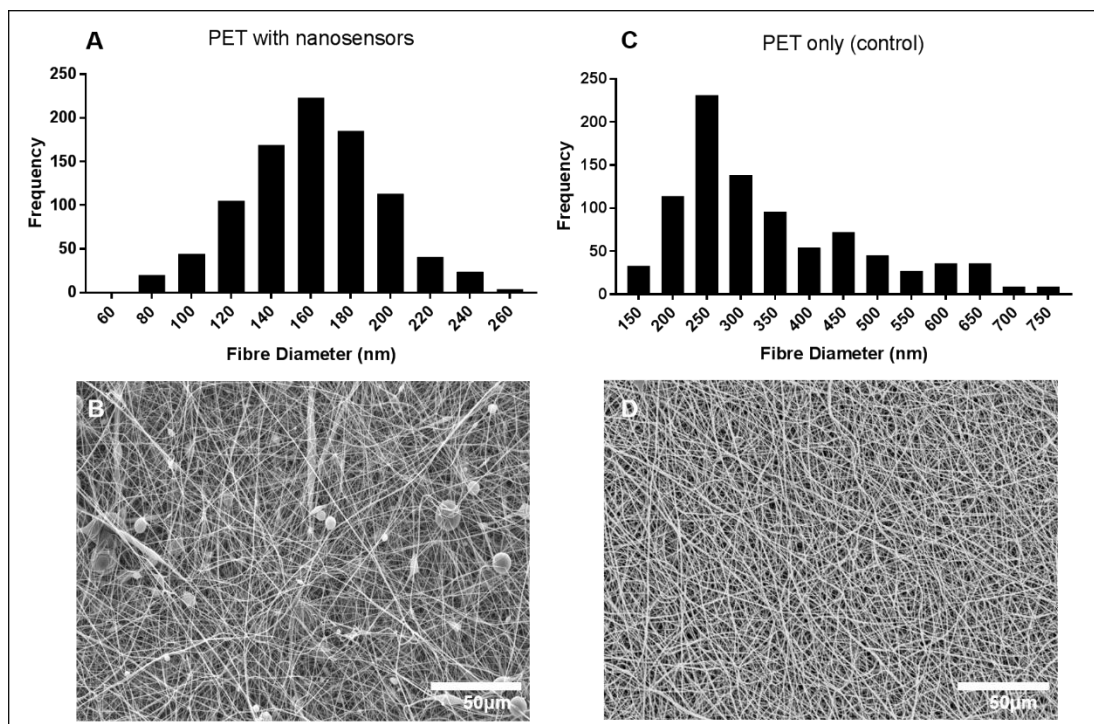


Figure 3.11 Fibre diameter distribution and representative SEM images of 10% (w/v) electrospun PET scaffolds with and without the incorporation of nanosensors $n=3$. (A-B) Electrospun PET with nanosensors, (C-D) Electrospun PET without nanosensors. Magnification $\times 500$, scale bar $50\mu\text{m}$.

3.3.2.1.2. Optical characterisation of electrospun PET sensor scaffolds

To determine whether PET was a suitable polymer for incorporation of the sensors for a pH response, and whether the sensors could successfully be incorporated into the scaffolds and provide an optical response after the electrospinning process, PET scaffolds with and without nanosensors were placed in buffers ranging from pH 3.5 – 8.0 and fluorescent images were acquired as shown in Figure 3.12A and Figure 3.13A.

Exposure of the PET/nanosensor scaffold to the excitation wavelength of 488nm for fluorophores FAM & OG showed a lack of additive response with slight fluctuations in fluorescence in Figure 3.12A. In addition, excitation of TAMRA to the wavelength 540nm similarly showed constant fluorescence with minimal change to pH in Figure 3.12C, but this was expected from the reference fluorophore. Compared to the blank

PET scaffold in Figure 3.13C, the fluorescence intensity is much higher with incorporation of the sensors. Therefore, PET is suitable for optical imaging, but the limited additive fluorescence response to pH change could be due to the low porosity of PET²⁴¹. Its low porosity makes it a good candidate for water resistance²⁴² and its known use for soft drinks, food packing and pharmaceuticals due to its outstanding barrier properties²⁴³. Therefore, the minimal porosity may prevent diffusion of the hydrogen ions throughout the fibres, subsequently restricting the interaction between the hydrogen ions and the fluorophores within the nanosensors. Therefore this prevents a change in fluorescence in relation to the pH, which would usually portray a sigmoidal pattern on a calibration curve. The very slight fluctuations in fluorescence intensity may be due to the orientation of the nanosensors in the fibres. Sensors positioned towards the edge of the fibre provide an easier access for the hydrogen ions to interact with the fluorophores in the sensors, in relation to sensors incorporated directly in the centre of the fibre.

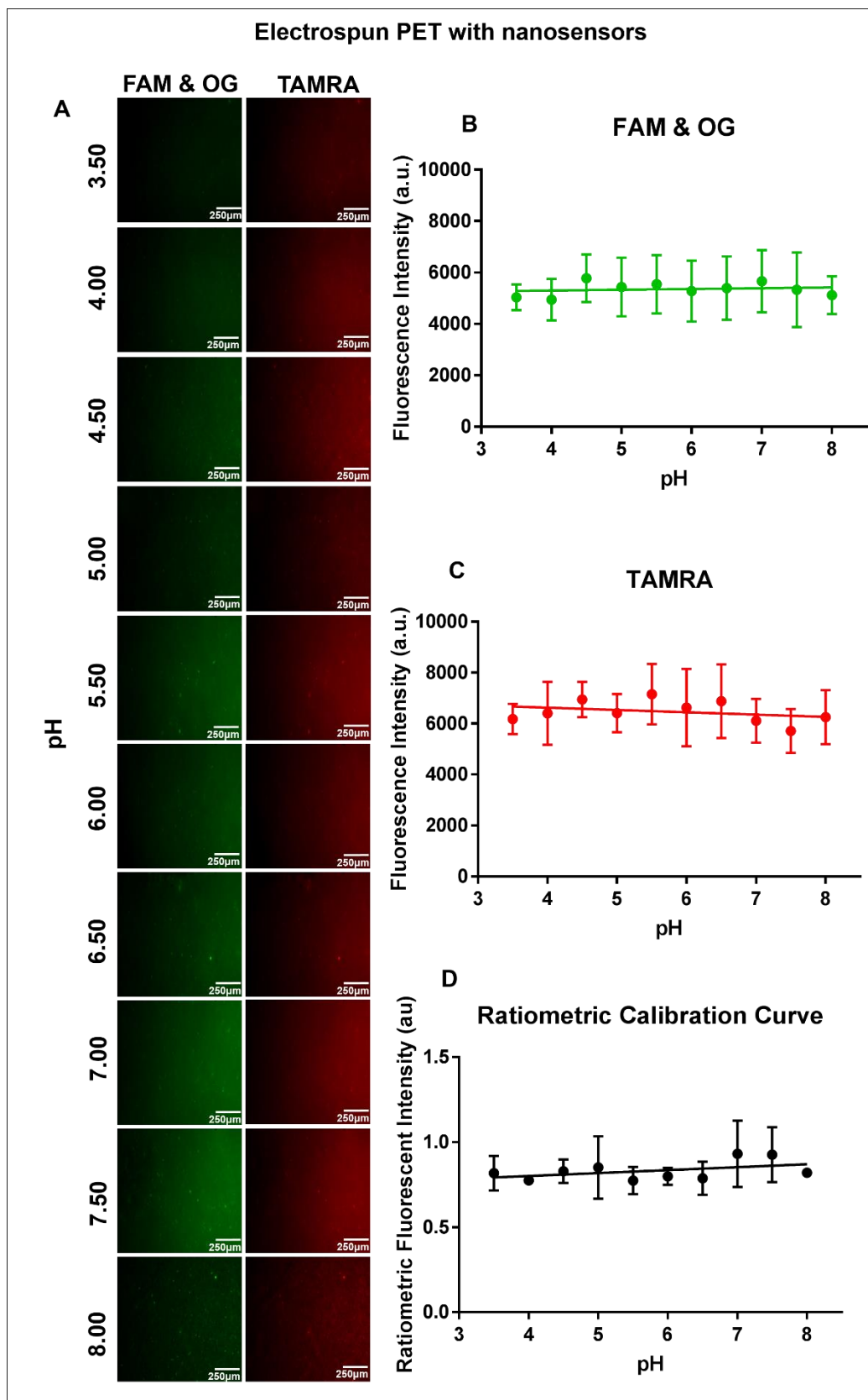


Figure 3.12 Optical characterisation of the pH response of electrospun PET scaffold with incorporated polyacrylamide nanosensors suspended in buffer solutions ranging from pH 3.5 – 8.0. (A) Representative fluorescence images showing a visual change in the green fluorescence intensity of pH sensitive FAM&OG, (B) emission curves of FAM&OG, (C) emission curve of TAMRA, (D) Ratiometric calibration curve for pH. Data shown are representative of $n=3 \pm SD$, scale bar = 250 μ m.

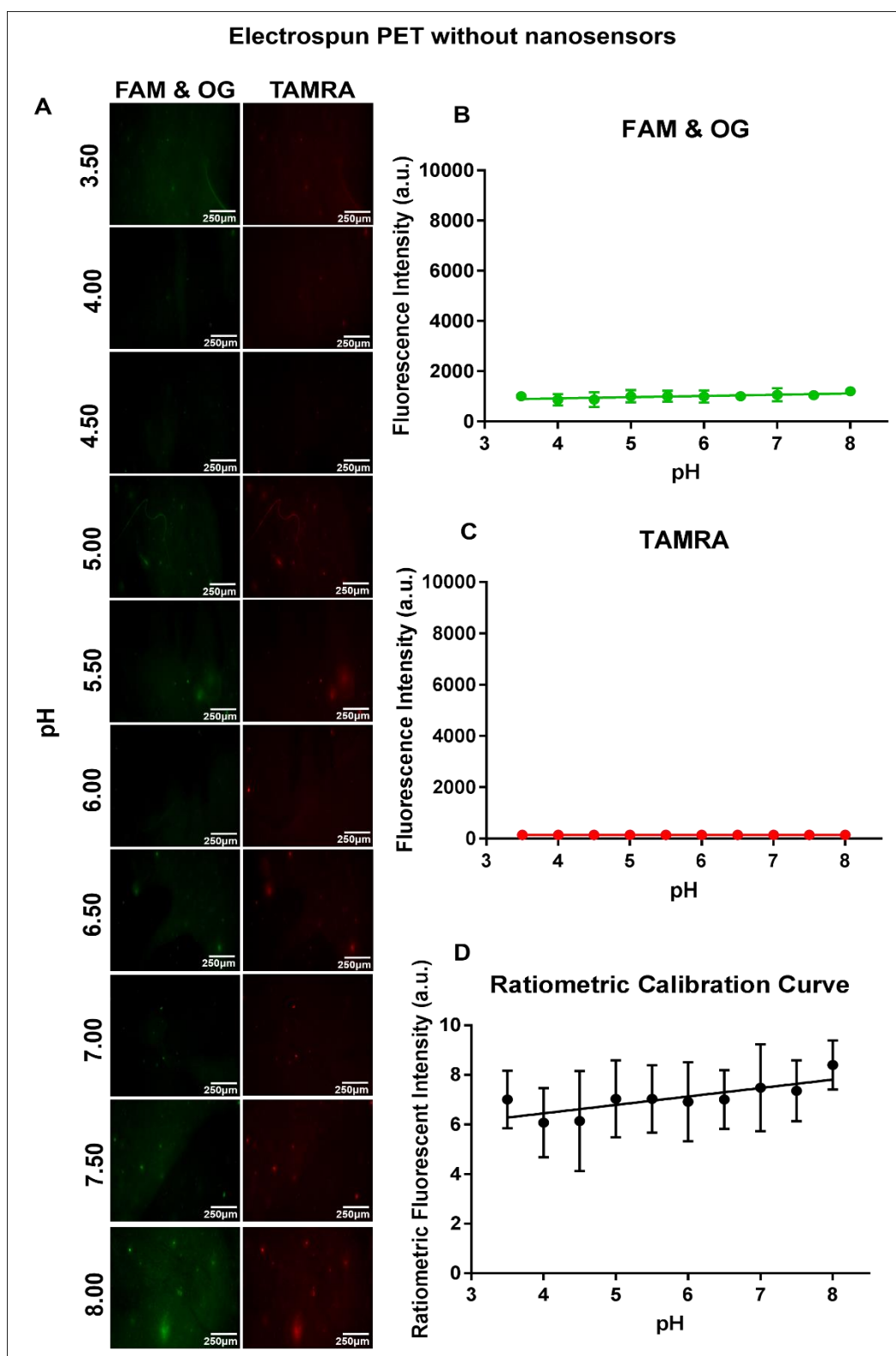


Figure 3.13 Optical characterisation of the electrospun PET without polyacrylamide nanosensors buffer solutions ranging from pH 3.5 – 8.0. (A) Representative fluorescent images showing a visual change in the green fluorescence intensity of pH sensitive FAM&OG, (B) emission curves of FAM&OG, (C) emission curve of TAMRA, (D) Ratiometric calibration curve for pH. Data shown are representative of $n=3 \pm SD$, scale bar = 250 μ m

3.3.2.2. Fabrication of electrospun gelatin sensor scaffold

Due to the lack of responsiveness of the PET/nanosensor scaffold thought to be a result of low porosity of PET, an alternative polymer was spun. Gelatin was selected due to its highly porous properties which be thought to be more successful in gaining a response from the pH nanosensors. The protocol for electrospun gelatin was adapted by Rose²⁴⁴, using 1,1,1,3,3,3-Hexafluoro-2-propanol as a solvent, detailed in section 2.3.1.

3.3.2.2.1. Morphology and fibre diameter characterisation of electrospun gelatin sensor scaffold

The scaffold morphology of the 8% (w/v) electrospun gelatin/nanosensor fibres were imaged using scanning electron microscopy. The SEM micrographs shown in Figure 3.14(B-C) show that both the gelatin/nanosensor and gelatin only (control) constructs display a smooth, bead free, uniform fibrous structure. This observation is interesting as the addition of sensors in this case did not compromise the structure of the fibres whereas the addition of sensors to the PET solutions yielded beaded fibres.

The fibre diameter of the nanofibres with and without nanosensors were characterised using ImageJ analysis and a histogram was produced displaying the distribution of measurements shown in Figure 3.14. The average fibre diameter was calculated using Graph Prism software, for the gelatin/nanosensor scaffold this was $1958.3 \pm 18.3\text{nm}$ (mean \pm SEM), and for the gelatin only control this was $2556.9 \pm 24.5\text{nm}$ (mean \pm SEM). Using an unpaired T-Test with Graph Prism software, a statistically significant ($p < 0.0001$) reduction in the fibre diameter was present with

the addition of the sensors, which displayed a similar effect observed with the addition of the sensors to the PET scaffold which is thought to be a result of an increase in zero-shear viscosity of the polymer solution and rapid evaporation of the solvent preventing fusion of the fibres²³⁹. However, in this case, the addition of the sensors did not cause the formation of beads. This could be due to a several number of factors, as the electrospinning process is effect by many different parameters. In this case, these may include the polymer properties, solvent choice, flow rate, polymer concentration and viscosity of the spinning solution.

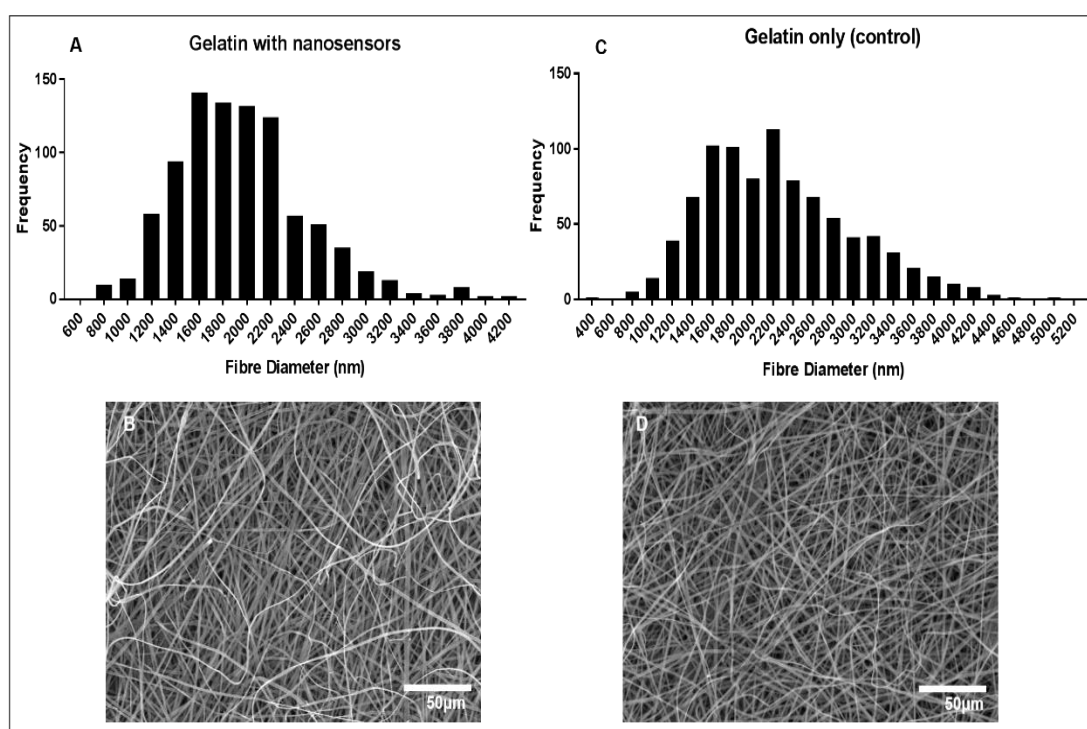


Figure 3.14 Fibre diameter distribution and representative SEM images of 10% (w/v) electrospun gelatin scaffolds with and without the incorporation of nanosensors $n=3$. (A-B) Electrospun gelatin with nanosensors, (C-D) Electrospun gelatin without nanosensors. Magnification $\times 500$, scale bar $50\mu\text{m}$.

3.3.2.2.2. Structural enhancement of electrospun gelatin scaffolds

Since gelatin is known to be mechanically weak, to enhance the structural integrity of the electrospun gelatin scaffold, crosslinking of individual scaffold areas was performed using 1.25% glutaraldehyde vapours.

3.3.2.2.3. Morphology and fibre diameter characterisation of crosslinked gelatin

SEM images of the electrospun gelatin scaffolds before and after crosslinking showed a difference in morphology of the fibres after glutaraldehyde crosslinking treatment. Figure 3.15C displays a more webbed appearance with the fusion of fibres a physical characteristic. High magnification of the uncrosslinked and crosslinked fibres were acquired as shown in Figure 3.16(C-D). The webbed structure agrees with findings by Sisson *et al*²⁴⁵ who also observed this effect when crosslinking gelatin with glutaraldehyde, as displayed in Figure 3.16(A-B) . The average fibre diameter of the uncrosslinked gelatin was $1958.3 \pm 18.3\text{nm}$ and after post crosslinking treatment was $2008.8 \pm 19.6\text{nm}$ (mean \pm SEM) which was slightly higher but found to have no statistical significant differences determined by unpaired T Test. Chaochai *et al*²⁴⁶ also found that crosslinked electrospun gelatin fibres with glutaraldehyde vapour were slightly larger than those not treated. In addition to Wu *et al*²⁴⁷ who did not observe any noticeable swelling in the glutaraldehyde treated nanofibres.

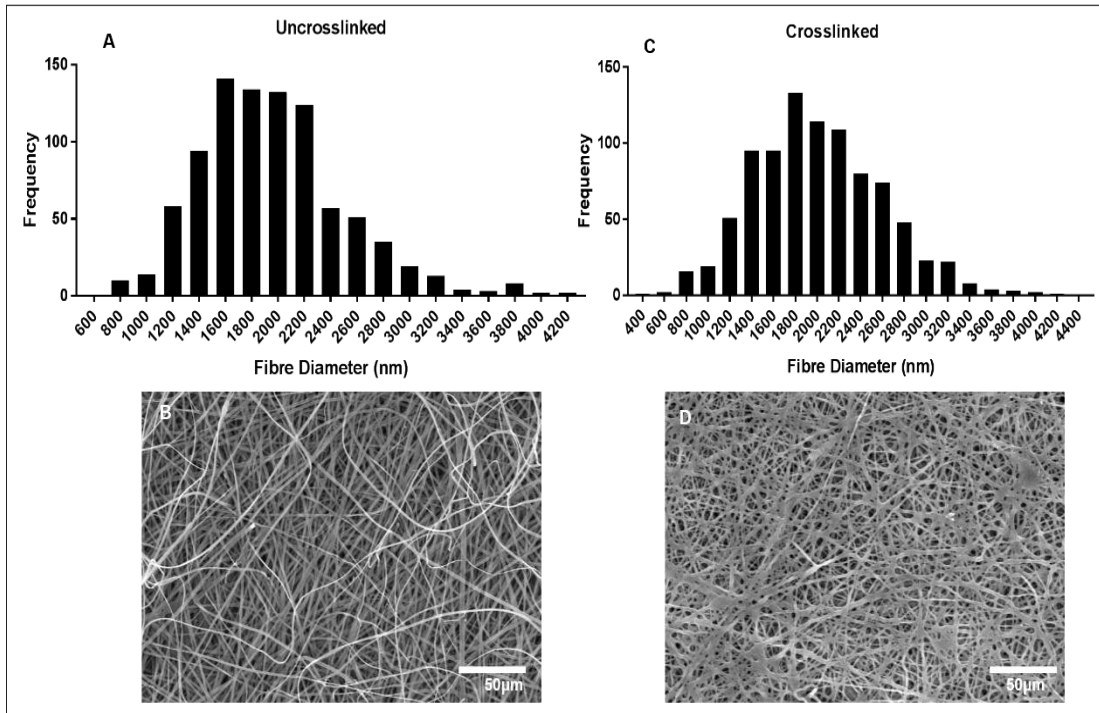


Figure 3.15 Fibre diameter distribution and representative SEM images of 10% (w/v) electrospun gelatin scaffolds with and without the incorporation of nanosensors $n=3$. (A-B) Uncrosslinked electrospun gelatin with nanosensors, (C-D) Crosslinked gelatin without nanosensors. Magnification $\times 500$, scale bar $50\mu\text{m}$.

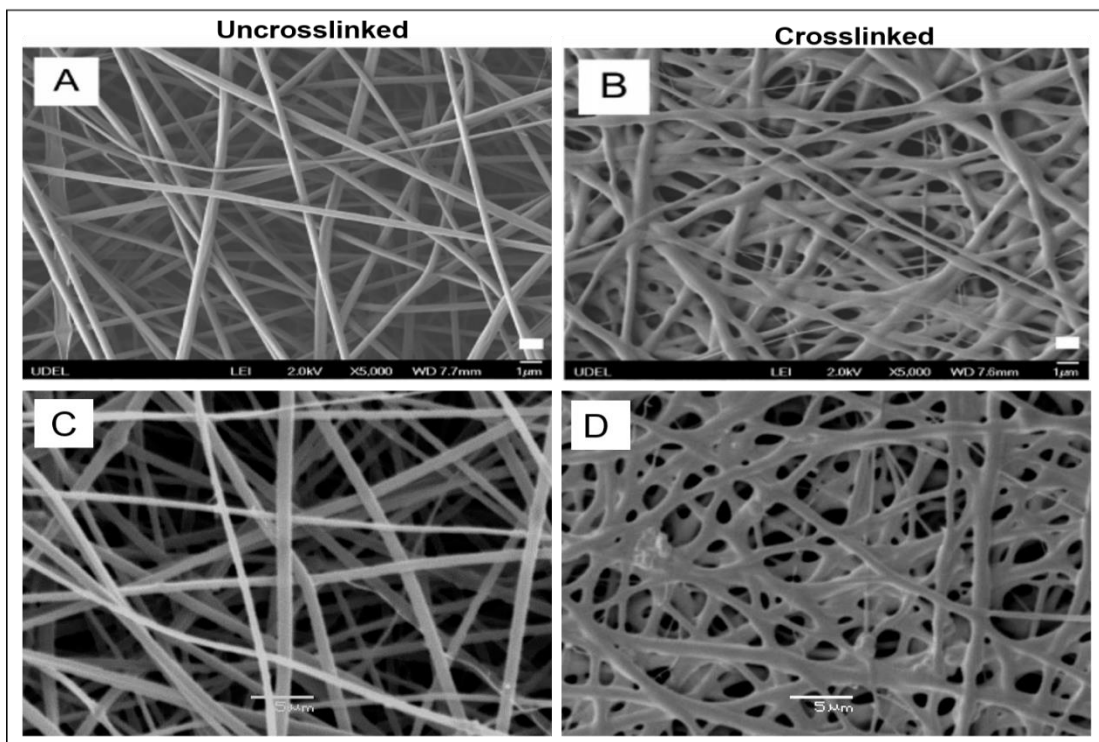


Figure 3.16 (A-B) Scanning electron micrographs of uncrosslinked vs crosslinked electrospun gelatin scaffolds, at $\times 5000$ magnification taken from Sisson *et al*²⁴⁵, scale bar = $1\mu\text{m}$. (C-D) SEM images of electrospun gelatin scaffolds with polyacrylamide nanosensors acquired at a similar magnification of $\times 3000$ for comparison, scale bar = $5\mu\text{m}$.

3.3.2.2.4. Water degradation of uncrosslinked electrospun gelatin scaffolds

To demonstrate the structural reinforcement of the scaffold by crosslinking with glutaraldehyde, a water droplet was placed on the centre of uncrosslinked and crosslinked gelatin. Figure 3.17 shows scanning electron micrographs that demonstrate the improved hydrolytic resistance of the crosslinked scaffold, and the complete water degradability of the uncrosslinked scaffold. This is in agreement with the observation that the non-crosslinked gelatin scaffold disintegrates/dissolves in water, whereas crosslinked scaffold is able to retain its structural integrity when immersed in water.

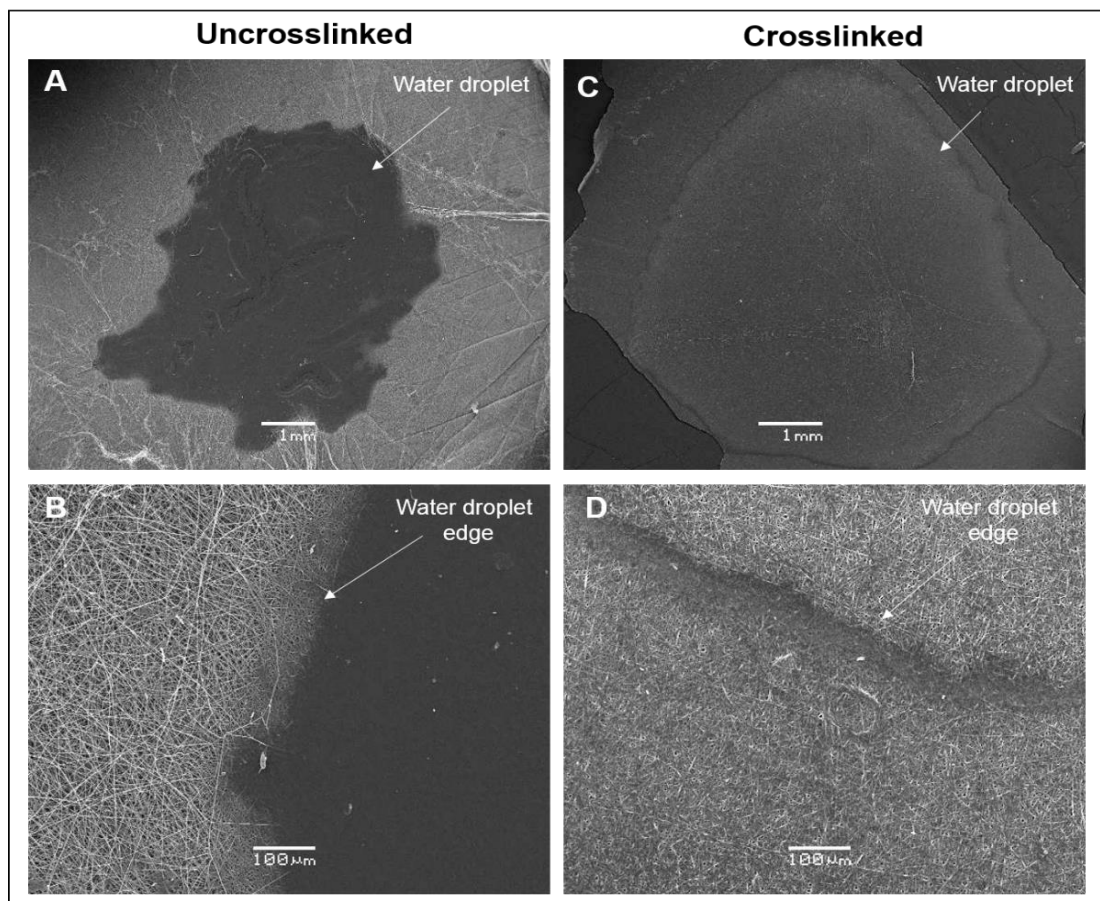


Figure 3.17 Representative scanning electron micrographs of water droplet placed on centre of electrospun uncrosslinked and crosslinked gelatin scaffold, water droplet degrades uncrosslinked scaffold, however crosslinked scaffold retains its structural integrity $n=3$.

3.3.2.2.5. Optical characterisation of electrospun gelatin scaffolds

To determine the pH responsiveness of the gelatin scaffolds, constructs were crosslinked and placed in buffers ranging from pH 3.5 – 8.0 and fluorescently imaged. The fluorescent images and graphs in Figure 3.18 display a change in the fluorescence intensity of the pH sensitive fluorophores FAM and OG corresponding to the pH changes, whilst the pH insensitive fluorophore TAMRA emission remains constant. Figure 3.18 shows the polyacrylamide nanosensors are uniformly distributed throughout the fibres with fluorescence scattered across the whole of the scaffold area. The ratiometric fluorescence intensity increases as the pH increases, similar to the pattern displayed in the nanosensors suspended in buffers alone, this demonstrates the ability of the scaffold to successfully report the hydrogen ion concentration within the scaffold environment. The peak fluorescence of the pH responsive FAM & OG dyes of the nanosensors alone in Figure 3.10B is larger than the peak fluorescence of the dyes incorporated within the scaffold Figure 3.18 which could be because with the nanosensors alone in the buffers the hydrogen ions can easily diffuse across the polyacrylamide matrix and interact with the fluorescent dyes, however with the gelatin scaffold the hydrogen ions need to diffuse through the gelatin fibres before they can enter the nanosensor matrix therefore slightly limiting/delaying their response.

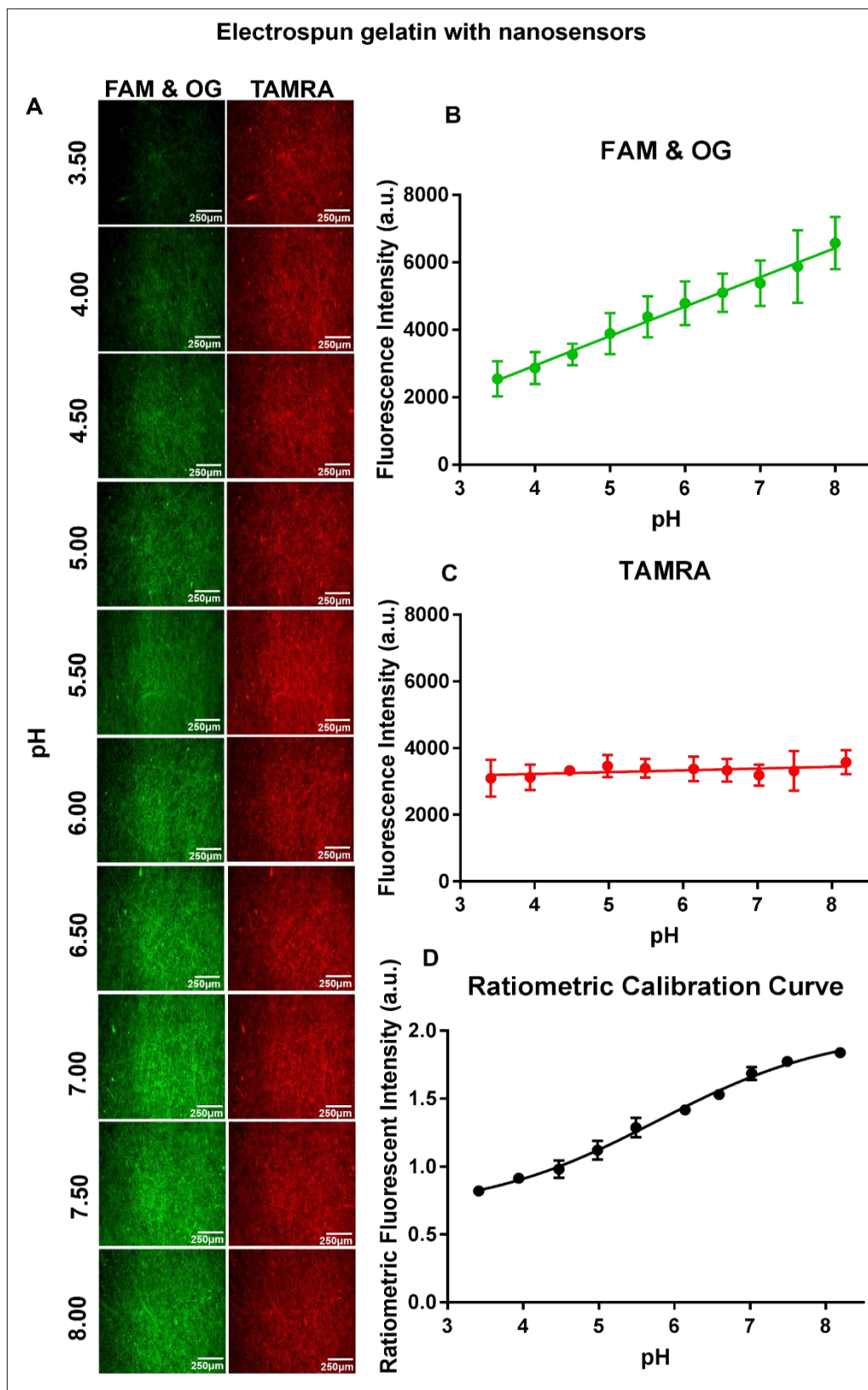


Figure 3.18 Optical characterisation of the pH response of polyacrylamide nanosensors incorporated in electrospun gelatin suspended in buffer solutions ranging from pH 3.5 – 8.0. (A) Representative fluorescent images showing a visual change in the green fluorescence intensity of pH sensitive FAM&OG, (B) emission curves of FAM&OG, (C) emission curve of TAMRA, (D) Ratiometric calibration curve for pH. Data shown are representative of $n=3 \pm SD$, scale bar = 250 μm .

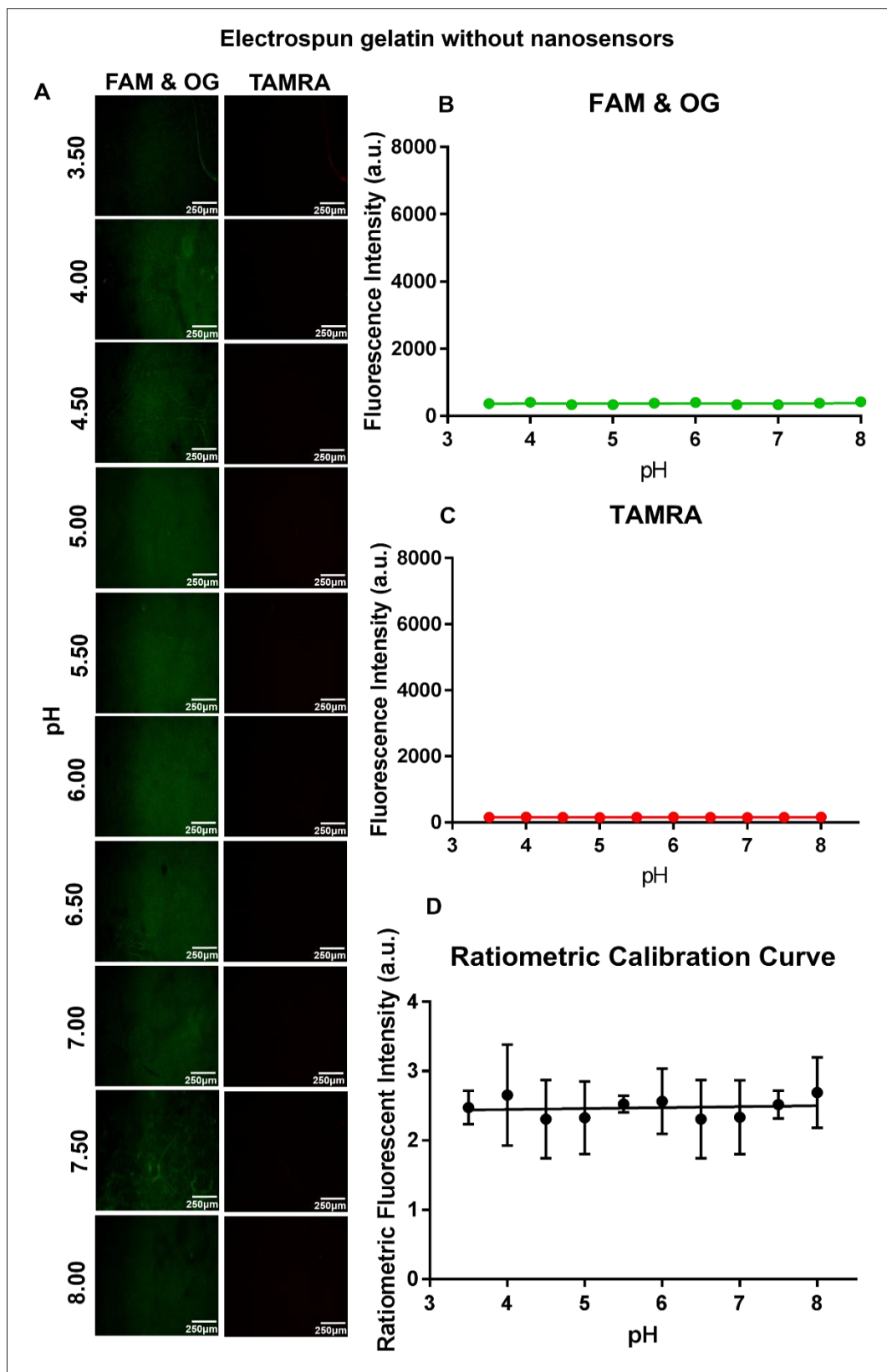


Figure 3.19 Optical characterisation of electrospun gelatin without polyacrylamide nanosensors suspended in buffer solutions ranging from pH 3.5 – 8.0. (A) Representative fluorescent images showing a visual change in the green fluorescence intensity of pH sensitive FAM&OG, (B) emission curves of FAM&OG, (C) emission curve of TAMRA, (D) Ratiometric calibration curve for pH. Data shown are representative of $n=3 \pm SD$, scale bar = 250 μ m.

3.4. Conclusion

Polyacrylamide nanosensors were synthesised and showed an additive pH response when suspended in a range of pH buffers. Electrospun polyethylene terephthalate scaffolds were successfully fabricated but displayed a compromised morphology with the addition of polyacrylamide nanosensors. Although the PET retained its optical activity after the electrospinning process, there was a lack of pH response from the construct thought to be due to the lack of permeability of the polymer, restricting the diffusion of hydrogen ions through the fibres and interacting with the nanosensors. Therefore making PET an unsuitable polymer for the self-reporting scaffold. On the other hand, gelatin was successfully electrospun with the incorporation of nanosensors and displayed smooth, uniform, bead-free microfibers. The gelatin, self-reporting scaffold was able to successfully display the same sigmoidal response as the nanosensors in suspension. To further enhance the mechanical strength of the electrospun gelatin scaffolds, glutaraldehyde was successfully used to crosslink the fibres.

Chapter 4 Evaluation of flow conditions and wound assays

The aim of this chapter is to optimise the incorporation of flow conditions into *in vitro* cultures in combination with PET and gelatin electrospun scaffolds to evaluate whether cell proliferation improves with enhanced nutrient and oxygen diffusion. In addition, flow conditions can recreate the mechanical stimulation conditions such as shear stress experienced by cells *in vivo* throughout the extracellular matrix of a tissue. Research over the last 2 decades has demonstrated the importance of flow in tissue organisation, cellular phenotype and their subsequent activity. To compare and observe the proliferative and migratory effects of cells exposed to static vs flow conditions, a novel concept of performing wound assays on electrospun scaffolds was explored. Electrospun PET was used for the optimisation of the wound assays due to its mechanically robust nature compared to gelatin. After optimisation of the PET wound model, the aim was to translate this to the self-reporting gelatin scaffold so the local pH of the wound could be monitored over time.

4.1. Introduction

Electrospun scaffolds have been shown to be promising in many tissue engineering and regenerative medicine applications. However, limitations can arise from their dense, thick, fibrous structure restricting oxygen diffusion throughout the scaffold²⁴⁸ and cellular infiltration which is important for the formation of a three-dimensional (3D) cell-scaffold construct. To enhance diffusion throughout the scaffolds, bioreactors can be used to provide a biomechanical and biochemical environment to control nutrient and oxygen transfer to the cells and metabolic

production⁸². Bioreactors have been shown to enhance nutrient transport by perfusion of medium through the interconnected pores of the scaffolds⁸⁵⁻⁸¹, which has in turn shown to significantly improve the core cell activity within the construct compared to static culture⁸¹.

4.1.1. 2-D wound assays

In vitro wound healing assays allow the investigation of cell migration and proliferation in wound repair²⁴⁹. Cell migration is the movement of cells in response to biological signals or environmental cues and play a key role in physiological processes such as tissue repair and wound healing. Wound assays typically involve injury of a confluent layer of cells. During healing, cells proliferate and migrate to repopulate the wounded area, the healing is monitored often by microscopy and the reduction in the wound area is quantified over time and evaluated. There are two categories of creating wound areas including the cell exclusion or cell depletion method. The cell exclusion uses a removable stencil to confine areas of growth, but causes little damage to cells along the edge of the cell-free area which can limit cell signalling²⁵⁰. Nyegaard et al²⁵¹ performed a cell exclusion zone assay by using a silicone stopper to monitor the cell migration of human small intestine epithelial cells. One of the advantages of this methods was that the 'wound' area was well defined, and there was no damage to the deposited ECM proteins. The cell depletion method involves a variety of methods to rupture cell-to-cell junctions and remove cells including electrical currents, thermal heating, laser ablation, (bio)chemicals and sharp objects to rupture cell-to-cell junctions and remove cells from a confluent cell culture as shown in Figure 4.1²⁵⁰. These methods have been reviewed by Stamm et al²⁴⁹ and Riahi et al²⁵².

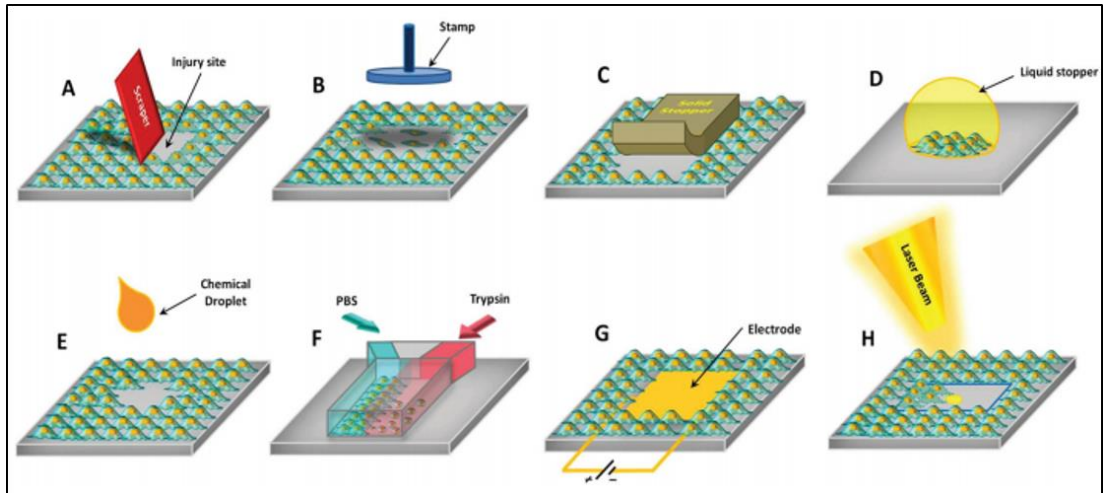


Figure 4.1 Schematic of wound healing assays taken from Riahi et al²⁵² based on (A) scratching, (B) stamping, (C) solid barrier, (D) liquid barrier, (E) droplet chemical assay, (F) microfluidic chemical assay, (G) electrical assay, and (H) laser ablation.

4.1.1.1. Scratch assays

The scratch assay is one of the most popular methods used to study cell migrations. The method is based on scratching a confluent cell monolayer in a 24 well plate using a pipette tip/scrapper as shown in Figure 4.1A, and capturing images over time to measure and quantify the wound area whilst cells migrate and attempt to recover the gap²⁵³. Some of the constraints of the scratch assay include the formation of irregular scratches limiting the reproducibility of the experiment. In addition, secreted extracellular matrix coatings on the cell culture dish may be scraped off when scratching²⁴⁹. Furthermore, removed cells can accumulate on the edge of the artificially introduced gap, which might impede data analysis, as well as affect consequent proliferation and migration necessary for wound closure²⁴⁹. In addition injury to the cells at the edge of the cell-free area release intracellular components and signalling molecules which are known to negatively influence cell migration²⁵⁰. However scratch assays are the most simplest and economical method to study cell migration *in vitro* and have been used for a variety of applications²⁵³. Ueck et al²⁵⁴ investigated diabetic wound healing by performing scratch assays with

human keratinocytes from diabetic donors. In addition, Demirci et al²⁵⁵ explored the effect of natural herbs on wound recovery of a scratch assay performed with human dermal fibroblasts.

4.1.1.2. Chemical assays

Cells can be wounded by using chemical methods. As shown in Figure 4.1E, a small drop of chemical such as sodium hydroxide is pipetted onto the centre of the cell monolayer which selectively removes cells in contact with the droplet. The size of the wound is controlled by the volume of the chemical applied²⁵². Legrand et al²⁵⁶ used sodium hydroxide to lyse cells and create a wound model to monitor airway epithelial cell migration. Alternative chemical assays involve the use of a biochemical such as trypsin to remove cells to create a wound area. Conde et al²⁵⁷ used a microfluidic device to culture endothelial cells, and then exposed them to a parallel flow of trypsin to create a wound by detachment of the exposed cells. The advantage of this system is that wound areas are reproducible and blood flow can also be simulated. A limitation is that the use of pumps to induce the flow can be expensive and the PDMS device does not allow the acquisition of images in real time.

4.1.2. 3-D wound models

It has become well known that cells cultured in 3D display different morphology, signalling, migration behaviour and metabolic function compared to 2D cultures²⁴⁹, therefore 2D wound models lack the complexity of 3D wound models. Constructs used for 3D wound healing assays are typically various models of artificial skin such as skin substitutes, skin equivalents or bioengineered skin²⁴⁹. The skin constructs

consist of a bilayer structure combining dermal and epidermal components²⁴⁹. Xie et al²⁵⁸ developed a 3D human skin equivalent wound model which contained a stratified surface layer of keratinocytes cultured at the air liquid interface. The wound was created by a biopsy punch which displayed wound closure in 48-72hrs using immunofluorescence and immunohistochemistry, which is comparable to the *in vivo* environment. Safferling et al²⁵⁹ also developed an *in vitro* 3-D skin wound model, but by purchasing commercially available epidermal full thickness cultures. A wound was created using a biopsy punch which demonstrated wound closure by immunofluorescence and immunohistochemistry. The advantage of these skin mimics, are that they incorporate multiple cell types to mimic the different layers of the skin and recreate the complex processes involved in wound healing.

Chen et al²⁶⁰ developed a 3D wound model by seeded fibroblasts into a collagen gel and performing a biopsy punch to create a wound area. The defect was then filled with collagen or with various solutions of fibrinogen and thrombin that polymerize into a 3D fibrin clot to mimic a wound bed. The different rates of cell migration into the fibrin or collagen filled defect were monitored over time using microscopy. Karamichos et al²⁶¹ also developed a 3D wound model by using a 3D collagen construct to study the migration of fibroblasts from a dense, compressed collagen matrix into a less dense surrounding matrix, this was monitored using confocal microscopy. However, the limitation of these models is that they only utilise one cell type²⁶⁰. Timm et al²⁶² report a 3D *in vitro* cell migration assay for toxicity screening in drug development applications which is similar to the wound healing concept. Cells were magnetically levitated to form 3D structures and magnetically patterned into 3D-ring shaped cultures. When the magnetic field was removed, the rings closed over time due to cell migration and proliferation, and cell-cell and cell-ECM interactions. The ring closure is a similar concept to the wound healing assay which has been performed in 2D to study cell migration. The rate of ring closure, was

found by measuring the outer diameter of the ring over time, the rate of closure was found to decrease with increasing toxic concentrations of the drug. Time-lapse images were taken using a mobile device, which had high enough resolution to capture individual wells. Some of the advantages of using magnetic levitation are that a scaffold is not required, and the 3D spheroids formed are uniform and rapidly formed²⁶³. However magnetic levitation is limited by the uncertain effect of the magnetic nanoparticles on the cells²⁶³.

We propose to develop an *in vitro* wound assay to study cell migration on electrospun scaffolds which has not yet been performed. The advantage of using an electrospun scaffold is that it mimics the extracellular matrix of the connective tissue where the most abundant cell type fibroblasts reside. By using electrospun scaffolds other cell types can be co-cultured on the scaffolds.

4.2. Results & Discussion

After showing that PET and gelatin could be successfully electrospun in Chapter 2, the next step was to show that these polymeric scaffolds could support tissue growth. We wanted to investigate how flow conditions would affect cell proliferation using both types of scaffolds. PET was initially used due to its mechanical robustness and easy handling compared to electrospun gelatin. A wound healing assay was performed on the structurally stable PET scaffolds to attempt to create a reproducible model to compare the effect of flow conditions on proliferation. In order to expose the cell-seeded PET scaffold to flow conditions, the Quasi-Vivo[®]500 bioreactor system combined with a peristaltic pump. The Quasi-Vivo[®]900 system was used to support flow conditions using the electrospun gelatin scaffolds as their integrity needed to be secured by CellCrowns[™], the dimensions of the CellCrowns[™] were only compatible with the QV900. Fibroblasts were the chosen cell type for flow exposure due to their predominance in the connective tissue, abundant extracellular matrix production and wound healing.

4.2.1. Calibrating flow rates of the Quasi-Vivo[®] system

To generate the flow conditions in the Quasi Vivo[®] system, a peristaltic Watson-Marlow was used. A peristaltic pump is ideal because it allows the recirculation of media, where cells can condition the media with growth factors and cytokines which is important for cell-cell signalling and growth. It is also more physiologically relevant compared to a single pass system permitted by syringe pumps for example. The peristaltic pump has flexible silicone tubing fitted which is exposed to set a of rollers run by an electric motor, these compress and release the tubing as the roller rotate. The squeezing action along the length of the tube creates a vacuum which draws in

fluid through the tubing. The flow rates were manually calibrated to give the flow rates in $\mu\text{L}/\text{min}$ by measuring the volume of media expelled in a single-pass set up of the Quasi-Vivo[®]500 after 10 minutes as described in section Figure 4.2A provides the measured volumes of media and respective flow rates, and Figure 4.2B displays a calibration curve relating the rpm and flow rate which displays a linear relationship. As expected, as the rpm increases the flow rate also increases. By using this data, specific flow rates can be determined which can be used as a comparison to flow rates used in other studies. One of the disadvantages to using this pump is that flow rates lower than $81\mu\text{L}/\text{min}$ cannot be used. However, smaller diameter tubing can be used to reduce flow rates, but due to the Luer dimensions for connecting the QV system together, smaller diameter tubing would not be feasible.

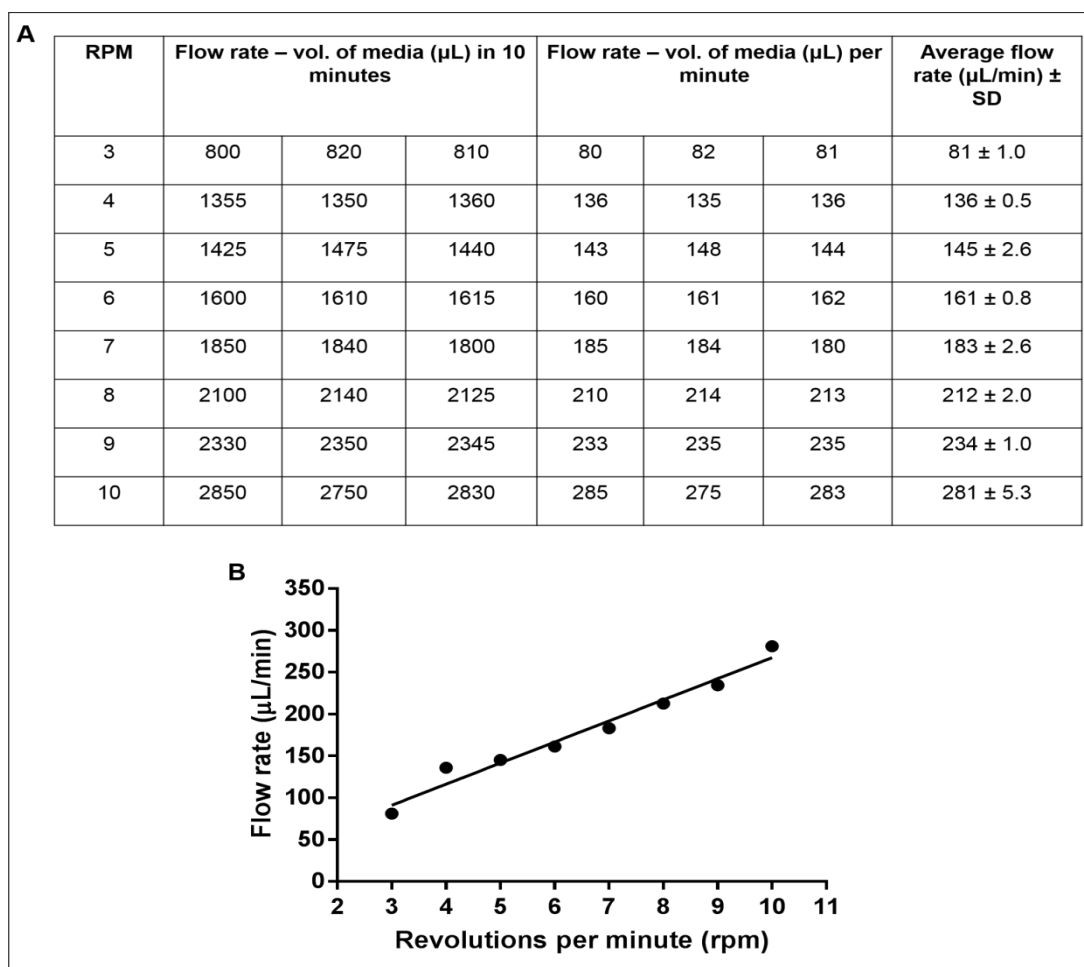


Figure 4.2 Calibration of Watson-Marlow peristaltic pump at a range of speeds (revolutions per minute). (A) Volume of media expelled after running the single flow Quasi-Vivo[®] set up (B) curve relating rpm and flow rate $\mu\text{L}/\text{min}$ $n=3$.

In order to achieve lower flow rates, a Parker-Hannifin peristaltic pump was used. Again the flow rates required manual calibration by setting up a single pass Quasi-Vivo[®] system. A disadvantage of using this pump was that the dial used to change the speed of the pumping action had no given specific values, therefore the flow rates had to be manually written on the pump and any slight movements of the dial drastically changed the flow rate.

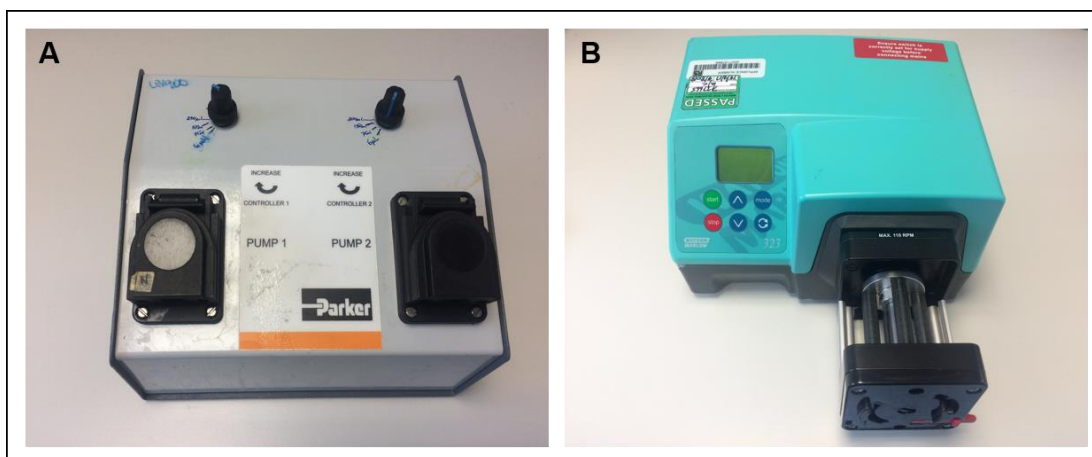


Figure 4.3 Peristaltic pumps (A) Parker Hannifin (B) Watson-Marlow.

4.2.2 Lung fibroblasts exposed to flow conditions using PET scaffold

When choosing a flow rate to generate shear stress, a variety of parameters should be considered. Studies have shown that cells can be highly sensitive to different flow rates and that low shear stresses are necessary to maintain cell function. However, if the flow rate is too low, cell proliferation may be inhibited as a result of limited oxygen diffusion creating hypoxic conditions²⁶⁴. But if the flow rate is too high, cell apoptosis may occur due to high shear stress exposure. At optimal flow conditions gene and protein expression can be stimulated²⁶⁵. Depending on the cell type, scaffold and application, different flow rates have been used.

Initial experiments involved culturing MRC-5 human lung fibroblasts on electrospun PET scaffolds and exposing them to a flow rate of $\sim 280\mu\text{L}/\text{min}$. Cell seeded scaffolds were placed on a scaffold platform towards the top of the bioreactor to directly expose them to the flow of media. Representative scanning electron micrographs displayed in Figure 4.4 were acquired to show the presence of cells and extracellular matrix deposition on the scaffold. The SEM micrographs show that when cells were exposed to static conditions, they were able to attach to the scaffold and form a confluent monolayer by Day 3, however exposure to flow conditions showed the detachment of the cells and an absence of ECM deposition by Day 2. This could be due to the high shear stress and impact angle of flow on the cells forcing the cells off the scaffold. The physiological flow rate of $\sim 280\mu\text{L}/\text{min}$ used in this experiment was based on a previous study by Vinci et al⁹⁹. The authors successfully cultured hepatocytes on 3-D polymer scaffolds within a multi-compartment bioreactor system, an early prototype of the Quasi-Vivo® 500 bioreactor and recirculated media at a flow rate of $250\mu\text{L}/\text{min}$. It was discovered that the metabolic turnover increased dramatically in 3-D dynamic cultures, compared to static monolayer cultures. In addition the cell density increased in 3-D scaffolds compared to 2-D due to the formation of cell aggregates, indicating the importance of both topographical and physical stimuluses. However, it is important to note that the hepatocytes were protected with a thin coating of gel due to their high sensitivity to flow which could have helped prevent detachment of the cells from the scaffold.

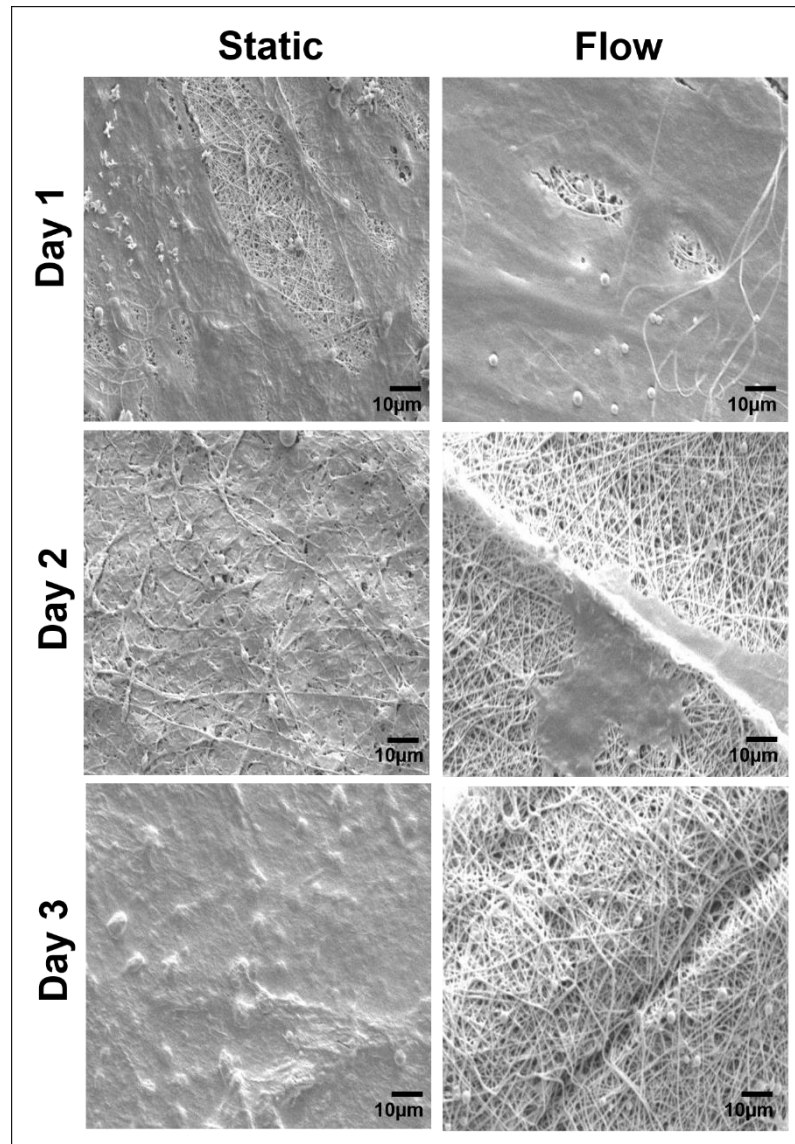


Figure 4.4 Representative scanning electron micrographs of MRC5 human lung fibroblasts cultured on PET scaffold exposed to static vs flow conditions $\sim 280\mu\text{L}/\text{min}$, scale bar = $10\mu\text{m}$.

As a result of the cell detachment at the flow rate of $\sim 280\mu\text{L}/\text{min}$, the flow rate was reduced by approximately half $\sim 145\mu\text{L}/\text{min}$. Flow rates of 75 and $150\mu\text{L}/\text{min}$ using the Quasi-Vivo® 900 system have been shown to induce changes in gene expression in dermal fibroblasts although this was only done for a duration of 24 hours so the long term effect of the flow is unknown. Scanning electron micrographs in Figure 4.5 showed that when exposed to flow conditions, cells attachment/ECM deposition was present for up to 2 days. After 3 days cell detachment is clear

compared to day 2 with very few cells remaining, indicating that again the shear stress is too high.

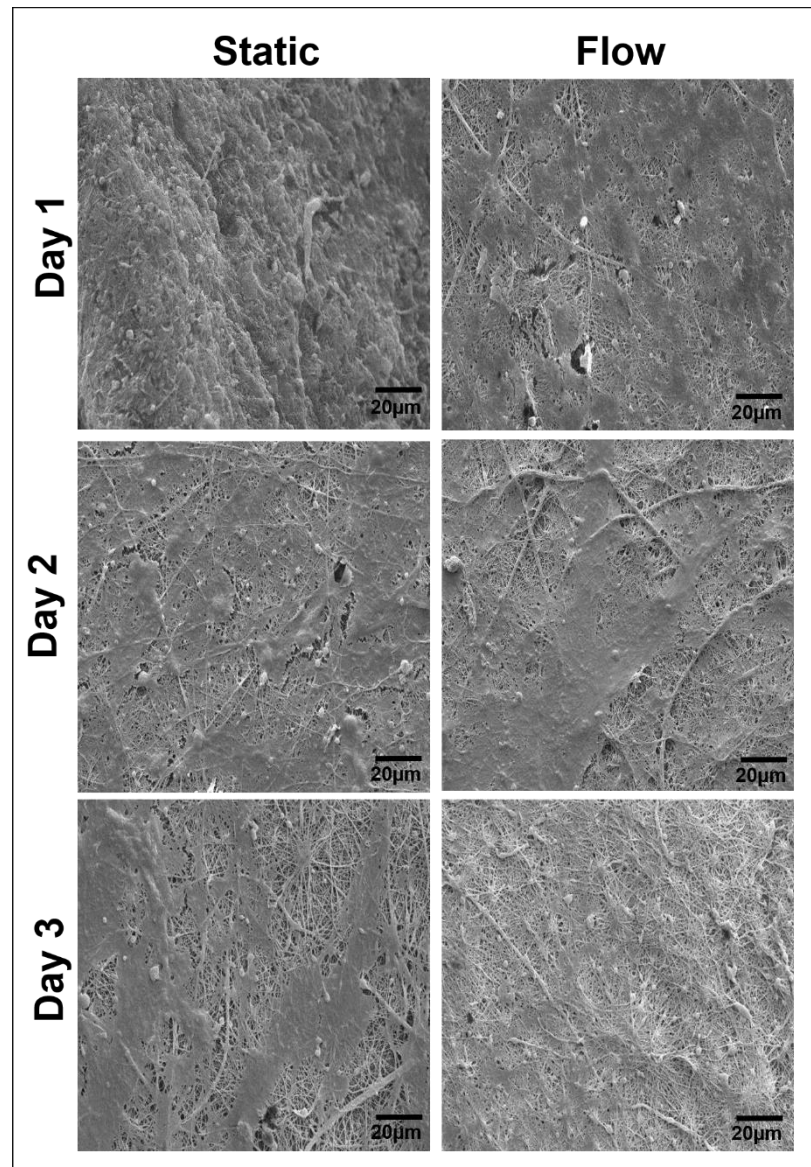


Figure 4.5 Representative SEM images of MRC5 lung fibroblasts cultured on electrospun PET scaffolds exposed to static vs flow conditions $\sim 145\mu\text{L}/\text{min}$, scale bar = $20\mu\text{m}$.

4.2.3. Mouse fibroblasts cultured on PET exposed to flow conditions

Due to the inability to successfully culture MRC5 lung fibroblasts in a reproducible manner under flow conditions, a mouse embryonic fibroblast cell line known for its

robustness was used for future experiments. The adherent NIH 3T3 cell line has been extensively used in microfluidic models due to its morphological and genetic stability²⁶⁶. In addition, by using an alternative peristaltic pump (Parker-Hannifin), a lower available flow rate of $\sim 8\mu\text{L}/\text{min}$ could be achieved. Therefore, NIH 3T3 fibroblasts were cultured on the PET scaffold and exposed to flow conditions at a rate of $\sim 8\mu\text{L}/\text{min}$. Instead of using scanning electron microscopy as done previously to characterise the cell seeded scaffolds, we used fluorescent staining as this can be more informative. Cells were fixed and an F-actin cytoskeleton, nuclear and Ki67 fluorescent stain was performed, in addition to an AlamarBlue[®] proliferation assay shown in Figure 4.6. For this particular flow experiment, a Ki67 stain was performed. Ki67 is a nuclear protein that is tightly linked to the cell cycle²⁶⁷. It is a marker of cell proliferation, as it is expressed in proliferating cells during mid G1 phase, increasing in level through S and G2, and peaking in the M phase of the cell cycle²⁶⁷. The reason why the Ki67 stain had been performed is because the AlamarBlue[®] data in Figure 4.6B showed a significant increase in proliferation at Day 3 of flow conditions, which is therefore reinforced by the increasing fluorescent intensity of the Ki67 stain. The F-actin stain in particular shows the presence of the cells attached to the scaffold in both static and flow conditions, indicating that the low flow conditions do not compromise the cell attachment. This increased proliferative effect is in agreement with several other studies, including the use of different cell types as described below. Kim et al²⁶⁸ et al grew 3T3 fibroblasts in 2D at a very low flow rate of $0.1\ \mu\text{L}/\text{min}$, and a higher flow rate of $5\mu\text{L}/\text{min}$ similar to the rate used in our study within a microfluidic device, and they showed that the higher flow rate had enhanced proliferation compared to the very low flow rate. Low flow rates of $0.2\text{mL}/\text{hr}$ have also been shown to enhance fibroblast growth and alignment in a microfluidic device compared to a static dish²⁶⁹. In a study by Park et al²⁷⁰ radial glial cells (RGC) which function as neural stem cells were cultured in a 2-Dimensional microfluidic device. They were exposed to a flow rate of $6.7\mu\text{L}/\text{min}$ which showed a significant increase

in the proliferative effect of the cultured RGCs over 5 days. Ca^{2+} signalling is considered the major contributor to proliferation in neural stem cells. Subsequently, the increase in proliferation was thought to be due to the activation of mechanosensitive Ca^{2+} channels of the cells, which mediate the Ca^{2+} entry upon shear stress. Haga et al²⁷¹ also demonstrate an increase in proliferation of smooth muscle cells in response to oscillatory shear stress. Their theory was that this effect was associated with the observed increased Akt phosphorylation which may be mediated with a PI3-dependent mechanism. Studies by Ng et al²⁷²⁻⁸⁶ have focused on using low flow rates between 10-12 $\mu\text{L}/\text{min}$ to investigate fibroblast cell alignment, which showed the cell and matrix alignment when exposed to interstitial flow conditions, however cell proliferation and viability was not quantified. Flow conditions are known to influence both biochemical and biophysical cues surrounding the cells²⁷³. The conversion of an external physical signal into a cellular response is referred to as mechanotransduction²⁷⁴. Integrins are transmembrane proteins which serve as mechanoreceptors and can transfer the mechanical stimulus signal from the outside of the cell (ECM) to the connecting cytoskeleton. Various cell types can respond in different ways due to their difference in integrin expression²⁷⁴, and regulate signalling pathways such as Rho, Rac, Cdc, FAK and Shc which in turn stimulate cell activity such as proliferation²⁷⁵. Further studies into the integrin expression, genes related to proliferation and growth factor/cytokine analysis should be performed in order to discover the differences cell growth.

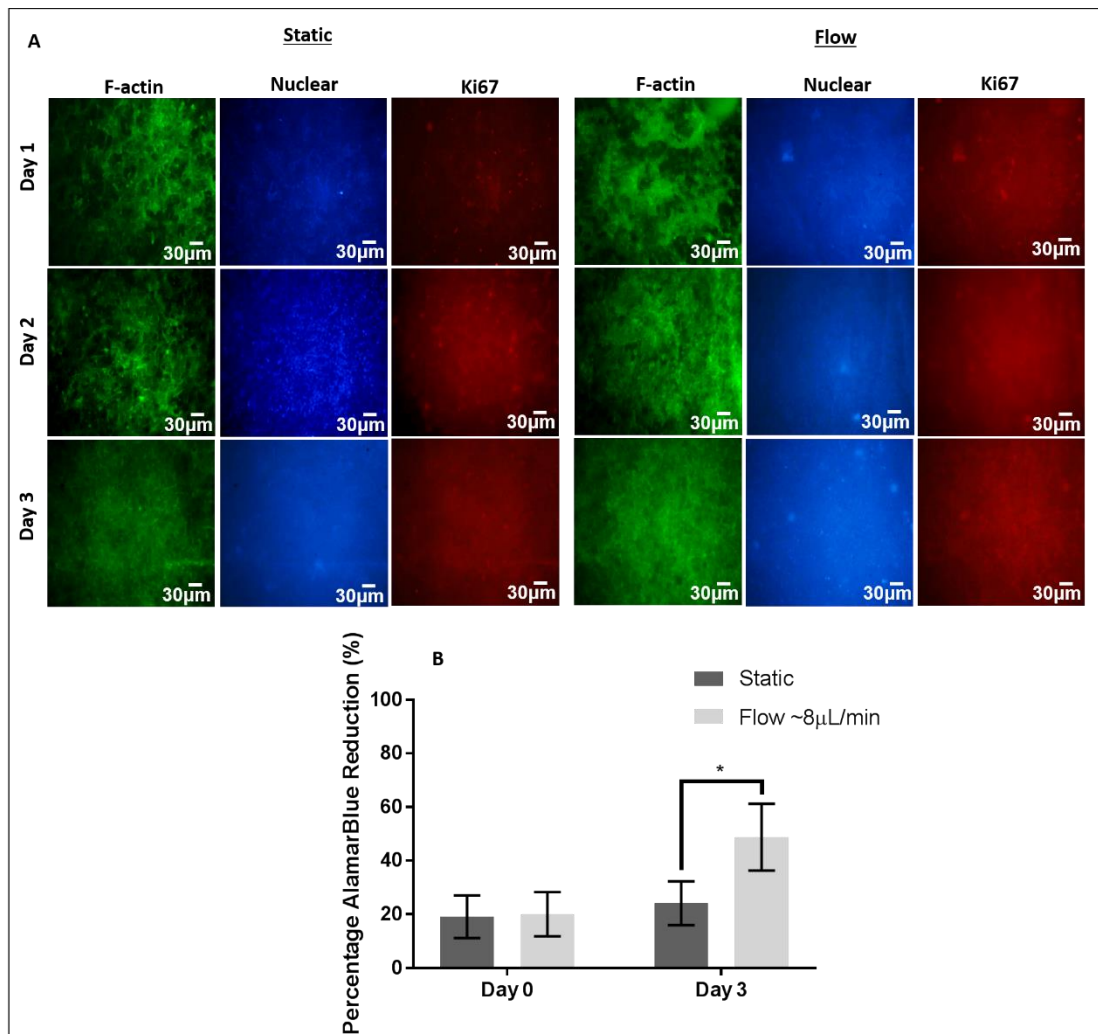


Figure 4.6 NIH 3T3 fibroblasts cultured on electrospun PET scaffolds exposed to static vs flow conditions, fluorescent images of cells cultured in static conditions stained with DAPI, AlexaFluor488 phalloidin and Ki67 (B) AlamarBlue[®] proliferation assay shows proliferation is significantly enhanced when exposed to flow conditions ~8µL/min, $p \leq 0.05$, $n=3$, scale bar = 30µm.

After observing the proliferative effect of the 3T3 fibroblasts, a Sirius red stain was performed to quantify the production of collagen in static vs flow conditions (~8µL/min). Figure 4.7C did not show a significant difference in the production of collagen. The photographic images appear to have a more consistent high production of collagen on Day 1, Day 2 and Day 3, whereas in static conditions the collagen production gradually increases over the time period. This observation is in agreement with a study involving the culture of chondrocytes which demonstrated a significant up-regulation of type II collagen production in perfused cultures compared

to static conditions up until 72 hours²⁷⁶. Furthermore, Wang et al²⁷⁷ also showed increased collagen production, they cultured human dermal fibroblasts on PolyActive™ 3-Dimensional scaffolds, which were subjected to mechanical stimulation via media flow in a spinner flask. The dynamic conditions resulted in a uniform distribution of cells through the scaffolds, and a significant higher number of fibroblasts and collagen (hydroxyproline) and glycosaminoglycan (GAG) deposition compared to static conditions.

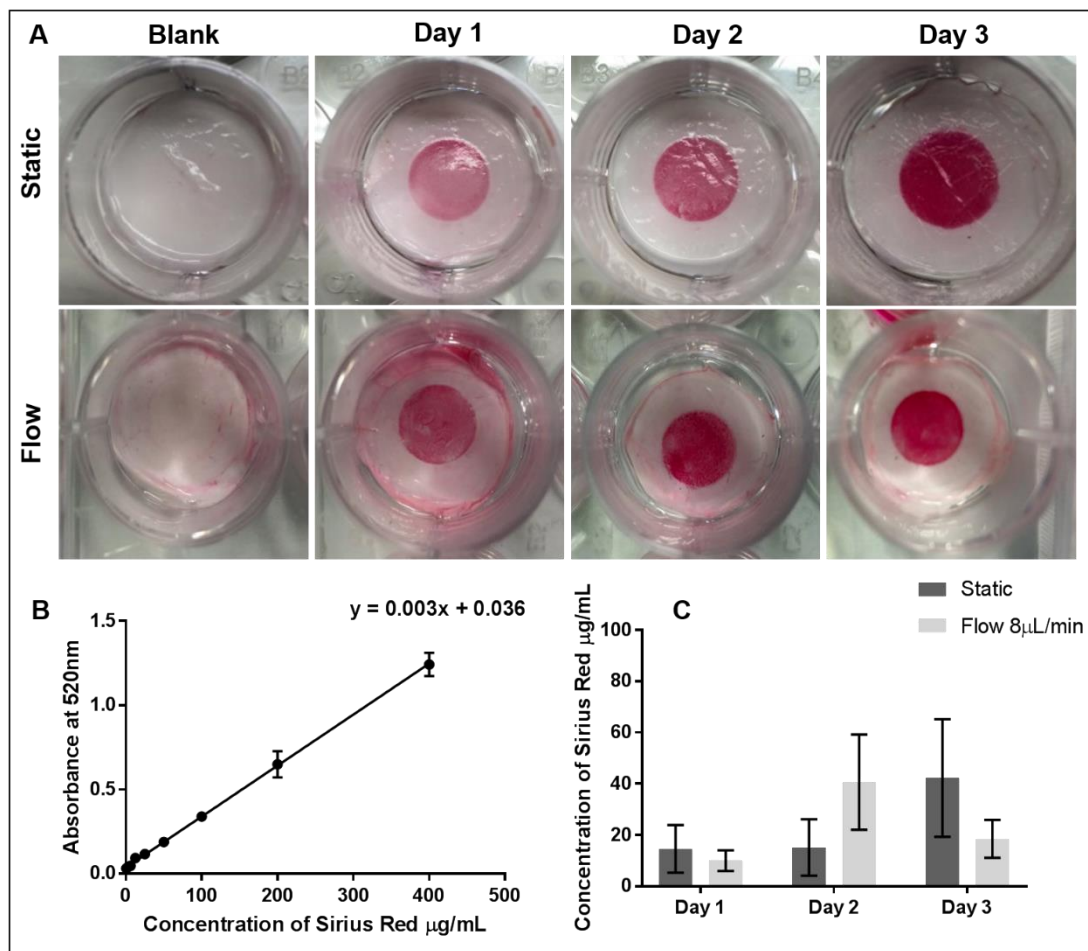


Figure 4.7 Sirius red stain on cell-seeded PET scaffold to show collagen production by NIH 3T3 fibroblasts exposed to static vs flow culture conditions, (B) Standard curve of known Sirius red concentrations vs absorbance (C) Concentration of bound Sirius Red to collagen produced by NIH 3T3 fibroblasts, $n=3$.

4.2.4. Mouse fibroblasts cultured on electrospun gelatin exposed to flow conditions

After evaluating the effect of flow conditions using the electrospun polyethylene terephthalate scaffold, we moved onto the use of the electrospun gelatin scaffold. The end goal was to use the self-reporting scaffold whilst exposed to flow conditions for *in situ* pH monitoring. For the following experiments, electrospun scaffold without the incorporation of nanosensors were used so subsequent fluorescent staining could be performed. The Quasi-Vivo[®] 900 bioreactor system was used instead of the Quasi-Vivo[®]500 bioreactor, this is because the more fragile electrospun gelatin scaffolds needed to be secured by CellCrowns[™] to keep the scaffold flat and even, and also preventing the scaffold from collapsing. The Quasi-Vivo[®]900 bioreactor had to be used instead of the QV500, as the dimensions of the QV900 did not cater to the size of the CellCrowns[™]. Another advantage of the QV900 is that it has an optical imaging window which allows imaging of the electrospun gelatin scaffold which is useful for *in situ* monitoring.

For flow experiments, the cell-seeded gelatin scaffolds were positioned at various heights within the bioreactor as shown in Figure 4.8, this was to investigate the effect on cell proliferation. Figure 4.8A shows the electrospun gelatin scaffold secured by the CellCrown[™], Figure 4.8B shows the CellCrown[™] ring which can be stacked into the base of the QV900 to raise the height of the cells secured in the CellCrown[™] as shown in Figure 4.8C. Mazzei et al⁹⁵ showed with computer modelling, different heights of the early Quasi-Vivo[®] prototype created different levels of shear stress within the bioreactor, even at the same flow rate which could therefore affect cell behaviour. Figure 4.8D shows the cell seeded scaffold positioned at the bottom of the bioreactor, Figure 4.8E the cell seeded scaffold is placed in the middle of the bioreactor with no CellCrown[™] insert required, Figure 4.8F the two ring inserts have been placed into the base of the bioreactor to raise

the level of the cell-seeded scaffold to the top of the bioreactor so the cells are exposed directly to the flow.

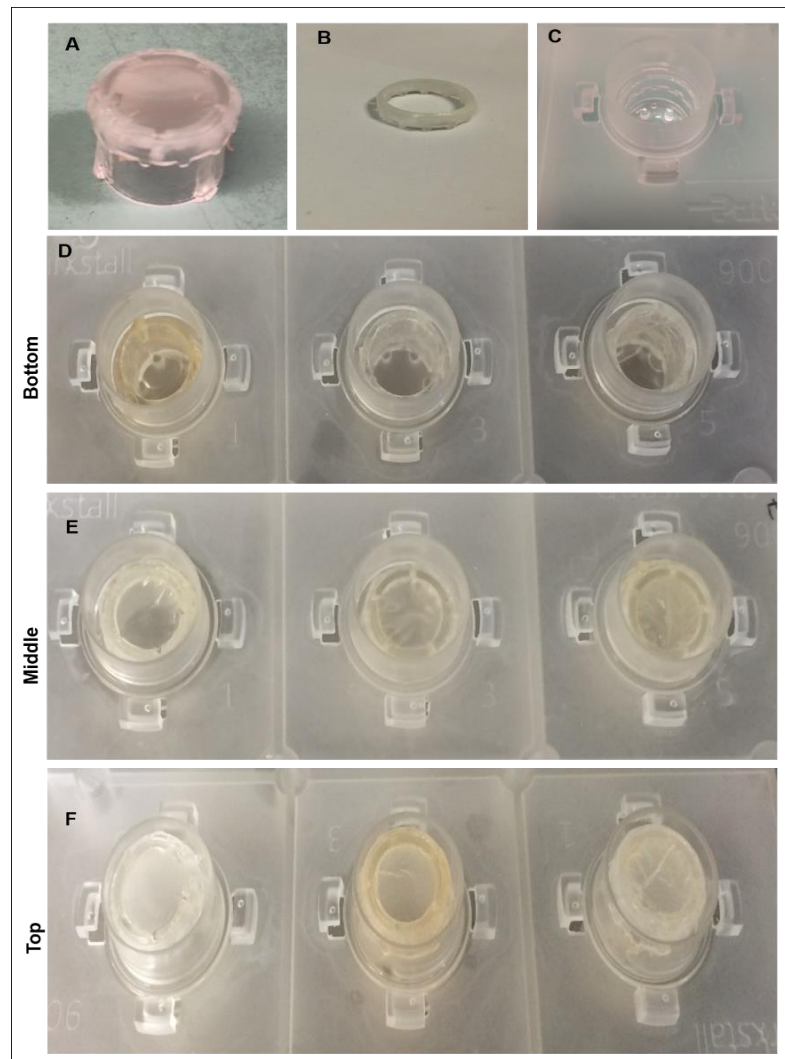


Figure 4.8 CellCrowns™ in the Quasi-Vivo®900 system, (A) electrospun gelatin scaffold secured by CellCrown™, (B) CellCrown™ ring, (C) CellCrown™ rings stacked into the QV900 well, (D) electrospun scaffold placed at the bottom of the bioreactor, (E) scaffold placed in the middle of the bioreactor, (F) scaffold placed towards the top of the bioreactor.

Figure 4.9 shows the scanning electron micrographs and proliferation rate of the fibroblasts cultured on the electrospun gelatin scaffolds whilst exposed to flow conditions. The experiments were set up for longer time periods of 7 days instead of 3/5 days to gain a better understanding of the long term effects of flow. The lowest flow rate of 8 μ L/min was used, this was based on the previous experiment using the

PET scaffold and mouse fibroblasts which showed a significant increase in the cell proliferation. Figure 4.9A shows scanning electron micrographs of the 3T3 fibroblasts seeded on the electrospun scaffolds whilst exposed to flow conditions. Cells in static conditions and cells positioned at different heights of the bioreactor were able to produce and deposit extracellular matrix proteins onto the scaffold. However, it would be useful if the ECM deposition was quantified, such as by a Sirius Red stain. Figure 4.9B shows a high magnification image of a 3T3 cell adhered to the electrospun gelatin scaffold. The AlamarBlue[®] data in Figure 4.9C shows the cells in the static conditions had a high increasing proliferation over the 7 day period compared to the flow conditions where cells were positioned closer to the flow exposure. Cells were able to proliferate when positioned at varied positions in the bioreactor. However, the cell proliferation was much higher when the cells are placed at the bottom of the bioreactor away from the direct impact to the flow, compared to the cells placed at the top. This could be because where cells are placed higher up in the bioreactor, closer the flow exposure they are exposed to a greater degree of shear stress which can cause cell detachment or compromise cell viability. However, the data from the previous experiment using the electrospun PET scaffold in Figure 4.6 showed a significant increase in proliferation, and these cells were placed at the top of the QV500 chamber.

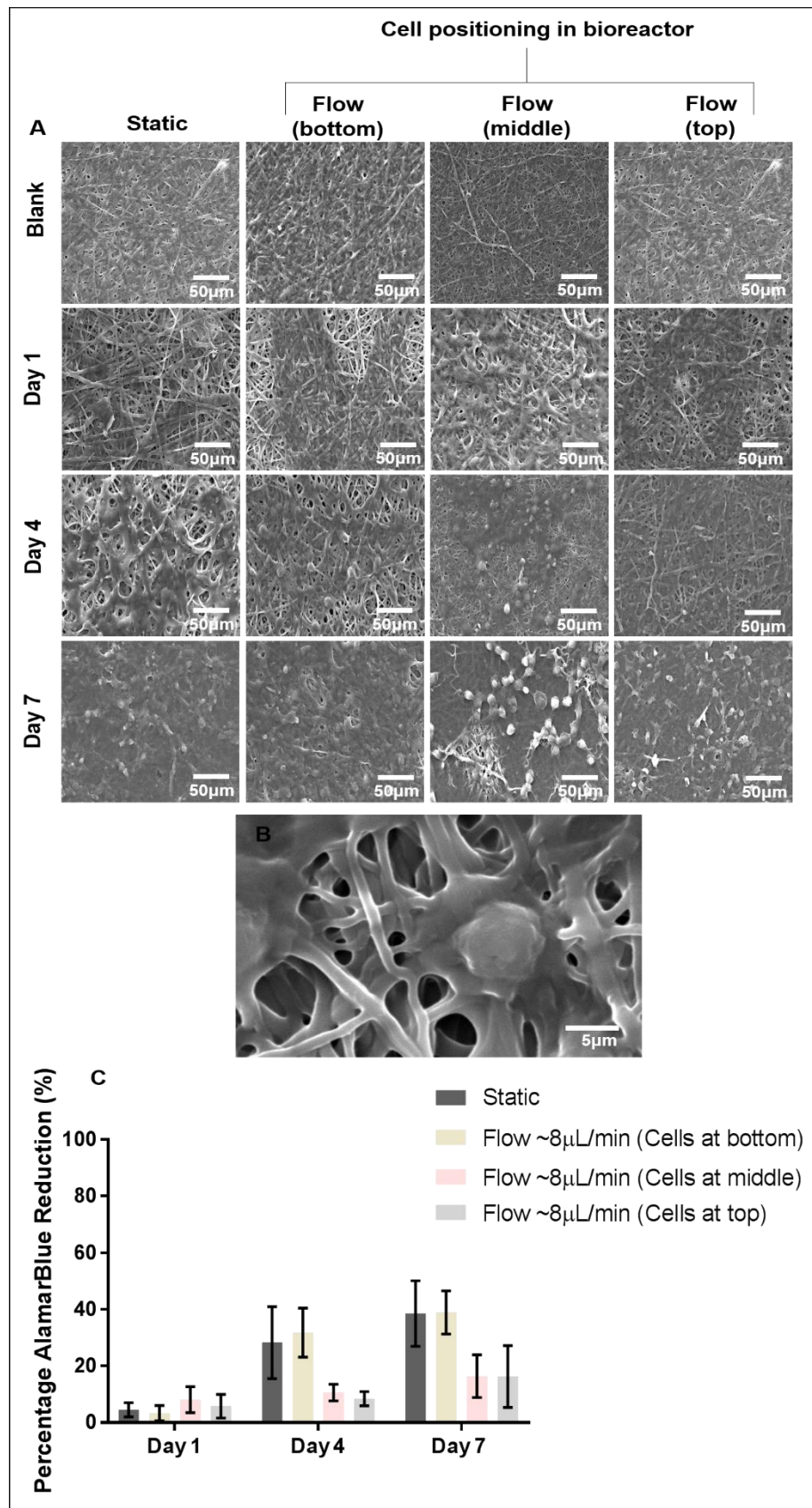


Figure 4.9 (A) High magnification $\times 500$ scanning electron micrographs of NIH 3T3 fibroblasts seeded on electrospun gelatin scaffold, (B) High magnification $\times 3500$ images of a fibroblast, (C) AlamarBlue proliferation assay comparing the proliferation of cells exposed differently to flow, $n=3$.

An F-actin cytoskeleton and nuclear fluorescent stain was also performed to observe cell distribution and morphology when cells were placed at the top of the bioreactor as shown in Figure 4.10. The fluorescent images in Figure 4.10A showed that the cells were not growing well with very few cells present after Day 4 and Day 7 when exposed to flow conditions, which agrees with the AlamarBlue[®] proliferation data in Figure 4.10B. The cells appear to have detached due to the flow conditions in compared to static. The poor proliferation is a surprising observation as a significant increase in proliferation of 3T3 fibroblasts was present when cultured on the PET scaffold in the QV500 bioreactor, in addition the fluorescent images showed cell attachment and even distribution. Furthermore, it would be expected that the cell attachment would prevail on the gelatin scaffolds as they are more biocompatible than synthetic polyethylene scaffolds. Reasons for the lack of cells under flow conditions could be due to several factors. Firstly, it could be due to the difference in properties between the QV500 bioreactor and the QV900 bioreactor. QV500 bioreactors are fabricated from gas permeable polydimethylsiloxane (PDMS) which allows diffusion of oxygen inside the bioreactors essential for cell survival²⁷⁸. In addition, the dimensions and configuration of the QV500 and QV900 is slightly different which could create differences in the shear stress applied to the cells. QV500 has a 1/16" inlet of tubing which is thinner than the 3/32" inlet of the QV900 bioreactor. Therefore with a bigger inlet, a greater shear stress could be applied to the cells. To confirm this theory, computer modelling should be performed in both the QV500 and QV900 as done by Mazzei et al⁹⁵ to model the shear stress.

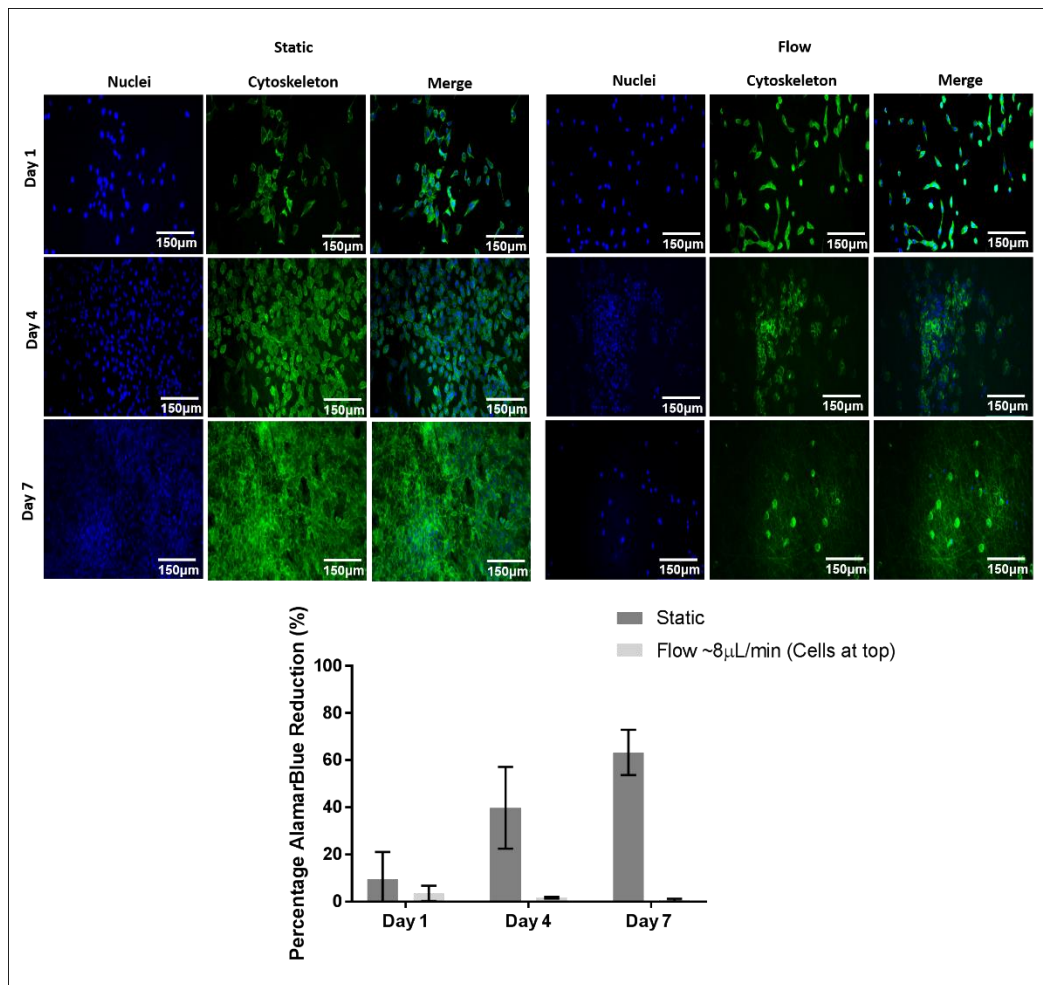


Figure 4.10 Fluorescently stained 3T3 fibroblasts cultured on gelatin scaffold whilst exposed to static vs flow conditions. Cells were placed at the top of the bioreactor and were exposed directly to the flow of medium at a rate of $8\mu\text{L}/\text{min}$, $n=3$, scale bar = $150\mu\text{m}$.

After the interesting results of the poor proliferation of the fibroblasts directly exposed to flow conditions, a different cell type was used. Human umbilical endothelial vein endothelial cells are adapted to exposure to high shear stress from the blood flow within the circulatory system. HUVECs were stained for F-actin cytoskeleton and nuclear stain which showed a reduced presence of cells as the culture time increased in both static and flow conditions as shown in Figure 4.11A. This was in agreement with the AlamarBlue[®] proliferation data which showed a decrease in both static and flow conditions in Figure 4.11B. Soliman et al²⁷⁹ demonstrated that different pore size and packing density of electrospun PCL fibres

significantly affect cell viability and proliferation. They found that microfibers with low packing density exhibited maximum cell adhesion and proliferation, which is what we would have expected to see.

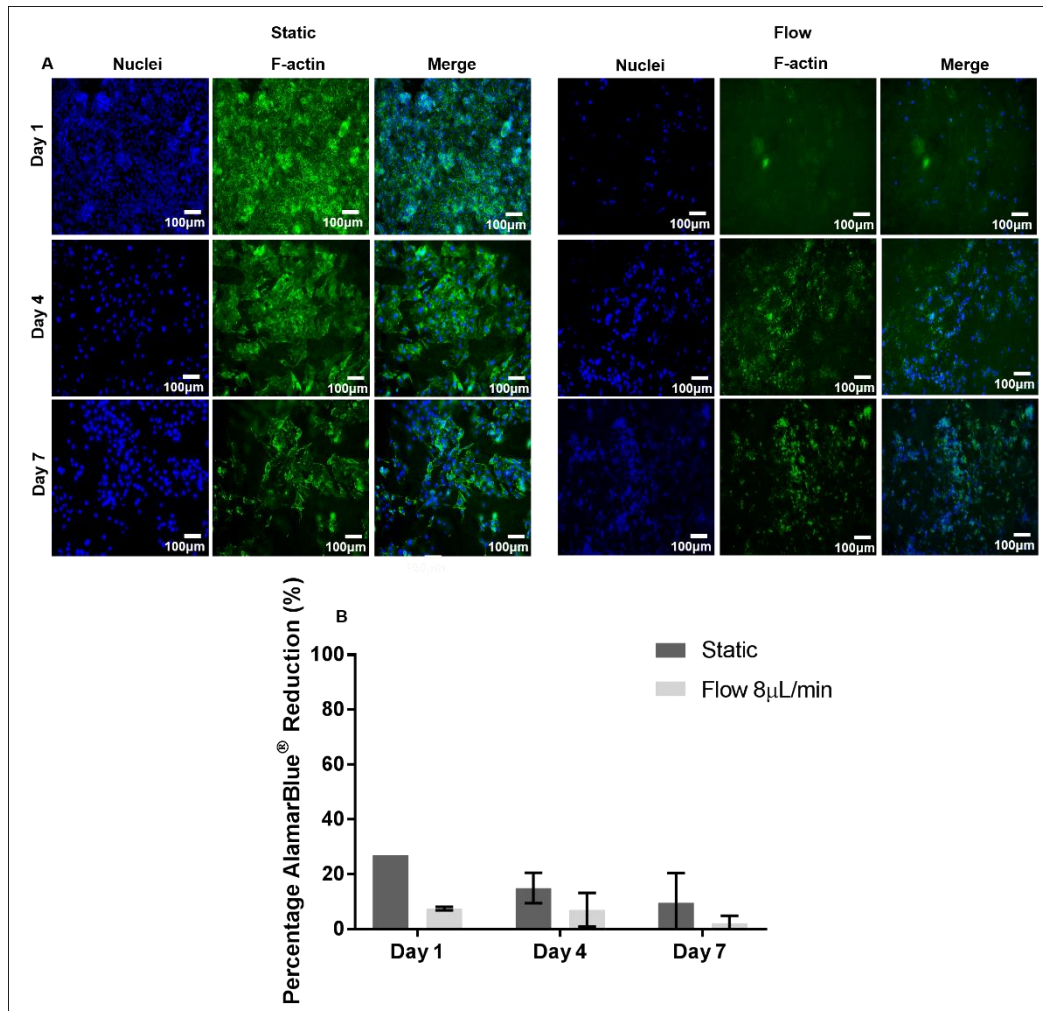


Figure 4.11 HUVECs seeded on electrospun gelatin scaffold exposed to a flow rate of 8 μ L/min, scale bar = 100 μ m.

4.2.5. Wound assays exposed to flow conditions

To further assess the effect of flow conditions on cell proliferation, a wound healing assay was performed initially in 2D and then on electrospun PET scaffolds. The wound healing assay is a common technique used to investigate cell migration and proliferation by measuring the rate of gap closure²⁸⁰.

4.2.5.1. Scratch assay on coverslips

The scratch assay involves creating a “wound gap” in a cell monolayer cultured in 2D by scratching with a sharp object. The “healing” of the gap by cell growth and migration towards to centre of the gap is monitored and quantified. Factors such as medium perfusion can alter the motility and/or growth of the cells leading to an increased or decreased healing of the gap²⁸¹. In this experiment, cells were cultured on acid-etched coverslips so they could easily be transferred into the bioreactors. Acid etching of coverslips is useful for adherent cells as it helps bind polypeptides to the glass subsequently promoting cell attachment. For flow conditions, a QV900 bioreactor system was used due to its optically transparent abilities. The coverslip was placed at the bottom of the bioreactor to allow *in situ* imaging through the optically transparent window at the base of the bioreactor, in turn providing images at different time points without the need for end point determination. Figure 4.12A shows a visual representation of the wound closure. The bright-field images shows the wound successfully recovered within 48 hours for both static and flow conditions with no distinct differences in the cell morphology. After 96 hours, cells exposed to flow conditions detached from the coverslip which may be due to the formation of a confluent sheet of cells which was pushed off the coverslip by the flow conditions. The percentage wound area was quantified using TScratch, which is an automated, simple analysis software tool developed by Gebäck et al²⁸² for wound healing assays. The software overcomes limitations of manual and highly subjective nature of open-area quantification by accelerating analysis using an automated, quantitative high-throughput system²⁸². The graphical user interface uses an analysis algorithm incorporated into MATLAB. Images are analysed by image segmentation and creating thresholds to accurately measure the grayscale area subsequently providing the percentage wound area of scratch assays. The reliability and reproducibility of the software prevents the need for manual time consuming

quantification of the wound areas. The percentage wound areas were quantified and displayed in Figure 4.12B, this shows a 0% wound gap area after 48 hours whilst exposed to static and flow conditions, in addition to no significant differences in percentage wound recovery in static vs flow conditions as determined by a T-test.

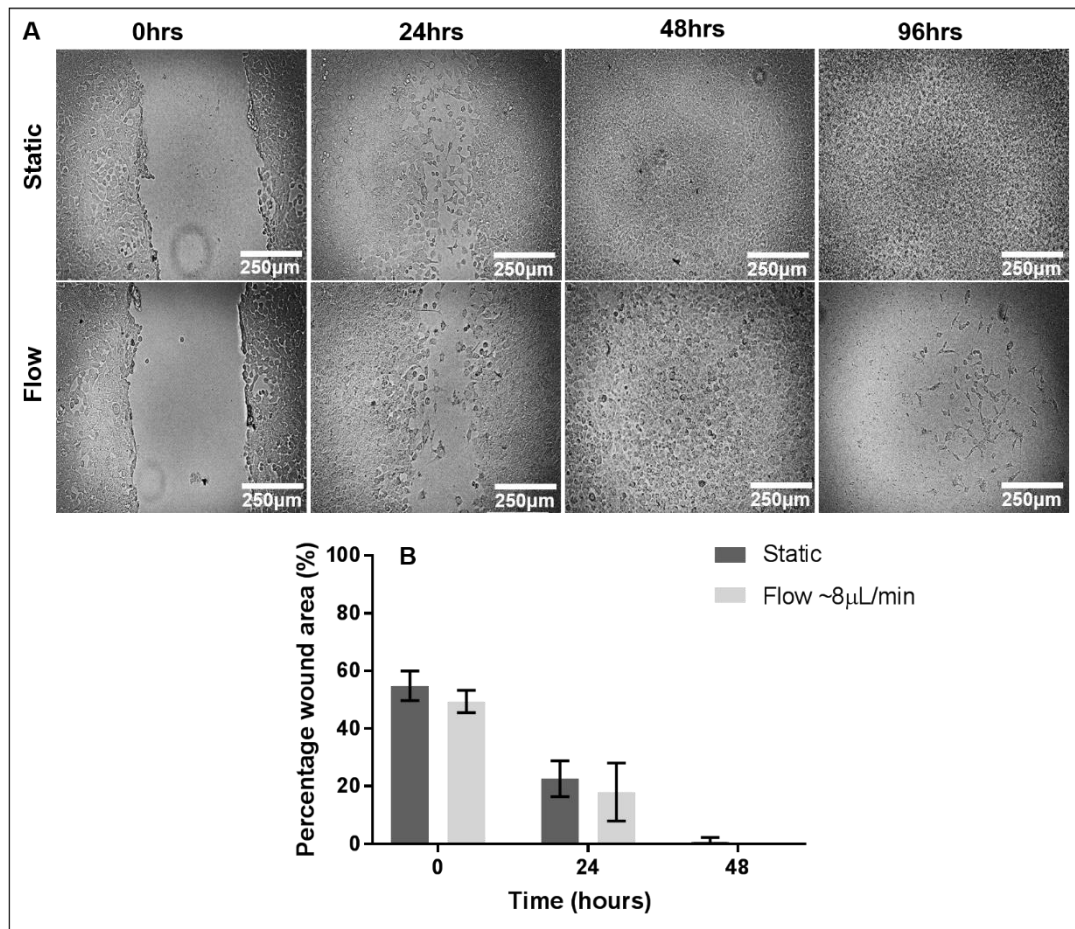


Figure 4.12 Wound closure in a scratch assay performed on confluent NIH 3T3 mouse fibroblasts on a coverslip by scratching with a 200µL pipette tip. (A) shows bright field microscopy images of the extent of the closure under static vs flow conditions, (B) quantifies the percentage wound closure calculated using TScratch software, no significant differences were observed, $n=3$, scale bar = 250µm.

To obtain a more informative understanding of the wound gap closure, a time-lapse experiment was performed to monitor the wound closure more frequently. In order to obtain higher contrast images, 3T3-GFP cells were used. A time-lapse experiment involves automatic acquisition of images at set time intervals using a microscope. A cover was placed over the dish containing the cell-seeded coverslip to maintain the carbon dioxide levels and the temperature at 37°C. Initially time lapse images were

acquired in static conditions only, images were acquired every 6 hours on the brightfield and fluorescent channels as shown in Figure 4.13. Again by 48 hours, the time lapse images show the successful gradual wound closure.

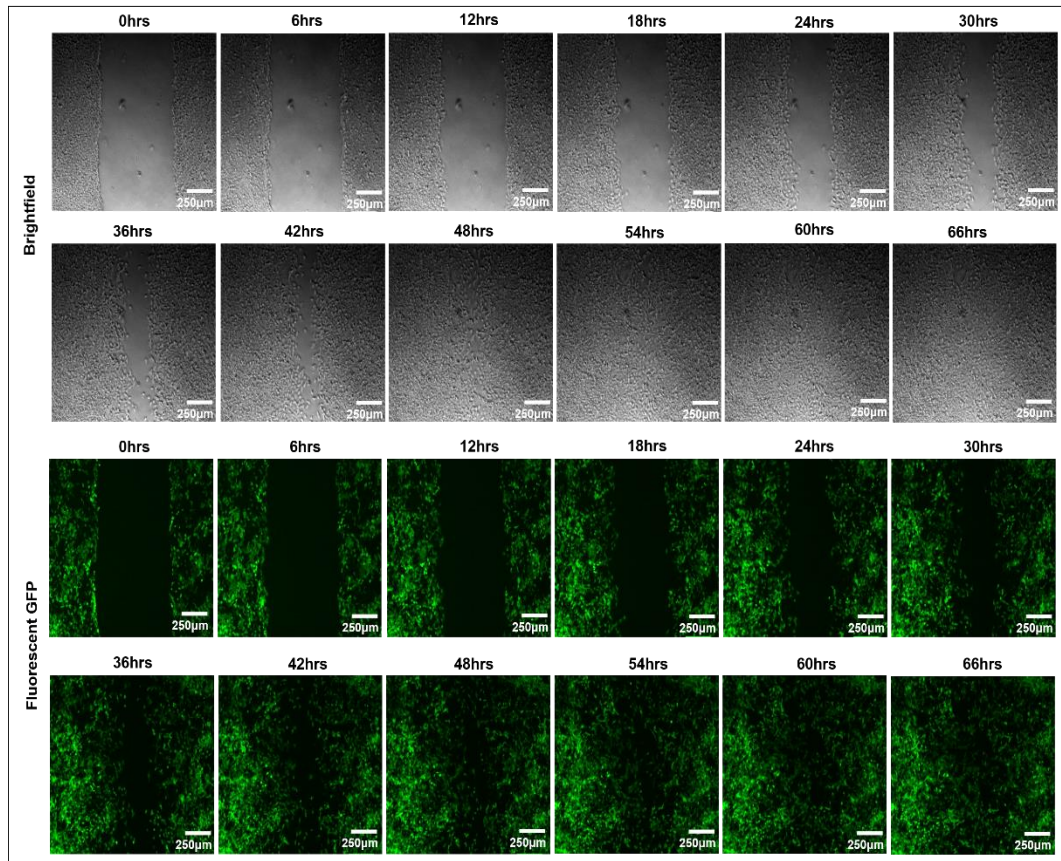


Figure 4.13 Brightfield and fluorescent time-lapse images of scratch assay performed on 3T3-GFP cells on a coverslip at x5 magnification, $n=1$, scale bar = 250 μm .

The next step was to demonstrate the ability to monitor the wound recovery in real time whilst exposed to flow conditions. However, in order to acquire time-lapse images whilst exposed to flow conditions, instrument modification would have been required to monitor the carbon dioxide levels. This is because of the geometry of the QV900 is non-standard and is not compatible with the carbon dioxide cover/supply. Overall, when developing physiologically relevant *in vitro* models with the ability to monitor *in situ*, there are often limitations that come with it.

4.2.5.2. Scratch assay on electrospun scaffold

After successful wound closure of the scratch assay performed on the coverslip, the technique was attempted on an electrospun scaffold. The electrospun scaffold was also combined with flow conditions to investigate the effect of flow on wound closure. A confluent layer of 3T3 cells were grown on the PET scaffold, and a scratch was performed across the centre of the scaffold using a pipette tip. An F-actin cytoskeleton was used to stain the cells for observation, and images were acquired using a fluorescent microscope at x2.5 magnification, the images were stitched together using Volocity software. Figure 4.14A shows the scratches were not as defined and reproducible as the 2-Dimensional assays performed on the coverslips. This may be due to the rough topography of the scaffold compared to the smooth coverslips. Figure 4.14A shows the wound gap in both static and flow conditions did not recover over the 48 hour period, although there was a prominent recovery when cultured on coverslips shown in Figure 4.12. To investigate this further, scanning electron micrographs were acquired as shown in Figure 4.14B. The SEM images show that cells are attempting to migrate across the wound area but stop at the edge which may be due to a change in the topography of the scaffold which appears to slope in the area of the scratch. An explanation for this could be because topography affects the arrangement of integrins found on the cell membrane of cells, subsequently affecting the formation of focal adhesions²⁸³. Integrins are heterodimeric transmembrane receptors that mediate cell adhesion to membranes²⁸⁴. They are nano-meter sized in range which enables them to distinguish topographic changes down to the nanometer scale²⁸³. Cells interact with topographical features through contact guidance. During initial adhesion to the micro-environment, cells use membrane protrusions such as filopodia and lamellipodia as contact guidance to probe and migrate along the surface²⁸³. On patterned surfaces, the distance between each topographical feature affects

whether the cell can sense the micro-environment. If the distance between each topographical feature is larger than what the filopodia can sense, the cell cannot establish focal adhesions, hence impairing cell migration and proliferation²⁸³. The topography can also affect the force balance between the cells and the construct by constraining the cell, actin cytoskeleton and integrin molecules at different levels. The mechanical perturbations are transmitted across the plasma membrane through transmembrane receptors directly inside the cytoplasm and change conformation of the actin cytoskeleton which can be indirectly converted into biochemical relevant signals activating subsequent pathways²⁸⁵. Rho-ROCK-Myosin pathway is involved in sensing topographic cues which has been shown to reduce proliferation²⁸⁶ and affect cell motility²⁸⁷. Therefore, further investigations into the pathways could be performed to provide a better understanding for the insufficient wound closure.

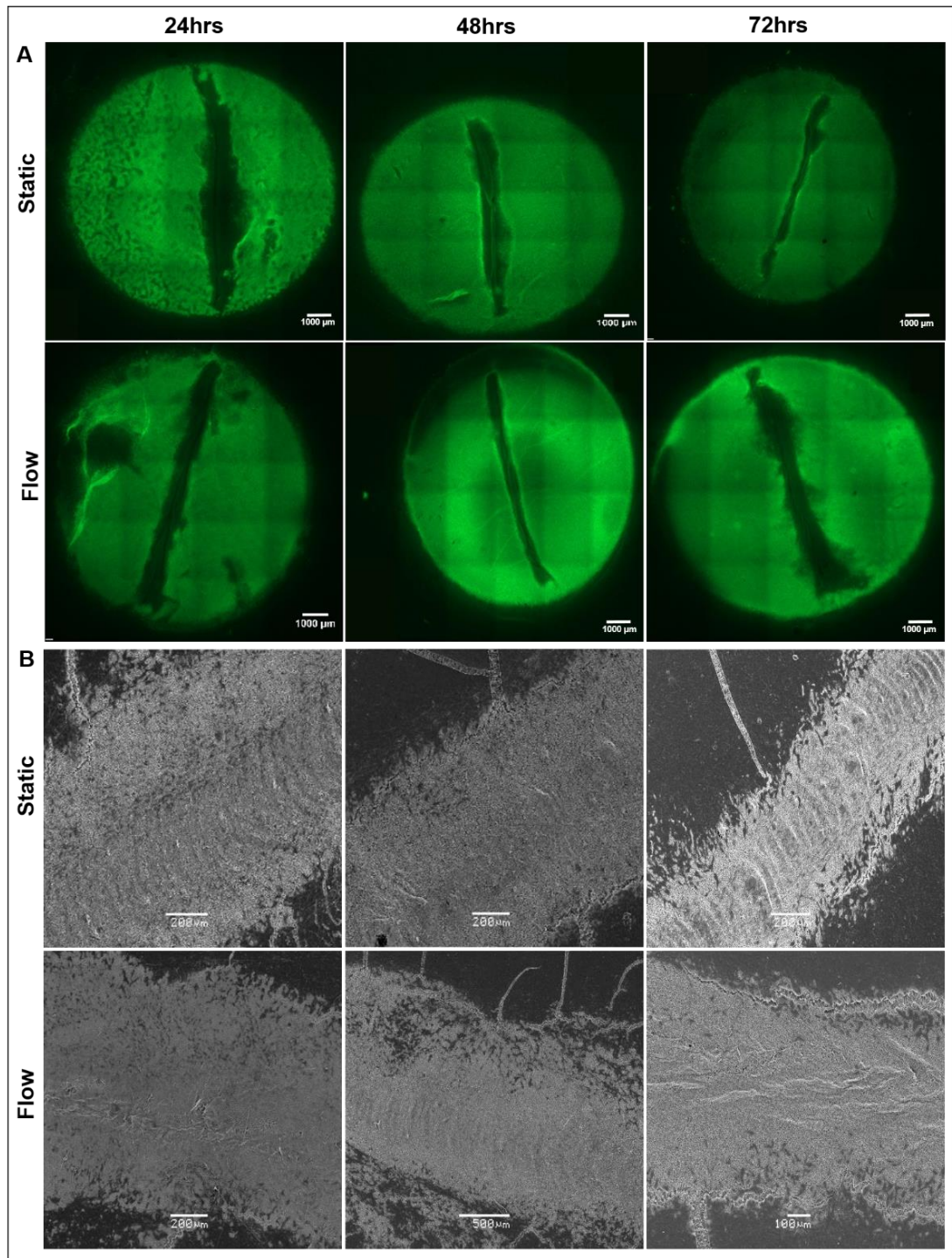


Figure 4.14 Wound healing scratch assay performed on confluent NIH 3T3 mouse fibroblasts seeded on electrospun polyethylene terephthalate scaffold using a 200 μ L pipette tip. (A) Cells fixed and stained with AlexaFluor488 phalloidin shows extent of wound closure under static vs flow conditions (B) Representative scanning electron microscopy images shows attempted migration of cells into the wound area, n=3.

4.2.5.3. Chemical wound assay

Due to the inability of cells to recover the wound area in the scratch assay performed on the electrospun scaffold thought to be a result of a change in topography, an alternative chemical wound assay was performed to compare the rate of wound gap closure between static and flow conditions. The technique for the chemical wound assay was adapted from a method used in animal models for developing treatments for corneal burns. Yifeng et al²⁸⁸ soaked 6-mm filter paper in 1M sodium hydroxide solution and placed it on the centre of the cornea for 30 seconds, fluorescein staining was used to measure the epithelial defect areas after fixation. In comparison to their *in vivo* study, much lower concentrations of 1mM sodium hydroxide were chosen for our *in vitro* wound assays on the scaffold due to the presence of a single, delicate layer of cells. The concentration chosen was not too harsh that the cells could not recover, and not too weak that the cells are not injured sufficiently to create a wound gap area. Separate scaffold samples were used to image, fix and stain the cells at different time points which stresses the importance of reproducibility of the wound area if comparing the rate of gap closure between static and flow conditions. Figure 4.15 shows on Day 1 exposed to static conditions, the wound area is much larger than it should be, as the filter paper size is 5mm. The large wound area may be due to spreading of residual sodium hydroxide from the filter paper which subsequently kills the cells. Due to the inconsistency of the wound gap production, the data between the static and flow conditions is not directly comparable. Although it can be observed that under flow conditions, the cells appear to be migrating over the gap area more compared to static conditions. However by the end of the 5 day period, the wound gap did not recover for either static or flow conditions and so the wound assay was repeated with a smaller piece of filter paper to create a smaller wound area for full wound gap closure.

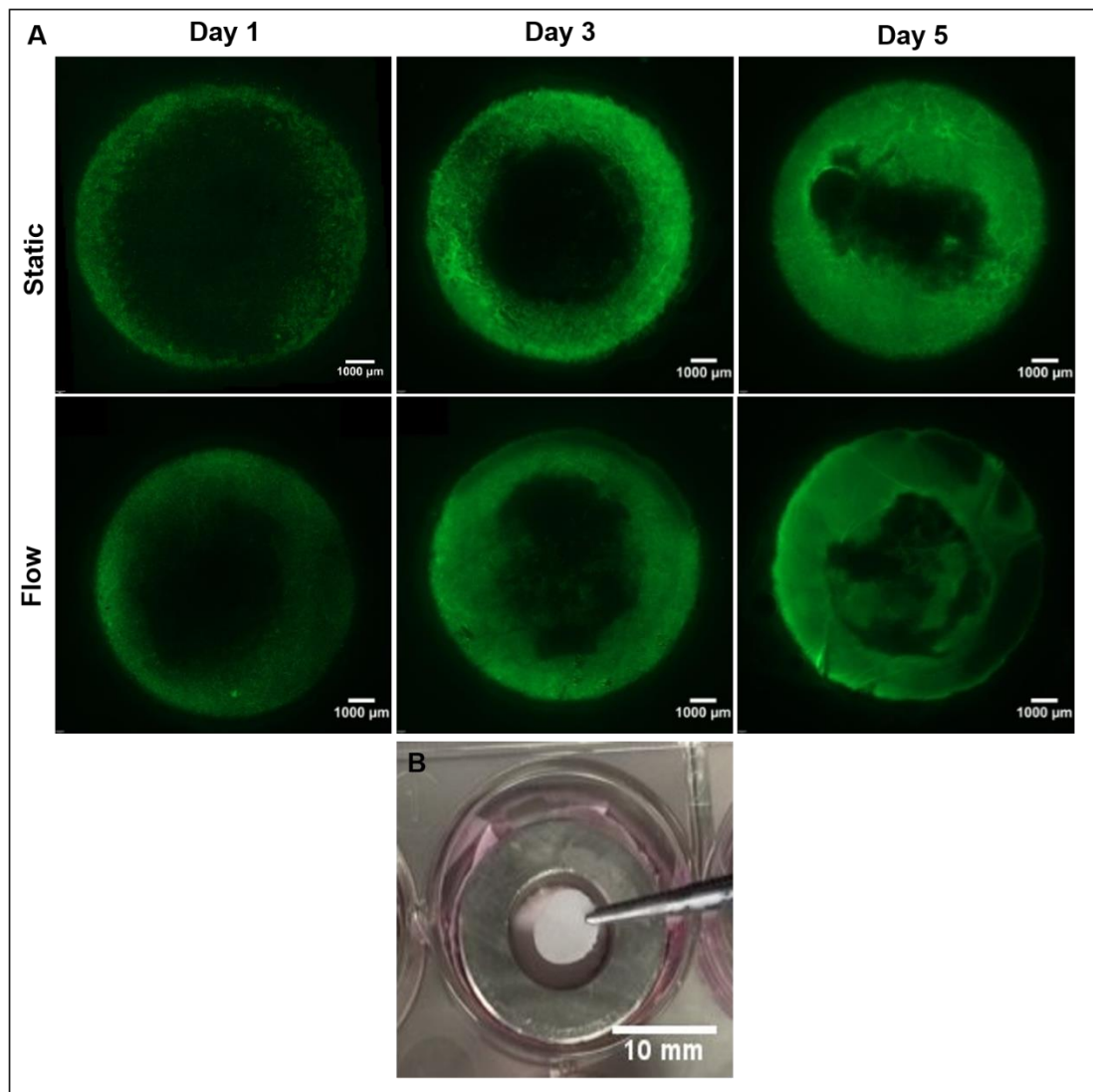


Figure 4.15 (A) Fluorescent images of 3T3 fibroblasts stained with Alexa-Fluor488 phalloidin. Chemical wound assay performed on confluent layer of cells seeded on electrospun polyethylene terephthalate scaffold. Wound area is depicted by the black area in the centre of the cell-seeded scaffold, scale bar 1000 μ m, data shown is representative of $n=3$ experiments, (B) Visual representation of chemical wound assay, 5mm filter paper soaked in 0.1mM sodium hydroxide and placed in centre of cell-seeded scaffold.

The chemical wound assay was repeated, however a smaller 5mm filter paper cut in half was used to reduce the size of the wound area to achieve full gap closure. However, Figure 4.16 shows even with a reduced size of the wound, the gap has not fully recovered in both static and flow conditions. It appears that by Day 5 for the static conditions, the wound area has recovered more compared to flow conditions. This was not the expected result, as previous data acquired in Figure 4.6B showed

a significant increase in proliferation when exposed to flow conditions. However, again due to the lack of reproducibility of the wound, the wound area could have been larger than it should have been, which could be why the wound gap has not recovered.

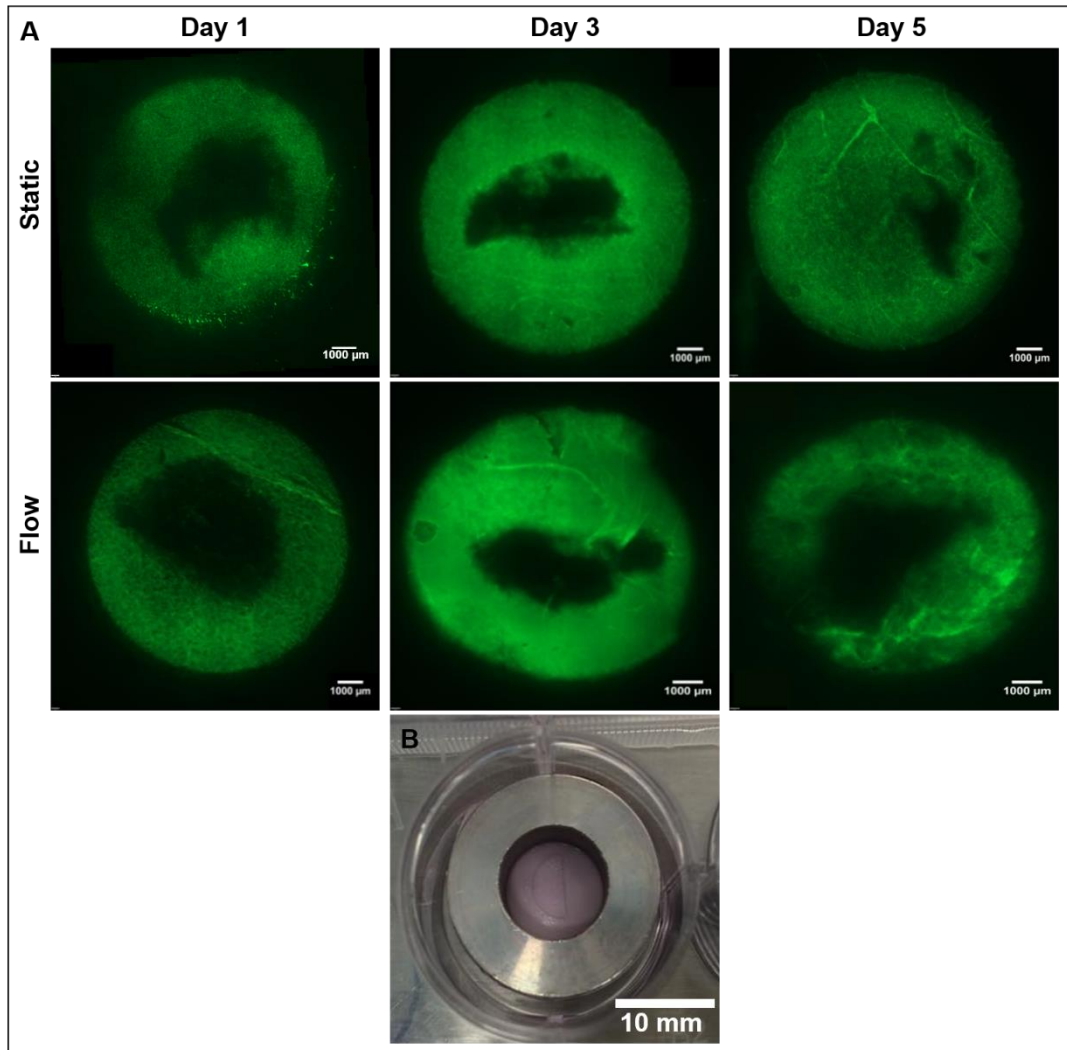


Figure 4.16 (A) Fluorescent images of 3T3 fibroblasts stained with Alexa-Fluor488 phalloidin. Chemical wound assay performed on confluent layer of cells seeded on electrospun polyethylene terephthalate scaffold. Wound area is depicted by the black area in the centre of the cell-seeded scaffold, scale bar = 1000μm, data shown is representative of n=3 experiments (B) , (B) Visual representation of chemical wound assay, 5mm filter paper cut in half soaked in 0.1mM sodium hydroxide and placed in centre of cell-seeded scaffold. Data shown is representative of n=3 experiments.

Due to the inconsistency of the wound gap area, different types of wound assays were performed to try and produce a reproducible wound area. A confluent layer of cells were grown on PET scaffolds, exposed to an injury and then fixed and stained

to show the extent of the wound. One of the types of injuries performed involved a burn, by heating a needle on a Bunsen burner for 3 seconds and then placing directly onto the scaffold for 3 seconds to burn the cells. However row A of Figure 4.17 displays a lack of reproducibility of the wound area. Another issue with this method was that the hot needle sometimes melted the scaffold leading to a likely change in the structure of the fibres. In addition, due to the small surface area of the needle, it heated up very quickly preventing precise control of the temperature. Other work involving a burn wound assay includes a study by Fernandes et al²⁸⁹. In this study, they used a microwave to induce thermal injury in 3T3 fibroblasts seeded on a glass dish, to investigate changes in their morphology and viability. This technique was found to be reproducible, however the recovery of the cells after injury was not investigated. Another wound assay method involved using 2mm x 2mm filter paper squares, soaking it in 0.1mM sodium hydroxide and using tweezers to place it on the scaffold for 3 seconds to create a small wound area. The fluorescent images in Figure 4.17B shows the formation of distorted squares which were not reproducible. Another wound method involved placing a filter paper strip (2mm x 5mm) soaked in sodium hydroxide carefully across the scaffold for several seconds which was easier to manually handle, however Figure 4.17C shows this did not create a reproducible wound area. Lastly, a cotton bud was soaked in sodium hydroxide and placed in the centre of the scaffold for 3 seconds. The fluorescent images in Figure 4.17D using the cotton bud technique displays a similar wound gap area. Therefore the wound assay using the cotton bud was performed and cultured over a period of 7 days to monitor the wound recovery.

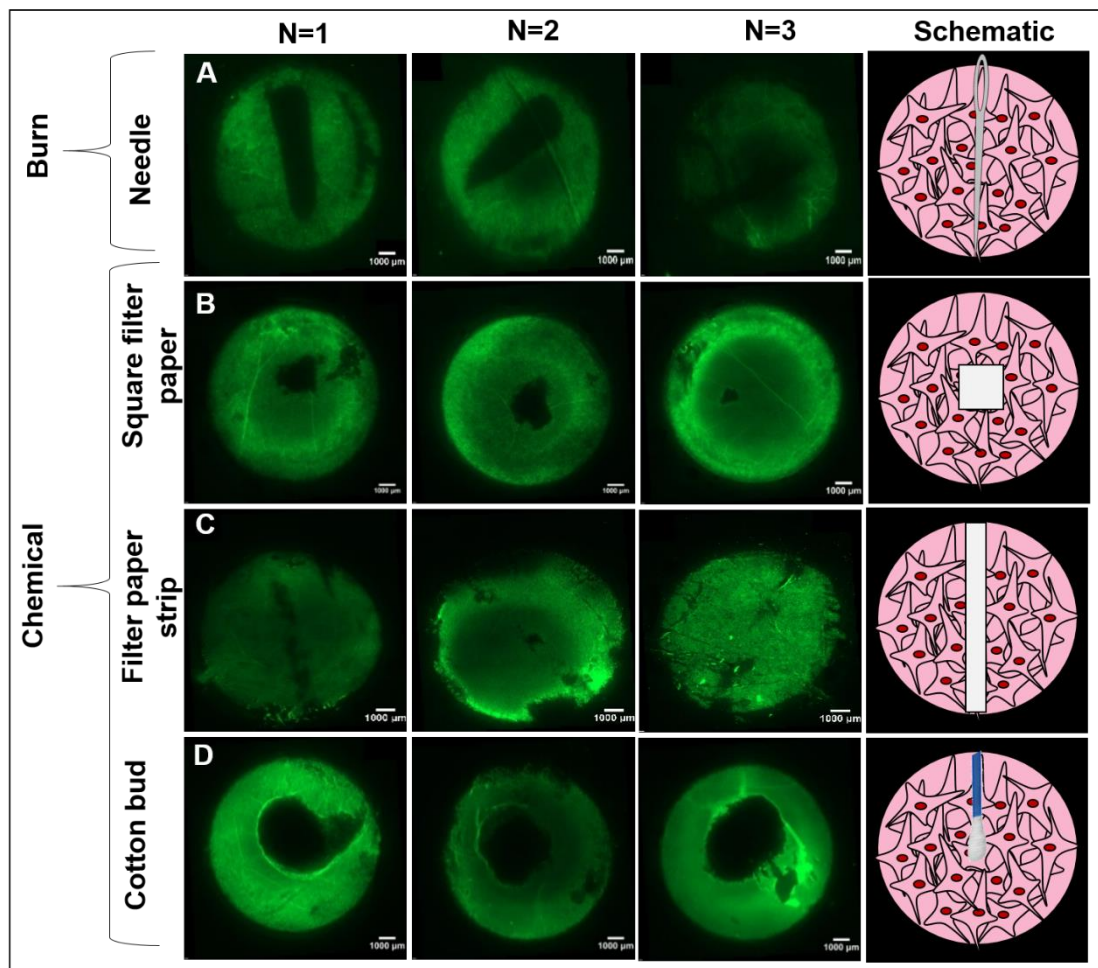


Figure 4.17 Fluorescent images of 3T3 fibroblasts stained with Alexa-Fluor488 phalloidin. Various wound assays performed on confluent layer of cells seeded electrospun polyethylene terephthalate. Wound assays include a burn assay using a needle, and chemical wound assays using different sized filter paper and cotton bud soaked in 0.1mM sodium hydroxide. Wound area is depicted by the black area in the centre of the cell-seeded scaffold, n=3. Schematic shows visual representation of performed wound assay (not to scale).

However, after repeating the chemical assay using the cotton bud, Figure 4.18 shows that the wound was unable to recover which may be due to physical trauma when placing the cotton bud on the scaffold or potentially uneven wound areas. Therefore, developing a chemical assay with high reproducibility on electrospun scaffolds is very challenging and requires further investigations/optimisation.

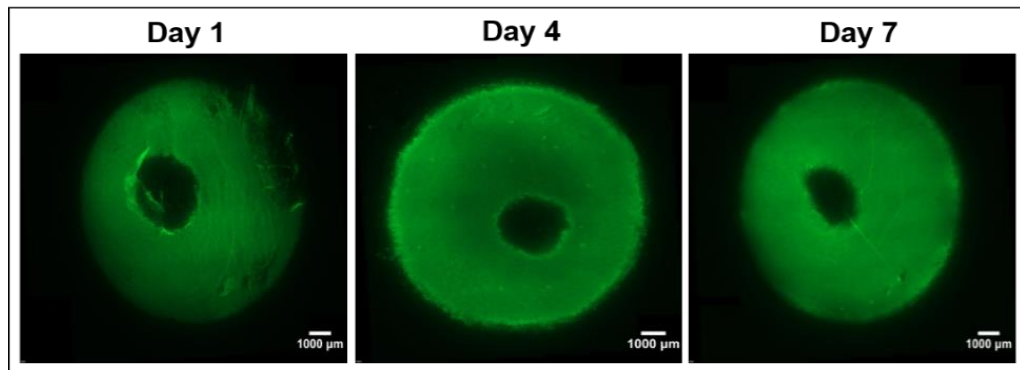


Figure 4.18 Cotton bud assay. Fluorescent images of 3T3 fibroblasts stained with Alexa-Fluor488 phalloidin. Cotton bud soaked in 0.1mM sodium hydroxide assay performed on confluent layer of cells seeded electrospun polyethylene terephthalate. Wound area is depicted by the black area in the centre of the cell-seeded scaffold, data shown is representative of $n=3$ experiments.

4.3. Conclusions

The data showed that at higher flow rates in the QV500, cell growth on electrospun scaffolds was compromised, as demonstrated by the lack of cell attachment to the scaffold. This is thought to be a result of the turbulence created due to the fluidic dynamics within the Quasi-Vivo[®]. At lower flow rates, using the QV500, and a more robust 3T3 cell line seeded on electrospun PET scaffolds, a significant increase in proliferation was observed compared to static conditions. This may be due to the enhanced nutrient and oxygen diffusion throughout the scaffold. However, exposing the 3T3 fibroblasts seeded on the electrospun gelatin scaffolds to flow conditions in the QV900, cell proliferation was compromised compared to static conditions. This may be because the dissimilar geometry of the perfusion systems and scaffolds can vastly differ in the local shear stresses experienced by the cells, even for the same input flow rate²⁹⁰. A successful scratch assay was performed on coverslips, which showed wound closure after 48 hours whilst exposed to flow conditions. At 96 hours however, cells detached from the scaffold which may be due to the flow conditions pushing the cell monolayer off the coverslip. However, data showed that creating a reproducible wound model on electrospun scaffolds is very challenging compared to the 2-Dimensional scratch assay and requires further optimisation and investigation.

Chapter 5 *In situ* pH measurements using self-reporting scaffolds

Many tissue engineers currently use invasive techniques or end point determination in order to monitor the extracellular pH of the microenvironment. Our aim is to improve current methods by developing a self-reporting scaffold to allow monitoring of long term cultures over time without the need to sacrifice the samples or introduce invasive techniques. In addition due to the existence of chemical gradients scaffolds, being able to quantify the local pH in specific regions is crucial, as it plays an important role when monitoring the conditions required for optimised cell growth. As discussed in Chapter 2, we have developed a novel technique for acquiring non-invasive pH measurements, whilst simultaneously utilising a platform which recreates the structural features and microenvironment of the extracellular matrix. In this Chapter, the scaffold will be used to acquire local pH measurements and used to measure the extracellular pH of long term cultures. This was not performed under flow conditions due to the lack of reproducibility of the results obtained.

5.1. Introduction

5.1.1. Importance of extracellular pH

Tissue engineering is a complex process which requires close monitoring at all stages of growth. Within a tissue, not only are cells surrounded by an extracellular matrix, they are bathed in an extracellular fluid which keeps the tissue hydrated and maintains homeostasis in different organs. The fluid contains nutrients, waste

metabolites and ions such as sodium (Na^+), chloride (Cl^-) and hydrogen (H^+) which are regulated within a certain range of values/concentration. Disruption of this homeostasis is considered to be a diseased state²⁹¹. The normal physiological extracellular pH of living tissue is maintained at pH 7.4²⁹², due to the continuous production and consumption of acids and bases by cells through chemical reactions²⁹³. However, the pH can vary due to changes in nutrition and oxygen supply, reprogramming of metabolic pathways and exocytosed protons/acid metabolites by cells, which results in acidification of the extracellular microenvironment²⁹⁴. Diseased tissues are often associated with lower extracellular pH, for example tumour tissues are associated with an acidic extracellular pH between 6.2– 6.9²⁹⁵, due to the production of acidic metabolites such as lactic acid as a result of anaerobic glycolysis in hypoxia²⁹⁶. Being able to monitor the acidic microenvironment is important because it has been shown to be a regulator of cellular phenotype²⁹⁶, and can affect tumour properties, including adhesion, migration, and drug resistance²⁹⁵. Therefore being able to accurately quantify extracellular pH of the microenvironment is important in providing insight into diseased states and optimal culture conditions. The extracellular pH can also be manipulated by modifying the H^+ diffusivity or buffering capacity as a target for therapy, instead of current methods that adjust the intracellular pH by targeting membrane bound transporter proteins²⁹³.

5.1.2. Techniques for monitoring extracellular pH

The pH of a solution specifies the acidity or basicity of an aqueous solution which indicates the concentration of hydrogen ions present. Many pH sensors come in a variety of forms and are used in many different biological and chemical applications. Most of the techniques used for pH monitoring can be invasive, and can introduce a

heightened risk of contamination into biological cultures or disturb the cellular microenvironment. One of the earliest methods of pH measurement involved the use of chemical indicators such as litmus paper, which changes colour during exposure to a particular pH, for example when litmus is added to a basic solution it turns blue, whereas when added to an acidic solution it turns red²⁹⁷. However, this type of method is not quantitative and lacks sensitivity.

5.1.3. pH electrodes

One of the most popular current approaches to pH sensing involves the use of pH electrodes, due to its high selectivity for hydrogen ions in solution, ability to measure small volumes, reliability and simplicity in use²⁹⁷. Commercial pH electrodes are usually combined with a reference electrode with a sensor¹⁶¹. Some of the advantages and limitations of pH probes have been reviewed by Monk²⁹⁸. If the electrode has been recently calibrated, the pH electrode will give a very rapid, accurate response. Purchasing electrodes are relatively cheap and draws a minimal current. The glass membrane of the electrode is chemically robust, however the glass is very fragile and can break²⁹⁸. Limitations associated with the pH electrode include constant re-calibration, if not done correctly this can lead to inaccurate pH measurements. Electrodes should be washed thoroughly between each use, and are susceptible to electrical interference and corrosion by alkaline solutions or fluoride ions limit its usefulness^{220,297}. The use of pH electrodes include monitoring the extracellular pH of tumours *in vivo*²⁹⁹, however pH electrodes are very invasive and when being used in tissue engineering applications, and can disturb the cellular microenvironment and introduce potential contaminants. Page 73 explains the principle behind how a pH electrode works.

5.1.4. Optical pH sensors

More recently, the development and use of optical pH sensors has become apparent. Their sensing ability is based on reversible changes in the indicator's structures induced by pH and translated into changes in spectroscopic phenomena such as absorption and fluorescence²⁹⁵. Optical sensors work by passing a beam of light through a light guide towards the end containing the sensor, interactions with the sensor alters the beam's intensity by absorption or fluorescence which is then monitored by a detector. Most fibre optic sensors utilise chromophores or indicator dyes, which are immobilised on part of the optical fibre resulting in pH sensitive changes within the fluorescence/absorption spectrum. Ionophores can be used to reversibly bind the electrolyte ions, which are incorporated into thin polymer films deposited at the end of an optical fibre, a lipophilic pH indicator is also added to the film. During the selective extraction of the ions, the pH indicator loses a proton to the sample to maintain charge neutrality in the film which results in a change of absorbance/fluorescence³⁰⁰. Disadvantages of using this technique is the sensitivity of the device which is related to the thickness of the pH sensitive layer²⁹⁷, in addition to the limited dynamic measurement range compared to electrochemical sensors³⁰⁰.

5.1.4.1. Fluorophores

Fluorescent pH sensors are also very popular, due to their high sensitivity and throughput, commercial availability, excellent spatiotemporal resolution, in addition to applications in 3D and *in vivo* biosensing²⁹⁵. The sensors come in the form of organic dyes, nanoparticles, and fluorescent proteins which act mainly as intracellular rather than extracellular pH indicators due to their easy entry into cells²⁹⁵. Fluorophores used for pH sensing should possess properties such as: excellent photostability, large Stokes shifts, and high quantum yield for optical

sensing²²⁰. However the use of fluorophores exposes the risk of non-specific binding, photobleaching and potential cytotoxicity of the dyes²²³.

5.1.5. Self-reporting scaffolds

As discussed in section 3.2, self-reporting scaffolds can be used for monitoring extracellular pH. There are several advantages of using self-reporting scaffolds compared to conventional methods of measuring pH. These include; pH can potentially introduce contaminants into cultures, in addition the probe can be invasive due to its large size, which can disturb the cellular microenvironment and affect cell activity. By incorporating miniaturised pH sensing nanosensors into scaffolds, the local pH of the cellular microenvironment can be monitored *in situ* and real time. This is important because it avoids end point determination of long term cultures, and the ability to monitor over long periods of time. After the successful development of the electrospun self-reporting scaffold in Chapter 3, this will be used to acquire local extracellular pH measurements of the cellular microenvironment.

5.2. Results & Discussion

5.2.1. Monitoring pH gradients using self-reporting scaffolds

Having demonstrated that the polyacrylamide nanosensors could be incorporated into electrospun gelatin fibres to create a responsive self-reporting scaffold in Chapter 3. The next step was to demonstrate the ability to acquire local pH changes in specific regions of the scaffold. Being able to monitor and control gradients of parameters such as oxygen and pH, is important in providing insight into producing 3D cultures with high cell viability³⁰¹ Self-reporting gelatin scaffolds and nanosensors suspended in water were calibrated by submerging in different pH buffers and using the same microscope settings to acquire fluorescent images as described in section 2.3.6. Automated image analysis was performed using MATLAB to convert the fluorescent ratiometric intensities of individual pixels to a corresponding colour to represent a specific pH as described in section 2.3.3.2.3. Figure 5.1 shows that using the MATLAB software, pH heat maps can be accurately produced for both the scaffolds and sensors. A pH heat map is a graphical representation of data where the individual values contained in a matrix are represented as colours. Figure 5.1A shows the pH could be accurately quantified as demonstrated by the clear colour change displayed in the heat maps as the pH is varied from pH 3.5 – 8.0. To enhance the distinction between the different pH values, upon scaffold calibration, the constructs were thoroughly washed and resuspended in the buffers to help push the hydrogen ions through the fibres for interaction with the nanosensors. At the lower and upper pH sensitivity boundaries pH 3.5 and pH 7.5 of the pH responsive fluorophores, it is clear to see in Figure 5.1A that there are black regions in the images. This is because the measurements are out of the pH sensing range. Figure 5.1(B-C) display the ratiometric calibration of the curves, achieved by taking a ratio

of the fluorescence response of pH-sensitive and pH-insensitive channels (λ_{em} 520 nm/ λ_{em} 577 nm) from the sensors and scaffolds suspended in buffer respectively. Both of which display the typical sigmoidal shape of the curve as expected. The scaffold ratiometric curve in Figure 5.1C displays slightly higher error (standard deviation) compared to the nanosensors in suspension, this could be due to residual buffers found on the scaffold from previous washes slightly altering the ratiometric intensities. In addition, due to imaging through the scaffold at different focal planes and imaging areas that may be uneven and out of focus, error could be introduced.

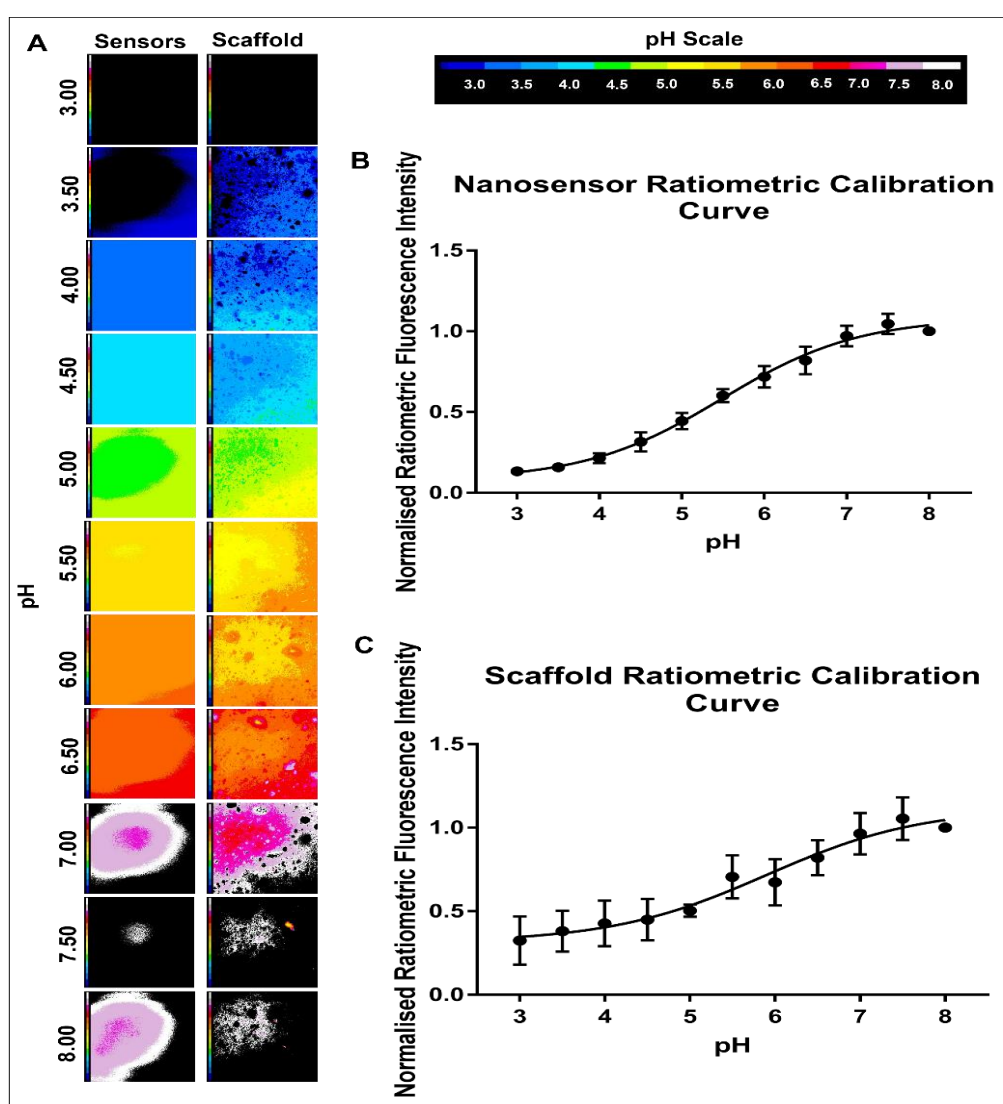


Figure 5.1 Calibration of polyacrylamide nanosensors in suspension and self-reporting scaffolds respectively submerged in different buffers, (A) pH heat maps produced using MATLAB, (B) Ratiometric calibration curve of nanosensors in suspension, (C) Ratiometric calibration curve of scaffold. Data shown is representative of $n=3$ experiments.

After showing the scaffolds can be calibrated showing a clear pH change in the heat maps, the ability to measure pH gradients was investigated. To display the gradient effect, and the ability of the dye to spread out over a small area, a small drop of green dye was placed in the centre of the scaffold, a small piercing was made in the centre of the scaffold as a reference point. Figure 5.2A shows that 2.5 μ L was a suitable volume to create a pH gradient across the scaffold as the dye spreads out across the centre of the scaffold. A small drop of hydrochloric acid of pH 2 was then placed on the centre of a self-reporting scaffold and imaged at the edge of the piercing using fluorescent microscopy to capture the pH gradient. As shown in Figure 5.2B, a pH gradient was observed with the addition of the acid, however it would have been expected in the heat map there would have been greater areas of blue at the edge of the piercing of the scaffold, as this represents a high acidity. Upon close observation of the pH heat map, there are local acidic hot spots in addition to black regions which indicate out of range values which could be too acidic for the sensing range. These black regions could also have been thought to be small holes within the scaffold, however the brightfield images confirm that this is not the case. Although the pH gradient does not show the expected colour change, what is apparent, is that a gradient is present and the local pH changes can be acquired. Chauhan et al¹⁶³ also used polyacrylamide nanosensors to demonstrated the ability to display a pH gradient using a heat map to monitor the intestinal pH of *Caenorhabditis elegans*. The lack of expected pH change may be due to the very small volume of acid placed on the scaffold. A larger volume of 100 μ L of different pH hydrochloric acid was then placed on the scaffold and imaged as shown in Figure 5.2C. The pH heat maps show a more distinct colour change compared to the smaller volume. With greater volumes containing the analyte of interest being placed on the scaffold, the hydrogen ions can more easily diffuse throughout the fibres for interaction with the nanosensors causing a change in fluorescence intensity. In Figure 5.2C, the scaffold exposed to water showed hot spots of yellow

acidic regions, this is likely due to the acidic residues remaining on the scaffold from previous exposure to acid which has not been completely washed off. However, this shows the ability to monitor differences in local pH of the scaffold. Another observation that can be made from the pH variation is that the self-reporting scaffold response is rapid since fluorescent images were immediately acquired after exposure to the solutions

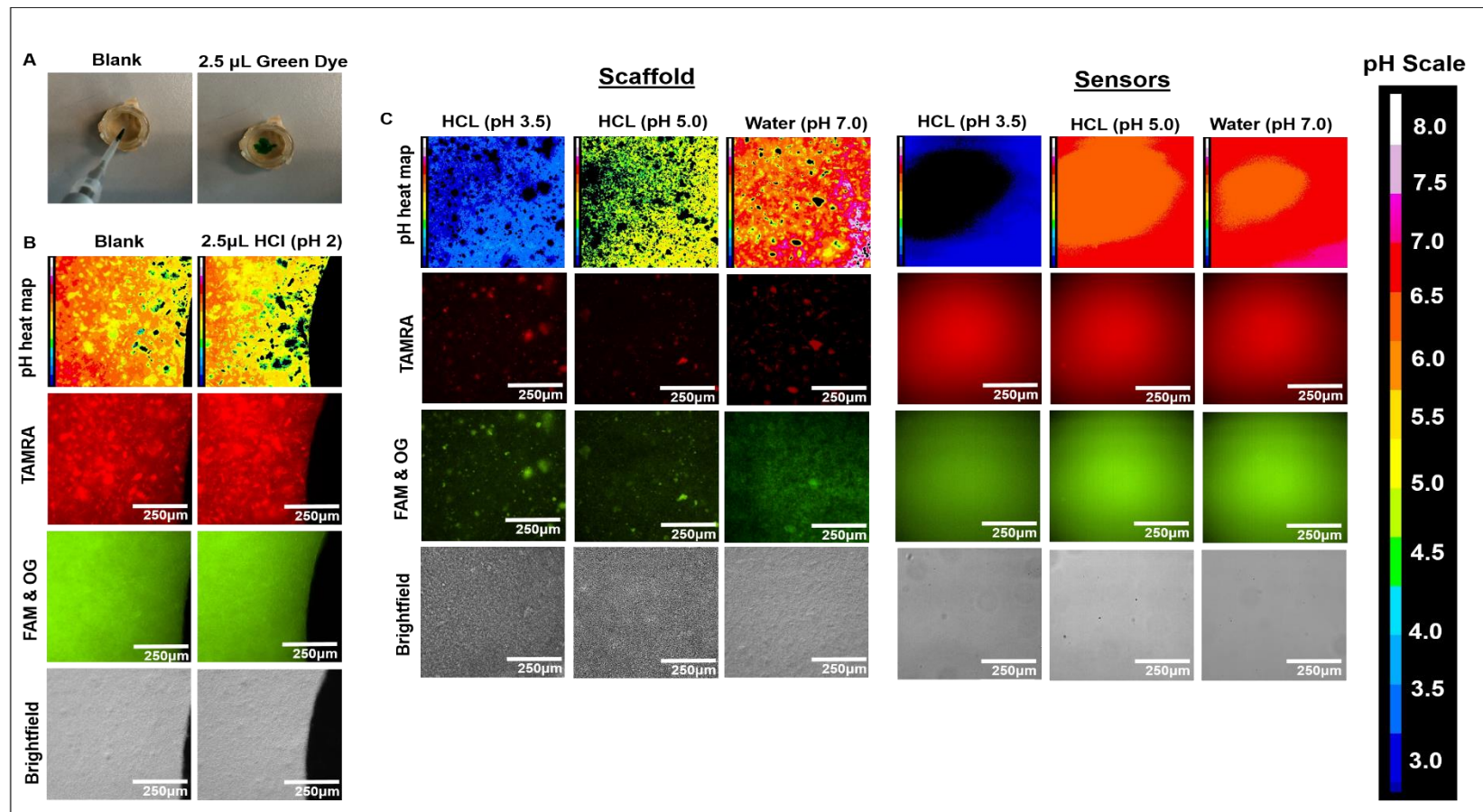


Figure 5.2 Heat maps generated by MATLAB and ImageJ software display pH gradients. (A) A 2.5 μ L drop of green dye was pipetted into the centre of a self-reporting scaffold to observe the spreading out of the dye and creation of a gradient. (B) Heat map shows the formation of a pH gradient before and after addition of a drop of pH2 hydrochloric acid, (C) Heat maps show the pH gradients in a self reporting scaffold, and suspension of nanosensors post addition of a larger volume (100 μ L) of HCl at different pH values, in addition to water, data shown is representative of $n=3$ experiments, scale bar = 250 μ m.

5.2.2. Culturing fibroblasts upon self-reporting scaffolds

The intended use of electrospun self-reporting scaffold is not only to report analyte concentration *in situ*, but to also act as a template of the ECM and support tissue growth. To confirm this, MRC-5 human lung fibroblasts were cultured on electrospun gelatin scaffolds with and without sensors to ensure the incorporation of nanosensors into the fibres did not compromise cell growth and proliferation. Scanning electron microscopy was performed to confirm the presence of cells and their healthy morphology. The scanning electron micrographs show the typical elongated shape of the cells on the scaffold, in addition to cell spreading and an increasing presence over time with no apparent differences between the scaffolds with and without the sensors in Figure 5.3A. Therefore indicating the self-reporting scaffold is capable of supporting cell growth. An AlamarBlue[®] proliferation assay was performed to monitor the proliferation of the cells over time, this also indicated a higher proliferation rate over time with no significant differences between the scaffold containing the sensors and the scaffold without, determined by a T-Test using Graph Prism Software, data shown in Figure 5.3B. Gnani et al³⁰² also showed an increase in proliferation rate of Schwann cells on electron gelatin fibres over a period of 7 days, in addition to normal spread morphology shown by fluorescent staining indicating good biocompatibility of gelatin fibres. In addition Tang et al³⁰³ cultured human induced pluripotent stem cells (hiPSCs) and found an increase number of cells on the gelatin fibres compared to a glass slide after 24 hour culture, along with the successful differentiation of the hiPSCs to cardiomyocytes. This therefore shows the ability of the electrospun gelatin scaffold to support culture of different cell types and is in agreement with previous reports^{302,303}.

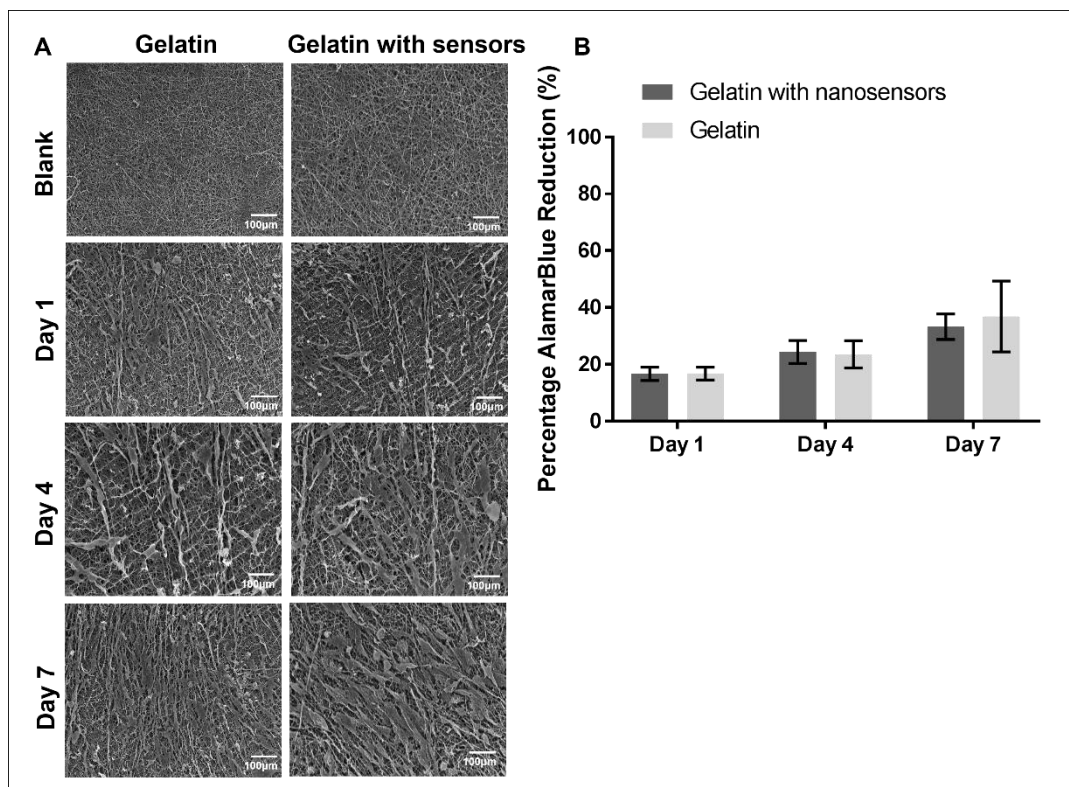


Figure 5.3 (A) Representative scanning electron micrographs of MRC5 human lung fibroblasts cultured on electrospun gelatin scaffolds with and without sensors, (B) AlamarBlue[®] proliferation assay, data shown is representative of n=3 experiments, n=3, scale bar = 100µm.

5.2.3. Effect of fibroblast culture on self-reporting scaffold calibration

After confirming fibroblasts were able to grow on the self-reporting scaffolds, the scaffolds were calibrated before cell seeding, and after 7 day culture with 3T3 fibroblasts to investigate whether the presence of cells affects the calibration of the scaffold, in addition the prolonged soaking in cell culture medium. The cell culture medium used was phenol red free and HEPES buffer free. This is because phenol red is highly fluorescent, so the absence of this compound from the media reduces the level of background noise¹³⁴, therefore improving the signal to noise ratio and providing more accurate quantification of the fluorescence produced by the nanosensors. In addition the removal of HEPES from the media prevented the buffering of the increasing acidic microenvironment due to the production of

metabolites of proliferation fibroblasts. Figure 5.4(A-C) displays no significant differences in the fluorescence intensities produced by the scaffolds before and after 7 day culture, which confirms the addition of cells to the scaffold does not interfere with the optical characterisation of the scaffolds. The presence of cells could have affected the calibration as they are known to exhibit autofluorescence sourced from NADH/NADPH, flavins and flavoproteins³⁰⁴. Although mitochondrial NADH has been shown to absorb light of wavelength $340 \pm 30\text{nm}$ and emits fluorescence at $460 \pm 50\text{nm}$ ³⁰⁵, which is out of the nanosensor fluorophores range. In addition, the autofluorescence of a single 3T3 fibroblast cell has been estimated to be equivalent to about 34,000 fluorescein molecules³⁰⁴. However, in this case no significant changes in fluorescent intensity were present.

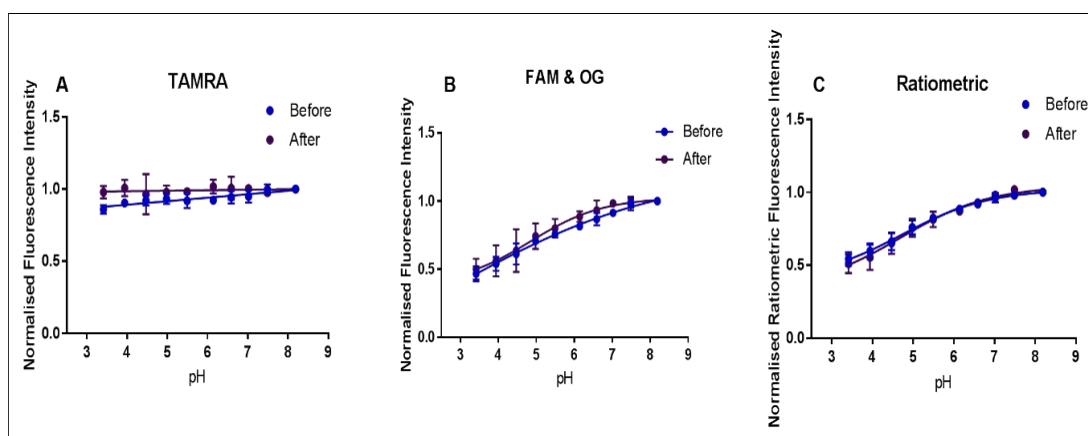


Figure 5.4 Calibration of self-reporting scaffolds by submerging in buffers ranging from pH 3.5 - 8.0, before and after cell seeding, data shown is representative of $n=3$ experiments.

5.2.4. Capability of self-reporting scaffold to monitor extracellular pH *in situ* whilst supporting fibroblast growth

To acquire the extracellular pH measurements, self-reporting scaffolds were fabricated and sterilised for subsequent seeding with 3T3 fibroblasts. The fibroblasts were preincubated with a fluorescent Hoechst nuclear stain for *in situ* visualisation of

the cells on the scaffold. Inverted fluorescence microscopy was used to acquire live *in situ* fluorescent images of the cell-seeded self-reporting scaffold at different time points (Day 1, Day 4 and Day 7) through a 12 well plate. Fluorescent images from the green and red channel were taken from three different areas of the cell-seeded scaffold as shown in Figure 5.5A and an average ratiometric measurement for each area was then obtained by dividing the green channel wavelength by the red provided in Figure 5.5C as R_i . When imaging the scaffold through the well plate containing the culture medium there were a couple of challenges. Firstly, there was the occasional presence of bubbles which interfered with the imaging, and secondly the scaffold was not completely flat and often creased making it difficult to find regions to image that were not out of focus. End point determination was performed on cell-seeded scaffolds run in parallel for scanning electron microscopy to confirm the presence of cells. Cell-seeded scaffolds cultured for 1, 4 and 7 days were then fixed with paraformaldehyde for subsequent calibration in buffers ranging from pH 3.5 – 8.0. Scaffolds were calibrated individually due to the slight shifts of the ratiometric curves shown in Figure 5.5B. This may be due to batch variation with the incorporated nanosensors, fluctuations in the light intensity with the fluorescence imaging or differences in the focal plane during imaging of the scaffold. However, no significant differences are present between the calibrations, but it is important to calibrate each scaffold individually for experimentation as slight changes in the calibration curve can alter the final pH output. After calibration of the scaffolds, the R_{max} , R_{min} , pKa (pH value at half normalised ratiometric fluorescence intensity) and hillslope of the calibration curve were extrapolated using GraphPrism as given in Figure 5.5C. Using these values, the relationship between intensity and pH can be modelled using the equation given in Figure 5.5D.

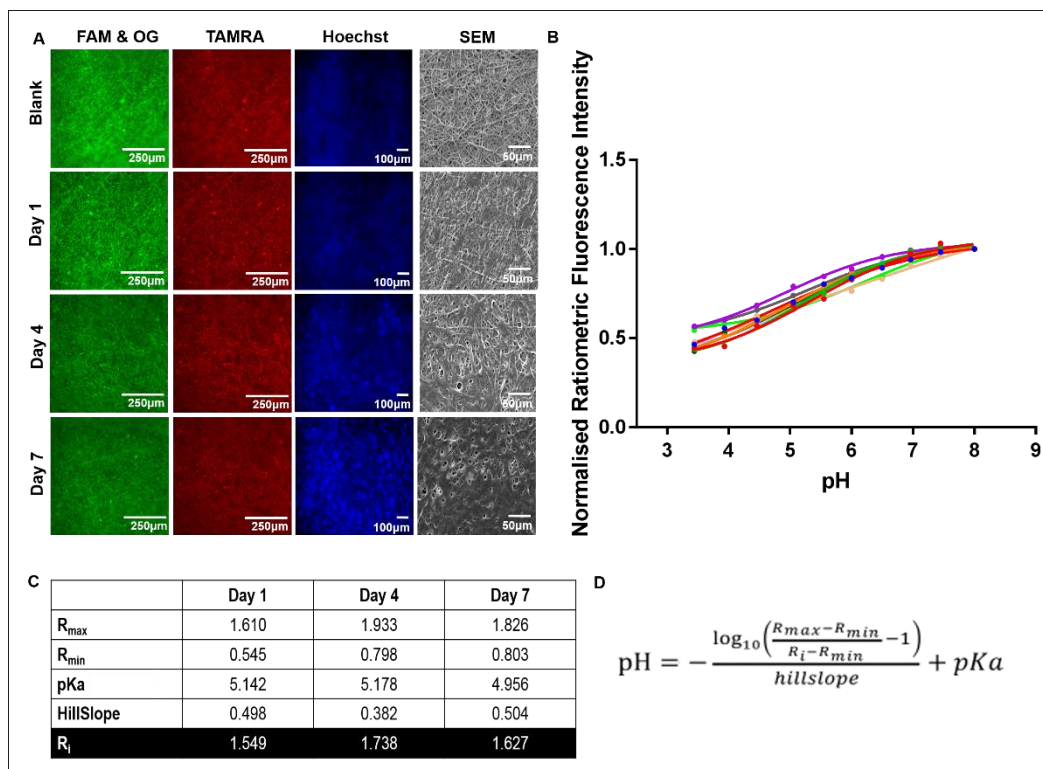


Figure 5.5 Data shown representative of $n=3$ experiments (A) Representative fluorescent images of the cell-seeded self-reporting scaffold, images taken of FAM&OG - scale bar = $250\mu m$, TAMRA - scale bar = $250\mu m$, Hoechst nuclear stain - scale bar = $100\mu m$, representative SEM images show ECM deposition across scaffold by cells - scale bar = $50\mu m$, (B) Individual calibration of self-reporting scaffolds, (C) Values extrapolated from ratiometric curves, and ratiometric intensities from fluorescent images, (D) equation linking fluorescent intensity to pH.

Using the values from Figure 5.5C and the equation in Figure 5.5D, the corresponding extracellular pH was determined as displayed in Figure 5.6(A-B). The acquired values show an expected decrease in the extracellular pH of the cell-seeded scaffolds from pH 7.5 to 6.3 over the 7 day period. The pH significantly decreases on Day 4 and Day 7 compared to the control scaffold. Extracellular pH measurements were also obtained using a semi-micro electrode given in Figure 5.6C as a comparison which also shows a decrease in pH. Differences in the self-reporting scaffold pH measurements and the pH electrode are apparent. This could be because the self-reporting scaffold is monitoring the specific local pH within the scaffold microenvironment, whereas the probe is measuring the analyte concentration within the media. In addition, the temperature was not controlled when

measuring the pH which could contribute to the differences in pH values. The overall reduction in pH is expected due to the increase of cell proliferation and subsequent production of metabolites from the cells. To monitor proliferation, an AlamarBlue assay was performed in parallel which shows increasing proliferation over the 7 day period in Figure 5.6D. Therefore the data demonstrates the ability to successfully determine the overall extracellular pH of the surface of the scaffold. However, ideally it would be useful to monitor the pH throughout the entire construct by using Z stacks to image from the top to the bottom of the scaffold. This is because gradients can exist in 3-Dimensional scaffolds and the centre of scaffolds are thought to suffer from hypoxia and a lack of nutrients so being able to monitor any pH change could provide insight into the cellular microenvironment. In addition, the long term rigidity of the scaffold is unknown after the 7 day period and whether the cells may remodel the scaffold, or if the scaffold will degrade eventually releasing the nanosensors in the culture. However, with the potential release of the sensors into the culture it is unlikely that the cells would uptake them. Desai et al, states that polyacrylamide nanosensors do not have physiochemical characteristics which favour uptake by the cells via endocytosis¹⁷². In order to favour uptake for intracellular pH measurements, they altered the properties of the nanosensors by adding a positive charge to the surface of the nanosensors. Another important point that should be made is that during the image acquisition, cells were exposed to room temperature which may have caused slight inaccuracies in the acquired pH measurements.

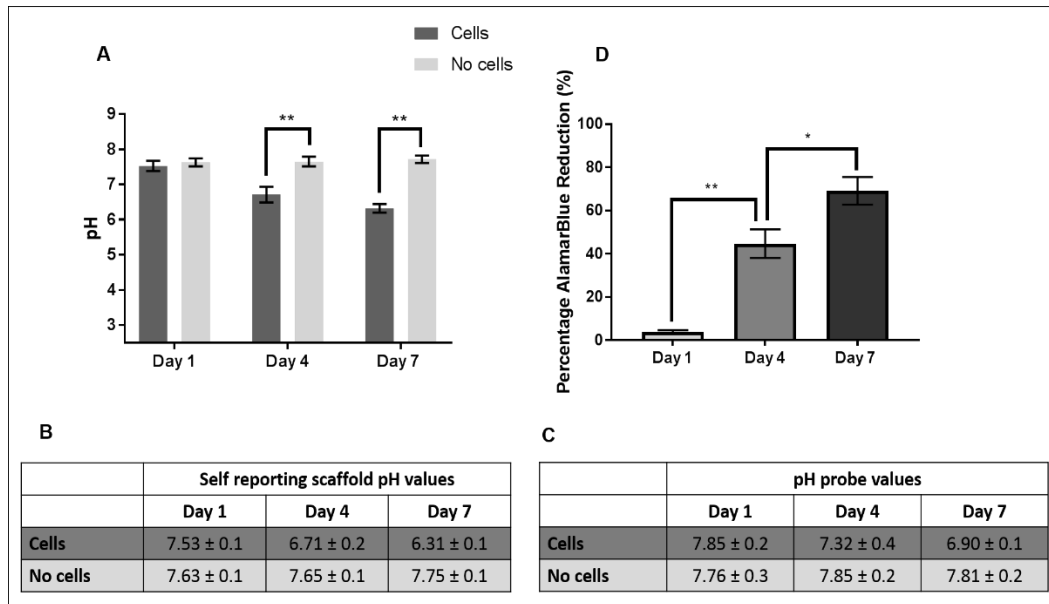


Figure 5.6 (A) Graph displaying the extracellular pH measurements of the cell seeded self reporting scaffold vs control self reporting scaffold with media only, (B) Specific values of extracellular pH measurements using the cell seeded scaffold vs scaffold with media only taken at 25°C, (C) pH probe values (D) AlamarBlue[®] proliferation assay**p<0.01, *P<0.05 n=3.

In addition, visual representations of the pH change were also acquired by using phenol-red containing cell culture medium. Phenol-red is a pH indicator and turns yellow when encountering acidic substances. The photo in Figure 5.7 shows the gradual colour change from red to orange to yellow, demonstrating the drop in pH as a result of acidic metabolite production.

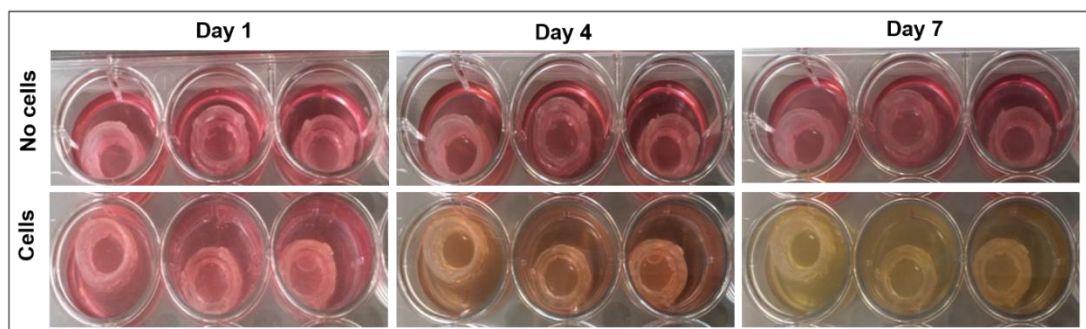


Figure 5.7 Photographs to display the visual change in pH of the medium surrounding 3T3 fibroblasts seeded on the self-reporting gelatin scaffold.

5.2.5. Biological application of using self-reporting scaffold to monitor pH changes due to different rates of proliferation

After confirming the ability of the self-reporting scaffold to acquire extracellular pH measurements *in situ*. The next aim was to show a biological application using the scaffold. A compound which has been shown to increase proliferation, which would therefore cause a significant decrease in extracellular pH as a result of the production of more waste metabolites. Cis-4-methylsphingosine was the compound of choice, it is a synthetic analogue of sphingosine-1-phosphate, which acts as a high affinity agonist at specific G-protein-coupled receptors located on the plasma membrane and is readily take up by cells³⁰⁶. Cis-4-methylsphingosine acts an intracellular messenger involved in signal transduction and cell growth regulation³⁰⁷. Cis-4-methylsphingosine has been shown to significantly increase the proliferation of NIH 3T3 fibroblasts when cultured in 2-Dimensions after 2 hours³⁰⁷. Therefore, to confirm this effect NIH 3T3 fibroblasts were seeded in 2-Dimensions at a density of $1.5 \times 10^5/500\mu\text{L}$ for 24 hours, then placed in serum starved medium for 24 hours to allow the cells to become quiescent before adding the cis-4-methylsphingosine for a further 24 hours. The proliferation of the cells were monitored using an AlamarBlue[®] proliferation assay, and images of the cells morphology and confluency was monitored using brightfield and fluorescent microscopy. Figure 5.8A shows that there is no evidence of compromised cell morphology or any differences in cell spreading and confluency with the addition of the compound. In addition, the proliferation assay data in Figure 5.8B shows a decrease in the proliferation with the treatment of cis-4-methylsphingosine compared to the untreated control, however the reduction in proliferation was not significant as confirmed by a T-Test.

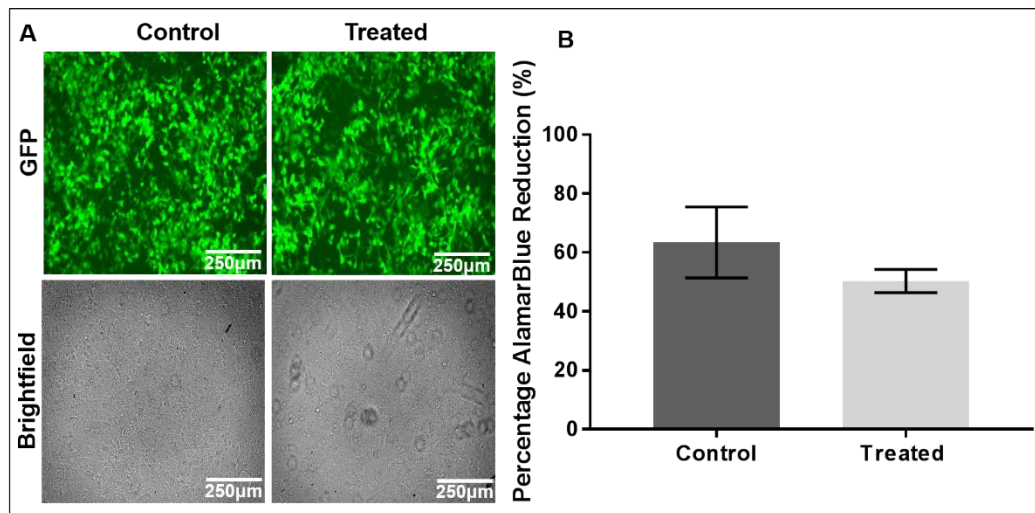


Figure 5.8 Treatment of 3T3-GFP NIH fibroblasts with *cis*-4-methyl sphingosine ($n=3$) (A) Fluorescent and brightfield images show no comprised morphology or confluency with the treatment (B) AlamarBlue[®] proliferation assay shows no significant reduction in proliferation after 24 hour treatment with *cis*-4-methyl sphingosine, scale bar = 250µm.

The suppressed proliferation was not the expected effect, as literature reports have demonstrated enhanced proliferation with the addition of sphingosine^{307,308,309}. Therefore, we performed a further study to investigate the suppressed proliferation. For this study, different cell densities were seeded in 2-Dimensions and exposed to the *cis*-4-methylsphingosine for 24 hours. Different densities were explored as cells can respond differently depending on cell confluence. Whether cells have free space to grow or are in contact with each other can have an effect on their cell signalling cascades and gene expression patterns. For example in a study by Alfieri, a drug was added to different densities of a cell line (Calu-3) which exhibited a significant difference in sensitivity to the drug.

Figure 5.9(A-B) shows there are no distinct changes in morphology between the treated and untreated GFP-tagged fibroblasts. Figure 5.9C displays a significant decrease in the cell proliferation at the lowest density of 150,000. At higher densities there was also a decrease in the cell proliferation although it was not significant. Therefore, a trend is common whereby the *cis*-4-methyl sphingosine is having a suppressive effect on the cellular proliferation. Although an increased proliferative

effect of fibroblasts was observed by Echten et al³⁰⁷, Braak et al³⁰⁶ found an opposing effect on neuronal cells whereby the cis-4-methylsphingosine accumulated intracellularly causing apoptosis. Shin et al³¹⁰ found that sphingosine-1-phosphate induced apoptosis in melanoma cells, in addition to Davaille et al³¹¹ who found apoptosis in human hepatic myofibroblasts. Therefore, given that there are conflicting reports in the literature as to the effect of sphingosine on cell proliferation, it is interesting that in our study, the addition of cis-4-methylsphingosine led to a reduction of proliferation in 3T3 fibroblasts.

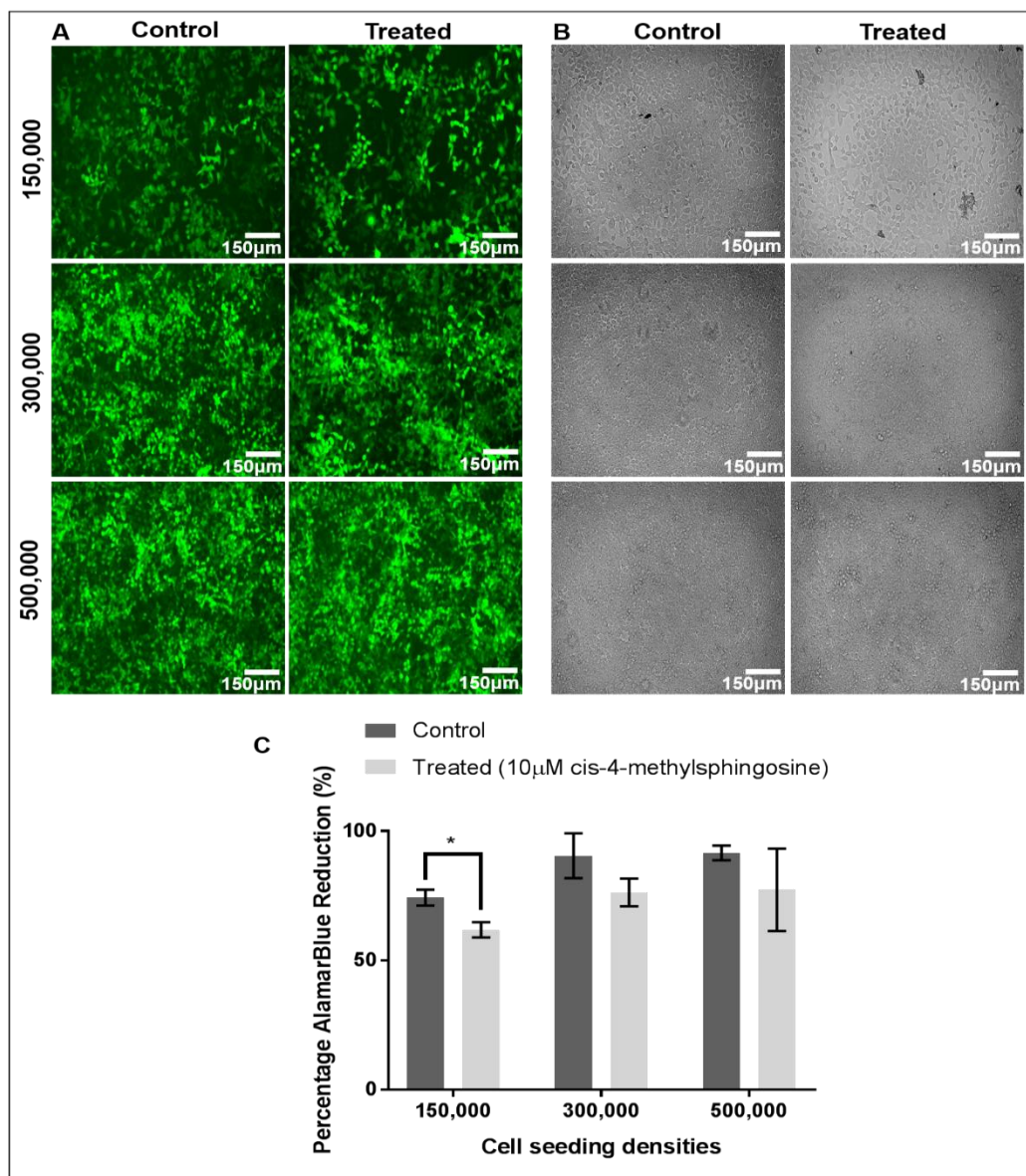


Figure 5.9 3T3-GFP fibroblasts cultured on coverslips at different densities incubated with and without 10µM cis-4-methylsphingosine, $p < 0.05$, $n=3$, scale bar = 150µm.

After observing the suppressive effect of the cis-4-methylsphingosine on the fibroblasts seeded in 2D, 3T3-GFP fibroblasts were cultured on self-reporting scaffolds to observe whether the cells still demonstrated a suppressed proliferation rate. Figure 5.10A shows scanning electron micrographs of the treated and non-treated fibroblasts. By Day 7, it is clear to see there is more ECM deposition on the control scaffold compared to the treated, this correlates with the proliferation data in Figure 5.10B where the cell proliferation is higher in the control compared to the treated, although not significant. Therefore higher proliferation means higher ECM deposition as more cells are available to secrete ECM proteins. At Day 1, the proliferation is also higher in the control conditions compared to the treated, again not significant. At Day 4, unexpectedly the proliferation is slightly higher but not significantly when treated compared to the non-treated. Overall, the proliferation data of the cells on the scaffold when treated with the compound is generally lower, (although not significant) compared to the control untreated, which agrees with the 2D data in Figure 5.8 and Figure 5.9.

The aim of this chapter was to demonstrate the use the self-reporting scaffold in a biological application. By adding the cis-4-methylsphingosine, the expected effect was to enhance proliferation and subsequently reduce the pH of the cellular microenvironment; however, this effect was not observed, so the self-reporting scaffold was not used to acquire extracellular pH measurements.

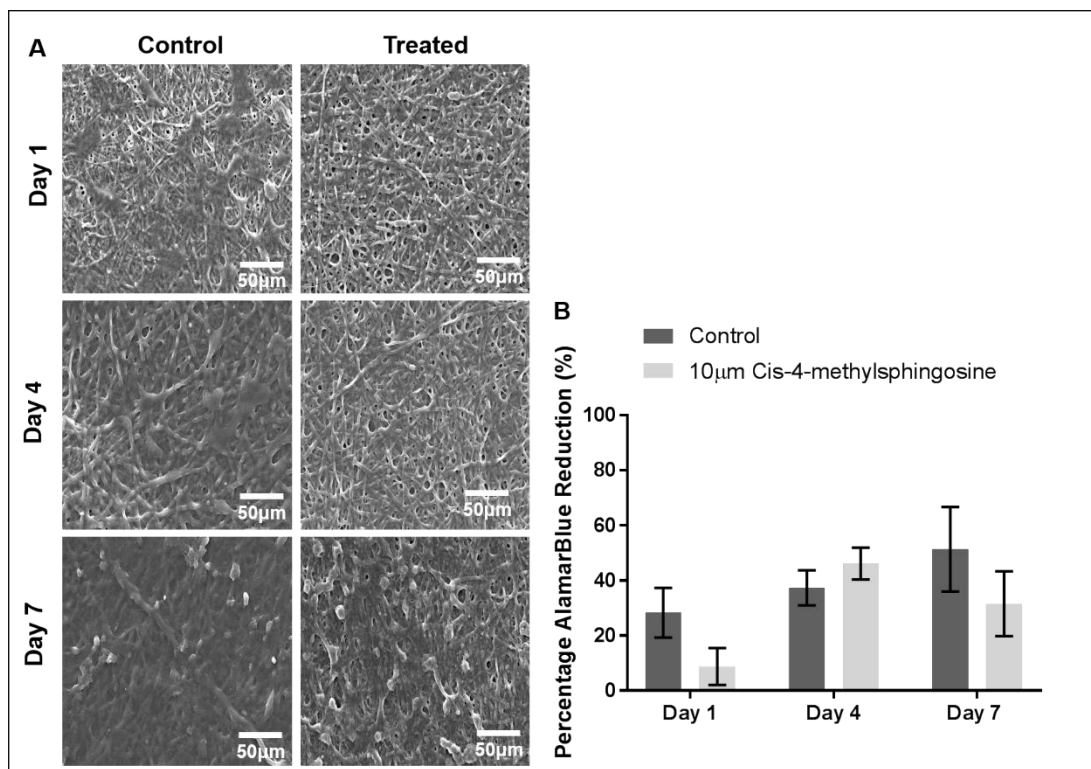


Figure 5.10 Data shown are representative of $n=3$ experiments. 3T3-GFP fibroblasts cultured on self-reporting scaffolds incubated with and without 10µM cis-4-methylsphingosine (A) Representative scanning electron micrographs of cells on scaffold, (B) AlamarBlue[®] proliferation data.

5.3. Conclusion

The scientific novelty of this work, was the ability of the self-reporting scaffold to monitor pH *in situ* in a non-invasive manner. The self-reporting scaffold was able to monitor pH gradients and pH values in specific areas across the scaffold which current pH monitoring techniques are limited by. The self-reporting scaffold remained responsive following the culture of the 3T3 fibroblasts within a sigmoidal shaped pH curve covering the pH range of 3.5 – 7.5, however it is important that individual areas of scaffold are calibrated separately due to slight shifts in the ratiometric curves which can lead to inaccuracies in the pH values. The extracellular pH of 3T3 fibroblasts was successfully monitored over a 7 day period, at time points Day 1, Day 4 and Day 7 which showed a drop in the pH as expected due to an accumulation of acidic waste metabolites. Furthermore, the addition of cis-4-

methylsphingosine did not significantly increase the proliferation rate of the fibroblasts as observed in the literature, unexpectedly, a suppressed effect was observed. However, the encouraging results from local pH measurements acquired using the self-reporting scaffold provide a promising tool to further understand the cellular microenvironment in tissue engineering and regenerative medicine applications.

Chapter 6 Conclusions & Future Work

6.1. Summary

This thesis has shown how we can improve current *in vitro* monitoring methods by the use of bioreactors, and incorporating fluorescent nanosensors into electrospun polymeric scaffolds to produce ratiometric, real time and non-invasive pH measurements of the extracellular microenvironment.

Chapter 3 describes how pH responsive optical nanosensors can be successfully synthesised and incorporated into polymeric electrospun scaffolds. By using polyacrylamide fluorescent nanosensors in our self-reporting scaffolds, the potential to develop a technology platform for *in situ* monitoring is permitted and limitations using commercially available single fluorophores can be overcome, such as leaching, non-specific binding, potential toxicity and narrow pH sensing range.

For nanosensor fabrication, two pH sensitive fluorophores with different pKa values and a pH insensitive fluorophore were incorporated into a biocompatible polyacrylamide matrix to provide a fluorescence response corresponding to a specific pH. The size characterisation of the sensors by dynamic light scattering provided an expected hydrodynamic diameter of 40nm¹⁶³. For optical characterisation, the nanosensors were placed in different pH buffer solutions. The fluorescent response from the pH sensitive fluorophores FAM and OG and the reference fluorophore TAMRA by excitation using the green and red wavelengths was quantified. The resulting change in fluorescent intensity upon pH change was due to the equilibrium distribution of the monoanion and dianion forms of the pH responsive fluorophores which was shown to be reversible. By taking a ratio of the

emissions of the pH sensitive fluorophores and the reference fluorophore, an expected sigmoidal shaped curve was produced displaying sensitivity within the full physiological between pH 3.5 – 7.5¹⁶³.

To develop the self-reporting scaffold, electrospinning was used to fabricate the constructs to support the sensing model. This is because electrospun scaffolds are thin, highly porous¹⁸⁰ and resemble the fibrous architecture of the native extracellular matrix³³. PET and gelatin were the chosen polymers for investigation of their compatibility as self-reporting scaffolds. The nanosensors were successfully incorporated into polyethylene terephthalate and gelatin scaffolds by electrospinning, as shown by the production of smooth, uniform fibres via SEM. These polymeric scaffolds mimic the structural architecture of the fibrous, native ECM and their spinning ability was not compromised by the addition of nanosensors. Since gelatin is known for its weaker structural integrity compared to synthetic polymer PET, gelatin was successfully crosslinked using glutaraldehyde to enhance its water degradability. The SEM micrographs displayed a typical webbed appearance post crosslinking²⁴⁵. Optical characterisation of the nanosensor incorporated scaffolds was performed by submerging the scaffolds in a range of buffer solutions from pH 3.5 – 7.5 and quantifying the emission fluorescent intensities. The PET scaffolds incorporated with nanosensors produced no additive pH response, which was thought to be due to a lack of porosity, preventing diffusion of the analytes through the fibres for subsequent interaction with the nanosensors. However, optical characterisation of gelatin scaffolds incorporated with nanosensors demonstrated a pH response within the full physiological range of pH 3.5 – 7.5.

Chapter 4 evaluates the differences in proliferation of fibroblasts when cultured on polymeric scaffolds and exposed to static and flow conditions. Flow conditions were incorporated into the model because perfusion has been shown to enhance nutrient and oxygen diffusion throughout scaffolds to improve cell viability and activity⁸². The

Quasi-Vivo[®] perfusion systems were used to expose fibroblasts to flow conditions due to their versatility, ability to accommodate scaffolds and its simple interconnected configuration. For the initial, preliminary experiments, the Quasi-Vivo[®]500 (QV500) system was used to expose the electrospun PET scaffolds to flow conditions. The cell-scaffold was placed at the top of the bioreactor so it was directly exposed to the flow of media. It was found that fibroblasts cultured on PET scaffolds at higher flow rates caused the removal of the cells from the construct thought to be due to the impact of the high shear stress. A low flow rate of 8 μ L/min showed a significant increase in cell proliferation compared to static conditions, which indicates the importance of flow in cell culture models as even the very low flow rates can have a significant effect on cell activity. The Quasi-Vivo[®]900 (QV900) system was used to expose the cell-seeded electrospun gelatin scaffolds to flow conditions, as the dimensions of the bioreactor were able to cater to the dimensions of the CellCrowns[™] which were used to secure the electrospun gelatin scaffolds. Since the QV900 system had larger bioreactor wells compared to the QV500, we were able to investigate the effect of the flow on the gelatin cell-seeded scaffold when placed in different positions of the bioreactor. The fibroblasts were exposed to a low flow rate of 8 μ L/min as performed in the QV500 with the PET scaffold but the fibroblasts did not exhibit the same proliferative effect. Therefore indicating that the experimental conditions optimised for the QV500 are not necessarily transferable to the QV900. In addition, HUVEC cells adapted to exposure to high shear were cultured in the QV900, but cell growth was compromised including in the static control conditions, which could be due to the structural properties of the electrospun scaffolds.

To investigate the proliferative effect of cells exposed to flow conditions, we attempted to develop a novel wound model on electrospun scaffolds. Initially, as proof of concept a conventional scratch assay in 2D was performed which presented

a fairly reproducible wound area and complete recovery of the wound, but no differences in the wound recovery was present when exposed to static vs flow conditions. Electrospun PET was used for initial preliminary experiments for wound optimisation on the electrospun scaffolds due to its structural integrity and ease to work with. Various wound assays were explored, including chemical, burn and scratch assays on the scaffold which presented challenges in producing a reproducible wound area on the scaffold due to the properties of the scaffold. When wounds performed on electrospun scaffolds were exposed to static and flow conditions, no significant differences in wound recovery were apparent, however due to the lack of reproducibility the results were not directly comparable.

Chapter 5 shows how the self-reporting scaffold can be used to acquire local pH measurements in a non-invasive manner. The self-reporting scaffold was able to monitor pH specific areas and gradients across the scaffold which current pH monitoring techniques are limited by. The self-reporting scaffold remained responsive following the culture of the 3T3 fibroblasts within a sigmoidal shaped pH curve covering the pH range of 3.5 – 7.5, however it is important that individual areas of scaffold are calibrated separately. The extracellular pH of 3T3 fibroblasts was successfully monitored over a 7 day period, at time points Day 1, Day 4 and Day 7 which showed a drop in the pH as expected due to an accumulation of acidic metabolites.

6.2. Future Work

Future work could involve utilising the self-reporting scaffolds to monitor the extracellular microenvironment to monitor parameters other than pH. Instead of using the pH sensitive fluorophores within the polyacrylamide nanosensors, the fluorophores could be substituted for an alternative sensing components to monitor

analytes such as oxygen, glucose and cytokines. Being able to monitor these additional parameters could provide further insight into the optimal conditions required for growth.

The self-reporting scaffold could be used for specific biological applications such as cancer, wound healing and tissue engineering grafts. Using the scaffold and cancerous cell lines, a cancerous tissue could be engineered. The incorporation of the pH sensing would allow the extracellular microenvironment to be closely monitored. Being able to monitor the pH of a tumour microenvironment is important as we know it has a more acidic extracellular pH compared to non-cancerous tissue. Therapeutics could be used to try and treat the engineered cancerous tissue and the pH could be monitored to see if the extracellular microenvironment can return to a more normal physiological pH. Being able incorporating oxygen sensing into an engineered cancerous model would also be very useful as tumours often suffer from hypoxia. Furthermore, the self-reporting scaffold could be used to engineer a tissue for a graft. Since grafts require long term culture, being able to monitor the microenvironment non-invasively means that the tissue does not require end point determination.

Culturing cells on scaffolds is one of the most common approaches to tissue engineering. However, some of the drawbacks of using scaffolds involves the lack of oxygen and nutritional supply to the centre of the scaffold which can result in hypoxia and necrosis of the cells which have migrated into the scaffold. The use of bioreactors can help overcome these limitations by providing a flow of media to help the diffusion of the nutrients and oxygen throughout the construct more evenly. To improve current monitoring methods, the aim of this study was to combine the ability to monitor pH *in situ*, with the incorporation of flow into the model using optically transparent bioreactors. The preliminary flow experiments in this study involved using the Quasi-Vivo[®] 500 perfusion system to provide a laminar flow. At a low flow

rate we demonstrated a significant increase in the proliferation of fibroblasts, whereas higher flow rates showed cell detachment. One of the limitations of this bioreactor is that it is not optically transparent which defeats the ability to monitor the microenvironment *in situ*. The more recently developed Quasi-Vivo[®]900 system overcomes this drawback with its optically transparent windows within the bioreactor. However, cell proliferation data showed that this system is not transferable from the Quasi-Vivo[®]500 as the incorporation of flow within the system limited cell proliferation of fibroblasts and endothelial cells. Therefore future work could involve further exploring the effect of different flow rates and alternative bioreactor systems.

Another aim of this study was to develop an *in vitro* wound healing model on electrospun scaffolds. This is important because most wound models are limited by being performed in 2-Dimensions on tissue culture plates, however, by using electrospun scaffolds we can create a more physiological relevant microenvironment by mimicking the fibrous structure of the extracellular matrix. One of the challenges of creating a wound model on the scaffolds, was that it lacked reproducibility due to the properties of the electrospun scaffolds, and therefore further investigations into how a reproducible model can be created should be performed. By using electrospun scaffolds with the incorporation of flow into the model, a more complex wound model with multiple cell types can be developed. Again, as we know the pH of a wound changes through the different stages of the recovery, therefore using the self-reporting scaffold as part of a wound model, the local pH of the wound can be monitored which can provide more insight into the wound healing process.

Chapter 7 References

1. The National Institute of Biomedical Imaging and Bioengineering. Tissue Engineering and Regenerative Medicine. (2016). Available at: <https://www.nibib.nih.gov/science-education/science-topics/tissue-engineering-and-regenerative-medicine>. (Accessed: 30th May 2017)
2. Katari, R., Peloso, A. & Orlando, G. Tissue Engineering and Regenerative Medicine: Semantic Considerations for an Evolving Paradigm. *Front. Bioeng. Biotechnol.* **2**, 1–6 (2015).
3. Stevenson, A. In vitro. *Oxford University Press* (2010). Available at: https://en.oxforddictionaries.com/definition/in_vitro. (Accessed: 30th May 2017)
4. Okamoto, M. & John, B. Synthetic biopolymer nanocomposites for tissue engineering scaffolds. *Prog. Polym. Sci.* **38**, 1487–1503 (2013).
5. Maltman, D. J. & Przyborski, S. a. Developments in three-dimensional cell culture technology aimed at improving the accuracy of in vitro analyses. *Biochem. Soc. Trans.* **38**, 1072–5 (2010).
6. O'Driscoll, C. *A virtual space odyssey*. (2004).
7. Hughes, J. P., Rees, S. S., Kalindjian, S. B. & Philpott, K. L. Principles of early drug discovery. *Br. J. Pharmacol.* **162**, 1239–1249 (2011).
8. Committee, A. in S. & Baker, T. R. H. N. *Animals (Scientific Procedures) Act 1986*. (2014).
9. Festing, S. & Wilkinson, R. The ethics of animal research. Talking Point on the use of animals in scientific research. *EMBO Rep.* **8**, 526–530 (2007).

10. Mestas, J. & Hughes, C. C. W. Of Mice and Not Men: Differences between Mouse and Human Immunology. *J. Immunol.* **172**, 2731–2738 (2004).
11. Howard, D., Buttery, L. D., Shakesheff, K. M. & Roberts, S. J. Tissue engineering: Strategies, stem cells and scaffolds. *J. Anat.* **213**, 66–72 (2008).
12. Wong, H. K. *et al.* Novel method to improve vascularization of tissue engineered constructs with biodegradable fibers. *Biofabrication* **8**, 15004 (2016).
13. Loon, S. L. M. van, Smits, A. I. P. M., Driessen-Mole, A., Baaijens, F. P. T. & Bouten, C. V. C. The immune response in situ tissue engineering of aortic heart valves. *Biomed. Eng. trends Mater. Sci.* (2013). doi:10.5772/52807
14. Ozcelik, H. *et al.* Cell Microenvironment Engineering and Monitoring for Tissue Engineering and Regenerative Medicine: The Citation Accessed Citable Link Cell Microenvironment Engineering and Monitoring for Tissue Engineering and Regenerative Medicine: The Recent Advances. **2014**, (2014).
15. Sbrana, T. & Ahluwalia, A. Engineering Quasi-Vivo® in Vitro Organ Models. *Adv. Exp. Med. Biol.* **745**, (2012).
16. Birnbaum, L. Generalised components of a 3-D tissue model. *National Institute of Environmental Health Sciences (NIEHS)* (2011). Available at: <https://www.niehs.nih.gov/news/newsletter/2011/august/science-symposium/>. (Accessed: 4th June 2017)
17. Routh, D. *Learning about cells*. (Mark Twain Media Inc., 2006).
18. Nature Education. *Essentials of Cell Biology*. (2014).
19. Taylor, C. Body Organisation. *The Kingfisher Science Encyclopedia* 98 (2000).

20. OpenStax. *Anatomy & Physiology*. (OpenStax, 2016).
21. Khan, S. & Hashmi, G. S. HISTOLOGY AND FUNCTIONS OF CONNECTIVE TISSUES: a review article. *Univ. J. Dent. Sci.* **1**, 1–2 (2015).
22. Gallik, S. Loose connective tissue. *Drupal* (2009). Available at: <http://histologyolm.stevegallik.org/node/99>. (Accessed: 6th June 2017)
23. Gattorno, M. & Martini, A. *Immunology and rheumatic diseases. Textbook of Pediatric Rheumatology* (Elsevier Inc., 2011). doi:10.1016/B978-1-4160-6581-4.10003-2
24. Kalluri, R. & Zeisberg, M. Fibroblasts in cancer. *Nat. Rev. Cancer* **6**, 392–401 (2006).
25. Tschumperlin, D. J. Fibroblasts and the Ground They Walk On. *Physiology* **28**, 380–390 (2013).
26. Lberts, B., Johnson, A. & Lewis, J. *Molecular Biology of the Cell*. (2002).
27. Theocharis, A. D., Skandalis, S. S., Gialeli, C. & Karamanos, N. K. Extracellular matrix structure. *Adv. Drug Deliv. Rev.* **97**, 4–27 (2016).
28. Lewin B, Cassimeris L, Lingappa V, P. G. in (Jones and Bartlett, 2007).
29. Chan, K. T., Cortesio, C. L. & Huttenlocher, A. Integrins in Cell Migration. 47–67 (2007). doi:10.1016/S0076-6879(07)26003-3
30. Papavasiliou, G., Sokic, S. & Turturro, M. in *Biotechnology - Molecular Studies and Novel Applications for Improved Quality of Human Life* (ed. Sammour, R.) (2012).
31. Dhandayuthapani, B., Yoshida, Y., Maekawa, T. & Kumar, D. S. Polymeric scaffolds in tissue engineering application: A review. *Int. J. Polym. Sci.* **2011**, (2011).

32. Plunkett, N. & O'Brien, F. J. Biomaterials & scaffolds for tissue engineering. *Mater. Today* **14**, (2011).
33. Harrington, H. *et al.* Immunocompetent 3D Model of Human Upper Airway for Disease Modeling and In Vitro Drug Evaluation. *Mol. Pharm.* (2014). doi:10.1021/mp5000295
34. Ghasemi-Mobarakeh, L. Structural properties of scaffolds: Crucial parameters towards stem cells differentiation. *World J. Stem Cells* **7**, 728 (2015).
35. Choi, S. W., Zhang, Y. & Xia, Y. Three-dimensional scaffolds for tissue engineering: The importance of uniformity in pore size and structure. *Langmuir* **26**, 19001–19006 (2010).
36. Wang, X., Ding, B. & Li, B. Biomimetic electrospun nanofibrous structures for tissue engineering. *Mater. Today* **16**, 229–241 (2013).
37. Chan, B. P. & Leong, K. W. Scaffolding in tissue engineering: General approaches and tissue-specific considerations. *Eur. Spine J.* **17**, (2008).
38. Li, X., Xie, J., Yuan, X. & Xia, Y. Coating Electrospun Poly (ϵ -caprolactone) Fibers with Gelatin and Calcium Phosphate and Their Use as Biomimetic Scaffolds for Bone Tissue Engineering Coating Electrospun Poly (ϵ -caprolactone) Fibers with Gelatin and Calcium Phosphate and Their Use as . *Society* 14145–14150 (2008). doi:10.1021/la802984a
39. Xing, Q. *et al.* Increasing Mechanical Strength of Gelatin Hydrogels by Divalent Metal Ion Removal : Scientific Reports : Nature Publishing Group. 1–10 (2014). doi:10.1038/srep04706
40. Attia, M., Santerre, J. P. & Kandel, R. A. The response of annulus fibrosus cell to fibronectin-coated nanofibrous polyurethane-anionic dihydroxyoligomer scaffolds. *Biomaterials* **32**, 450–460 (2011).

41. Zhang, H., Liang, J., Ding, Y. & Li, P. The controlled release of growth factor via modified coaxial electrospun fibres with emulsion or hydrogel as the core. *Mater. Lett.* **181**, 119–122 (2016).
42. Wang, C. & Wang, M. Electrospun multicomponent and multifunctional nanofibrous bone tissue engineering scaffolds. *J. Mater. Chem. B* **5**, 1388–1399 (2017).
43. Bhatia, S. in *Natural Polymer Drug Delivery Systems: Nanoparticles, Plants, and Algae* 95–118 (Springer International Publishing, 2016). doi:10.1007/978-3-319-41129-3_3
44. Sampath, U. G. T. M., Ching, Y. C., Chuah, C. H., Sabariah, J. J. & Lin, P. C. Fabrication of porous materials from natural/synthetic biopolymers and their composites. *Materials (Basel)*. **9**, 1–32 (2016).
45. Wosek, J. Fabrication of composite polyurethane/hydroxapatite scaffolds using solvent-casting leaching technique. *Adv. Mater. Sci.* **15**, 67 (2015).
46. Annabi, N. *et al.* Controlling the porosity and microarchitecture of hydrogels for tissue engineering. *Tissue Eng. Part B. Rev.* **16**, 371–83 (2010).
47. Thadavirul, N., Pavasant, P. & Supaphol, P. Development of polycaprolactone porous scaffolds by combining solvent casting, particulate leaching, and polymer leaching techniques for bone tissue engineering. *J. Biomed. Mater. Res. - Part A* **102**, 3379–3392 (2014).
48. Hollister, S. J. Porous scaffold design for tissue engineering. *Nat. Mater.* **4**, 518–24 (2005).
49. Loh, Q. L. & Choong, C. Three-dimensional scaffolds for tissue engineering applications: role of porosity and pore size. *Tissue Eng. Part B. Rev.* **19**, 485–502 (2013).

50. Sopyan, I., Rahim, T. & Abdurrahim, T. Recent Progress on the Development of Porous Bioactive Calcium Phosphate for Biomedical Applications. *Recent Patents Biomed. Eng.* **1**, 213–229 (2008).
51. Janik, H. & Marzec, M. A review: Fabrication of porous polyurethane scaffolds. *Mater. Sci. Eng. C* **48**, 586–591 (2015).
52. Garg, T., Singh, O., Arora, S. & R.S.R, M. Scaffold: A Novel Carrier for Cell and Drug Delivery. *Crit. Rev. Ther. Drug Carr. Syst.* **29**, 1–63 (2012).
53. Oh, S. H., Kang, S. G., Kim, E. S., Cho, S. H. & Lee, J. H. Fabrication and characterization of hydrophilic poly(lactic-co-glycolic acid)/poly(vinyl alcohol) blend cell scaffolds by melt-molding particulate-leaching method. *Biomaterials* **24**, 4011–4021 (2003).
54. Offeddu, G. S., Ashworth, J. C., Cameron, R. E. & Oyen, M. L. Multi-scale mechanical response of freeze-dried collagen scaffolds for tissue engineering applications. *J. Mech. Behav. Biomed. Mater.* **42**, 19–25 (2015).
55. Zhu, N. & Che, X. Biofabrication of Tissue Scaffolds. *Adv. Biomater. Sci. Biomed. Appl.* 316–328 (2013). doi:10.5772/54125
56. Mad Jin, R. *et al.* Porous PCL/Chitosan and nHA/PCL/Chitosan Scaffolds for Tissue Engineering Applications: Fabrication and Evaluation. *J. Nanomater.* **2015**, 1–8 (2015).
57. Lu, T., Li, Y. & Chen, T. Techniques for fabrication and construction of three-dimensional scaffolds for tissue engineering. *Int. J. Nanomedicine* **8**, 337–350 (2013).
58. Kim, S.-S., Sun Park, M., Jeon, O., Yong Choi, C. & Kim, B.-S. Poly(lactide-co-glycolide)/hydroxyapatite composite scaffolds for bone tissue engineering. *Biomaterials* **27**, 1399–1409 (2006).

59. Bak, T., Kook, M., Jung, S. & Kim, B. Biological Effect of Gas Plasma Treatment on CO₂ Gas Foaming / Salt Leaching Fabricated Porous Polycaprolactone Scaffolds in Bone Tissue Engineering. **2014**, (2014).
60. Chen, H., Blitterswijk, C. V. A. N. & Moroni, L. Fabrication of nanofibrous scaffolds for tissue engineering applications. *Woodhead Publ. Online* (2013). doi:10.1533/9780857097231.1.158
61. Akbarzadeh, R. & Yousefi, A. M. *Effects of processing parameters in thermally induced phase separation technique on porous architecture of scaffolds for bone tissue engineering. Journal of Biomedical Materials Research - Part B Applied Biomaterials* **102**, (2014).
62. Yen, C., He, H., Lee, L. J. & Ho, W. S. W. Synthesis and characterization of nanoporous polycaprolactone membranes via thermally- and nonsolvent-induced phase separations for biomedical device application. *J. Memb. Sci.* **343**, 180–188 (2009).
63. Conoscenti, G. *et al.* PLLA scaffolds produced by thermally induced phase separation (TIPS) allow human chondrocyte growth and extracellular matrix formation dependent on pore size. *Mater. Sci. Eng. C* **80**, 449–459 (2017).
64. Do, A., Khorsand, B., Geary, S. M. & Salem, A. K. 3D Printing of Scaffolds for Tissue Regeneration Applications. *Adv Heal. Mater* **4**, 1742–1762 (2015).
65. Sun, K., Li, R., Jiang, W., Sun, Y. & Li, H. Comparison of three-dimensional printing and vacuum freeze-dried techniques for fabricating composite scaffolds. *Biochem. Biophys. Res. Commun.* **477**, 1085–1091 (2016).
66. Chia, H. N. & Wu, B. M. Recent advances in 3D printing of biomaterials. *J. Biol. Eng.* **9**, 4 (2015).
67. Wu, G. H. & Hsu, S. H. Review: Polymeric-based 3D printing for tissue

- engineering. *J. Med. Biol. Eng.* **35**, 285–292 (2015).
68. de Azevedo Gonçalves Mota, R. C., da Silva, E. O., de Lima, F. F., de Menezes, L. R. & Thiele, A. C. S. 3D Printed Scaffolds as a New Perspective for Bone Tissue Regeneration: Literature Review. *Mater. Sci. Appl.* **7**, 430–452 (2016).
69. Bhardwaj, N. & Kundu, S. C. Electrospinning: a fascinating fiber fabrication technique. *Biotechnol. Adv.* **28**, 325–47 (2010).
70. Haider, A., Haider, S. & Kang, I. K. A comprehensive review summarizing the effect of electrospinning parameters and potential applications of nanofibers in biomedical and biotechnology. *Arab. J. Chem.* (2015). doi:10.1016/j.arabjc.2015.11.015
71. Pillay, V. *et al.* A Review of the Effect of Processing Variables on the Fabrication of Electrospun Nanofibers for Drug Delivery Applications. **2013**, 22 (2013).
72. Ru, C. *et al.* Suspended, Shrinkage-Free, Electrospun PLGA Nanofibrous Scaffold for Skin Tissue Engineering. *ACS Appl. Mater. Interfaces* **7**, 10872–10877 (2015).
73. Khajavi, R., Abbasipour, M. & Bahador, A. Electrospun biodegradable nanofibers scaffolds for bone tissue engineering. *J. Appl. Polym. Sci.* **133**, (2016).
74. Kong, B. & Mi, S. Electrospun scaffolds for corneal tissue engineering: A review. *Materials (Basel)*. **9**, (2016).
75. P Prabhakaran, M., Kai, D., Ghasemi-Mobarakeh, L. & Ramakrishna, S. Electrospun biocomposite nanofibrous patch for cardiac tissue engineering. *Biomed. Mater.* **6**, 55001 (2011).

76. Mirjalili, M. & Zohoori, S. Review for application of electrospinning and electrospun nanofibers technology in textile industry. *J. Nanostructure Chem.* **6**, 207–213 (2016).
77. Askari, P., Zahedi, P. & Rezaeian, I. Three-layered electrospun PVA/PCL/PVA nanofibrous mats containing tetracycline hydrochloride and phenytoin sodium: A case study on sustained control release, antibacterial, and cell culture properties. *J. Appl. Polym. Sci.* **133**, 1–9 (2016).
78. Kim, B. J. *et al.* Accelerated skin wound healing using electrospun nanofibrous mats blended with mussel adhesive protein and polycaprolactone. *J. Biomed. Mater. Res. - Part A* **105**, 218–225 (2017).
79. Sin, D. *et al.* Polyurethane (PU) scaffolds prepared by solvent casting/particulate leaching (SCPL) combined with centrifugation. *Mater. Sci. Eng. C* **30**, 78–85 (2010).
80. Van der Schueren, L., De Schoenmaker, B., Kalaoglu, Ö. I. & De Clerck, K. An alternative solvent system for the steady state electrospinning of polycaprolactone. *Eur. Polym. J.* **47**, 1256–1263 (2011).
81. Warren, S. M. *et al.* A novel flow-perfusion bioreactor supports 3D dynamic cell culture. *J. Biomed. Biotechnol.* **2009**, (2009).
82. Salehi-nik, N. *et al.* Engineering Parameters in Bioreactor 's Design : *Biomed Res. Int.* **2013**, (2015).
83. Kumar, A. in *Supermacroporous Cryogels: Biomedical and Biotechnological Applications* 221 (2016).
84. Rangarajan, S., Madden, L. & Bursac, N. Use of flow, electrical, and mechanical stimulation to promote engineering of striated muscles. *Ann. Biomed. Eng.* **42**, 1391–1405 (2014).

85. Gaspar, D. A., Gomide, V. & Monteiro, F. J. The role of perfusion bioreactors in bone tissue engineering. *Biomatter* **4**, 1–9 (2012).
86. Ng, C. P. & Swartz, M. a. Mechanisms of interstitial flow-induced remodeling of fibroblast-collagen cultures. *Ann. Biomed. Eng.* **34**, 446–454 (2006).
87. Ismadi, M.-Z. *et al.* Flow Characterization of a Spinner Flask for Induced Pluripotent Stem Cell Culture Application. *PLoS One* **9**, e106493 (2014).
88. Sucosky, P., Osorio, D. F., Brown, J. B. & Neitzel, G. P. Fluid Mechanics of a Spinner-Flask Bioreactor. *Biotechnol. Bioeng.* **85**, 34–46 (2004).
89. Stiehler, M. *et al.* Effect of dynamic 3-D culture on proliferation, distribution, and osteogenic differentiation of human mesenchymal stem cells. *J. Biomed. Mater. Res. - Part A* **89**, 96–107 (2009).
90. U. Maver, T. Maver, Z. Peršin, M. Mozetič, A. Vesel, M. G. and K. S.-K. World's largest Science , Technology & Medicine Open Access book publisher
Title : ' Amyloid ' — Historical Aspects. *Polym. Sci.* (2013). doi:10.5772/63266
91. Skardal, A., Sarker, S. F., Crabbé, A., Nickerson, C. A. & Prestwich, G. D. The generation of 3-D tissue models based on hyaluronan hydrogel-coated microcarriers within a rotating wall vessel bioreactor. *Biomaterials* **31**, 8426–8435 (2010).
92. Yu, X., Botchwey, E. a, Levine, E. M., Pollack, S. R. & Laurencin, C. T. Bioreactor-based bone tissue engineering: the influence of dynamic flow on osteoblast phenotypic expression and matrix mineralization. *Proc. Natl. Acad. Sci. U. S. A.* **101**, 11203–8 (2004).
93. Wang, L. *et al.* Repair of segmental bone defect using totally vitalized tissue engineered bone graft by a combined perfusion seeding and culture system. *PLoS One* **9**, (2014).

94. Przyborski, S. *Technology platforms for 3D cell culture*. (John Wiley & Sons, 2017).
95. Mazzei, D., Guzzardi, M. a, Giusti, S. & Ahluwalia, a. A low shear stress modular bioreactor for connected cell culture under high flow rates. *Biotechnol. Bioeng.* **106**, 127–37 (2010).
96. Minuth, W. W. & Denk, L. Supportive development of functional tissues for biomedical research using the MINUSHEET® perfusion system. *Clin. Transl. Med.* **1**, 22 (2012).
97. Vinci, B. *et al.* An in vitro model of glucose and lipid metabolism in a multicompartmental bioreactor. *Biotechnol. J.* **7**, 117–26 (2012).
98. Vinci, B. *et al.* Modular bioreactor for primary human hepatocyte culture: medium flow stimulates expression and activity of detoxification genes. *Biotechnol. J.* **6**, 554–64 (2011).
99. Vinci, B. *et al.* In vitro liver model using microfabricated scaffolds in a modular bioreactor. *Biotechnol. J.* **5**, 232–241 (2010).
100. Leester-Schaedel, M., Lorenz, T., Juergens, F. & Richter, C. *Fabrication of Microfluidic Devices*. (Springer, 2016). doi:10.1007/978-3-319-26920-7
101. Pagliari, S. *et al.* A multistep procedure to prepare pre-vascularized cardiac tissue constructs using adult stem cells, dynamic cell cultures, and porous scaffolds. *Front. Physiol.* **5 JUN**, 1–12 (2014).
102. Rashidi, H., Alhaque, S., Szkolnicka, D., Flint, O. & Hay, D. C. Fluid shear stress modulation of hepatocyte-like cell function. *Arch. Toxicol.* **90**, 1757–1761 (2016).
103. Ucciferri, N. *et al.* In vitro toxicological screening of nanoparticles on primary human endothelial cells and the role of flow in modulating cell response.

Nanotoxicology **8**, 697–708 (2014).

104. Ltd, K. QV500 Cell culture chamber. (2017). Available at: <http://www.kirkstall.com/qv500/>. (Accessed: 29th August 2017)
105. Giusti, S. *et al.* A novel dual-flow bioreactor simulates increased fluorescein permeability in epithelial tissue barriers. *Biotechnol. J.* **9**, 1175–1184 (2014).
106. K, Groschwitz and S, H. Intestinal Barrier Function: Molecular Regulation and Disease Pathogenesis. *J Allergy Clin Immunol* **124**, 3–22 (2009).
107. Ltd, K. QV600 Cell culture chamber. (2017). Available at: <http://www.kirkstall.com/qv600/>. (Accessed: 29th August 2017)
108. Nithiananthan, S., Crawford, A., Cooper Knock, J., Lambert, D. W. & Whawell, S. A. Physiological Fluid Flow Moderates Fibroblast Responses to TGF- β 1. *J. Cell. Biochem.* **890**, 878–890 (2016).
109. Ltd, K. QV900 Cell culture chamber. (2017). Available at: <http://www.kirkstall.com/qv900/>. (Accessed: 29th August 2017)
110. Ward, A., Quinn, K. P., Bellas, E., Georgakoudi, I. & Kaplan, D. L. Noninvasive metabolic imaging of engineered 3D human adipose tissue in a perfusion bioreactor. *PLoS One* **8**, e55696 (2013).
111. Abbott, R. D. *et al.* Long term perfusion system supporting adipogenesis. *Methods* **84**, 84–89 (2015).
112. Kiyatec. 3DKUBE Cell Migration. (2017). Available at: <http://www.shop.kiyatec.com/3DKUBE-Cell-Migration-3D030.htm>. (Accessed: 20th June 2017)
113. Velve-Casquillas, G., Le Berre, M., Piel, M. & Tran, P. T. Microfluidic tools for cell biological research. *Nano Today* **5**, 28–47 (2010).

114. Bhatia, S. N. & Ingber, D. E. Microfluidic organs-on-chips. *Nat. Biotechnol.* **32**, 760–772 (2014).
115. Tang, S. & Whitesides, G. Basic microfluidic and soft lithographic techniques. *Optofluidics Fundam. Devices, Appl.* 7–32 (2010).
116. Halldorsson, S., Lucumi, E., Gómez-Sjöberg, R. & Fleming, R. M. T. Advantages and challenges of microfluidic cell culture in polydimethylsiloxane devices. *Biosens. Bioelectron.* **63**, 218–231 (2015).
117. Huh, D. A human breathing lung-on-a-chip. *Ann. Am. Thorac. Soc.* **12**, S42–S44 (2015).
118. Harrington, H. C. *et al.* Electrospun PLGA fibre sheets incorporating fluorescent nanosensors: self-reporting scaffolds for application in tissue engineeringfile:///C:/Users/paxsa7/Downloads/852112.pdf. *Anal. Methods* **5**, 68 (2013).
119. Papantoniou, I. *et al.* Three-Dimensional Characterization of Tissue-Engineered Constructs by Contrast-Enhanced Nanofocus Computed Tomography. *Tissue Eng. Part C Methods* **20**, 177–187 (2014).
120. Kotecha, M., Klatt, D. & Magin, R. L. Monitoring Cartilage Tissue Engineering Using Magnetic Resonance Spectroscopy, Imaging, and Elastography. *Tissue Eng. Part B Rev.* **19**, 470–484 (2013).
121. Boubriak, O. A., Urban, J. P. G. & Cui, Z. Monitoring of metabolite gradients in tissue-engineered constructs. *J. R. Soc. Interface* **3**, 637–648 (2006).
122. Hasan, A. *et al.* Recent advances in application of biosensors in tissue engineering. *Biomed Res. Int.* **2014**, (2014).
123. Perestrelo, A. R., ??guas, A. C. P., Rainer, A. & Forte, G. Microfluidic organ/body-on-a-chip devices at the convergence of biology and

- microengineering. *Sensors (Switzerland)* **15**, 31142–31170 (2015).
124. Shin, S. R. *et al.* Label-Free and Regenerative Electrochemical Microfluidic Biosensors for Continual Monitoring of Cell Secretomes. *Adv. Sci.* **4**, 1–14 (2017).
 125. GS, S., CV, A. & Mathew, B. B. Biosensors: A Modern Day Achievement. *J. Instrum. Technol.* **2**, 26–39 (2014).
 126. Hammond, J. L., Formisano, N., Estrela, P., Carrara, S. & Tkac, J. Electrochemical biosensors and nanobiosensors. *Essays Biochem.* **60**, 69–80 (2016).
 127. Săndulescu, R., Tertîş, M., Cristea, C. & Bodoki, E. in *New Materials for the Construction of Electrochemical Biosensors* (2015).
 128. Stradiotto, N. R., Yamanaka, H. & Zanoni, M. V. B. Electrochemical sensors: a powerful tool in analytical chemistry . *Journal of the Brazilian Chemical Society* **14**, 159–173 (2003).
 129. Chaplin, M. Amperometric biosensors. (2014). Available at: <http://www1.lsbu.ac.uk/water/enztech/amperometric.html>.
 130. Thévenot, D. R., Toth, K., Durst, R. A. & Wilson, G. S. Electrochemical biosensors: Recommended definitions and classification. *Biosens. Bioelectron.* **16**, 121–131 (2001).
 131. Long, F., Zhu, A. & Shi, H. Recent advances in optical biosensors for environmental monitoring and early warning. *Sensors (Basel)*. **13**, 13928–13948 (2013).
 132. Damborsky, P., vitel, J. & Katrlík, J. Optical biosensors. *Essays Biochem.* **60**, 91–100 (2016).
 133. Jankowska, D. A. *et al.* Simultaneous detection of pH value and glucose

- concentrations for wound monitoring applications. *Biosens. Bioelectron.* **87**, 312–319 (2017).
134. A.Ettinger and T.Wittmann. Fluorescence Live Cell Imaging. *Methods Cell Biol.* **123**, 77–94 (2014).
135. Jensen, E. C. Overview of Live-Cell Imaging: Requirements and Methods Used. *Anat. Rec.* 1–8 (2013).
136. Tian, L., Levée, V., Mentag, R., Charest, P. & Séguin, A. Green fluorescent protein as a tool for monitoring transgene expression in forest tree species. *Tree Physiol.* **19**, 541–546 (1999).
137. Noguchi, T. & Golden, S. Bioluminescent and fluorescent reporters in circadian rhythm studies. 1–24
138. Buck, S. M., Xu, H., Brasuel, M., Philbert, M. A. & Kopelman, R. Nanoscale probes encapsulated by biologically localized embedding (PEBBLEs) for ion sensing and imaging in live cells. *Talanta* **63**, 41–59 (2004).
139. Clark, H. A., Hoyer, M., Parus, S., Philbert, M. A. & Kopelman, R. Optochemical Nanosensors and Subcellular Applications in Living Cells. *Microchim. Acta* **131**, 121–128 (1999).
140. Di Si, T. E., Lee, Y.-E. K. & Kopelman, R. Nanoparticle PEBBLE Sensors for Quantitative Nanomolar Imaging of Intracellular Free Calcium Ions. *Anal* **84**, 978–986 (2012).
141. Park, E. J., Brasuel, M., Behrend, C., Philbert, M. A. & Kopelman, R. Ratiometric Optical PEBBLE Nanosensors for Real-Time Magnesium Ion Concentrations Inside Viable Cells. *Anal. Chem.* **75**, 3784–3791 (2003).
142. Xu, H., Aylott, J. W. & Kopelman, R. Fluorescent nano-PEBBLE sensors designed for intracellular glucose imaging. *Analyst* **127**, 1471–1477 (2002).

143. Marín, M. J., Galindo, F., Thomas, P. & Russell, D. A. Localized intracellular pH measurement using a ratiometric photoinduced electron-transfer-based nanosensor. *Angew. Chemie - Int. Ed.* **51**, 9657–9661 (2012).
144. Lee, Y. K. & Smith, R. Nanoparticle PEBBLE sensors in live cells and in vivo. *Annu Rev Anal Chem* **57–76** (2010). doi:10.1146/annurev.anchem.1.031207.112823.Nanoparticle
145. RUSNANO. High-Tech Synthesis of Colloidal Quantum Dots Begins in Dubna. (2011). Available at: <http://en.rusnano.com/press-centre/news/88604>. (Accessed: 31st August 2017)
146. Roy, P., Dutta, A. & Chang, S. Development and evaluation of a functional bioreactor for CO fermentation into ethanol. *Bioresour. Bioprocess.* **3**, 4 (2016).
147. Timm, A. C., Shankles, P. G., Foster, C. M., Doktycz, M. J. & Retterer, S. T. Characterization of extended channel bioreactors for continuous-flow protein production. *J. Vac. Sci. Technol. B, Nanotechnol. Microelectron. Mater. Process. Meas. Phenom.* **33**, 06FM02 (2015).
148. Gallo–Ramírez, L. E., Nikolay, A., Genzel, Y. & Reichl, U. Bioreactor concepts for cell culture-based viral vaccine production. *Expert Rev. Vaccines* **14**, 1181–1195 (2015).
149. Reinecke, T., Biechele, P., Schulte, V., Scheper, T. & Zimmermann, S. Low-cost sensor system for non-invasive monitoring of cell growth in disposable bioreactors. *Procedia Eng.* **120**, 548–551 (2015).
150. Lourenço, N. D., Lopes, J. A., Almeida, C. F., Sarraguça, M. C. & Pinheiro, H. M. Bioreactor monitoring with spectroscopy and chemometrics: A review. *Anal. Bioanal. Chem.* **404**, 1211–1237 (2012).

151. Acosta, M. a, Kostov, Y. & Leach, J. B. Microfluidic bioreactors as tools for monitoring cell microenvironment. 200–200 (2007).
152. Sun, S., Ungerböck, B. & Mayr, T. Imaging of oxygen in microreactors and microfluidic systems. *Methods Appl. Fluoresc.* **3**, 34002 (2015).
153. Shaegh, S. A. M. *et al.* A microfluidic optical platform for real-time monitoring of pH and oxygen in microfluidic bioreactors and organ-on-chip devices. *Biomicrofluidics* **10**, (2016).
154. Carstea, E. Fluorescence Spectroscopy as a Potential Tool for in-situ Monitoring of Dissolved Organic Matter in Surface Water Systems. *Water Pollut.* 3–68 (2012). doi:10.5772/1418
155. Johnson, I. D. & Davidson, M. W. Jablonski Energy Diagram. *Olympus America Inc.* (2012). Available at: <http://www.olympusmicro.com/primer/java/jablonski/jabintro/>. (Accessed: 4th June 2017)
156. Combs, C. A. Fluorescence Microscopy: A concise guide to Current Imaging Methods. *Curr. Protoc. Neurosci.* 1–19 (2010). doi:10.1002/0471142301.ns0201s50.Fluorescence
157. Nobel Media AB. The Transmission Electron Microscope. (2017). Available at: <https://www.nobelprize.org/educational/physics/microscopes/tem/>. (Accessed: 24th September 2017)
158. Gul Amin. White LEDs Printed on Paper. (Linköping University, Sweden, 2012).
159. Ilya Sherman. Resolution Of An Electron Microscope. *An encyclopedia of scientific essays* (2000).
160. Kong, T. C. U. of H. Principle of TEM. (2017). Available at: <http://www.hk->

phy.org/atomic_world/tem/tem02_e.html. (Accessed: 24th September 2017)

161. Allen, J. R. pH Electrodes, Ion-Selective Electrodes, and Oxygen Sensors: Electrochemical Sensors Used in the Medical Field. *Lab. Med.* **34**, 544–547 (2003).
162. Vanysek, P. The Glass pH Electrode. *Electrochem. Soc. Interface* 19–20 (2004).
163. Chauhan, V. M., Orsi, G., Brown, A., Pritchard, D. I. & Aylott, J. W. Mapping the pharyngeal and intestinal pH of *Caenorhabditis elegans* and real-time luminal pH oscillations using extended dynamic range pH-sensitive nanosensors. *ACS Nano* **7**, 5577–87 (2013).
164. Pharmacy, U. E. S. of. Buffers and Buffer Capacity. Available at: <https://pharmlabs.unc.edu/labs/opthalmics/buffers.htm>. (Accessed: 31st January 2018)
165. Tim Soderberg. in *Organic Chemistry Textbook Maps* (2016).
166. Lower, S. in *General Chemistry Textbook Maps* (2017).
167. Heather Voigt. in *Chemical Equilibria* (2017).
168. Jim Clark. THEORIES OF ACIDS AND BASES. (2017). Available at: <https://www.chemguide.co.uk/physical/acidbaseeqia/theories.html>. (Accessed: 31st January 2018)
169. Norberg, P. & Mastro, G. in *Physical and Theoretical Chemistry* (2017).
170. Kevin R. Siebenlist. Acids , Bases , and Buffers. 1–5 (2011).
171. Team, I. Buffers and Salts. (2006). Available at: http://interchemnet.um.maine.edu/data/labs/Buf_8973.htm. (Accessed: 24th January 2018)

172. Desai, A. Development of optical pH nanosensors for biological insights into the intracellular trafficking of nanomedicines. (University of Nottingham, 2014).
173. Wolfbeis, O. S. Fiber-Optic Chemical Sensors and Biosensors. 3269–3284 (2004). doi:10.1021/ac040049d
174. Agarwal, S., Wendorff, J. H. & Greiner, A. Use of electrospinning technique for biomedical applications. *Polymer (Guildf)*. **49**, 5603–5621 (2008).
175. Casasola, R., Thomas, N. L., Trybala, A. & Georgiadou, S. Electrospun poly lactic acid (PLA) fibres: Effect of different solvent systems on fibre morphology and diameter. *Polymer (Guildf)*. **55**, 4728–4737 (2014).
176. Wulkersdorfer, B. *et al.* Bimodal porous scaffolds by sequential electrospinning of poly(glycolic acid) with sucrose particles 436178. *Int. J. Polym. Sci.* **2010**, (2010).
177. Sadeghi, A. R. *et al.* Surface modification of electrospun PLGA scaffold with collagen for bioengineered skin substitutes. *Mater. Sci. Eng. C* **66**, 130–137 (2016).
178. Baker, S. R., Banerjee, S., Bonin, K. & Guthold, M. Determining the mechanical properties of electrospun poly-ε-caprolactone (PCL) nanofibers using AFM and a novel fiber anchoring technique. *Mater. Sci. Eng. C* **59**, 203–212 (2016).
179. Wang, C., Lee, M. & Wu, Y. Solution-Electrospun Poly(ethylene terephthalate) Fibers: Processing and Characterization. (2012).
180. Bosworth, L. & Downes, S. in *Wound dressings* 327 (Woodhead Publishing, 2011).
181. Anezka Lengalova, Alenka Vesel, Yakai Feng, and V. S. Biodegradable

- Polymers for Medical Purposes . *Int. J. Polym. Sci.* 1–2 (2016).
doi:10.1007/978-94-009-4390-2_5
182. Lim, Y., Gwon, H., Jeun, J. P. & Nho, Y. Preparation of Cellulose-based Nanofibers Using Electrospinning. *Nanofibers* 179–188 (2010).
doi:10.5772/8153
183. Tayerani, E., Ghoreishi, S. M., Habibi, N., Pastorino, L. & Ruggiero, C. Electrospun chitosan nanofibers for tissue engineering. *14th IEEE International Conference on Nanotechnology* 943–946 (2014).
doi:10.1109/NANO.2014.6968179
184. Sheikh, F. A. *et al.* 3D electrospun silk fibroin nanofibers for fabrication of artificial skin. *Nanomedicine Nanotechnology, Biol. Med.* **11**, 681–691 (2015).
185. Zhang, Y. Z., Venugopal, J., Huang, Z. M., Lim, C. T. & Ramakrishna, S. Crosslinking of the electrospun gelatin nanofibers. *Polymer (Guildf)*. **47**, 2911–2917 (2006).
186. Jiang, Q., Reddy, N., Zhang, S., Roscioli, N. & Yang, Y. Water-stable electrospun collagen fibers from a non-toxic solvent and crosslinking system. *J. Biomed. Mater. Res. - Part A* **101 A**, 1237–1247 (2013).
187. Espíndola-González, A. *et al.* Natural-Synthetic hybrid polymers developed via electrospinning: The effect of PET in chitosan/starch system. *Int. J. Mol. Sci.* **12**, 1908–1920 (2011).
188. Huang, Z. M., Zhang, Y. Z., Ramakrishna, S. & Lim, C. T. Electrospinning and mechanical characterization of gelatin nanofibers. *Polymer (Guildf)*. **45**, 5361–5368 (2004).
189. Aramwit, P., Jaichawa, N., Ratanavaraporn, J. & Srichana, T. A comparative study of type A and type B gelatin nanoparticles as the controlled release

- carriers for different model compounds. *Mater. Express* **5**, 241–248 (2015).
190. Elliott, D. E., Davis, F. J., Mitchell, G. R. & Olley, R. H. Structure development in electrospun fibres of gelatin. *J. Phys. Conf. Ser.* **183**, 12021 (2009).
 191. Chaplin, M. Gelatin. Available at: <http://www1.lsbu.ac.uk/water/gelatin.html>. (Accessed: 2nd April 2017)
 192. Lee, H., Lim, S., Birajdar, M. S., Lee, S. H. & Park, H. Fabrication of FGF-2 immobilized electrospun gelatin nanofibers for tissue engineering. *Int. J. Biol. Macromol.* **93**, 1559–1566 (2016).
 193. Wang, H. *et al.* Fabrication and characterization of electrospun gelatin-heparin nanofibers as vascular tissue engineering. *Macromol. Res.* **21**, 860–869 (2013).
 194. Yao, C.-H., Yeh, J.-Y., Chen, Y.-S., Li, M.-H. & Huang, C.-H. Wound-healing effect of electrospun gelatin nanofibres containing *Centella asiatica* extract in a rat model. *J. Tissue Eng. Regen. Med.* **11**, 1–937 (2017).
 195. Mindru, T. B., Mindru, I. B., Malutant, T. & Tura, V. Electrospinning of high concentration gelatin solutions. *J. Optoelectron. Adv. Mater.* **9**, 3633–3638 (2007).
 196. Zhan, J. & Lan, P. The Review on Electrospun Gelatin Fiber Scaffold. *J. Res. Updat. Polym. Sci.* **1**, 59–71 (2012).
 197. Chong, E. J. *et al.* Evaluation of electrospun PCL/gelatin nanofibrous scaffold for wound healing and layered dermal reconstitution. *Acta Biomater.* **3**, 321–330 (2007).
 198. Pereira, I. H. L. *et al.* Elaboration and characterization of coaxial electrospun poly(ϵ -caprolactone)/gelatin nanofibers for biomedical applications. *Adv. Polym. Technol.* **33**, 1–10 (2014).

199. Siimon, K., M?isavald, K., Siimon, H. & J?rvek?lg, M. Increasing mechanical strength of electrospun gelatin nanofibers by the addition of aluminum potassium sulfate. *J. Appl. Polym. Sci.* **132**, 2–6 (2015).
200. You, Y., Sun, X., Cui, Q., Wang, B. & Ma, J. The Retention and Drainage Behavior of Cross-linked Gelatin with Glutaraldehyde in a Papermaking System. **11**, 6162–6173 (2016).
201. Apostolov, A. A., Boneva, D., Vassileva, E., Mark, J. E. & Fakirov, S. Mechanical Properties of Native and Crosslinked Gelatins. 2041–2048 (1999).
202. Panzavolta, S. *et al.* Electrospun gelatin nanofibers: Optimization of genipin cross-linking to preserve fiber morphology after exposure to water. *Acta Biomater.* **7**, 1702–1709 (2011).
203. Chou, S.-F., Luo, L.-J., Lai, J.-Y. & Ma, D. H.-K. Role of solvent-mediated carbodiimide cross-linking in fabrication of electrospun gelatin nanofibrous membranes as ophthalmic biomaterials. *Mater. Sci. Eng. C* **71**, 1145–1155 (2017).
204. Chemical Industry Education Centre. Polyesters. Available at: <http://www.essentialchemicalindustry.org/polymers/polyesters.html>. (Accessed: 2nd April 2017)
205. Khodadoust, M., Mohebbi-Kalhari, D. & Jirofti, N. Fabrication and Characterization of Electrospun Bi-Hybrid PU/PET Scaffolds for Small-Diameter Vascular Grafts Applications. *Cardiovasc. Eng. Technol.* (2017). doi:10.1007/s13239-017-0338-6
206. Maitz, M. F. Applications of synthetic polymers in clinical medicine. *Biosurface and Biotribology* **1**, 161–176 (2015).

207. Ma, Z., Kotaki, M., Yong, T., He, W. & Ramakrishna, S. Surface engineering of electrospun polyethylene terephthalate (PET) nanofibers towards development of a new material for blood vessel engineering. *Biomaterials* **26**, 2527–2536 (2005).
208. G. E. Morris, J. C. Bridge, O. M. I. Eltboli, M. P. Lewis, A. J. Knox, J. W. Aylott, C. E. Brightling, A. M. Ghaemmaghami, and F. R. A. J. R. Human airway smooth muscle maintain in situ cell orientation and phenotype when cultured on aligned electrospun scaffolds. *Am. J. Physiol. - Lung Cell. Mol. Physiol.* **307**, L38–L47 (2014).
209. Lei, Y., Remy, M., Labrugere, C. & Durrieu, M. C. Peptide immobilization on polyethylene terephthalate surfaces to study specific endothelial cell adhesion, spreading and migration. *J. Mater. Sci. Mater. Med.* **23**, 2761–2772 (2012).
210. Gustafsson, Y. *et al.* Viability and proliferation of rat MSCs on adhesion protein-modified PET and PU scaffolds. *Biomaterials* **33**, 8094–8103 (2012).
211. Mahalingam, S., Raimi-Abraham, B. T., Craig, D. Q. M. & Edirisinghe, M. Solubility–spinnability map and model for the preparation of fibres of polyethylene (terephthalate) using gyration and pressure. *Chem. Eng. J.* **280**, 344–353 (2015).
212. Weng, L. & Xie, J. Smart Electrospun Nanofibers for Controlled Drug Release: Recent Advances and New Perspectives. *Curr Pharm Des* **21**, 1944–1959 (2015).
213. Ranganath, A. S., Ganesh, V. A., Sopiha, K., Sahay, R. & Baji, A. Thermoresponsive electrospun membrane with enhanced wettability. *RSC Adv.* **7**, 19982–19989 (2017).

214. Venugopal, A. P., Cespedes, O. & Russell, S. J. Controlling Dielectric and Magnetic Properties of PVdF / Magnetite Nanocomposite Fibre Webs. *Int. J. Polym. Sci.* **2014**, (2014).
215. Syu, J.-H. *et al.* Electrospun Fibers as a Solid-State Real-Time Zinc Ion Sensor with High Sensitivity and Cell Medium Compatibility. *Adv. Funct. Mater.* **23**, 1566–1574 (2013).
216. You, M.-H. *et al.* Colorimetric Humidity Sensors Based on Electrospun Polyamide/CoCl₂ Nanofibrous Membranes. *Nanoscale Res. Lett.* **12**, 360 (2017).
217. Wang, L. *et al.* Electrospinning pH-Responsive Block Copolymer Nanofibers. *Adv. Mater.* **19**, 3544–3548 (2007).
218. Di, W., Czarny, R. S., Fletcher, N. A., Krebs, M. D. & Clark, H. A. Comparative Study of Poly (ε-Caprolactone) and Poly(Lactic-co-Glycolic Acid) -Based Nanofiber Scaffolds for pH-Sensing. *Pharm. Res.* **33**, 2433–2444 (2016).
219. Gentile, P., Chiono, V., Carmagnola, I. & Hatton, P. V. An overview of poly(lactic-co-glycolic) Acid (PLGA)-based biomaterials for bone tissue engineering. *Int. J. Mol. Sci.* **15**, 3640–3659 (2014).
220. Qi, J. *et al.* Fluorescent pH Sensors for Broad-Range pH Measurement Based on a Single Fluorophore. *Anal. Chem.* **87**, 5897–5904 (2015).
221. Desai, A. S., Chauhan, V. M., Johnston, A. P. R., Esler, T. & Aylott, J. W. Fluorescent nanosensors for intracellular measurements: Synthesis, characterization, calibration, and measurement. *Front. Physiol.* **4 JAN**, 1–15 (2014).
222. Clark, H. A., Hoyer, M., Philbert, M. A. & Kopelman, R. Optical nanosensors

- for chemical analysis inside single living cells. 1. Fabrication, characterization, and methods for intracellular delivery of PEBBLE sensors. *Anal. Chem.* **71**, 4831–4836 (1999).
223. Aylott, J. W. Optical nanosensors—an enabling technology for intracellular measurements. *Analyst* **128**, 309–312 (2003).
224. Zhang, X. *et al.* pH-Sensitive Fluorescent Dyes: Are They Really pH-Sensitive in Cells? *Mol. Pharma* **10**, 1910–1917 (2013).
225. Ferrari, L., Rovati, L., Fabbri, P. & Pilati, F. Disposable fluorescence optical pH sensor for near neutral solutions. *Sensors (Switzerland)* **13**, 484–499 (2013).
226. Mottram, L., Boonyarattanakalin, S., Kovel, R. E. & Peterson, B. R. The Pennsylvania Green Fluorophore: A Hybrid of Oregon Green and Tokyo Green for the Construction of Hydrophobic and pH Insensitive Molecular Probes. *Org Lett* **8**, 581–584 (2006).
227. Søndergaard, R. V, Henriksen, J. R. & Andresen, T. L. Design, calibration and application of broad-range optical nanosensors for determining intracellular pH. *Nat. Protoc.* **9**, 2841–2858 (2014).
228. Hornig, S., Schulz, A., Mohr, G. & Heinze, T. Fluorescent Polysaccharide Nanoparticles for pH Sensing. *J. Photopolym. Sci. Technol.* **22**, 671–673 (2009).
229. Korzeniowska, B. *et al.* Intracellular pH-Sensing Using Core/Shell Silica Nanoparticles. *Journal of Biomedical Nanotechnology* **10**, 1336–1345
230. Allard, E. & Larpent, C. Core-Shell Type Dually Fluorescent Polymer Nanoparticles for Ratiometric pH-Sensing. *J. Polym. Sci. Part A Polym. Chem.* **46**, 6206–6213 (2008).

231. Sun, H., Scharff-Poulsen, A. M., Gu, H. & Almdal, K. Synthesis and characterization of ratiometric, pH sensing nanoparticles with covalently attached fluorescent dyes. *Chem. Mater.* **18**, 3381 (2006).
232. Burns, A., Sengupta, P., Zedayko, T., Baird, B. & Wiesner, U. Core/shell fluorescent silica nanoparticles for chemical sensing: Towards single-particle laboratories. *Small* **2**, 723–726 (2006).
233. Gao, F., Tang, L., Dai, L. & Wang, L. A fluorescence ratiometric nano-pH sensor based on dual-fluorophore-doped silica nanoparticles. *Spectrochim. Acta - Part A Mol. Biomol. Spectrosc.* **67**, 517–521 (2007).
234. Ji, J., Rosenzweig, N., Griffin, C. & Rosenzweig, Z. Synthesis and application of submicrometer fluorescence sensing particles for lysosomal pH measurements in murine macrophages. *Anal. Chem.* **72**, 3497–3503 (2000).
235. Schulz, A., Wotschadlo, J., Heinze, T. & Mohr, G. J. Fluorescent nanoparticles for ratiometric pH-monitoring in the neutral range. *J. Mater. Chem.* **20**, 1475 (2010).
236. Lobnik, A., Turel, M. & Urek, Š. K. in *Advances in Chemical Sensors* (2016). doi:10.5772/711
237. Instruments, M. INFORM WHITE PAPER DYNAMIC LIGHT SCATTERING. 1–6 (2011).
238. Kalia, S. & Haldorai, Y. in *Advances in Polymer Science* 93 (Springer, 2015).
239. Andersson, R. L., Cabedo, L., Hedenqvist, M. S., Olsson, R. T. & Ström, V. Superparamagnetic [sic] nanofibers by electrospinning. *RSC Adv.* **6**, 21413–21422 (2016).
240. Htwe, S. S. *et al.* Investigating NF-κB signaling in lung fibroblasts in 2D and 3D culture systems. *Respir. Res.* **16**, 144 (2015).

241. Ma, P. X. & Elisseeff, J. in *Scaffolds in Tissue Engineering* 324 (Taylor & Francis Group, 2008).
242. Wang, B., Wang, J., Zhao, S., Yin, Z. & Li, C. Waterproof and Moisture Permeability Performance of Laminated Fabrics with Electrospun Nano Fibrous Membrane. *J. Text. Eng Fash. Technol ogy* **2**, (2017).
243. Venkatachalam, S. *et al.* in *Polyester* (ed. Saleh, H. E.-D. M.) (2012). doi:10.5772/711
244. Rose, J. B. Development of Clinically Adoptable Gelatin - based Grafts for the Treatment of Corneal Blindness. (2014).
245. Sisson, K., Zhang, C., Farach-Carson, M. C., Chase, D. B. & Rabolt, J. F. Evaluation of cross-linking methods for electrospun gelatin on cell growth and viability. *Biomacromolecules* **10**, 1675–1680 (2009).
246. Chaochai, T., Imai, Y., Furuike, T. & Tamura, H. Preparation and Properties of Gelatin Fibers Fabricated by Dry Spinning. *Fibers* **4**, 2 (2016).
247. Wu, S.-C. *et al.* Cell adhesion and proliferation enhancement by gelatin nanofiber scaffolds. *J. Bioact. Compat. Polym.* **26**, 565–577 (2011).
248. Farris, A., Rindone, A. & Grayson, W. Oxygen Delivering Biomaterials for Tissue Engineering. *J. Mater. Chem. B* (2016). doi:10.1039/C5TB02635K
249. Stamm, A. *et al.* In vitro wound healing assays - State of the art. *BioNanoMaterials* **17**, 79–87 (2016).
250. Sticker, D., Lechner, S., Jungreuthmayer, C., Zanghellini, J. & Ertl, P. Microfluidic Migration and Wound Healing Assay Based on Mechanically Induced Injuries of Defined and Highly Reproducible Areas. *Anal. Chem.* **89**, 2326–2333 (2017).
251. Nyegaard, S., Christensen, B. & Rasmussen, J. T. An optimized method for

- accurate quantification of cell migration using human small intestine cells. *Metab. Eng. Commun.* **3**, 76–83 (2016).
252. Riahi, R., Yang, Y., Zhang, D. D. & Wong, P. K. Advances in Wound-Healing Assays for Probing Collective Cell Migration. *J. Lab. Autom.* **17**, 59–65 (2012).
253. Liang, C.-C., Park, A. Y. & Guan, J.-L. In vitro scratch assay: a convenient and inexpensive method for analysis of cell migration in vitro. *Nat. Protoc.* **2**, 329–333 (2007).
254. Ueck, C. *et al.* Comparison of in-vitro and ex-vivo wound healing assays for the investigation of diabetic wound healing and demonstration of a beneficial effect of a triterpene extract. *PLoS One* **12**, 1–16 (2017).
255. Demirci, S., Doğan, A., Demirci, Y. & Şahin, F. In vitro wound healing activity of methanol extract of *Verbascum speciosum*. *Int. J. Appl. Res. Nat. Prod.* **7**, 37–44 (2014).
256. Legrand, C. *et al.* Airway epithelial cell migration dynamics. MMP-9 role in cell-extracellular matrix remodeling. *J. Cell Biol.* **146**, 517–529 (1999).
257. Conde, a J., Salvatierra, E., Podhajcer, O., Fraigi, L. & Madrid, R. E. Wound healing assay in a low-cost microfluidic platform. *J. Phys. Conf. Ser.* **477**, 12035 (2013).
258. Xie, Y. *et al.* Development of a Three-Dimensional Human Skin Equivalent Wound Model for Investigating Novel Wound Healing Therapies. *Tissue Eng. Part C Methods* **16**, 1111–1123 (2010).
259. Safferling, K. *et al.* Wound healing revised: A novel reepithelialization mechanism revealed by in vitro and in silico models. *J. Cell Biol.* **203**, 691–709 (2013).

260. Chen, Z., Yang, J., Wu, B. & Tawil, B. A Novel Three-Dimensional Wound Healing Model. *J. Dev. Biol.* **2**, 198–209 (2014).
261. Karamichos, D., Lakshman, N. & Petroll, M. W. An Experimental Model for Assessing Fibroblast Migration in 3-D Collagen Matrices. *Cell Motil. Cytoskelet.* **66**, 1–9 (2009).
262. Timm, D. M. *et al.* A high-throughput three-dimensional cell migration assay for toxicity screening with mobile device-based macroscopic image analysis. *Sci. Rep.* **3**, 3000 (2013).
263. Chackalamannil, S., Rotella, D. & Ward, S. *Comprehensive Medicinal Chemistry III.* (Elsevier Science, 2017).
264. Giusti, S. *et al.* Environmental Control in Flow Bioreactors. *Processes* **5**, 16 (2017).
265. Hasan, A. in *Tissue Engineering for Artificial Organs: Regenerative Medicine, Smart Diagnostics and Personalized Medicine* 312 (John Wiley & Sons, 2017).
266. Pappas, D. *Practical Cell Analysis.* (John Wiley & Sons, 2010).
267. Tan, P. H. *et al.* Immunohistochemical detection of Ki67 in breast cancer correlates with transcriptional regulation of genes related to apoptosis and cell death. *Mod Pathol* **18**, 374–381 (2005).
268. Kim, L., Vahey, M. D., Lee, H.-Y. & Voldman, J. Microfluidic arrays for logarithmically perfused embryonic stem cell culture. *Lab Chip* **6**, 394–406 (2006).
269. Korin, N., Bransky, A., Dinnar, U. & Levenberg, S. A parametric study of human fibroblasts culture in a microchannel bioreactor. *Lab Chip* **7**, 611–617 (2007).

270. Park, M. G., Heeyeong, J., Lee, S.-H. & Lee, C. J. Flow Shear Stress Enhances the Proliferative Potential of Cultured Radial Glial Cells Possibly Via an Activation of Mechanosensitive Calcium Channel. **26**, 1–11 (2017).
271. Haga, M., Yamashita, A., Paszkowiak, J., Sumpio, B. E. & Dardik, A. Oscillatory shear stress increases smooth muscle cell proliferation and akt phosphorylation. *J. Vasc. Surg.* **37**, 1277–1284 (2003).
272. Ng, C. P. & Swartz, M. a. Fibroblast alignment under interstitial fluid flow using a novel 3-D tissue culture model. *Am. J. Physiol. Heart Circ. Physiol.* **284**, H1771-7 (2003).
273. Dan, L., Chua, C. K. & Leong, K. F. Fibroblast response to interstitial flow: A state-of-the-art review. *Biotechnol. Bioeng.* **107**, 1–10 (2010).
274. Kurulgan Demirci, E. *et al.* Genome-Wide Gene Expression Analysis of NIH 3T3 Cell Line Under Mechanical Stimulation. *Cell. Mol. Bioeng.* **4**, 46–55 (2011).
275. Katsumi, a. Integrins in Mechanotransduction. *J. Biol. Chem.* **279**, 12001–12004 (2003).
276. Gemmiti, C. V & Guldberg, R. E. Fluid Flow Increases Type II Collagen Deposition and Tensile Mechanical Properties in Bioreactor-Grown Tissue-Engineered Cartilage. *Tissue Eng.* **12**, 469–479 (2006).
277. Wang, H. J., Bertrand-De Haas, M., Riesle, J., Lamme, E. & Van Blitterswijk, C. A. Tissue engineering of dermal substitutes based on porous PEGT/PBT copolymer scaffolds: Comparison of culture conditions. *J. Mater. Sci. Mater. Med.* **14**, 235–240 (2003).
278. Lamberti, A., Marasso, S. L. & Cocuzza, M. RSC Advances PDMS membranes with tunable gas permeability for micro fluidic applications †.

- RSC Adv.* **4**, 61415–61419 (2014).
279. Soliman, S. *et al.* Controlling the porosity of fibrous scaffolds by modulating the fiber diameter and packing density. *J. Biomed. Mater. Res. - Part A* **96 A**, 566–574 (2011).
280. Jonkman, J. E. N. *et al.* An introduction to the wound healing assay using live-cell microscopy. *Cell Adh. Migr.* **8**, 440–451 (2016).
281. Chen, Y. Scratch Wound Healing Assay. *J. Chem. Inf. Model.* **53**, 1689–1699 (2013).
282. Geback, T., Schulz, M. M. P., Koumoutsakos, P. & Detmar, M. TScratch: A novel and simple software tool for automated analysis of monolayer wound healing assays. *Biotechniques* **46**, 265–274 (2009).
283. Hoon, J. L., Tan, M. H. & Koh, C. The Regulation of Cellular Responses to Mechanical Cues by Rho GTPases. (2016). doi:10.3390/cells5020017
284. Danen, E. H. J. in *Madame Curie Bioscience Database [Internet]* (2013).
285. Miyoshi, H. & Adachi, T. Topography Design Concept of a Tissue Engineering Scaffold for Controlling Cell Function and Fate Through Actin Cytoskeletal Modulation. *Tissue Eng. Part B Rev.* **20**, 609–627 (2014).
286. Chaudhuri, P. K., Pan, C. Q., Low, B. C. & Lim, C. T. Topography induces differential sensitivity on cancer cell proliferation via Rho-ROCK-Myosin contractility. *Sci. Rep.* **6**, 19672 (2016).
287. Doyle, A. D., Petrie, R. J., Kutys, M. L. & Yamada, K. M. Dimensions in Cell Migration. *Curr. Opin. Cell Biol.* **25**, 642–649 (2013).
288. Ke, Y. *et al.* Polysaccharide hydrogel combined with mesenchymal stem cells promotes the healing of corneal alkali burn in rats. *PLoS One* **10**, 1–18 (2015).

289. Carolina Morais Fernandes, A. I. *et al.* Development of experimental in vitro burn model Scientific and intellectual content of the study, interpretation of data and critical revision. *Acta Cirúrgica Bras.* **29**, 15–20 (2014).
290. Porter, B., Zael, R., Stockman, H., Guldberg, R. & Fyhrie, D. 3-D computational modeling of media flow through scaffolds in a perfusion bioreactor. *J. Biomech.* **38**, 543–549 (2005).
291. John E. Hall. *Guyton and Hall Textbook of Medical Physiology E-Book.* (Elsevier, 2016).
292. Paradise, R. K., Lauffenburger, D. A. & van Vliet, K. J. Acidic extracellular pH promotes activation of integrin $\alpha 5 \beta 1$. *PLoS One* **6**, (2011).
293. Swietach, P., Vaughan-Jones, R. D., Harris, A. L. & Hulikova, A. The chemistry, physiology and pathology of pH in cancer. *Philos. Trans. R. Soc. Lond. B. Biol. Sci.* **369**, 20130099 (2014).
294. Zhang, L. *et al.* Ratiometric fluorescent pH-sensitive polymers for high-throughput monitoring of extracellular pH. *RSC Adv.* **6**, 46134–46142 (2016).
295. Ke, G. *et al.* A Cell-Surface-Anchored Ratiometric Fluorescent Probe for Extracellular pH Sensing. *ACS Appl Mater Interfaces* **6**, 15329–15334 (2014).
296. Kato, Y. *et al.* Acidic extracellular microenvironment and cancer. *Cancer Cell Int.* **13**, 89 (2013).
297. Korostynska, O., Arshak, K., Gill, E. & Arshak, A. Review on State-of-the-art in Polymer Based pH Sensors. *Comput. Eng.* **7**, 3027–3042 (2007).
298. Monk, P. M. S. *Physical Chemistry: Understanding our Chemical World.* (Wiley, 2008).
299. Veronica, E. *et al.* Acidity generated by the tumor microenvironment drives local invasion. *Cancer Res.* **73**, 1524–1535 (2014).

300. Gohshi, Y., Huber, J. F. K. & Townshend, T. *TRAC: Trends in Analytical Chemistry*. (Elsevier).
301. Harrington, H., Rose, F. R. A. J., Aylott, J. W. & Ghaemmaghami, A. M. Self-reporting Scaffolds for 3-Dimensional Cell Culture. *J. Vis. Exp.* 50608 (2013). doi:10.3791/50608
302. Gnani, S. *et al.* The effect of electrospun gelatin fibers alignment on schwann cell and axon behavior and organization in the perspective of artificial nerve design. *Int. J. Mol. Sci.* **16**, 12925–12942 (2015).
303. Tang, Y. *et al.* Induction and differentiation of human induced pluripotent stem cells into functional cardiomyocytes on a compartmented monolayer of gelatin nanofibers. *Nanoscale* **8**, 14530–14540 (2016).
304. Pawley, J. in *Handbook of biological confocal microscopy* 367 (Springer, 2006).
305. Blacker, T. S. *et al.* Separating NADH and NADPH fluorescence in live cells and tissues using FLIM. *Nat. Commun.* **5**, 3936 (2014).
306. Ter Braak, M. *et al.* Cis-4-methylsphingosine is a sphingosine-1-phosphate receptor modulator. *Biochem. Pharmacol.* **81**, 617–625 (2011).
307. Echten-deckert, G. Van, Schick, A., Heinemann, T. & Schnieders, B. Phosphorylated cis -4-Methylsphingosine Mimics the Mitogenic Effect of Sphingosine-1-phosphate in Swiss 3T3 Fibroblasts *. **273**, 23585–23589 (1998).
308. Calise, S. *et al.* Sphingosine 1-phosphate stimulates proliferation and migration of satellite cells. *Biochim. Biophys. Acta - Mol. Cell Res.* **1823**, 439–450 (2012).
309. Katsuma, S. *et al.* Signalling mechanisms in sphingosine 1-phosphate-

promoted mesangial cell proliferation. 1217–1230 (2002).

310. Shin, J. H., Choi, G. S., Kang, W. H. & Myung, K. B. Sphingosine 1-phosphate triggers apoptotic signal for B16 melanoma cells via ERK and caspase activation. *J. Korean Med. Sci.* **22**, 298–304 (2007).
311. Davaille, J., Li, L., Mallat, A. & Lotersztajn, S. Sphingosine 1-phosphate triggers both apoptotic and survival signals for human hepatic myofibroblasts. *J. Biol. Chem.* **277**, 37323–37330 (2002).

